An Integrated Model of Shear Wave Anisotropy in the Vicinity of a Hydraulic Fracture

by

Colin D. Brisco

A thesis submitted in partial fulfillment of the requirements for the degree of

Master of Science

in

GEOPHYSICS

Department of Physics
University of Alberta

Abstract

This thesis explores the effect of fluid substitution, pore-pressure diffusion and stresses due to hydraulic fracturing on the elastic velocities and microcrack orientations in the surrounding rock. I develop a workflow incorporating three main components to model the velocity field around the fracture. Fracture induced confining-stresses are analytically modelled using Eshelby's inclusion method, pore-pressure diffusion is numerically modelled and the resulting anisotropic velocity is found by modelling preferential opening/closing of a microcrack distribution using the Anisotropic Poroelasticity model. I investigate two categories of subsurface scenario: an isotropic reservoir experiencing an uniaxial confining-stress perturbation and an anisotropic reservoir experiencing pore-pressure diffusion and a triaxial confining-stress perturbation. I find that the simplified uniaxial-stress implementation is inadequate in approximating the triaxial stress with pore-pressure diffusion implementation, and the region around a hydraulic fracture can be divided into four spatiotemporal zones of differing modelled characteristics: the proximal, compressive, shear and tensile zones.

Preface

Portions of this thesis have been presented at national and international conferences. The material presented in Chapter 3 is based on work that was presented in a poster session at the 2016 GeoConvention in Calgary, Alberta. The material presented in Chapters 4 and 5 is based on work that was presented orally at the 2017 Society of Exploration Geophysicists Annual International Meeting in Houston, Texas.

Acknowledgements

I would like to acknowledge several people who have helped me along the way and whose contributions were integral in the production of this thesis. Thank you to my supervisor, Professor Mirko Van der Baan, who provided valuable discussion, feedback, suggestions and advice. My supervisory committee, including Professors Doug Schmitt and Claire Currie, provided a helpful sounding boarding for my ideas and research direction. Thank you to the sponsors of the Microseismic Industry Consortium and NSERC, whose funding made this research possible. Most importantly, I would like to thank my wife, Michelle, for supporting me through the many hours of researching and writing this thesis.

Contents

List of Tables

List of Figures

List of Symbols

Symbol	Definition
α	effective-stress coefficient
$\alpha_\circ$	spheroidal aspect ratio
β_H	intermediate term in Hudson's Cracked Media calculations
Γ_{HS}	intermediate term in Hashin-Shtrikman-Walpole calculations
γ	term describing crack geometry
γ_G	coefficient of gas adiabatic bulk modulus
γ_{max}	maximum dilation of pore space
δ_{ij}	Kroenecker delta
ϵ	normalized crack density
$\boldsymbol{\epsilon_{**}}$	eigenstrain tensor
$\boldsymbol{\epsilon_\circ}$	far-field strain tensor
$\epsilon_\circ$	initial normalized crack density
$\boldsymbol{\epsilon_t}$	prescribed eigenstrain tensor
ζ_{HS}	intermediate term in Hashin-Shtrikman-Walpole calculations
η	fluid dynamic viscosity
$\Theta(\omega)$	intermediate term in Eshelby exterior point tensor calculations
$\Theta_i(\omega)$	intermediate term in Eshelby exterior point tensor calculations
θ	azimuth in spherical coordinates
ι	intermediate term in diffusivity calculations
κ	permeability tensor
κ_H	intermediate term in Hudson's Cracked Media calculations
Λ_{HS}	intermediate term in Hashin-Shtrikman-Walpole calculations

Symbol	Definition
Λ_{ijkl}	4th-order tensor of dimensionless combinations of Lamé parameters
μ	shear modulus
μ^{HS+}	upper shear modulus Hashin-Shtrikman-Walpole bound
μ^{HS-}	lower shear modulus Hashin-Shtrikman-Walpole bound
$\mu_\circ$	matrix material shear modulus
μ_{dry}	dry rock shear modulus
μ_{HM}	Hertz-Mindlin effective dry-rock shear modulus
μ_I	shear modulus of a crack filling material
μ_{max}	maximum shear modulus of N constituent phases
μ_{min}	minimum shear modulus of N constituent phases
μ_{sat}	fluid-saturated medium effective shear modulus
μ_{soft}	soft-sand model effective dry-rock shear modulus
μ_{stiff}	stiff-sand model effective dry-rock shear modulus
μ_z	takes the value of either μ_{max} or μ_{min}
ν	matrix material Poisson's ratio
$\nu_\circ$	fluid-saturated poroelastic medium Poisson's ratio
ρ	density
$\rho(\omega)$	intermediate term in Eshelby exterior point tensor calculations
ρ'	oil pseudo-density
$\rho_\circ$	reference oil density at standard P-T conditions
ρ_B	brine density
ρ_{eff}	effective medium density
ρ_{fluid}	pore-fluid density
ρ_G	true density of oil with dissolved gas at saturation
$\rho_I(\omega)$	intermediate terms in Eshelby exterior point tensor calculations
ρ_{oil}	density of oil containing dissolved gas at non-standard P-T conditions
ρ_P	pressure-adjusted oil density
ρ_{rock}	matrix material density

Symbol	Definition
ρ_W	pure water density
$\boldsymbol{\sigma}$	triaxial stress tensor
$\boldsymbol{\sigma(x)}$	position dependent external stress field
$\boldsymbol{\sigma}_\circ$	initial far-field stress tensor
$\sigma_\circ$	initial lithostatic stress
σ_c	critical stress of crack closure
σ_{eff}	scalar lithostatic effective stress
σ_H	maximum horizontal principle stress
σ_h	minimum horizontal principle stress
σ_{ij}	confining stress
σ'_{ij}	effective stress
σ_{litho}	lithostatic confining stress
σ_n	stress normal to the crack face
$\boldsymbol{\sigma_t}$	prescribed eigenstress tensor
σ_v	vertical principle stress
ϕ	porosity
$\phi_\circ$	porosity corresponding to a coordination number of 9
ψ	inclination in spherical coordinates
$\psi_\circ$	angle measured from the x_3 axis at which cracks begin to close
Ω	orientation in spherical coordinates (ψ, θ)=$(inclination, azimuth)$
$d\Omega$	normalized differential element of solid angle
ω	intermediate term in Eshelby exterior point tensor calculations
ω_{ij}	coefficients of P-wave velocity in pure water
$\boldsymbol{A}$	4th-order elastic-phase "mismatch tensor"
A	cross-sectional area normal to the pressure gradient
(a, b, c)	semi-axes of a spheroidal crack
(a_1, a_2, a_3)	semi-axes of an ellipsoidal body
APE model	anisotropic poroelasticity model

Symbol	Definition
API	American Petroleum Institute's oil gravity
$\boldsymbol{B}$	4th-order elastic-phase "mismatch tensor"
B_o	coefficient of true oil density with dissolved gas
b_G	coefficient of Z_G and f_G
C	average number of contacts per grain
$\boldsymbol{C^E}$	4th-order effective elasticity tensor of a cracked stressed rock
$\boldsymbol{C^D}$	4th-order perturbation tensor due to a parallel crack distribution
$\boldsymbol{C^G}$	4th-order perturbation tensor due to crack geometry
$\boldsymbol{C^M}$	4th-order effective elasticity tensor of a solid rock matrix
$\boldsymbol{C^R}$	4th-order effective elasticity tensor of a fluid-saturated porous rock
$\boldsymbol{C^r}$	4th-order effective elasticity tensor of a fluid-saturated porous rock at reservoir depth
$\boldsymbol{C^s}$	4th-order effective elasticity tensor of a fluid-saturated porous rock in a zero-stress state
$\boldsymbol{C_\circ}$	initial isotropic 4th-order stiffness tensor of the matrix
$\boldsymbol{C_1}$	isotropic 4th-order stiffness tensor of the inclusion material
C_{ij}	isotropic stiffness coefficients expressed in Voigt notation
$\boldsymbol{C_{ISO}}$	matrix of isotropic stiffness coefficients expressed in Voigt notation
c_{cr}	crack compressibility
CZP	compressive zone point
D	scalar diffusivity
D_{ij}	components of the diffusivity tensor
E_G	coefficient of Z_G and gas adiabatic bulk modulus
$f_\circ$	initial spheroidal fracture radius
f_G	coefficient of gas adiabatic bulk modulus
f_i	volume fraction of the i^{th} phase
f_w	spheroidal fracture half-width
G	gas gravity

Symbol	Definition
g	crack aspect ratio after a confining stress perturbation is applied
$g(\omega)$	intermediate term in Eshelby tensor calculations
$g_\circ$	initial crack aspect ratio
GOR	gas-oil ratio
$\boldsymbol{G(x)}$	4th-order Eshelby exterior point tensor
H	intermediate term in diffusivity calculations
$\boldsymbol{I}$	4th-order identity tensor
int_1	crack distribution search interval for inclination of orientation
int_2	crack distribution search interval for azimuth of orientation
int_3	propagation direction search interval for azimuth and inclination
K	bulk modulus
K^{HS+}	upper bulk modulus Hashin-Shtrikman-Walpole bound
K^{HS-}	lower bulk modulus Hashin-Shtrikman-Walpole bound
$K_\circ$	matrix material bulk modulus
K_{dry}	dry rock bulk modulus
K_f	fracture toughness
K_{fluid}	pore fluid bulk modulus
K_G	adiabatic bulk modulus of gas
K_{HM}	Hertz-Mindlin effective dry-rock bulk modulus
K_I	bulk modulus of a crack filling material
K_{max}	maximum bulk modulus of N constituent phases
K_{min}	minimum bulk modulus of N constituent phases
K_{sat}	fluid-saturated medium effective bulk modulus
K_{soft}	soft-sand model effective dry-rock bulk modulus
K_{stiff}	stiff-sand model effective dry-rock bulk modulus
K_z	takes the value of either K_{max} or K_{min}
M	intermediate term in diffusivity calculations
M_i	corresponding elastic modulus of the i^{th} phase

Symbol	Definition
M_R	lower Reuss bound of a desired elastic modulus
M_V	upper Voigt bound of a desired elastic modulus
M_v	intermediate term in anisotropic velocity calculations
N	number of constituent phases
N_{cr}	number of cracks
N_m	a poroelastic modulus
$\hat{\boldsymbol{n}}$	outward facing unit normal vector
P	pressure
∇P	pressure gradient
P_d	intermediate term in diffusivity calculations
P_{inject}	injection pressure
P_{pore}	pore pressure
P_r	pseudo-pressure
p	dimensionless excess pore-fluid pressure
p_f	pore-fluid pressure in a crack
p_{fo}	initial pore-fluid pressure in a crack
PWA_T	P-wave velocity anisotropy of a transversely isotropic medium
$\mathbf{Q}$	vector volumetric fluid velocity field
$\boldsymbol{R}$	4th-order rotation tensor
R	gas constant ($8.31441 J/g{\cdot}mol{\cdot}deg$)
R_G	the gas-oil ratio at standard P-T conditions
r	normalized pore-fluid compressibility
$\boldsymbol{S}$	4th-order Eshelby interior point tensor
S	salinity
$S^{(m)}$	intermediate term in Eshelby tensor calculations
s_{ij}	dimensionless differential stress
s_v	dimensionless vertical differential stress
SWA	S-wave velocity anisotropy in a single propagation direction

Symbol	Definition
SWA_{max}	maximum *SWA* over all propagation directions
SWA_T	S-wave velocity anisotropy of a transversely isotropic medium
SWA_{vert}	*SWA* for propagation in the vertical direction
T	temperature
T_a	absolute temperature
T_r	pseudo-temperature
t	time
t_{inject}	injection duration
t_{model}	modelling duration
TZP	tensile zone point
U_1	intermediate term in Hudson's Cracked Media calculations
U_3	intermediate term in Hudson's Cracked Media calculations
V	volume
v_B	P-wave velocity in brine
v_p	P-wave velocity
Δv_p	a measure of P-wave velocity sensitivity;
	separation between parameter velocity curves for a specific porosity
$v_{p,fluid}$	pore-fluid P-wave velocity
$v_{p,matrix}$	rock matrix P-wave velocity
$v_{p,oil}$	P-wave velocity in oil with dissolved gas
$\Delta v_{p,total}$	a measure of P-wave velocity sensitivity;
	total P-wave velocity change over a range of effective stress
v_{qp}	quasi P-wave phase velocity
v_{qsv}	quasi S-wave phase velocity
Δv_s	a measure of S-wave velocity sensitivity;
	separation between parameter velocity curves for a specific porosity
$\Delta v_{s,total}$	a measure of S-wave velocity sensitivity;
	total S-wave velocity change over a range of effective stress

Symbol	Definition
v_{sh}	pure S-wave phase velocity
v_W	P-wave velocity in pure water
$\boldsymbol{x}$	position vector
Z_G	coefficient of gas density at non-standard P-T conditions
z_{soft}	intermediate term in the soft-sand model calculations
z_{stiff}	intermediate term in the stiff-sand model calculations

Chapter 1

Introduction

1.1 Hydraulic Fracturing

The technique of hydraulic fracturing has been known for over 70 years with the first hydraulic fracturing experiment being performed in 1947 (King, 2012). By 2012 the Society of Petroleum Engineers estimates that approximately 2.5 million hydraulic fracturing treatments had been completed globally. The process of hydraulic fracturing is primarily used to maximize recovery of hydrocarbons from producing reservoirs and to facilitate hydrocarbon recovery from unconventional reservoirs, such as shale-gas and tight-gas plays (Van der Baan et al., 2013). The introduction of horizontal drilling coupled with improvements in hydraulic fracturing technology has led to a boom in unconventional resource production. In 2000 only 1% of the total hydrocarbon gas production in the United States originated from shale-gas fields. Compare that to 2016 where the United States Energy Information Administration estimates that approximately 70% of dry natural gas produced in the United States originated from shale-gas and tight-gas fields (US EIA, 2016). Figure 1.1 illustrates that in North America alone there are several untapped prospective shale plays, indicating that there is still room for growth in the unconventional sector. This potential for growth is reflected in the United States Energy Information Ad-

ministrations 2040 projection for dry natural gas production, see Figure 1.2. By 2040, approximately 85% of the total United States dry natural gas production is projected to originate from shale-gas and tight-gas plays with the majority of growth expected from shale-gas plays.

Improved hydrocarbon recovery is not the only useful application of hydraulic fracturing. For example, the efficiency of heat transfer in enhanced geothermal systems has been improved by hydraulically fracturing hot impermeable crystalline rock, such as granite (Shao et al., 2015).

Figure 1.1: A map of current and prospective shale plays in North America. Source: US EIA (2016).

The process of hydraulic fracturing first involves drilling a well, either vertical or horizontal, into a target formation. Then fluids are injected into the formation via the well-bore under high pressures with the goal of inducing the growth of a fracture or fracture network into the reservoir (Van der Baan et al.,

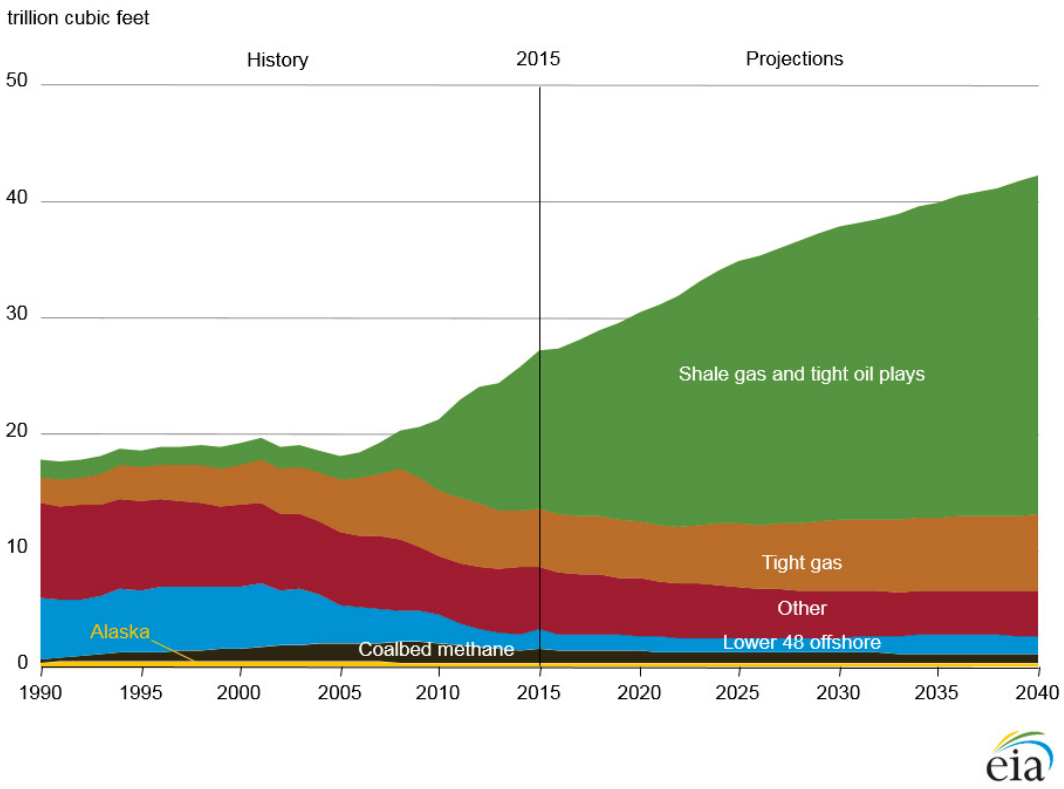

Figure 1.2: United States dry natural gas production broken down by source for 1990 to 2015 with projections of production extended to 2040. Source: US EIA (2016).

2013). High pressures are needed in order to reverse the flow of fluids back into the reservoir (King, 2012). The fracture or fracture network will enhance reservoir drainage by increasing the effective permeability of the reservoir rock by creating high permeability flow paths through the fractures themselves. The volume of the reservoir that has been connected to the well-bore by the high permeability flow paths is referred to as the stimulated reservoir volume. The fracturing fluids often contain a granular proppant to help maintain the fracture aspect ratio during production. Hydraulic fractures are typically two to three millimetres in width and are often oriented such that the plane of the fracture is perpendicular to the minimum confining-stress direction.

1.2 Thesis Motivation

In order to estimate the stimulated volume of the reservoir, a complete 'image' of the hydraulic fracture network is needed. However, there are no direct methods of completely imaging a fracture in the subsurface. Borehole cameras can be used to directly image the extent of a fracture at the borehole walls (King, 2012). This method requires a clear fluid in the borehole and most cameras do not function under high pressures. More importantly, images obtained with a borehole camera fail at capturing the full extent of the fracture into the rock formation.

There are several indirect methods of estimating the stimulate volume including tilt meter measurements and microseismic event locations. Event locations of microseismic events provide the most complete 'image' and are commonly used to create a map of the fracture system. Microseismic measurements allow for near real-time mapping of the fracture system. However, there is currently a large degree of uncertainty inherent in event location positioning and this can lead to an incomplete or incorrect fracture map (Van der Baan et al., 2013). This uncertainty can lead to different service companies obtaining different event locations using the same dataset.

One source of uncertainty is that current emphasis is placed on mapping brittle failure but evidence indicates that only a small portion of the total energy injected into the subsurface is released through brittle failure (Maxwell et al., 2009). Up to 85% of the input energy may be released aseismically or at frequencies that are too low to be detected using current recording instruments (Maxwell et al., 2008; Boroumand and Eaton, 2012).

Another source of event location uncertainty stems from the demand for near real-time hypocentre locations. Currently, real-time microseismic processing requires automation and information reduction. Uncertainty arises from the use of different event location algorithms, the choice of how to consistently pick

P- an S-wave arrivals in large datasets and the choice of the most appropriate velocity model (Van der Baan et al., 2013).

A recent study by Nolte et al. (2017) shows that time-lapse seismic observations of variation in S-wave splitting over time can be used to detect pore-pressure increases in the subsurface. S-wave splitting is caused by orthogonally polarized S-waves having different velocities which is caused by anisotropy. S-wave splitting and elastic anisotropy are discussed in more detail in Chapter 2 and Chapters 4 to 6. Velocity anisotropy can be caused by the opening and closing of preferentially oriented fractures and cracks, for instance due to changes in pore-pressure and/or elastic-stress perturbations, such as those occurring during hydraulic fracturing treatments. S-wave splitting as a result of pore-pressure changes has been observed in the field. Any three component microseismic dataset could contain information regarding S-wave splitting. Therefore, if we understand the processes acting around a given hydraulic fracture that influence seismic velocities, we can predict the velocity character that will manifest in the vicinity of a hydraulic fracture and vice versa.

The goal of this thesis to develop an additional tool that can be used along with tilt meter measurements and microseismic event locations to create hydraulic fracture maps with lower associated uncertainty. To achieve this goal we develop a model that integrates the geomechanics of hydraulic fracture opening/closing and the rock physics of seismic velocity determination. Hence, observations of seismic velocity changes and changes in velocity anisotropy may enable a more accurate 'image' of the fracture system. Additionally, this model may be used with seismic velocity measurements to reveal information about the reservoir in-situ stress field that can aid operators in optimizing fracture treatments.

1.3 Thesis Organization

This thesis is organized into an introduction chapter, Chapter 1, followed by five stand-alone studies, Chapters 2 to 6, and ending with a summary chapter, Chapter 7. The summary chapter also includes a section on suggested future work that could extend the body of knowledge produced in this thesis. The five stand-alone studies follow a logical progression of topics involved in building an integrated model of velocity anisotropy in the vicinity of a hydraulic fracture, as outlined below.

1.3.1 Chapter 2 - A Review of Processes Affecting Seismic Velocities

In Chapter 2, we discuss the processes that occur in the vicinity of a hydraulic fracture that affect seismic velocities. We introduce the processes of fluid invasion, pore-pressure perturbation and confining-stress change. Then we discuss the predicted effect of each process on P- and S-wave velocities and the predicted effect on elastic anisotropy.

1.3.2 Chapter 3 - Isotropic Velocity Sensitivity

In Chapter 3, we consider the case of a hydraulic fracture in an isotropic medium. We develop a workflow to model the isotropic P- and S-wave velocity response to fluid invasion, pore-pressure perturbation and confining-stress change. Then we perform a sensitivity analysis on the model input parameters and discuss the results in regards to the volume of rock around a hydraulic fracture.

1.3.3 Chapter 4 - Pore-Pressure Diffusion and Confining-Stress Modelling

In Chapter 4, we consider the case of a hydraulic fracture growing in a low-porosity, isotropic reservoir. We develop a workflow to model triaxial confining-stress change and hydrostatic pore-pressure perturbation in the vicinity of the fracture. Then we combine the stress and pressure changes as effective stress change and discuss the results in the context of the predicted effect on seismic velocities.

1.3.4 Chapter 5 - Uniaxial Stress: Anisotropic Velocity Sensitivity

In Chapter 5, we consider the case of a hydraulic fracture in an initially isotropic medium that contains an isotropic distribution of microcracks. We assume that the permeability of the medium is very small and we ignore pore-pressure changes. We focus on the large region adjacent to the fracture faces that experiences compressive stress and we assume that the compressive stress in this region is uniaxial. Then we use the Anisotropic Poroelasticity model of Crampin and Zatsepin (1997) and Zatsepin and Crampin (1997) to model the anisotropic velocity response and we perform a sensitivity analysis on the model input parameters. Finally, we discuss the results in regards to the volume of rock around a hydraulic fracture.

1.3.5 Chapter 6 - Triaxial Stress: Shear Wave Anisotropy

In Chapter 6, we consider the case of a hydraulic fracture growing in an initially anisotropic medium. The initial anisotropy is the result of a triaxial in-situ stress field causing an anisotropic microcrack distribution. We develop a workflow model the heterogeneous anisotropic S-wave velocity response in the vicinity of the fracture by integrating a modified version of Crampin and

Zatsepin (1997) and Zatsepin and Crampin (1997)'s Anisotropic Poroelasticity model with the pore-pressure perturbation and triaxial confining-stress change models from Chapter 4. Finally, we discuss the results in regards to the volume of rock around a hydraulic fracture.

1.3.6 Chapter 7 - Summary and Future Work

Chapter 7 contains the conclusions and the recommendations for future research.

Chapter 2

A Review of Processes Affecting Seismic Velocity

As a hydraulic fracture is propagated and held open by the injected high pressure fluids, several processes occur simultaneously that change the physical environment in the rock volume surrounding the fracture. These processes include pore-pressure diffusion, fracturing fluid invasion and rock matrix deformation (Cipolla et al., 2011; Warpinski, 1994; Warpinski et al., 2004). Figure 2.1 illustrates the relative regions of influence of pore-pressure diffusion, fracturing fluid invasion and rock matrix deformation. A decaying pressure gradient is created between the high-pressure fracture and the lower-pressure, far field, reservoir pore space. This pressure gradient drives the displacement of reservoir pore fluids by fracturing fluids. The fracturing fluids flow through the walls of the fracture into the porous reservoir rock and into existing natural fractures that intersect the hydraulic fracture. Additionally, the opening of a fracture involves the displacement of rock away from a plane oriented along the median of the fracture. This displacement induces perturbations to the in-situ confining-stress field in the rock volume near the fracture. The combined effect of these three processes will alter the bulk mechanical properties of the reservoir close to a hydraulic fracture and these changes should be detectable using

seismic data.

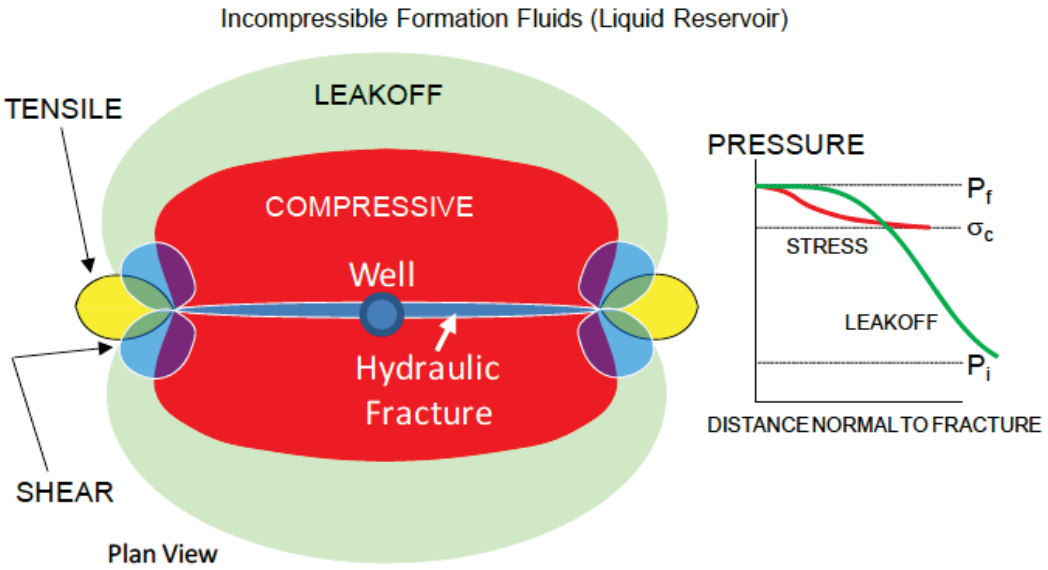

Figure 2.1: A horizontal cross-section through a vertical hydraulic fracture extending from a vertical well illustrating the relative zones of influence of pore pressure, rock deformation and crack propagation in the surrounding region, modified from Cipolla et al. (2011). The term leakoff refers to pore-pressure changes due to fluid invasion into the pore system of the reservoir. The spatial extent of the leakoff region is time dependent and at the initiation of fluid injection has a much smaller spatial extent than shown here. This cross-section is a "snapshot" in time after fluid invasion has had sufficient time to reach the present spatial extent. In this figure, Cipolla et al. (2011) denotes fluid injection pressure as P_f, confining stress as σ_c and initial pore pressure as P_i. We limit the use of Cipolla et al. (2011)'s symbology to this figure alone.

2.1 Pore-Pressure Diffusion

During a hydraulic fracture treatment the pressure in the fracture is raised above that of the in-situ reservoir pore pressure. This creates a spatial pressure gradient that decays with increasing distance from the fracture (Howard, 1970). The pressure gradient itself will also decay with increasing time from the termination of the treatment. The shape of this spatiotemporal pressure gradient is controlled by many parameters including, the difference between fracture

and reservoir pressure, the reservoir and natural fracture permeabilities, reservoir porosity, and the fracture and reservoir fluid density and compressibility (Warpinski, 1994). For example, a highly-compressible gas saturated reservoir will exhibit a steep pressure gradient due to the inefficiency of a compressible gas in communicating pressure through the pore system. However, in a liquid-saturated reservoir the pressure gradient will be more gradual, and will extend a further distance from the fracture.

By considering the effect of elevated pore pressure in the region of a single spherical fluid-filled pore we can understand the resultant changes in rock density and seismic velocities. Increased pressure within a pore tends to force the surrounding rock grains apart, thus tending to increase the volume of the pore. The effective density, ρ_{eff}, of the effective medium describing a porous rock is given by the following equation:

$$\rho_{eff} = (1 - \phi)\rho_{rock} + \phi\rho_{fluid}\,, \tag{2.1}$$

where ϕ is the porosity of the effective medium, ρ_{rock} is the density of the rock and ρ_{fluid} is the density of the pore fluid (Jaeger et al., 2007). Equation 2.1 shows that an increase in porosity will result in a decrease in effective density, as solid rock is generally more dense than common pore saturating fluids (i.e. brine and hydrocarbons). A decrease in effective density will tend to cause an increase in S-wave velocity. This can be seen by considering the equation for S-wave velocity in a homogeneous, isotropic, elastic medium:

$$v_s = \sqrt{\frac{\mu}{\rho_{eff}}}\,, \tag{2.2}$$

where v_s is the S-wave velocity, μ is the shear modulus and ρ_{eff} is the effective density of the medium (Mavko et al., 2009). The shear modulus is determined only by rock matrix properties as it is insensitive to changes in pore fluids. The effect of increased pore pressure on P-wave velocity can be seen by considering

Wyllie's time-average equation for P-wave velocity in porous, isotropic, fluid-saturated rock under high pressure. Based on laboratory measurements on porous sedimentary rocks, Wyllie et al. (1956) gave a empirical expression for P-wave velocity, v_p, in fluid-saturated porous rock,

$$\frac{1}{v_p} = \frac{\phi}{v_{p,fluid}} + \frac{1-\phi}{v_{p,matrix}}\,, \tag{2.3}$$

where $v_{p,fluid}$ is the P-wave velocity in the fluid, $v_{p,matrix}$ is the P-wave velocity in the matrix alone, and ϕ is the porosity of the rock. Typical sedimentary rocks have P-wave velocities in the range of 5480-7925 m/s (Mavko et al., 2009), whereas fluid hydrocarbons and water typically have P-wave velocities that are less than 2000 m/s (Batzle and Wang, 1992). Equation 2.3 is interpreted by (Mavko et al., 2009) as the P-wave travel time through the fluid-saturated rock is the sum of the travel time through the rock matrix and the fluid-filled pore. Hence, increasing the volume of pore space will increase the relative contribution of travel time through the pore fluid, resulting in a lower P-wave velocity in the fluid-saturated rock. It should be noted that while the concept of travel time through small pores is not physically valid for exploration seismic signals which have wavelengths on the order of tens or hundreds of meters, Wyllie's empirical relationship nonetheless approximates lab observations and we simply use it to demonstrate the concept of P-wave velocity sensitivity to pore pressure.

2.2 Fluid Invasion

A hydraulic fracture is filled with a high-pressure fracturing fluid and is surrounded by a porous reservoir that is characterized by lower-pressure pore fluids. The resulting pressure gradient will drive fracturing-fluid flow through the surfaces of the fracture. The fluid flow can be modelled based on Darcy's Law as given by Mavko et al. (2009):

$$\mathbf{Q} = -\frac{\kappa}{\eta} A \nabla P, \tag{2.4}$$

where $\mathbf{Q}$ is the vector volumetric fluid velocity field, κ is the permeability tensor, η is the dynamic viscosity of the fluid, A is the cross-sectional area normal to the pressure gradient, and ∇P is the pressure gradient. Formation fluid will be replaced with the fracturing fluid in a temporally expanding zone around the hydraulic fracture.

The effect of fluid substitution on seismic velocities can be seen by considering the isotropic P-wave, v_p, and S-wave, v_s, velocity equations for a fluid-saturated poroelastic effective medium, for example (Jaeger et al., 2007):

$$v_p = \sqrt{\frac{3K_{sat} + \frac{4}{3}\mu_{sat}}{\rho_{eff}}}, \tag{2.5}$$

and

$$v_s = \sqrt{\frac{\mu_{sat}}{\rho_{eff}}}, \tag{2.6}$$

where ρ_{eff} is the effective density given by equation 2.1, K_{sat} and μ_{sat} are the effective bulk modulus and effective shear modulus of the saturated medium respectively. The effect of pore-fluid substitution on seismic velocities is twofold. First, variation in fluid density will inversely effect seismic velocity. Second, variation in elastic moduli of the effective medium will directly effect seismic velocity. The low frequency Gassmann-Biot theory can be used to predict the expected change in the relevant elastic moduli (Gassmann, 1951; Biot, 1956). Mavko et al. (2009) give the Gassmann equations for effective bulk and shear moduli of a fluid saturated rock respectively as:

$$K_{sat} = K_{dry} + \frac{(1 - \frac{K_{dry}}{K_\circ})^2}{\frac{\phi}{K_{fluid}} + \frac{(1-\phi)}{K_\circ} - \frac{K_{dry}}{K_\circ^2}}, \tag{2.7}$$

and

$$\mu_{sat} = \mu_{dry}, \tag{2.8}$$

where K_{dry} is the bulk modulus of the dry rock, K_{fluid} is the bulk modulus of the pore fluid, $K_\circ$ is the bulk modulus of the matrix material, ϕ is the porosity, and μ_{dry} is the shear modulus of the dry rock. Combining equation 2.6 and equation 2.8 we see that the S-wave velocity is only affected by the change in density of a replacing fluid. In the case of a higher-density fluid replacing a lower-density fluid, for example brine replacing fluid hydrocarbons, S-wave velocity will tend to decrease. Conversely, in the case of increasing gas saturation, that is a low density fluid replacing high density fluid, S-wave velocity will tend to increase as shown in Figure 2.2.

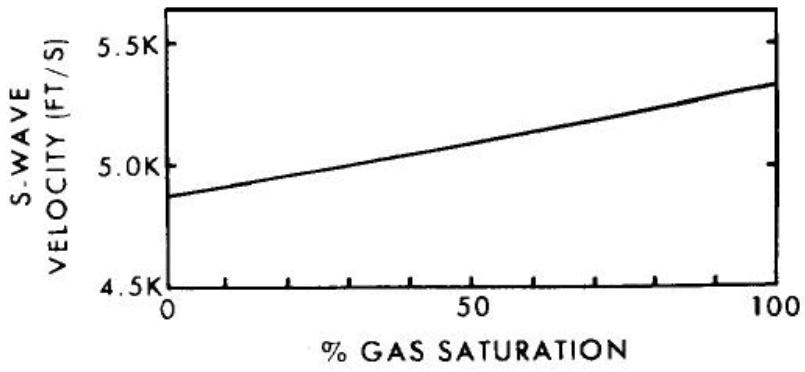

Figure 2.2: Theoretical S-wave velocities calculated using the equations from Gassmann (1951) for increasing gas saturation in a thirty-five percent porosity sandstone buried at 1828 meters, modified from Ostrander (1985).

By considering equations 2.5 and 2.7 we see that P-wave velocity is affected by variations in both fluid density and effective bulk modulus, with the bulk modulus being the dominant contributor. The effect of fluid substitution on P-wave velocity can be seen in Figure 2.3 where Landro (2001) used the Gassmann equation for effective bulk modulus calibrated to well log data to model the effect of increasing water saturation of P-wave velocity. Increasing the water

saturation tends to increase the effective density and the effective bulk modulus. The increase in density tends to decrease P-wave velocity and the increase in bulk modulus tends to increase the P-wave velocity. Figure 2.3 clearly shows that the effect of increasing bulk modulus overwhelms the effect of increasing density resulting in a positive correlation between water saturation and P-wave velocity.

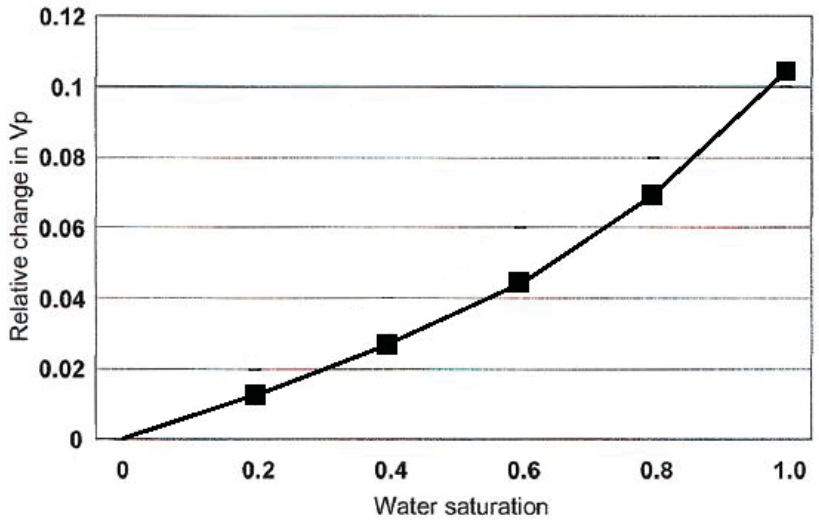

Figure 2.3: Theoretical P-wave velocities calculated using the equations from Gassmann (1951) calibrated to wells in the Gullfaks field, North Sea for increasing water saturation, modified from Landro (2001).

2.3 Matrix Deformation

When a hydraulic fracture is opened under pressure a volume of rock is displaced in a direction normal to the face of the fracture. This displacement induces changes in the confining-stress distribution surrounding the fracture. Analytic solutions to model the changes in stress have been developed for several simple crack geometries (Green and Sneddon, 1950; Eshelby, 1957). These models assume a constant uniform pressure in the crack and an effective matrix medium that is homogenous, isotropic, linear-elastic. Warpinski et al. (2013)

use the pressurized 3D elliptical crack model of Green and Sneddon (1950) to calculate the perturbation of confining stress in the three principle directions. As seen in Figure 2.4, moving in a direction normal to the crack face the total normal stress is increased, with the largest increase in compressive stress experienced in the direction normal to the crack face. In contrast, moving in a direction parallel to the crack at the crack tip, the change in confining stress is seen to be tensile in both horizontal principle directions and nearly zero in the vertical direction as seen in Figure 2.5. There will be a zone of shear stress between the compressive and tensile zones. The equations used for the calculations can be found in Warpinski et al. (2004). The magnitude of stress change is determined by the size of the fracture, the pressure maintained in the fracture, and the elastic moduli of the rock.

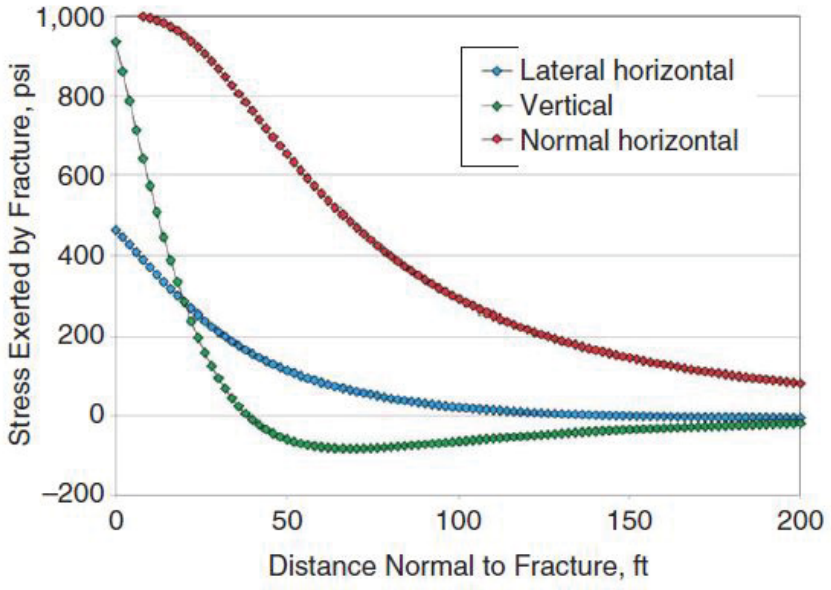

Figure 2.4: Magnitude of induced stress as a function of distance from a vertical hydraulic fracture in the direction normal to the fracture face in the plane containing the centreline of the fracture, modified from Warpinski et al. (2013).

Consider the case in which the reservoir in the vicinity of a hydraulic fracture has a dual character porosity of macro- and micro-porosity. The macro-pore

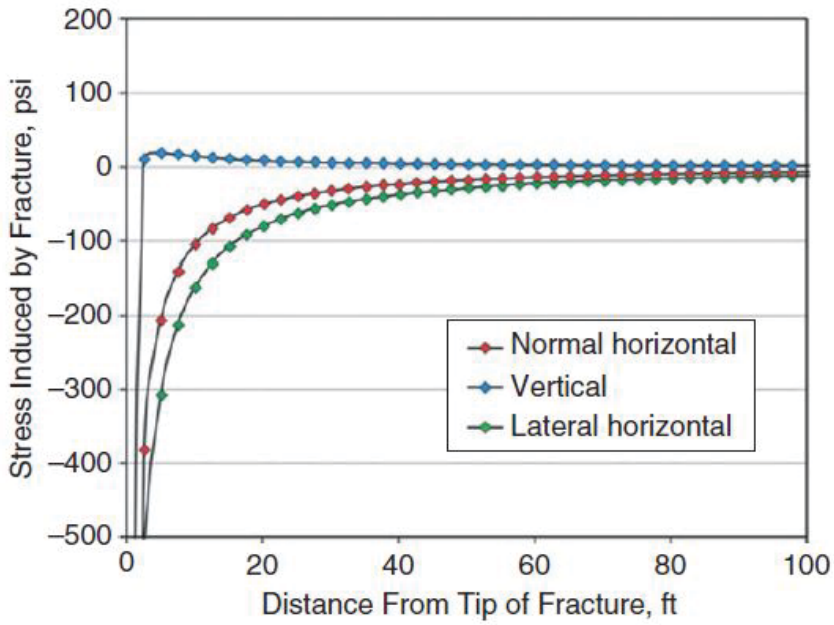

Figure 2.5: Magnitude of induced stress as a function of distance from a vertical hydraulic fracture in the direction ahead of the length tip of the fracture in the plane of the fracture, modified from Warpinski et al. (2013).

system consists of stiff approximately equant shaped pores and the micro-pore system consists of an isotropic (random) distribution of compliant microcracks. After the fracture is opened, the region adjacent to the fracture face will experience an increase in compressive stress. The porosity of the macro-pore system will tend to be reduced and the isotropic P-wave and S-wave velocities will tend to change in the opposite direction from that due to a pore-pressure increase. Now, recall that the confining-stress increase adjacent to the fracture face is the largest in the direction normal to the plane of the fracture. We can approximate this stress change as an uniaxial compression and consider the behaviour of the micro-pore system. An uniaxial compression will tend to close those microcracks with face-normals that are parallel or nearly parallel to the direction of compression. In contrast, those microcracks with face-normals perpendicular or nearly perpendicular to the direction of compression will tend to remain open, see Figure 2.6. This results in the development of an anisotropic microcrack

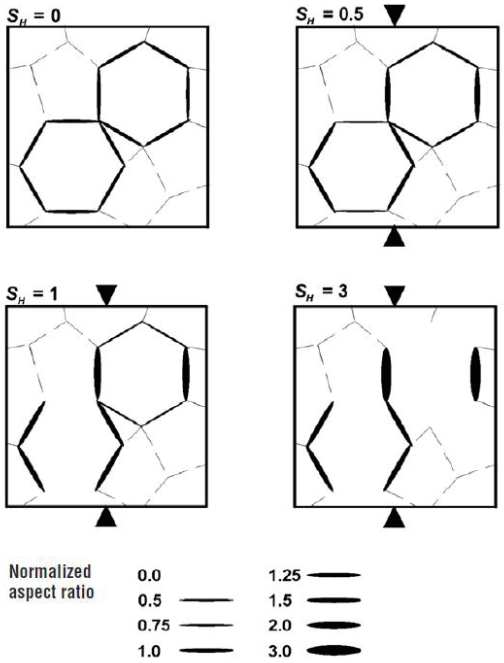

Figure 2.6: Illustration of the development of preferential microcrack orientation in an initially isotropic distribution of vertical microcracks under conditions of increased maximum horizontal stress, S_H. This figure is modified from Crampin (2003).

distribution, and consequently an elastically anisotropic matrix (Nur, 1971). Using ultrasonic wave measurements on uniaxially and triaxially stressed rock samples, many studies have demonstrated that an anisotropic microcrack distribution will influence the elastic anisotropy of the rock as a whole (Sayers et al., 1990; Scott et al., 1993; Nur and Simmons, 1969). In general, these studies revealed that seismic wave velocity is most reduced when the normals to the planes of the preferentially aligned microcracks are parallel to either the direction of wave propagation or polarization, see Figure 2.7.

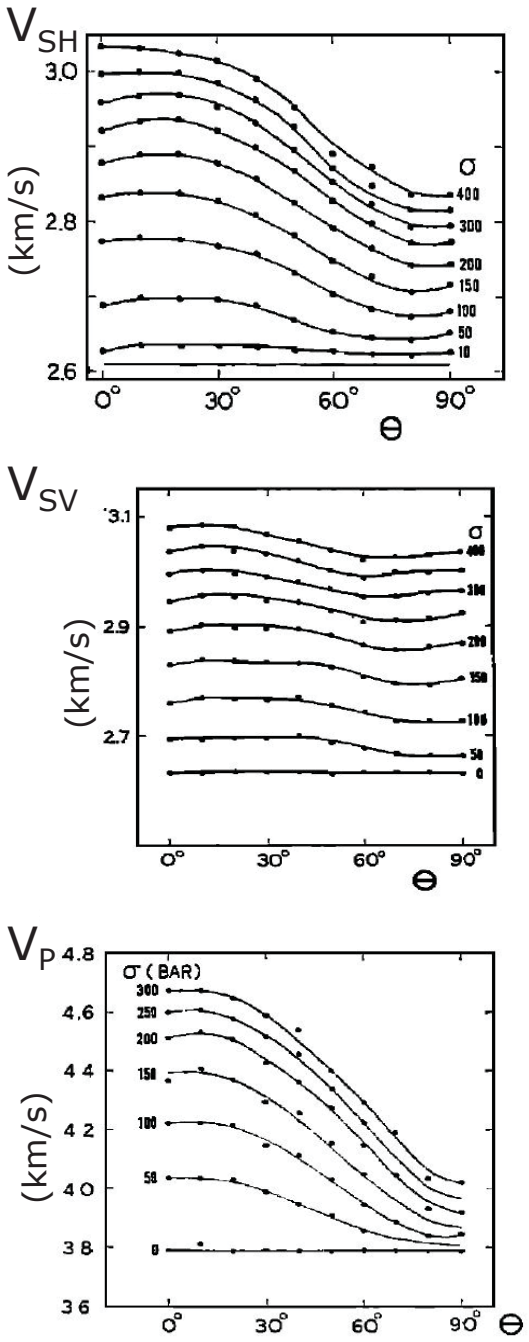

Figure 2.7: P-wave and S-wave velocities for various magnitudes of uniaxial applied stress as a function of the angle of propagation, θ, with respect to the axis of applied stress, modified from (Nur and Simmons, 1969). The plane of polarization for v_{SH} always contains the direction of uniaxial stress. Nur and Simmons (1969) obtained these results from labratory measurements made on samples of Barre granite.

2.4 Pore Pressure and Confining Stress Combined

To consider the combined effect of elevated pore pressure and perturbations of confining stress on density, seismic velocity, and fracture orientations we need to introduce the effective-stress concept. Effective stress, σ'_{ij}, is defined the difference between the confining stress, σ_{ij}, and the pore pressure, P_{pore}, with the pore pressure scaled by an effective-stress coefficient, α (Brandt, 1955). By convention, compressive stress and pressure are assigned positive values. The general form of effective stress is given by,

$$\sigma'_{ij} = \sigma_{ij} - \alpha P_{pore}\delta_{ij}, \tag{2.9}$$

with δ_{ij} being the Kroenecker delta. Berryman (1992) and Zimmerman (1991) theoretically predict that elastic moduli of a porous monomineralic rock are a function of effective stress with the effective-stress coefficient equal to one. The assumption of a monomineralic reservoir matrix may not always be appropriate, and Mavko et al. (2009) note that experimental results show the effective-stress coefficient for elastic moduli is often less than one. It can be seen from equation 2.9 that a pore-pressure increase and/or confining-stress decrease will result in a decrease in effective stress. Conversely, a pore-pressure decrease and/or confining-stress increase will result in an increase in effective stress.

The effective density of rock will tend to vary in direct proportion to effective stress. The relation between effective stress and microcrack orientation is more complex, also depending on the magnitude of the critical stress of individual microcracks. The critical stress is the minimum stress required to collapse a microcrack applied in the direction normal to the crack face. Consider an isotropic distribution of uniform penny-shaped microcracks contained in a homogeneous rock matrix. A penny-shaped crack is the special case of an ellipsoidal body with semi-axes ($a_1 \ll a_2 = a_3$) and the aspect ratio is given

by ($\frac{a_1}{a_2} << 1$). Zatsepin and Crampin (1997) give the critical stress, σ_c, of a penny-shaped crack as:

$$\sigma_c = \frac{1}{c_{cr}} = (\frac{\pi}{2})\frac{g_\circ \mu_\circ}{(1-\nu)}\,, \tag{2.10}$$

where c_{cr} is crack compressibility, $g_\circ$ is the initial aspect ratio of the microcrack, and ν and $\mu_\circ$ are respectively the Poisson's ratio and shear modulus of the rock matrix. Let us assume a simple scenario of an uniaxial confining-stress increase. If this confining-stress increase is larger than the increase in pore pressure and the resulting effective stress is equal to the crack critical stress, any microcracks with face normals aligned in the same direction as the uniaxial stress will collapse. Conversely, microcracks with face normals oriented in any other direction will remain open. Fracture anisotropy, and consequently elastic anisotropy, will develop as seen in Figure 2.6. Alternatively, if the resulting effective stress is less than the crack critical stress then microcracks of all orientations will remain open and no fracture anisotropy will develop. The same is always true if the increase in confining stress is less than the increase in pore pressure.

The Hertz-Mindlin grain contact model can be utilized to show the connection between effective stress and the reservoir dry-rock bulk modulus and shear modulus, hence the P-wave and S-wave velocities (Mavko et al., 2009). The model was developed by Mindlin (1949) to describe a precompacted, unconsolidated, dry, random packing of identical spherical grains experiencing lithostatic confining stress in terms of dry-rock bulk and shear moduli, K_{dry} and μ_{dry} respectively. It is assumed in the model that there is no slip between grains and no relative grain rotation. The effective moduli are given by Dvorkin and Nur (1996) as,

$$K_{dry} = \sqrt[3]{\frac{C^2(1-\phi)^2\mu_\circ^2}{18\pi^2(1-\nu)^2}\sigma_{eff}}, \tag{2.11}$$

and

$$\mu_{dry} = \left[\frac{5-4\nu}{5(2-\nu)}\right] \sqrt[3]{\frac{3C^2(1-\phi)^2\mu_\circ^2}{2\pi^2(1-\nu)^2}\sigma_{eff}}, \tag{2.12}$$

where C is the average number of contacts per grain, ϕ is porosity, $\mu_\circ$ is the shear modulus of the solid grains, ν is the Poisson's ratio of the solid grains, and σ_{eff} is a scalar lithostatic effective stress given by equation 2.9. In general, seismic velocities increase with increasing effective stress and by extension decreasing pore pressure. This is in agreement with the Hertz-Mindlin model, as seen in Figure 2.8. The obvious drawbacks to using the Hertz-Mindlin model to describe reservoir rock are that real reservoirs are fluid or gas saturated, they are commonly consolidated, and the grains are not identical or perfectly spherical.

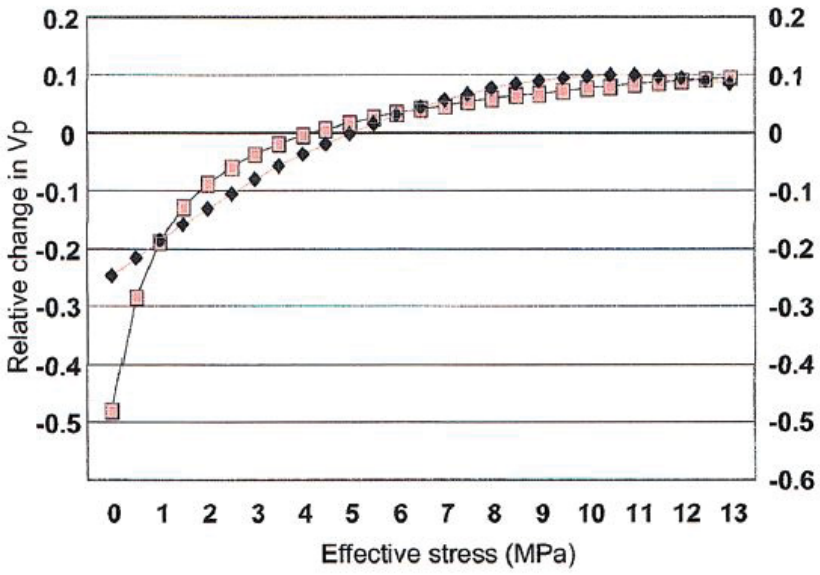

Figure 2.8: Relative change in P-wave velocity as a function of increased effective stress, modified from (Landro, 2001). The squares represent measurements made on twenty-nine dry rock core samples from the Gullfaks field, North Sea and the black diamonds represent a second-order approximation. Negative relative velocity change corresponds to increased pore pressure or decreased confining stress. Positive relative velocity change corresponds to decreased pore pressure or increased confining stress.

2.5 Implications

The net effect of pore-pressure diffusion, fluid invasion and matrix deformation is the creation of four spatiotemporal zones surrounding a hydraulic fracture: the proximal zone, the compressive zone, the tensile zone and the shear zone. The velocity behaviour in each of the four zones is discussed in the Subsections 2.5.1 to 2.5.4 by considering the case of a hydraulic fracture in a reservoir that initially contains a macropore system of equant pores and a micropore system of isotropically distributed penny-shaped microcracks. The spatial extent of the four zones depends on reservoir, pore fluid and hydraulic fracture properties, the details of which are discussed in Chapter 4. Figure 2.9 shows the relative spatial extent of each zone for two reservoir scenarios. In the first scenario, the reservoir has a very low permeability and pore-pressure diffusion is limited to a narrow region adjacent to the hydraulic fracture. In the second scenario, the reservoir permeability is high and pore-pressure diffusion extends further from the hydraulic fracture. The temporal dependancy is explained by considering a growing hydraulic fracture versus a fracture of fixed size. As the hydraulic fracture is growing, all four zones will continue to grow. If the fracture stops growing, the extent of the confining-stress perturbations will remain constant but the extent of pore-pressure changes will continue to expand.

2.5.1 Proximal Zone

The proximal zone is the region directly adjacent to the hydraulic fracture that experiences fluid replacement, the largest pore-pressure increase, and the largest confining-stress perturbation. In the case of a brine fracturing fluid and a hydrocarbon reservoir fluid, fluid replacement will tend to increase the effective density and decrease S-wave and P-wave isotropic velocities. Increased pore pressure tends to open all pores, both macro- and micro-sized ones, resulting in a decrease in S-wave and P-wave isotropic velocities. Increased pore

pressure on its own will not result in the development of anisotropy because all microcracks are initially open. However, the proximal zone also experiences a confining-stress perturbation and can be subdivided into two zones of triaxial confining-stress change. One region adjacent to the fracture tip experiences a reduction in confining stress and a second region adjacent to the fracture face experiences an increase in confining stress. In the tip proximal zone, the decrease in confining stress acts in concert with the increased pore pressure, resulting in no velocity anisotropy development and a decrease in S-wave and P-wave isotropic velocities. In the face proximal zone, confining-stress increase will tend to close preferentially oriented microcracks and the pore-pressure increase will act in opposition to open all microcracks. If pore-pressure diffusion effects dominate then S-wave and P-wave isotropic velocities will tend to decrease and stress-induced fracture and velocity anisotropy will not develop. However, if confining-stress effects dominate then S-wave and P-wave isotropic velocities will tend to increase and preferentially oriented microcracks will tend to close, resulting in the development of stress-induced microcrack and velocity anisotropy.

2.5.2 Compressive Zone

The region normal to the hydraulic fracture face from the outer surface of the face proximal zone to a variable distance from the hydraulic fracture face is the compressive zone. The transition from the proximal zone to the compressive zone is loosely defined as the extent of significant pore-pressure increase. As is discussed in Chapters 4 and 6, the determination of what constitutes a significant pore-pressure increase depends on several reservoir, pore-fluid and microcrack parameters, including but not limited to reservoir velocities, pore-fluid compressibility and initial microcrack aspect ratio. The same balance of pore-pressure and confining-stress increase exhibited in the proximal zone exists here, but with the confining-stress perturbations being generally larger in

magnitude than the pore-pressure increases. As seen in Figure 2.9, the relative size of the proximal zone is affected by reservoir permeability and can be seen by considering two end-member scenarios. In the first scenario, the reservoir has high permeability and the pore-pressure gradient is effectively communicated through the pore system such that it extends beyond a distance of one half the hydraulic fracture height. At distances greater than one half the hydraulic fracture height the effect of confining-stress increase will be negligible (Warpinski, 2009). In this scenario, the compressive zone is entirely absent and only the proximal zone exists. In the alternate scenario, the reservoir has very low permeability and the pore-pressure gradient decays to negligible values rapidly. In this scenario, the proximal zone is confined to the region immediately adjacent to the fracture and the compressive zone extends perpendicular to the fracture face to a distance of one half the hydraulic fracture height.

2.5.3 Tensile Zone

The tensile zone is a relatively small region extending from the outer surface of the tip proximal zone in directions parallel and sub-parallel to the fracture plane. This region will experience tensile stress with the largest perturbations occurring at the transition from the tip proximal zone (Warpinski et al., 2013). Figure 2.9 shows that the relative size of the tensile zone is affected in a similar way to that of the compressive zone.

2.5.4 Shear Zone

The shear zone is a relatively small transition region between the tensile zone and the compressive zone that experiences shear stresses (Warpinski et al., 2013). If the effective stress in a particular direction exceeds the microcrack closure stress then there is potential for preferential microcrack orientation and velocity anisotropy to develop. However, the transitional nature of the

stress field in this zone will tend to limit the potential for velocity change and anisotropy development. Figure 2.9 shows that the relative size of the shear zone is affected in a similar way to that of the compressive zone.

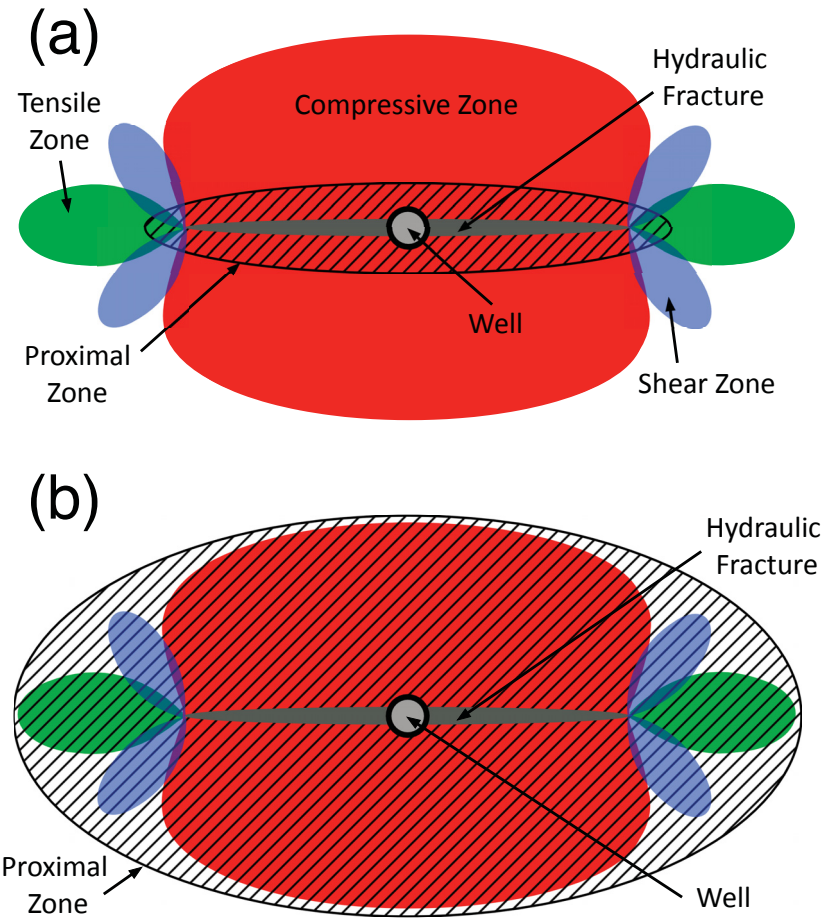

Figure 2.9: A horizontal cross-section through a vertical hydraulic fracture extending from a vertical well illustrating the four spatiotemporal zones in the surrounding region, modified from Cipolla et al. (2011). Red, blue and green indicate a regions experiencing respectively an increase in compressive, shear and tensile stress. The area with black diagonal lines indicates a region experiencing significant pore-pressure increase. For simplicity, we assume that the extent of fluid invasion corresponds to the extend of pore-pressure increase; however, this is not always true. Panel (a) shows the case of a low-permeability reservoir at t minutes after the initiation of injection and panel. Note that the compressive zone has the largest spatial extent. Panel (b) shows the case of a high-permeability reservoir at the same time. Note that the proximal zone has the largest spatial extent.

2.6 Conclusions

The volume of rock surrounding a hydraulic fracture experiences fluid invasion, pore-pressure increase, and triaxial confining-stress perturbation. These three processes combine to change the isotropic P-wave and S-wave velocities in the surrounding reservoir rock, creating four zones of varying size. Fundamental principles can be employed to predict the combined effect of these three processes on the bulk density and the effective elastic constants of the rock, in addition to the range of orientations of microcrack distributions contained within the rock. Furthermore, information regarding bulk density and preferentially aligned microcrack distribution can be used to forward model the resulting changes in P-wave and S-wave velocities, as well as the development of velocity anisotropy. Consequently, is possible to obtain information regarding effective stress and microcrack orientation using several different sources of seismic data, including microseismic, reflection seismic, and VSP datasets. This thesis will explore the exact dependence of stress, pore pressure and fluid saturation changes on the elastic velocities in detail in the following chapters.

Chapter 3

Isotropic Velocity Sensitivity Analysis

3.1 Introduction

As a hydraulic fracture is propagated and held open by the injected high-pressure fluids, several processes occur simultaneously that change the density and the elastic properties in the rock volume surrounding the fracture. These processes include pore-pressure diffusion, fracturing fluid invasion and rock matrix deformation (Warpinski, 1994; Warpinski et al., 2004; Cipolla et al., 2011). The combination of these three effects leads to complex spatial and temporal variations in the elastic velocities as discussed in Chapter 2. For instance, the increase in pore pressure may lead to a porosity increase, thus decreasing the P- and S-wave isotropic velocities. Conversely, when a hydraulic fracture is opened, a volume of rock is displaced in a direction normal to the face of the fracture. This displacement induces changes in the confining-stress distribution surrounding the fracture. An increase in confining stress increases both P- and S-wave isotropic velocities. Finally, replacement of the original reservoir fluids with fracturing fluids can either increase or decrease the isotropic velocities depending on the actual fluid properties.

The material presented in this chapter is based on work that was presented in a poster session at the 2016 GeoConvention in Calgary, Alberta (Brisco and Van der Baan, 2016). In this chapter, we consider the case where a hydraulic fracture treatment is performed in an initially isotropic porous rock. In general, this leads to an heterogeneous triaxial stress perturbation at all spatial points in the vicinity of the fracture and this causes the development of velocity anisotropy (Nur and Simmons, 1969; Warpinski et al., 2004). However, as a first step to understanding the interaction of confining stress, pore pressure and seismic velocities we assume a simplified case of lithostatic (i.e. scalar) stress change. This can be thought of as the mean stress change. Pore-pressure changes are necessarily hydrostatic (i.e. scalar) in nature. We conduct an input parameter sensitivity analysis for changes in isotropic P- and S-wave velocities in response to variations in pore fluid, lithostatic stress and pore pressure.

3.2 Theory

To predict seismic velocities in a fluid-saturated reservoir the elastic moduli and density of an effective medium representing the rock are required. This can be seen by considering the equations for P-wave velocity, equation 2.5, and S-wave velocity, equation 2.6, in a fluid-saturated poroelastic effective medium. Effective density, equation 2.1, is calculated as the sum of the densities of the individual components of the medium weighted by their volume fractions. In this case, the components are the minerals comprising the rock matrix and the fluids contained in the pore space.

Most natural rock is comprised of more than one mineral and pore fluids are often a mixture of several fluids, so the matrix density and pore density are themselves effective densities that can be calculated as a weighted average of the individual constituents. The effective elastic moduli of a mixture of solid grains and pore fluid can be predicted if the volume fraction and elastic

moduli of the constituent phases are known in addition to the geometry of the pore network (Mavko et al., 2009). If no assumptions are made regarding pore geometry then it is not possible to obtain a precise value for the effective elastic moduli. However, as discussed in Subsection 3.2.2, it is possible to determine the bounds of possible moduli for the given mixture. Using these bounds as a guide, it is possible to estimate the effective elastic moduli such that rock containing a highly compliant pore geometry will have moduli close to the lower bound and rock containing a stiff pore geometry will have moduli close to the upper bound.

The physical properties for several common minerals can be seen in Table 3.1 and the physical properties of common pore fluids are discussed in Subsection 3.2.1.

Table 3.1: Density and isotropic elastic moduli of several common minerals. Values are from Bass (1995) and Smyth and Mccormick (1995) as reported by Schmitt (2015).

Mineral	**α-Quartz**	**Albite**	**Anorthite**	**Calcite**	**Dolomite**
Density (kg/m^3)	2648	2610	2765	2712	3795
Adiabatic Bulk Modulus (GPa)	37.8	56.9	84.2	73.3	94.9
Shear Modulus (GPa)	44.3	28.6	39.9	32	45.7

The low frequency Gassmann-Biot theory can be used to predict the expected change in the effective elastic moduli of a fluid-saturated poroelastic medium when a new pore-saturating fluid replaces the initial fluid (Gassmann, 1951; Biot, 1956). To solve the fluid substitution problem, as discussed in Subsection 3.2.3, the Gassmann equations require the porosity and the predicted/estimated effective bulk moduli of the saturated rock, the pore fluid and the matrix material.

Equation 2.9 for effective stress can be expressed in a simplified scalar form

if the confining stress, σ_{litho}, is lithostatic and we assume an effective-stress coefficient of one as follows:

$$\sigma_{eff} = \sigma_{litho} - P_{pore}\,, \tag{3.1}$$

where σ_{eff} is scalar effective stress and P_{pore} is pore pressure. It can be seen from equation 3.1 that a pore-pressure increase and/or lithostatic-stress decrease will result in a decrease in effective stress. Conversely, a pore-pressure decrease and/or lithostatic-stress increase will result in an increase in effective stress. The Hertz-Mindlin grain contact model can be utilized to show the connection between effective stress and the dry-rock bulk and shear moduli, see Subsection 3.2.4 (Mavko et al., 2009).

3.2.1 Properties of Gas and Fluids

The majority of pore fluid in sedimentary basins is brine, a mixture of water and mostly NaCl (Schmitt, 2015). In contrast, the pore fluid in hydrocarbon reservoirs can be a mixture of brine, gas and oil. Batzle and Wang (1992) use empirical measurements to give the following approximate formulae for P-wave velocity and density of brines, hydrocarbon gases and oils. In the following expressions, density values are in g/cm^3 and velocity values are in m/s. Using density and velocity, the relevant bulk moduli can be found using equation 2.5.

Brine

The density of brine, ρ_B, is

$$\begin{aligned}\rho_B =& \rho_W + S\,\{0.668 + 0.44\,S + 10^{-6}[300\,P - 2400\,PS \\ &+ T\,(80 + 3\,T - 3300\,S - 13\,P + 47\,PS)]\},\end{aligned} \tag{3.2}$$

where S is salinity, T is temperature in $^{\circ}C$, P is pressure in MPa and ρ_W is the density of pure water is given by

$$\begin{aligned}\rho_W =& 1 + 10^{-6}(-80\,T - 3.3\,T^2 + 0.00175\,T^3 + 489\,P \\ &- 2\,TP + 0.016\,T^2P - 1.3 \times 10^{-5}T^3P \\ &- 0.333\,P^2 - 0.002\,TP^2).\end{aligned} \tag{3.3}$$

Salinity is the concentration of NaCl dissolved in water given as a fraction of one. The P-wave velocity in brine, v_B, can be expressed as the P-wave velocity in pure water, v_W, adjusted for salinity and pressure-temperature conditions,

$$\begin{aligned}v_B =& v_W + S(1170 - 9.6\,T + 0.055\,T^2 - 8.5 \times 10^{-5}T^3 \\ &+ 2.6\,P - 0.0029\,TP - 0.0476\,P^2) \\ &+ S^{\frac{3}{2}}(780 - 10\,P + 0.16\,P^2) - 820\,S^2\end{aligned} \tag{3.4}$$

and

$$v_W = \sum_{i=0}^{4}\sum_{j=0}^{3}\omega_{ij}T^iP^j\,, \tag{3.5}$$

where the coefficients ω_{ij} are

$$\begin{aligned}
&\omega_{00} = 1402.85 && , && \omega_{02} = 3.437 \times 10^{-3}\,, \\
&\omega_{10} = 4.871 && , && \omega_{12} = 1.739 \times 10^{-4}\,, \\
&\omega_{20} = -0.04783 && , && \omega_{22} = -2.135 \times 10^{-6}\,, \\
&\omega_{30} = 1.487 \times 10^{-4} && , && \omega_{32} = -1.455 \times 10^{-8}\,, \\
&\omega_{40} = -2.197 \times 10^{-7} && , && \omega_{42} = 5.230 \times 10^{-11}\,, \\
&\omega_{01} = 1.524 && , && \omega_{03} = -1.197 \times 10^{-5}\,, \\
&\omega_{11} = -0.0111 && , && \omega_{13} = -1.628 \times 10^{-6}\,, \\
&\omega_{21} = 2.747 \times 10^{-4} && , && \omega_{23} = 1.237 \times 10^{-8}\,, \\
&\omega_{31} = -6.503 \times 10^{-7} && , && \omega_{33} = 1.327 \times 10^{-10}\,, \\
&\omega_{41} = 7.987 \times 10^{-10} && \text{and} && \omega_{43} = -4.614 \times 10^{-13}\,.
\end{aligned} \tag{3.6}$$

Gas

Hydrocarbon gas can be a mixture of many component gases. This gas mixture can be characterized simply by its gravity, G, which is the ratio of gas density to air density at standard temperature and pressure conditions (Mavko et al., 2009). The density of gas at non-standard conditions is approximately given by

$$\rho_G \approx \frac{28.8\,GP}{Z_G R\,T_a}\,, \tag{3.7}$$

where

$$\begin{aligned} &Z_G = a_G P_r + b_G + E_G, \\ &E_G = 0.109(3.85 - T_r)^2 e^{\{-[0.45+8(0.56-\frac{1}{T_r})^2]\frac{P_r^{1.2}}{T_r}\}}, \\ &b_G = 0.642\,T_r - 0.007\,T_r^4 - 0.52, \\ &a_G = 0.03 + 0.00527(3.85 - T_r)^3\,. \end{aligned} \tag{3.8}$$

T_a is the absolute temperature in Kelvin, P is pressure in MPa, G is the gas gravity and R is the gas constant ($8.31441 J/g\cdot mol\cdot deg$). P_r and T_r are a pseudo-pressure and pseudo-temperature respectively and are calculated as

$$P_r = \frac{P}{4.892 - 0.4048\,G} \quad \text{and} \quad T_r = \frac{T_a}{94.72 + 170.75\,G}\,. \tag{3.9}$$

The adiabatic bulk modulus of gas, K_G, measured in MPa is approximated by

$$K_G \approx \frac{P\gamma_G}{1 - \frac{f_G P_r}{Z_G}}\,, \tag{3.10}$$

where

$$\gamma_G = 0.85 + \frac{5.6}{P_r + 2} + \frac{27.1}{(P_r + 3.5)^2} - 8.7e^{-0.65(P_r+1)} \tag{3.11}$$

and

$$f_G = 1.2\, E_G \left\{ - \left[0.45 + 8\big(0.56 - \frac{1}{T_r}\big)^2 \right] \frac{P_r^{0.2}}{T_r} \right\} + a_G\,. \tag{3.12}$$

Oil

Hydrocarbon oils tend to be very complex mixtures of component organic compounds (Schmitt, 2015). An oil mixture can be characterized by its reference density, $\rho_\circ$, at standard pressure-temperature conditions and the gas-oil ratio (Mavko et al., 2009). In-situ oil can contain a large volume of dissolved gas. If the oil is brought to lower pressure-temperature conditions the dissolved gas will tend to be released from solution. The gas-oil ratio is the volume ratio of liberated gas to remaining oil at standard pressure-temperature conditions and is measured in L/L. The density of oil containing dissolved gas, ρ_{oil}, at non-standard conditions is given by

$$\rho_{oil} = \frac{\rho_P}{[0.972 + 3.81 \times 10^{-4}(T + 17.78)^{1.175}]}\,, \tag{3.13}$$

where the pressure-adjusted density, ρ_P, is

$$\begin{aligned} \rho_P =& \rho_G + (0.00277P - 1.71 \times 10^{-7} P^3)(\rho_G - 1.15)^2 \\ &+ 3.49 \times 10^{-4} P\,, \end{aligned} \tag{3.14}$$

where ρ_G is the true density of oil with dissolved gas at saturation given by

$$\rho_G = (\rho_\circ + 0.0012\, GR_G) B_o^{-1}\,, \tag{3.15}$$

where

$$B_o = 0.972 + 0.00038 \left[2.4\, R_G \left(\frac{G}{\rho_\circ} \right)^{1/2} + T + 17.8 \right]^{1.175} \tag{3.16}$$

and

$$\rho_\circ = \frac{141.5}{API + 131.5}\,, \tag{3.17}$$

where API is the American Petroleum Institute's oil gravity measured in degrees and $\rho_\circ$ is a reference oil density measured at $15.6°C$ and atmospheric pressure. The P-wave velocity in oil with dissolved gas, $v_{p,oil}$, is

$$\begin{aligned} v_{p,oil} = 2096 \left(\frac{\rho'}{2.6 - \rho'} \right)^{1/2} - 3.7\, T + 4.64\, P \\ + 0.0115 \left[4.12 \left(\frac{1.08}{\rho'} - 1 \right)^{1/2} - 1 \right] TP\,, \end{aligned} \tag{3.18}$$

where ρ' is a pseudo-density as given by

$$\rho' = \frac{\rho_\circ}{B_o} (1 + 0.001\, R_G)^{-1}. \tag{3.19}$$

3.2.2 Effective Elastic Media: Mixtures

The simplest bounds for the elastic moduli of an isotropic linearly elastic mixture of mineral grains and/or pore fluids are the Voigt-Reuss bounds (Mavko et al., 2009). For the upper Voigt bound, by assuming all of the constituents experience the same strain, Schmitt (2015) gives the isostrain average equation as

$$M_V = \sum_{i=1}^{N} f_i M_i\,, \tag{3.20}$$

where M_V is the desired elastic modulus, N is the number of constituent phases, f_i is the volume fraction of the i^{th} phase and M_i is the corresponding elastic

modulus of the i^{th} phase. M_V can be any desired elastic modulus, for example bulk modulus or shear modulus. The physical interpretation of the upper Voigt bound is the stiffer constituent dominates the behaviour of the mixture (Barkved, 2012). For the lower Reuss bound, by assuming all of the constituents experience the same stress, Reuss (1929) gives the isostress average equation as

$$M_R = \sum_{i=1}^{N} \frac{f_i}{M_i}\,, \tag{3.21}$$

where M_R is the desired elastic modulus, N is the number of constituent phases, f_i is the volume fraction of the i^{th} phase and M_i is the corresponding elastic modulus of the i^{th} phase. As with the Voigt bound, M_R can be any desired elastic modulus. The physical interpretation of the lower Reuss bound is the softer constituent dominates the behaviour of the mixture (Barkved, 2012). Hill (1963) shows that the Reuss bound describes the exact bulk modulus of a mixture when all of the constituents have the same shear modulus. Hence, the Reuss bound gives the exact equation for the bulk modulus of a mixture of fluids and/or gases when the constituent shear moduli are all zero.

An alternative to the Voigt-Reuss bounds that gives a smaller deviation between the upper and lower limits are the Hashin-Shtrikman-Walpole bounds (Hashin and Shtrikman, 1963; Walpole, 1966). For a mixture of 50% quartz and 50% calcite with no porosity, Schmitt (2015) shows the Voigt-Reuss bounds deviate by $< 3\%$ for shear modulus and 11% for bulk modulus, whereas the Hashin-Shtrikman-Walpole bounds deviate by $< 1\%$. By assuming a simple mixture comprised of two phases, the physical interpretation of the Hashin-Shtrikman-Walpole bounds can be described (Mavko et al., 2009). The entire volume of the mixture is filled by an assembly of spherical cores of one phase coated with a uniform shell of the second phase. The core plus shell units are of a wide variety of sizes such that there is no empty space. For each individual

core plus shell unit, the thickness of each shell is such that volume fraction of the unit is the same as the mixture. The upper bound is obtained when the cores are comprised of the softer phase and the lower bound is obtained when the cores are comprised of the stiffer phase. Berryman (1995) gives a general form of the Hashin-Shtrikman-Walpole bounds that is valid for mixtures of N components as follows:

$$\begin{aligned} K^{HS+} &= \Lambda_{HS}(\mu_{max}), \\ K^{HS-} &= \Lambda_{HS}(\mu_{min}), \\ \mu^{HS+} &= \Gamma_{HS}(\zeta_{HS}(K_{max}, \mu_{max})) \quad \text{and} \\ \mu^{HS-} &= \Gamma_{HS}(\zeta_{HS}(K_{min}, \mu_{min}))\,, \end{aligned} \tag{3.22}$$

where

$$\begin{aligned} \Lambda_{HS}(\mu_z) &= \langle \frac{1}{K(r) + \frac{4}{3}\mu_z} \rangle^{-1} - \frac{4}{3}\mu_z, \\ \Gamma_{HS}(\mu_z) &= \langle \frac{1}{\mu(r) + \mu_z} \rangle^{-1} - \mu_z \quad \text{and} \\ \zeta_{HS}(K_z, \mu_z) &= \frac{\mu_z}{6}\left(\frac{9K_z + 8\mu_z}{K_z + 2\mu_z}\right), \quad \text{where} \quad r \in [1, ..., N]\,. \end{aligned} \tag{3.23}$$

K^{HS+} is the bulk modulus upper bound, K^{HS-} is the bulk modulus lower bound and K_z takes the value of either K_{max} or K_{min} which are respectively the largest and smallest bulk moduli of the N constituent phases. Likewise, μ^{HS+} is the shear modulus upper bound, μ^{HS-} is the shear modulus lower bound and μ_z takes the value of either μ_{max} or μ_{min} which are respectively the largest and smallest shear moduli of the N constituent phases. The brackets $\langle\rangle$ indicate an average over the medium, which is equivalent to a volume fraction weighted average of the constituent phases (Mavko et al., 2009). The average of the Hashin-Shtrikman-Walpole bounds provide a very good estimate of the effective

elastic moduli of a multimineralic rock matrix and a reasonably good estimate of the effective elastic moduli of an isotropic, fluid-saturated, poroelastic rock.

3.2.3 Low Frequency Gassmann-Biot Theory

The elastic properties of a fluid-saturated porous rock are sensitive to the elastic properties of the pore filling fluid. Hence, if a new fluid replaces an initial pore fluid, the elastic properties of the rock will change. If the rock is isotropic, the low frequency Gassmann-Biot theory introduced in Chapter 2 can be used to predict the elastic moduli of the dry rock frame (Gassmann, 1951; Biot, 1956). The Gassmann equations make no assumptions regarding pore geometry, so it is compatible with Hashin-Shtrikman-Walpole average estimates of elastic moduli. Mavko et al. (2009) give the rearranged Gassmann equations 2.7 and 2.8 as:

$$K_{dry} = \frac{K_{sat}\left(\frac{\phi K_\circ}{K_{fluid}} + 1 - \phi\right) - K_\circ}{\frac{\phi K_\circ}{K_{fluid}} + \frac{K_{sat}}{K_o} - 1 - \phi} \tag{3.24}$$

and

$$\mu_{dry} = \mu_{sat}\,, \tag{3.25}$$

where K_{dry} is the effective dry rock bulk modulus, K_{sat} is the effective bulk modulus of the saturated rock, K_{fluid} is the effective bulk modulus of the pore fluid, $K_\circ$ is the effective bulk modulus of the matrix material, ϕ is the porosity μ_{dry} is the effective dry rock shear modulus and μ_{sat} is the effective shear modulus of the saturated rock. The dry rock bulk modulus, K_{dry}, corresponds to the drained rock bulk modulus and is generally unknown for in-situ rock. Recall, using equation 2.7 we can predict the bulk modulus of a fluid saturated rock.

3.2.4 Pressure Sensitive Effective Elastic Media

Hertz-Mindlin Model

As discussed in Chapter 2, the Hertz-Mindlin grain contact model can be utilized to show the connection between effective stress and the dry-rock bulk and shear effective moduli, hence the P- and S-wave velocities (Mavko et al., 2009). The model was developed by Mindlin (1949) to describe a precompacted, unconsolidated, dry, random packing of identical spherical grains experiencing lithostatic stress in terms of effective bulk, K_{HM}, and effective shear, μ_{HM}, dry-rock moduli. Long wavelength seismic waves like those typically used in exploration seismic are assumed in the model. The effective dry-rock moduli are given by Dvorkin and Nur (1996) as

$$K_{HM} = \sqrt[3]{\frac{C^2(1-\phi)^2\mu^2}{18\pi^2(1-\nu)^2}\sigma_{eff}} \tag{3.26}$$

and

$$\mu_{HM} = \left[\frac{5-4\nu}{5(2-\nu)}\right]\sqrt[3]{\frac{3C^2(1-\phi)^2\mu^2}{2\pi^2(1-\nu)^2}\sigma_{eff}}\,, \tag{3.27}$$

where C is the average number of contacts per grain, ϕ is porosity, μ is the shear modulus of the solid grains, ν is the Poisson ratio of the solid grains, and σ_{eff} is a lithostatic effective stress. Equations 3.26 and 3.27 are equivalent to equations 2.11 and 2.12 with the symbols for the dry-rock moduli, K_{dry} and μ_{dry}, replaced with K_{HM} and μ_{HM}. The updated symbols will provide clarity in the following section where there are more than one set of dry-rock moduli. Smith et al. (1929) found that a shaken, tamped, random packing of identical spheres has a porosity of $\sim$ 0.36 and a coordination number of $\sim$ 9. The Hertz-Mindlin model can be extended to more realistic grain packing scenarios through one of several models, for example the soft-sand model, the stiff-sand model and the intermediate stiff-sand model (Mavko et al., 2009).

Effective stress sensitivity is accounted for in the sand models through the Hertz-Mindlin effective dry-rock moduli, K_{HM} and μ_{HM}.

Soft-Sand Model

The soft-sand model enables the prediction of effective elastic moduli for an uncemented sand with porosity lower than 0.36 (Mavko et al., 2009). The model assumes an isotropic framework of identical elastic spherical grains consistent with the Hertz-Mindlin model. The framework has a porosity, $\phi_\circ$ of 0.36 and a coordination number of 9. Conceptually, a lower value of porosity, ϕ, is achieved by deposition of cement away from grain contacts. The effective elastic moduli are calculated by using a heuristic modified Hashin-Shtrikman lower bound as follows:

$$K_{soft} = \left[\frac{\frac{\phi}{\phi_\circ}}{K_{HM} + \frac{4}{3}\mu_{HM}} + \frac{1 - \frac{\phi}{\phi_\circ}}{K_\circ + \frac{4}{3}\mu_{HM}} \right]^{-1} - \frac{4}{3}\mu_{HM} \tag{3.28}$$

and

$$\mu_{soft} = \left[\frac{\frac{\phi}{\phi_\circ}}{\mu_{HM} + z_{soft}} + \frac{1 - \frac{\phi}{\phi_\circ}}{\mu_\circ + z_{soft}} \right]^{-1} - z_{soft}\,, \tag{3.29}$$

where K_{soft} is the effective dry-rock bulk modulus, μ_{soft} is the effective dry-rock shear modulus, K_{HM} is the Hertz-Mindlin effective dry-rock bulk modulus, μ_{HM} is the Hertz-Mindlin effective dry-rock shear modulus, $K_\circ$ is the bulk modulus of the solid grains, $\mu_\circ$ is the shear modulus of the solid grains and

$$z_{soft} = \frac{\mu_{HM}}{6}\left(\frac{9K_{HM} + 8\mu_{HM}}{K_{HM} + 2\mu_{HM}} \right). \tag{3.30}$$

The model connects two end members in porosity-elastic modulus space. At zero porosity, the modulus is equal to that of the solid mineral grains and at high porosity, the Hertz-Mindlin model predicts the pressure-dependent modulus.

Stiff-Sand and Intermediate Stiff-Sand Model

The stiff-sand model uses the same format as the soft-sand model but connects the two end members with a heuristic modified Hashin-Shtrikman upper bound as follows:

$$K_{stiff} = \left[\frac{\frac{\phi}{\phi_\circ}}{K_{HM} + \frac{4}{3}\mu_\circ} + \frac{1 - \frac{\phi}{\phi_\circ}}{K_\circ + \frac{4}{3}\mu_\circ} \right]^{-1} - \frac{4}{3}\mu_\circ \tag{3.31}$$

and

$$\mu_{stiff} = \left[\frac{\frac{\phi}{\phi_\circ}}{\mu_{HM} + z_{stiff}} + \frac{1 - \frac{\phi}{\phi_\circ}}{\mu_\circ + z_{stiff}} \right]^{-1} - z_{stiff}\,, \tag{3.32}$$

where K_{stiff} is the effective dry-rock bulk modulus, μ_{stiff} is the effective dry-rock shear modulus, K_{HM} is the Hertz-Mindlin effective dry-rock bulk modulus, μ_{HM} is the Hertz-Mindlin effective dry-rock shear modulus, $K_\circ$ is the bulk modulus of the solid grains, $\mu_\circ$ is the shear modulus of the solid grains and

$$z_{stiff} = \frac{\mu_\circ}{6}\left(\frac{9K_\circ + 8\mu_\circ}{K_\circ + 2\mu_\circ} \right). \tag{3.33}$$

The intermediate stiff-sand model uses the soft-sand model with an larger artificial coordination number but with the stipulation that if the predicted effective elastic modulus, either bulk or shear, is larger than the corresponding modulus predicted by the stiff-sand model, then the stiff-sand modulus is used.

3.3 Method

We develop three workflows in order to conduct an input parameter sensitivity analysis for changes in isotropic P- and S-wave velocities in response to variations in pore fluid, lithostatic stress and pore pressure. The basic methodology is the same for testing the sensitivity of the change in isotropic velocity resulting from fluid replacement, variation in lithostatic stress and variation in

pore pressure. The first step is to set the default input parameters, including fluid properties (i.e. API, gas-oil ratio , gas gravity, salinity and initial pore fluid type), depth, rock properties (i.e. porosity and matrix mineralogy). The density and bulk modulus of the pore fluid are then obtained using equations 3.2 to 3.19. If the pore fluid is a mixture of fluids, the effective bulk moduli can be found using the Reuss average, equation 3.21.

Next, the elastic moduli of the rock matrix are determined. If the rock matrix is monomineralic, the moduli are selected directly from Table 3.1. The minerals list in Table 3.1 represent common minerals found in sedimentary rock. If the rock matrix is multimineralic, the moduli are estimated by taking the arithmetic mean of the Hashin-Shtrikman-Walpole upper and lower bounds, as seen in equations 3.22 and 3.23. The dry-rock effective elastic moduli are then obtained using an appropriate effective medium model, where Gassmaan's equations 3.24 and 3.25 are used for fluid substitution and the Hertz-Mindlin model is used for effective-pressure sensitive moduli.

Next, the effective bulk modulus and the effective density of the fluid-saturated rock are calculated respectively with Gassmann's equation 2.7 and a volume-fraction weighted average of the rock-matrix density and the pore-fluid density, equation 2.1. Rock-matrix and pore-fluid density can themselves be effective densities if they consist of more than one phase. In this case, a modified version of equation 2.1 is used to calculate the effective densities of the rock matrix and the pore fluid where ϕ represents the volume fraction of the individual phases.

Finally, isotropic P- and S-wave velocities of the fluid-saturated rock are calculated using equations 2.5 and 2.6. Although the workflow framework is consistent, there are minor but important differences in the details involved in several steps for testing the sensitivity of the change in isotropic velocity resulting from fluid replacement, variation in pore pressure and variation in lithostatic confining stress. These differences are outlined in the following Sub-

sections 3.3.1 to 3.3.3 and illustrated in Figures 3.1 to 3.3.

3.3.1 Fluid Replacement

Figure 3.1 outlines the basic steps involved in modelling the isotropic velocity response to fluid replacement. To simulate fluid invasion during a hydraulic fracture treatment, the isotropic velocities of an increasingly brine-saturated porous rock, from the initially 100 % hydrocarbon-saturated (either gas or oil) rock to a final 100 % brine-saturation, are calculated. Hence, the fluid bulk modulus and effective density need to be obtained for all pore fluid mixtures using equations 3.2 to 3.19 which feed into equation 3.21 for the fluid moduli and equation 2.1 for effective density. Next, the rock matrix effective moduli are calculated as the average of the Hashin-Shrikman-Walpole upper and lower bounds of a mixture of the matrix mineral constituents, equations 3.22 and 3.23. Additionally, the determination of the saturated-rock elastic properties requires the estimation of the effective elastic moduli of the 100 % brine-saturated rock using the average of the Hashin-Shtrikman-Walpole upper and lower bounds a second time for a mixture of the rock matrix and the pore fluid. The dry-rock bulk modulus is then obtained using Gassmann's equation 3.24 with the 100 % brine-saturated rock bulk modulus and the rock matrix bulk modulus. Then Gassmann's equation 2.7, with the previously obtained dry-rock bulk modulus and the rock matrix bulk modulus, is used to calculate bulk moduli for the full range (from 100 % to 0 % hydrocarbon saturation) of hydrocarbon/brine-saturated rock. Finally, the effective density from equation 2.1 and the elastic moduli from equations 3.22, 3.25 and 2.7 for the fluid saturated rock are combined in equations 2.5 and 2.6 to give the desired P- and S-wave velocity.

The order of determining the dry-rock bulk modulus in equation 3.24 is important. Using the bulk modulus of the 100 % brine-saturated rock from the average of the Hashin-Shtrikman-Walpole bounds, equations 3.22 and 3.23, results in a relatively constant dry-rock bulk modulus for a given porosity.

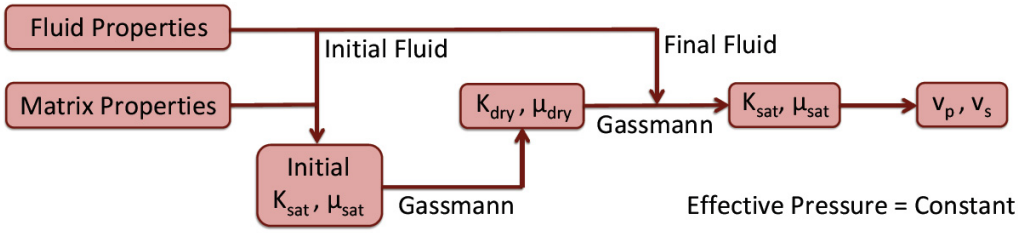

Figure 3.1: The basic workflow for modelling the isotropic velocity response to fluid replacement where K_{sat} and K_{dry} are respectively the fluid-saturated and dry-rock bulk moduli and μ_{sat} and μ_{dry} are respectively the fluid-saturated and dry-rock shear moduli.

However, if we use the bulk modulus of the hydrocarbon-saturated rock, the calculated dry-rock bulk modulus varies for a given porosity depending on the physical properties of the saturating hydrocarbon, and this will produce non-physical results for velocity sensitivity.

The sensitivity of isotropic velocities to variation in the input parameters of porosity, API, gas-oil ratio , gas gravity, salinity, pore pressure and temperature is tested by comparing the velocity change for a range of values of a single parameter while holding all other parameters constant. The default temperature and pore-pressure conditions are calculated for a depth of $3km$ assuming a temperature gradient of $25^oC/km$ and a pore-pressure gradient of $\sim 10MPa/km$. It is important to note that effective stress is assumed constant for the fluid substitution problem, so dry rock bulk/shear moduli remain unchanged. The default setting for the parameters are as follows: the rock matrix is 70% quartz and 30% calcite, 10% porosity, $25^oAPI, 40L/L\,R_G$, gas gravity of 1 and 0.05 salinity. These parameter settings are representative of a moderate-weight hydrocarbon oil in a simple cemented sandstone reservoir of moderate porosity.

3.3.2 Lithostatic Stress

Varying effective stress while assuming a constant pore pressure can simulate lithostatic-stress variation in a reservoir, since effective stress is defined as the difference between the lithostatic stress and the pore pressure, equation 3.1. Hence, fluid properties are constant and are calculated in the same way as described in Subsection 3.3.1 for constant pore pressure obtained by assuming an average water column density of $1000\,kg/m^3$. Figure 3.2 outlines the basic steps involved in modelling the isotropic velocity response to lithostatic-stress variation.

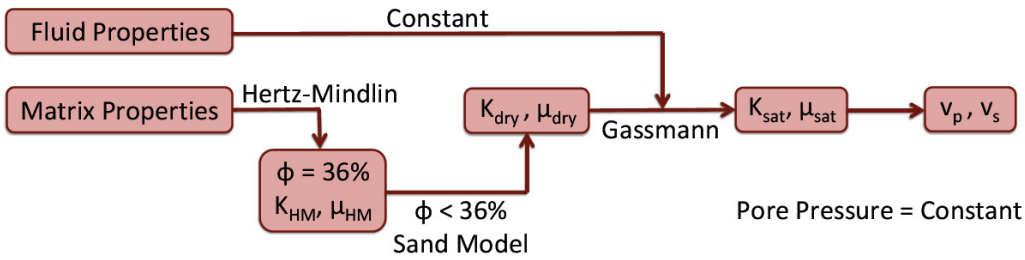

Figure 3.2: The basic workflow for modelling the isotropic velocity response to lithostatic-stress variation where ϕ denotes porosity. K_{HM}, K_{sat} and K_{dry} are respectively the Hertz-Mindlin, the fluid-saturated and the dry-rock bulk moduli and μ_{HM}, μ_{sat} and μ_{dry} are respectively the Hertz-Mindlin, the fluid-saturated and the dry-rock shear moduli.

First, the effective density of the saturated rock is calculated using equation 2.1. Next, the rock matrix effective moduli are calculated as the average of the Hashin-Shrikman-Walpole upper and lower bounds of a mixture of the mineral constituents, equations 3.22 and 3.23. The dry-rock elastic moduli of a 36% porosity grain-pack are then calculated using the Hertz-Mindlin equations 3.26 and 3.27 with the rock matrix elastic moduli as inputs. The Hertz-Mindlin dry-rock elastic moduli and the rock matrix elastic moduli are then fed into one of the sand model equations to obtain an estimate of the dry-rock elastic moduli of a grain-pack with less than 36% porosity: use equations 3.28 to

3.30 for the soft-sand model, equations 3.31 to 3.33 for the stiff-sand model and intermediate stiff-sand model. Next, the saturated-rock bulk modulus is calculated with Gassmann's equations 3.25 and 2.7 using the sand-model dry-rock bulk modulus and the rock matrix bulk modulus. Finally, the effective density from equation 2.1 and the elastic moduli from equations 3.25 and 2.7 for the fluid-saturated rock are combined in equations 2.5 and 2.6 to give the desired P- and S-wave velocity.

The sensitivity of isotropic velocities to variation in the input parameters of porosity, depth and pore fluid type is tested for the various sand models by observing the velocity change for a range of values of a single parameter while holding all other parameters constant.

3.3.3 Pore Pressure

Varying effective stress while assuming a constant lithostatic stress can simulate pore-pressure variation in a reservoir, since effective stress is defined as the difference between the lithostatic stress and the pore pressure, equation 3.1. The procedure for calculating isotropic P- and S-wave velocity is the same as discussed for lithostatic stress (Subsection 3.3.2) with the exception that new fluid properties must calculated for each value of pore pressure using equations 3.2 to 3.19 which feed into equation 3.21 for fluid moduli and equation 2.1 for effective density. Figure 3.3 outlines the basic steps involved in modelling the isotropic velocity response to pore-pressure variation.

The sensitivity of velocity change to variation in the input parameters of porosity, depth and pore fluid type is tested for the soft-, stiff- and intermediate stiff-sand models by observing the velocity change for a range of values of a single parameter while holding all other parameters constant. The confining stress is obtained by assuming an average overburden density of $2400\,kg/m^3$ and the same parameter defaults are used as in the Subsection 3.3.1.

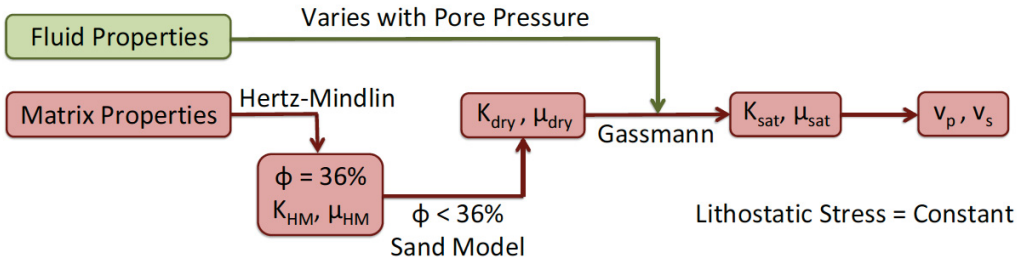

Figure 3.3: The basic workflow for modelling the isotropic velocity response to pore-pressure variation where ϕ denotes porosity. K_{HM}, K_{sat} and K_{dry} are respectively the Hertz-Mindlin, the fluid-saturated and the dry-rock bulk moduli and μ_{HM}, μ_{sat} and μ_{dry} are respectively the Hertz-Mindlin, the fluid-saturated and the dry-rock shear moduli.

3.4 Results and Discussion

3.4.1 Fluid Replacement

To evaluate the sensitivity of velocity change for each input parameter, we first show the P- and S-wave velocity response to increasing gas saturation at various porosity values (Figures 3.4 and 3.5). Figures 3.6 to 3.9 then show the dependence of P-wave velocity respectively for variations in gas gravity, pore pressure, temperature and salinity with increasing gas saturation. Finally, Figures 3.10 and 3.11 show the dependence of S-wave velocity respectively for variations in gas gravity and salinity with increasing gas saturation. To link Figures 3.4 to 3.11 to a hydraulic fracture treatment, keep in mind that initially the reservoir will be close to 100 % gas saturation and as the treatment progresses the fracturing fluid will replace some to all of the gas, thus decreasing gas saturation. For simplicity we assume the fracturing fluid to be brine. Hence, moving from right to left along a particular curve simulates time passed in the vicinity of a hydraulic fracture.

P- and S-wave velocities are significantly sensitive to porosity, as seen in Figures 3.4 and 3.5 respectively. Figure 3.4 shows that for porosities greater than 5%, P-wave velocity decreases or remains constant when gas saturation

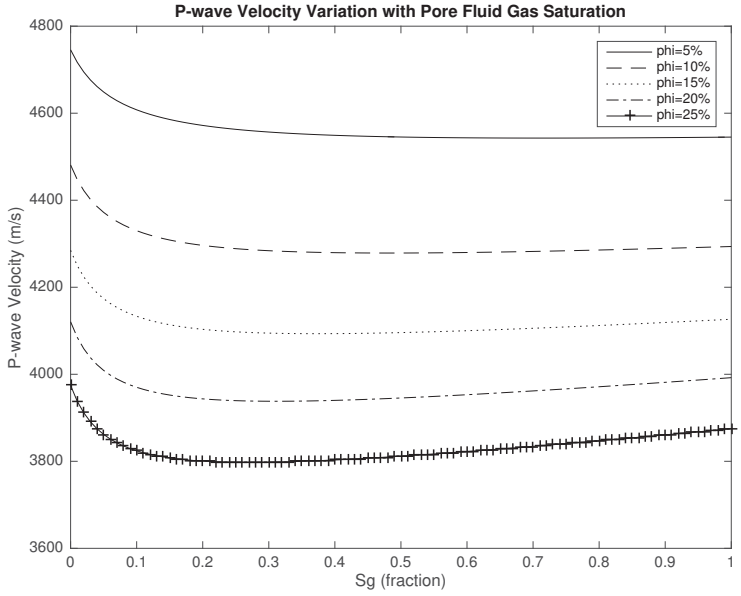

Figure 3.4: P-wave velocity versus gas saturation at various porosity values. The parameter default conditions are $25^{o}API$, $40\,L/L\,R_G$, gas gravity of 1, 0.05 salinity, $30\,MPa$ pore pressure and $75°C$ temperature.

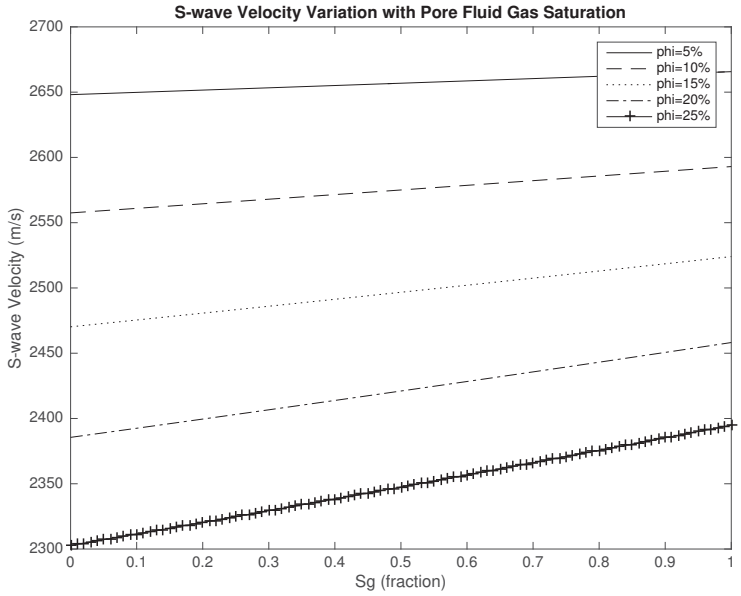

Figure 3.5: S-wave velocity versus gas saturation at various porosity values. All other parameters are set to the default conditions stated in Figure 3.4.

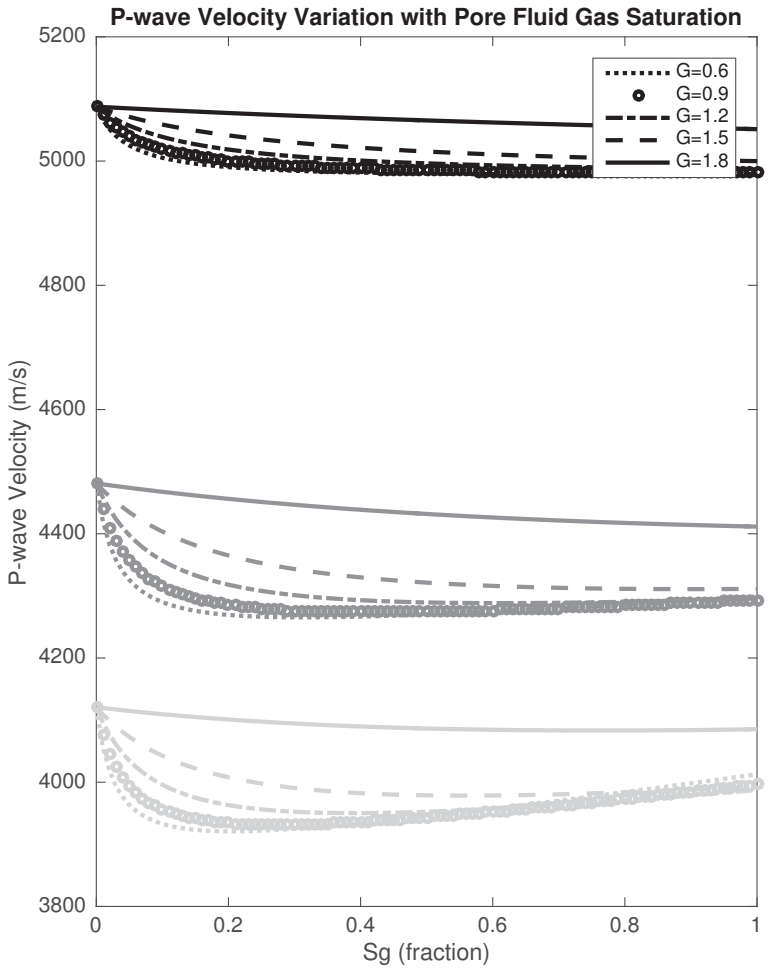

Figure 3.6: P-wave velocity versus gas saturation at various gas gravity values shown for 1% (black), 10% (dark grey) and 20% (light grey) porosity values. All other parameters are set to the default conditions stated in Figure 3.4.

decreases from 100% to roughly 20%. However, if gas saturation decreases below 20%, P-wave velocity responds with a sharp increase. In contrast, for porosity less than or equal to 5%, P-wave velocity always shows an increase with decreasing gas saturation but with a smoother increase as gas saturation decreases below 20%. Figure 3.5 shows that S-wave velocity consistently decreases linearly with decreasing gas saturation but with a steeper gradient for higher porosity. The behaviour of P- and S-wave velocity can be explained

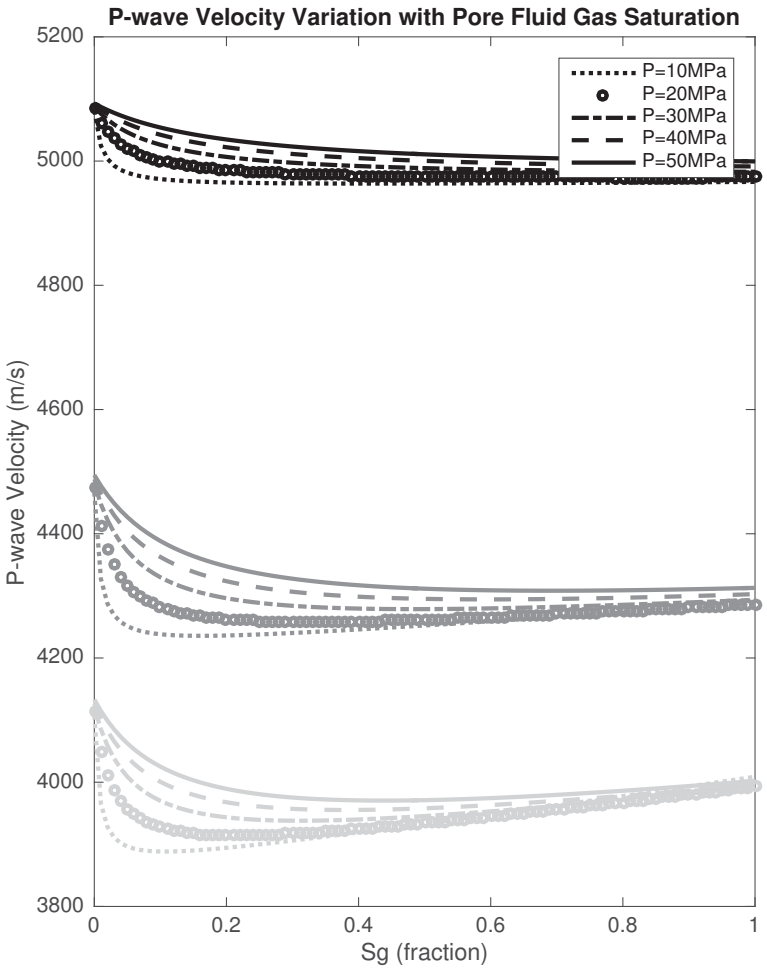

Figure 3.7: P-wave velocity versus gas saturation at various pore-pressure values shown for 1% (black), 10% (dark grey) and 20% (light grey) porosity values. All other parameters are set to the default conditions stated in Figure 3.4.

by considering equations 2.5 and 2.6. As gas saturation decreases, the effective density of the rock increases while the effective shear modulus remains unchanged resulting in a S-wave velocity decrease. The effective bulk modulus increases as gas saturation decreases and the amount of bulk modulus increase relative to density decrease controls the P-wave velocity response. For large porosity, as gas saturation decreases from 100% to 20%, the approximately linear decrease in P-wave velocity is caused by density decrease being the dominate

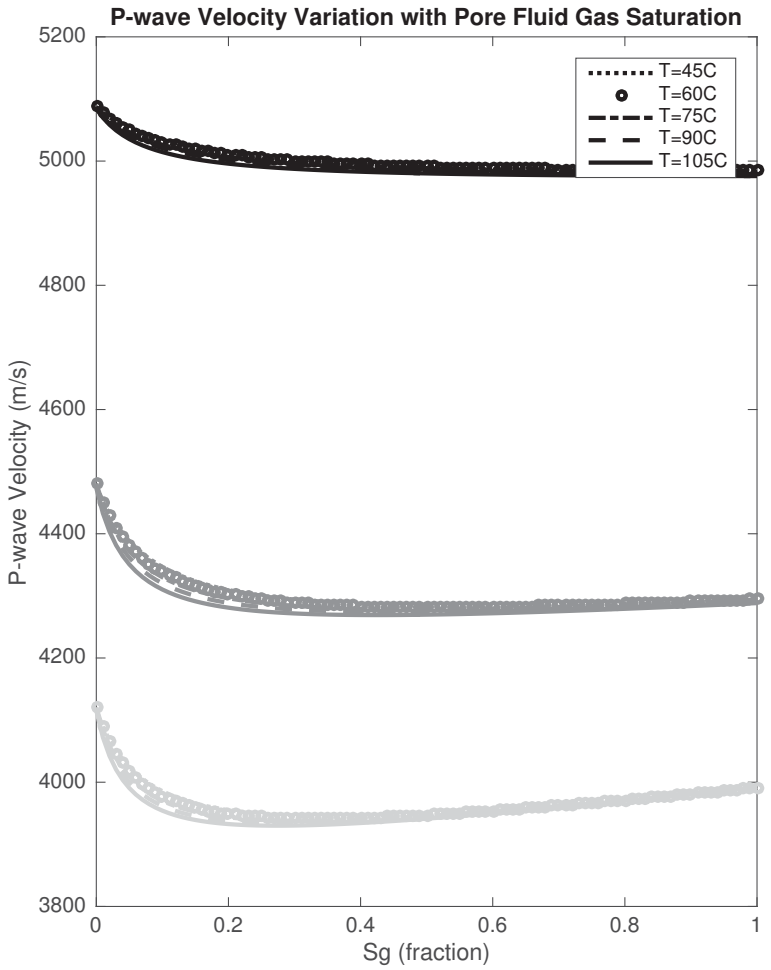

Figure 3.8: P-wave velocity versus gas saturation at various temperature values shown for 1% (black), 10% (dark grey) and 20% (light grey) porosity values. All other parameters are set to the default conditions stated in Figure 3.4.

factor (Ostrander, 1985). However, as gas saturation decrease below 20%, the non-linear P-wave velocity increase is caused by changes in the effective bulk modulus being the dominant factor. This has important implications near a hydraulic fracture in a greater than 10% porosity reservoir. If the fracturing fluid leaves 20% gas saturation in the pore space, the P-wave velocity will show no change or a slight decrease. However, if the fracturing fluid replaces more than 80% of the gas, the P-wave velocity will show an increase.

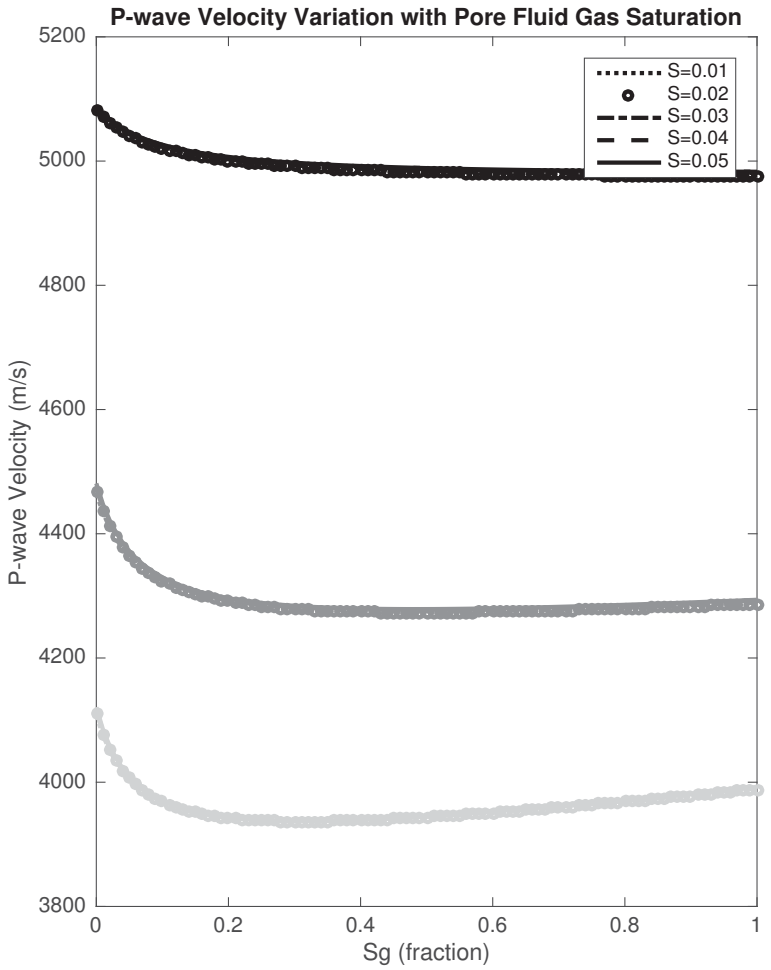

Figure 3.9: P-wave velocity versus gas saturation at various salinity values shown for 1% (black), 10% (dark grey) and 20% (light grey) porosity values. All other parameters are set to the default conditions stated in Figure 3.4.

The terms Δv_p and Δv_s are used to describe the velocity sensitivity to a particular input parameter. For example, consider Figure 3.6 which shows P-wave velocity change with gas saturation for five values of the input parameter gas gravity ($G = 0.6$, 0.9, 1.2, 1.5, 1.8) at three porosity values ($\phi = 1\%$, 10%, 20%). The values of gas gravity are differentiated by line style and the porosity values are indicated by grey scale. The term Δv_p refers to the separation between the individual gas gravity curves for a specific porosity. For a 20%

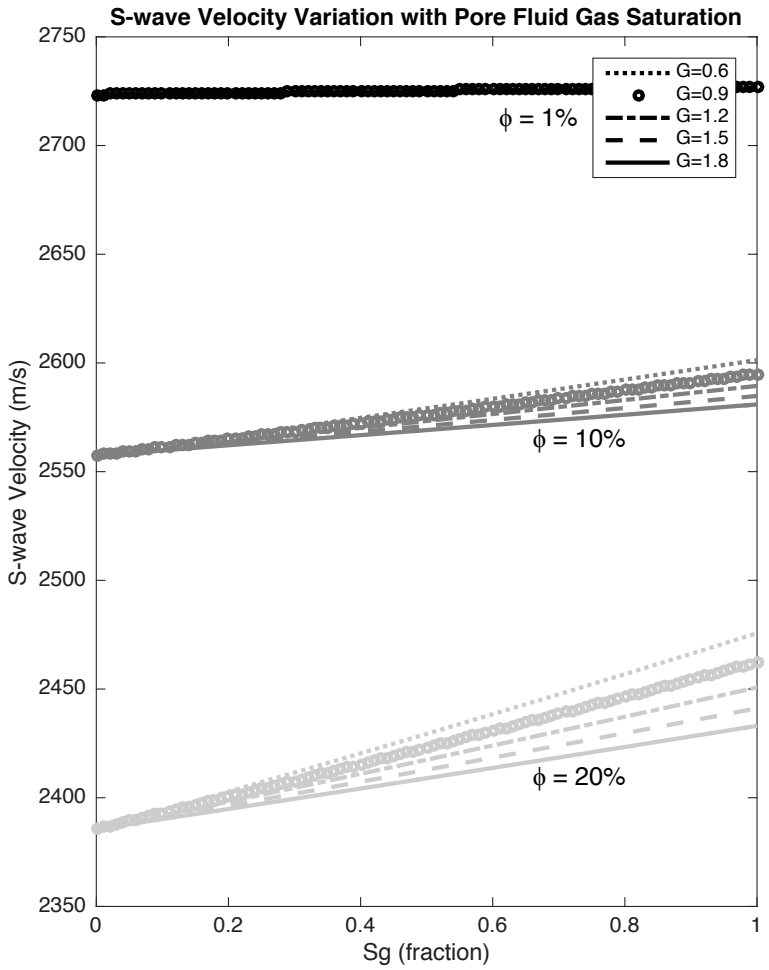

Figure 3.10: S-wave velocity versus gas saturation at various gas gravity values shown for 1% (black), 10% (dark grey) and 20% (light grey) porosity values. All other parameters are set to the default conditions stated in Figure 3.4. This plot is representative of pore-pressure sensitivity but with pore-pressure sensitivity showing less variation at 10% and 20% porosity.

porosity Δv_p is relatively large when gas saturation is 15% and moderate when gas saturation is 100%. More specifically, at 100% gas saturation Δv_p is very small for gas gravity in the range of $0.6 - 1.5$ but is moderate when these gas gravity curves are compared to the 1.8 gas gravity curve. Table 3.2 provides a quick-access summary of the velocity sensitivity terms used in this chapter.

Over the input parameter ranges tested, Δv_p is most sensitive to variation

Table 3.2: A summary of velocity sensitivity terms.

Term	**Definition**
Δv_p	The separation between the parameter P-wave velocity curves for a specific porosity.
Δv_s	The separation between the parameter S-wave velocity curves for a specific porosity.
$\Delta v_{p,total}$	The total P-wave velocity change over a range of effective stress for a single sand model at a single depth.
$\Delta v_{s,total}$	The total S-wave velocity change over a range of effective stress for a single sand model at a single depth.

in gas gravity and pore pressure with only minor sensitivity to temperature and almost no sensitivity to salinity, as seen in Figures 3.6 to 3.9 respectively. As seen in Figure 3.6, total v_p change with 100% fluid replacement is larger for smaller values of gas gravity. This is due to larger gas gravity values having densities and bulk moduli closer to that of brine. Figure 3.7 shows that total v_p change with 100% fluid replacement is larger for smaller values of pore pressure and this is due to a highly-compressible gas having density and bulk moduli closer to that of a less-compressible brine at high pore pressures. Additionally, Δv_p shows a higher sensitivity to gas gravity, pore pressure and temperature at high porosity. Plots for API and gas-oil ratio are not shown as they are not input parameters for brine or gas, so Δv_p is insensitive to them.

Over the input parameter ranges tested, Δv_s is most sensitive to variation in gas gravity with minor sensitivity to pore pressure (Figures 3.10 and 3.11 respectively) and almost no sensitivity to salinity and temperature. The sensitivity of Δv_s to salinity, seen in Figure 3.11, is representative of the corresponding plot for temperature. Figure 3.10 shows that Δv_s sensitivity to gas gravity increases with increasing porosity. The sensitivity of Δv_s to gas gravity, seen in Figure 3.10, is representative of the same plot for pore pressure but with pore pressure showing less sensitivity at 10% and 20% porosity. The initial and final pore fluids have a large difference in density and a larger porosity will result in the fluid portion of the saturated rock having a larger influence

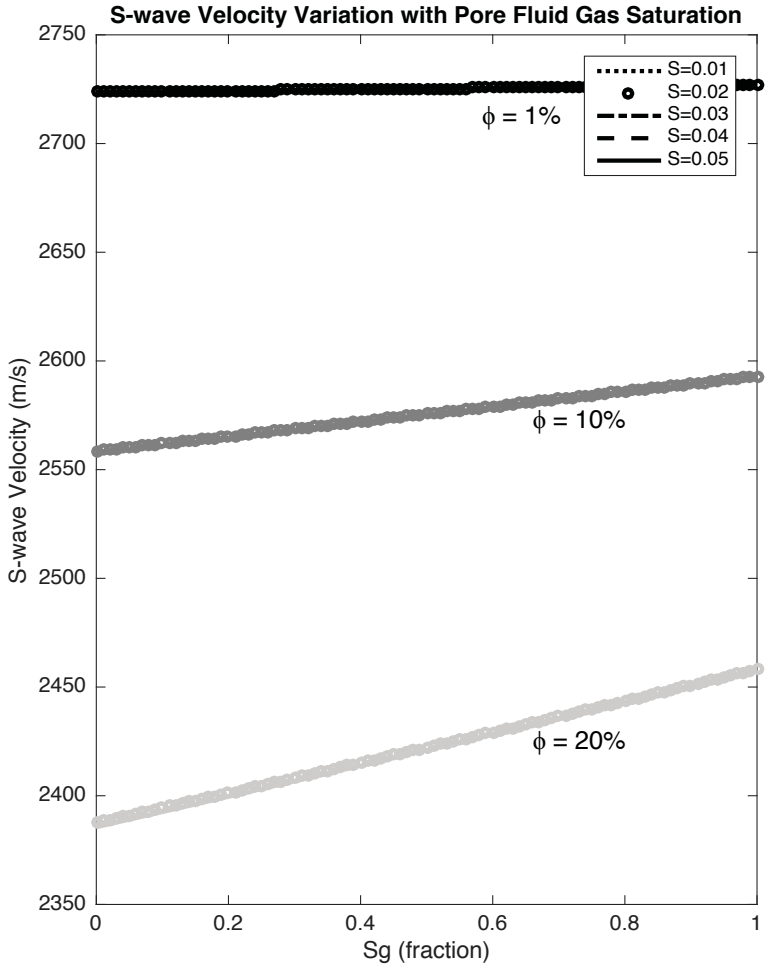

Figure 3.11: S-wave velocity versus gas saturation at various salinity values shown for 1% (black), 10% (dark grey) and 20% (light grey) porosity values. All other parameters are set to the default conditions stated in Figure 3.4. This plot is representative of temperature sensitivity.

on the effective density of the saturated rock. Expectedly, in very low porosity reservoirs Δv_s appears to be insensitive to all pore-fluid input parameters.

In the case of an initially oil-saturated rock, Figures 3.12 and 3.13 show the dependence of P-wave velocity respectively for variations in API and gas gravity with increasing oil saturation. The sensitivity of Δv_p to API, seen in Figure 3.12, is representative of the same plots for gas-oil ratio, temperature and pore pressure. The sensitivity of Δv_p to gas gravity, seen in Figure 3.13,

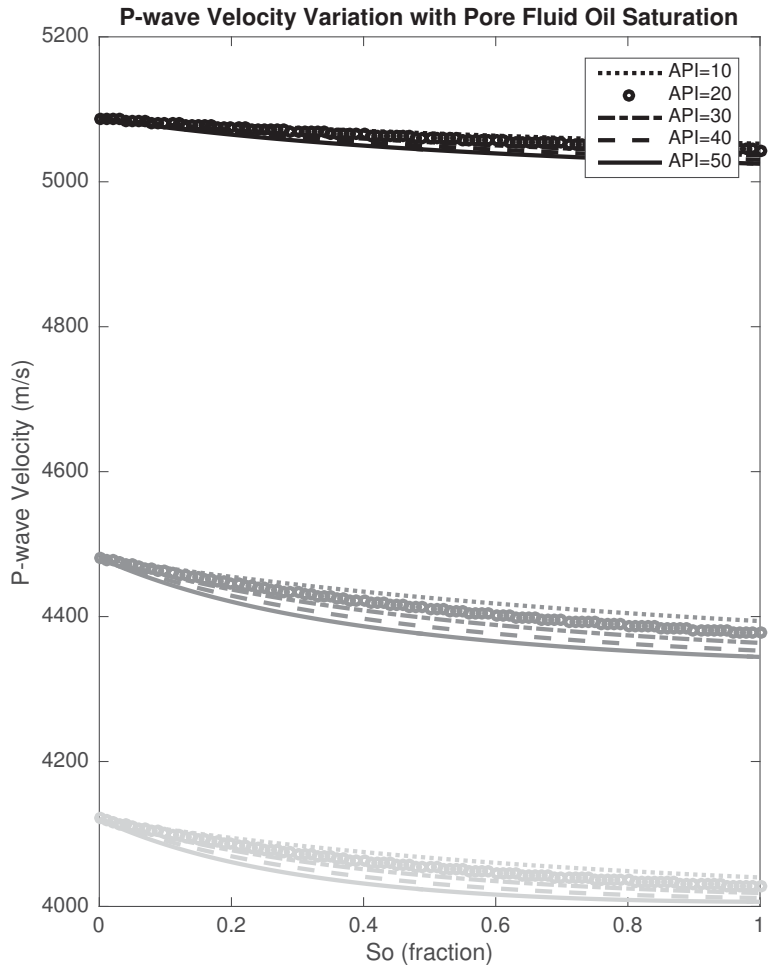

Figure 3.12: P-wave velocity versus oil saturation at various API values shown for 1% (black), 10% (dark grey) and 20% (light grey) porosity values. All other parameters are set to the default conditions stated in Figure 3.4. This plot is also representative of the gas-oil ratio, temperature and pore-pressure sensitivity.

is representative of the same plot for salinity. Figures 3.14 and 3.15 then show the dependence of S-wave velocity respectively for variations in API and gas gravity with increasing gas saturation. The sensitivity of Δv_s to gas gravity, seen in Figure 3.15, is representative of the same plots for gas-oil ratio, salinity, temperature and pore pressure. The same method of linking Figures 3.12 to 3.15 to a hydraulic fracture treatment that was used for gas saturation can be

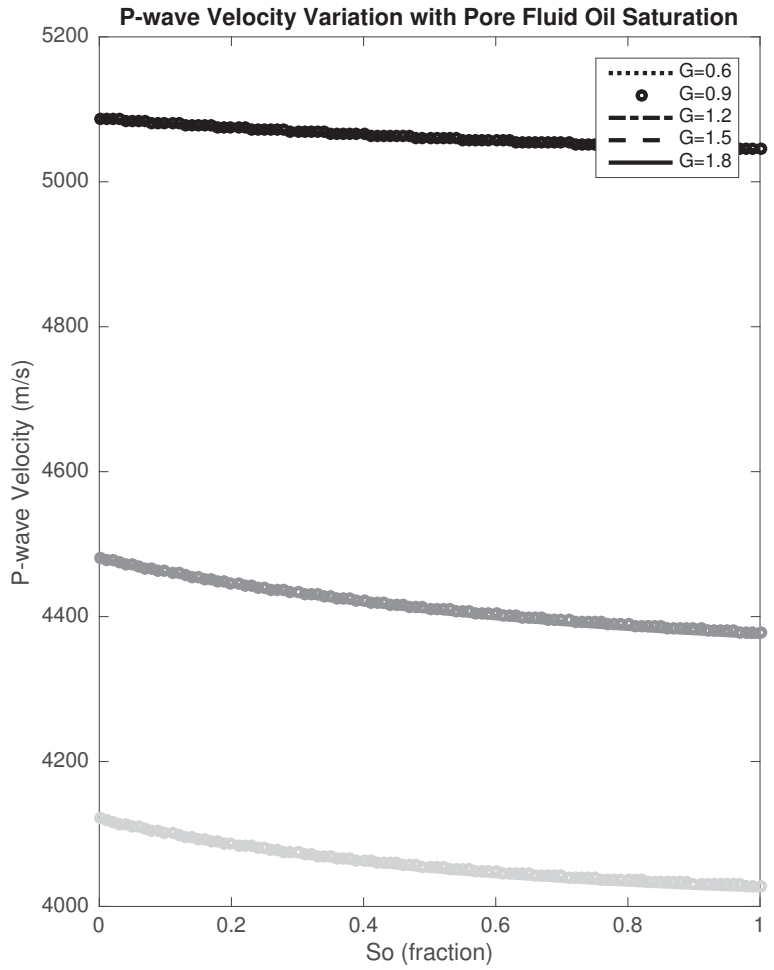

Figure 3.13: P-wave velocity versus oil saturation at various gas gravity values shown for 1% (black), 10% (dark grey) and 20% (light grey) porosity values. All other parameters are set to the default conditions stated in Figure 3.4. This plot is also representative of salinity sensitivity.

used here. That is, moving from right to left along a particular curve simulates time passed in the vicinity of a hydraulic fracture.

Over the input parameter ranges tested, Δv_p is moderately sensitive to variation in API, pore pressure, temperature and gas-oil ratio (Figure 3.12) with little sensitivity to gas gravity and salinity (Figure 3.13). The sensitivity of Δv_p to API, pore pressure, temperature and gas-oil ratio is greater at high porosity values. Also, Δv_s shows minor sensitivity to API at high porosity and

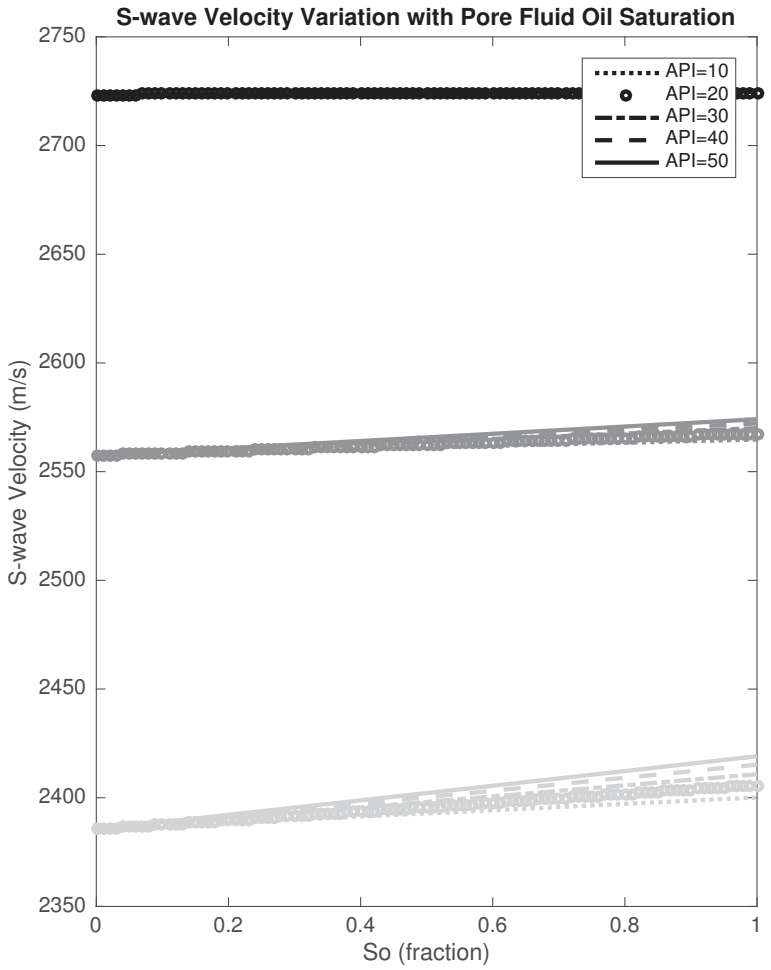

Figure 3.14: S-wave velocity versus oil saturation at various API values shown for 1% (black), 10% (dark grey) and 20% (light grey) porosity values. All other parameters are set to the default conditions stated in Figure 3.4.

is relatively insensitive to all other pore-fluid input parameters (Figure 3.14). In this case, Δv_s is only slightly sensitive to porosity because oil and brine have relatively similar density, especially at low API.

If all input parameters are set to the default values and we compare Δv_p and Δv_s in an initially gas-saturated rock to Δv_p and Δv_s in an initially oil-saturated rock, the change in velocities are greater when brine replaces gas. This is due to the larger difference in density and bulk modulus between brine

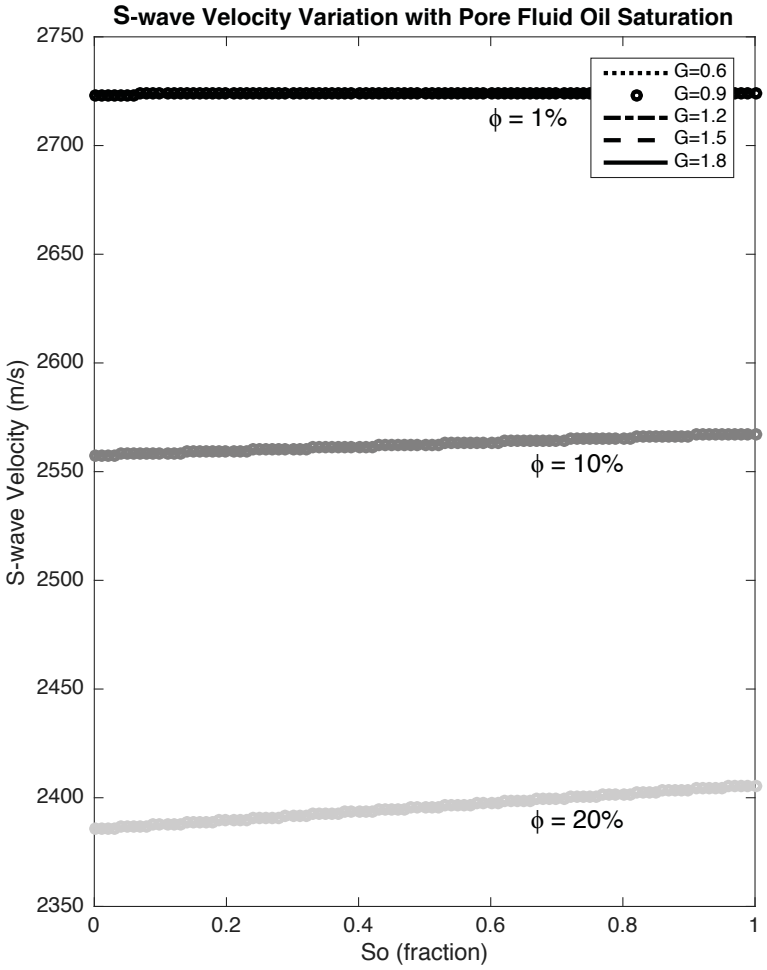

Figure 3.15: S-wave velocity versus oil saturation at various gas gravity values shown for 1% (black), 10% (dark grey) and 20% (light grey) porosity values. All other parameters are set to the default conditions stated in Figure 3.4. This plot is also representative of the gas-oil ratio, salinity, temperature and pore-pressure sensitivity.

and gas than between brine and oil.

3.4.2 Lithostatic-Stress Variation

In the previous subsection we investigated the effect of changing pore pressure while assuming the effective stress remained constant. In the next two subsections we investigate the effect of varying the effective stress by assuming

either pore pressure (Subsection 3.4.2) or lithostatic stress (Subsection 3.4.3) is constant.

To investigate velocity sensitivity to lithostatic stress, the pore pressure is assumed constant and any change in effective stress must be due to lithostatic-stress change. We first show the P-wave velocity response to increasing effective stress for gas, oil and brine saturated rock at various porosity values at various depths (Figure 3.16). Figures 3.17 to 3.20 then show the dependence of P- and S-wave velocity respectively on variation in effective stress for the soft-sand model and the stiff-sand model at a single depth of $2\,km$. We now introduce an additional sensitivity term, $\Delta v_{p,total}$, that is defined as the total P-wave velocity change when effective stress increases from $\approx 0\,MPa$ to $\approx 55\,MPa$. The term $\Delta v_{s,total}$ is analogous for S-wave velocity. Recall, Table 3.2 at the end of this section provides a quick-access summary of the velocity sensitivity terms used in this chapter.

Figure 3.16 shows P-wave velocity response to variable effective stress for gas, oil and brine saturated rock shown for three porosity values (ϕ = 1%, 10%, 20%) using the soft-sand model at four depths (depth = $1\,km$, $2\,km$, $3\,km$, $4\,km$). The dashed vertical lines respectively indicate the initial lithostatic stress at each depth ($\sigma_{litho} = 24\,MPa$, $47\,MPa$, $71\,MPa$, $94\,MPa$). The type of fluid saturating the rock is differentiated by line style, the porosity values are indicated by grey scale and there is no differentiation for depth. For example, a solid black line represents a brine saturated rock with 1% porosity at $1km, 2km, 3km$ and $4km$ depths. It is seen that the Δv_p between the four depth curves for each of the fluid-fill/porosity combinations is very small. The behaviour of S-wave velocity response to effective stress is similar to that observed in Figure 3.16, and therefore is not shown.

Figure 3.17 shows the dependence of P-wave velocity on variation in effective stress for the soft-sand model at a single depth of $2\,km$. Increasing porosity results in a larger $\Delta v_{p,total}$ for all saturation-fluid curves. However, at a given

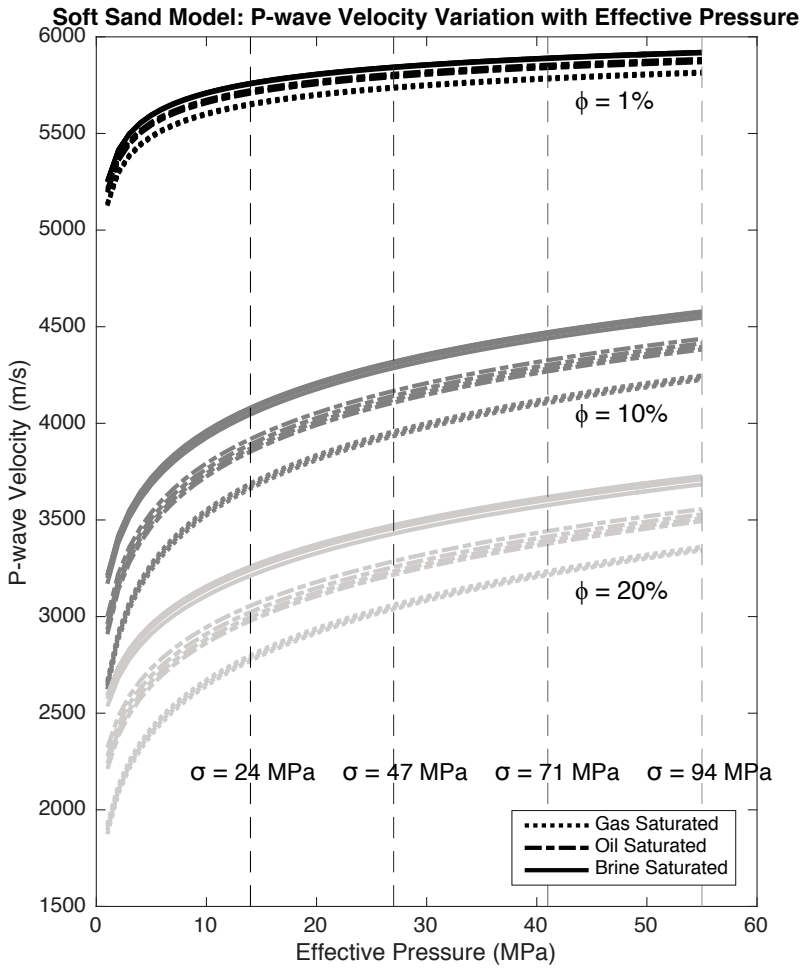

Figure 3.16: P-wave velocity versus effective stress for gas, oil and brine saturated rock shown for 1% (black), 10% (dark grey) and 20% (light grey) porosity values using the soft-sand model at various depths ($1\,km$, $2\,km$, $3\,km$, $4\,km$). The velocity curves for each depth are mostly overlapping. However, in the case where there is a slight separation between the curves, the velocity curves for greater depths are have slightly larger velocity magnitudes. The dashed vertical lines indicate the initial lithostatic stress at each depth from left to right. Variation in effective stress is due to lithostatic-stress variation and all other parameters are set to the default conditions stated in Figure 3.4.

porosity the $\Delta v_{p,total}$ is similar regardless of saturation fluid. Also, Δv_p between the three saturation-fluid curves is small at low porosity but is significantly larger at moderate and high porosity. The shape of the P-wave velocity curve

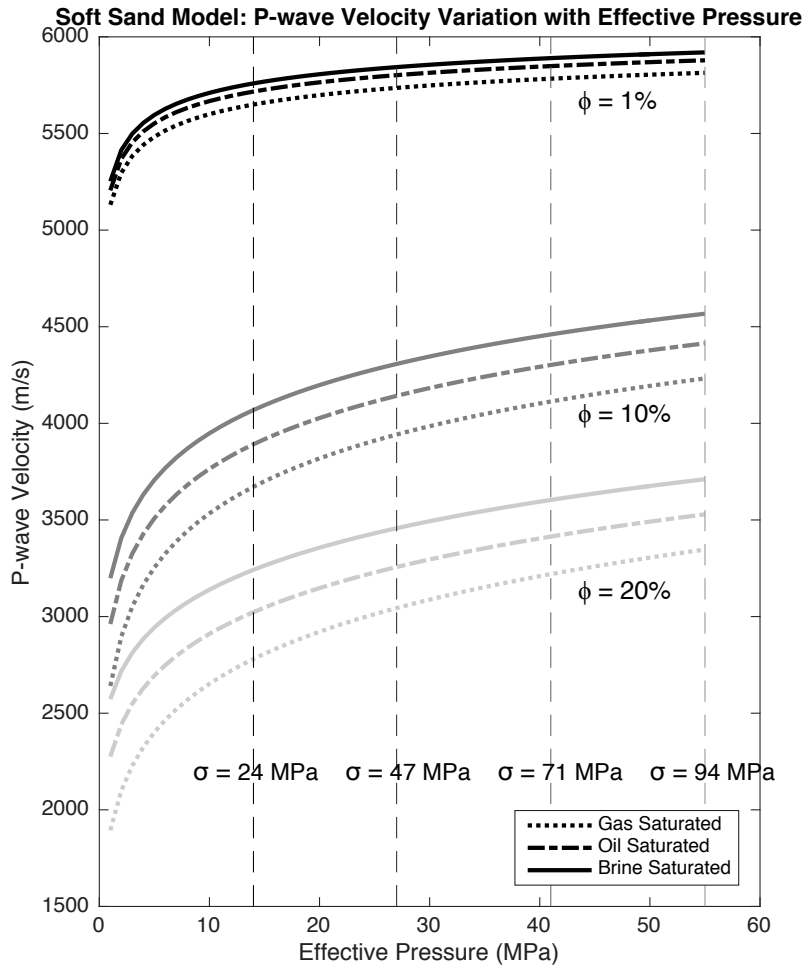

Figure 3.17: P-wave velocity versus effective stress for gas, oil and brine saturated rock shown for 1% (black), 10% (dark grey) and 20% (light grey) porosity values using the soft-sand model at $2\,km$ depth. Variation in effective stress is due to lithostatic-stress variation and all other parameters are set to the default conditions stated in Figure 3.4.

in Figure 3.17 illustrates two things. First, for an equal magnitude deviation from an initial effective stress, an effective stress increase will always result in a smaller magnitude change in P-wave velocity than an effective stress decrease. Second, P-wave velocity is more sensitive to effective stress variation at a low initial effective stress. In general, lower effective stresss are encountered at shallow depth. Hence, the increase in lithostatic stress due to a hydraulic

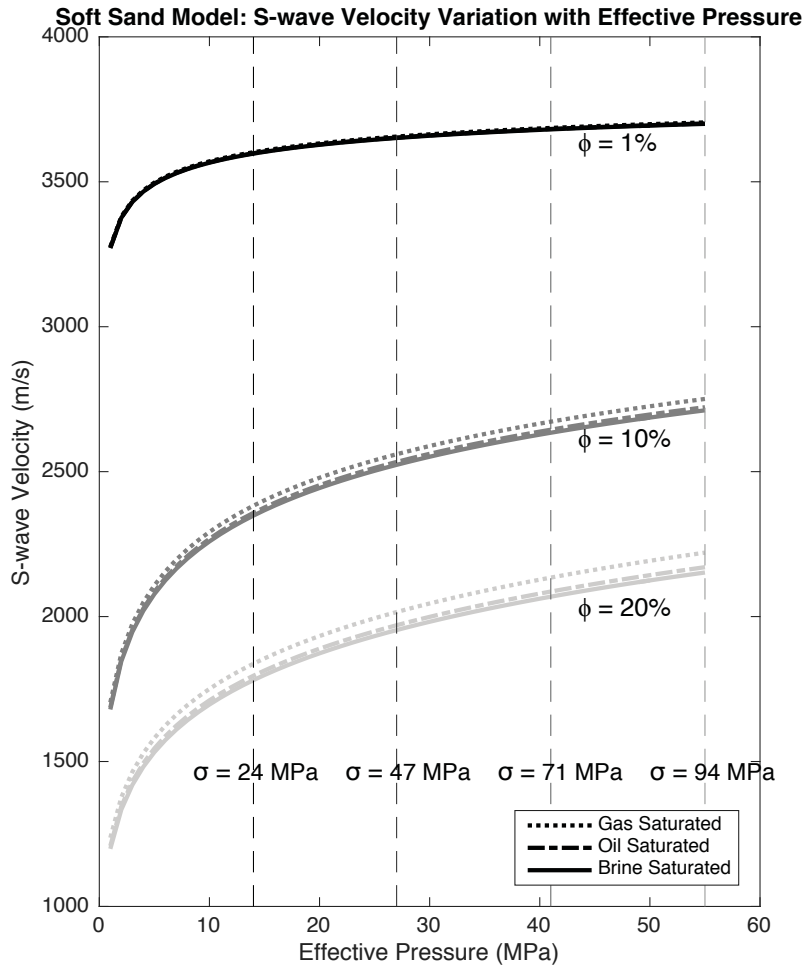

Figure 3.18: S-wave velocity versus effective stress for gas, oil and brine saturated rock shown for 1% (black), 10% (dark grey) and 20% (light grey) porosity values using the soft-sand model at $2\,km$ depth. Variation in effective stress is due to lithostatic-stress variation and all other parameters are set to the default conditions stated in Figure 3.4).

fracture will result in a smaller increase in P-wave velocity in a reservoir at greater depth.

The dependence of S-wave velocity on variation in effective stress for the soft-sand model at a single depth of $2\,km$ is similar to that of P-wave velocity with two noticeable differences (Figure 3.18). First, the Δv_s between the three saturation-fluid curves is very small regardless of porosity and second, the

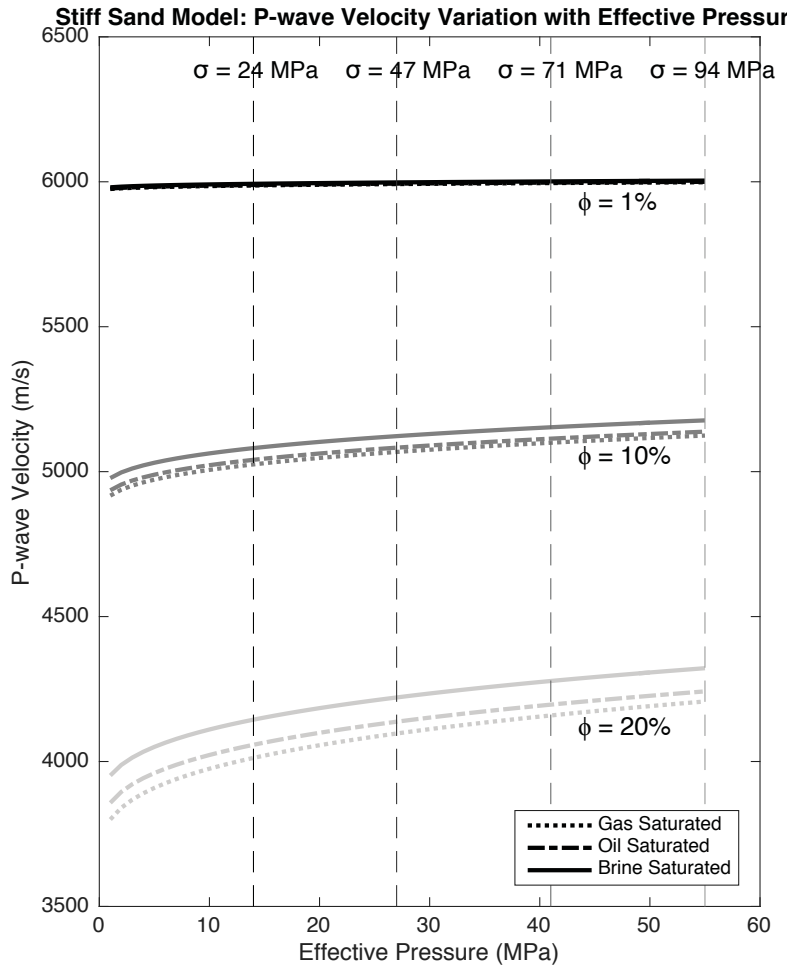

Figure 3.19: P-wave velocity versus effective stress for gas, oil and brine saturated rock shown for 1% (black), 10% (dark grey) and 20% (light grey) porosity values using the stiff-sand model at $2\,km$ depth. Variation in effective stress is due to lithostatic-stress variation and all other parameters are set to the default conditions stated in Figure 3.4.

$\Delta v_{s,total}$ of each curve is smaller than the $\Delta v_{p,total}$ of the corresponding curve.

The change in P- and S-wave velocity with effective stress is sensitive to the sand model used, as seen by respectively comparing Figure 3.17 to Figure 3.19 and comparing Figure 3.18 to Figure 3.20. Figures 3.19 and 3.20 show that $\Delta v_{p,total}$ and $\Delta v_{s,total}$ are smaller for the stiff-sand model for all fluid types and porosity values. This is the result of the physical properties of a stiff rock

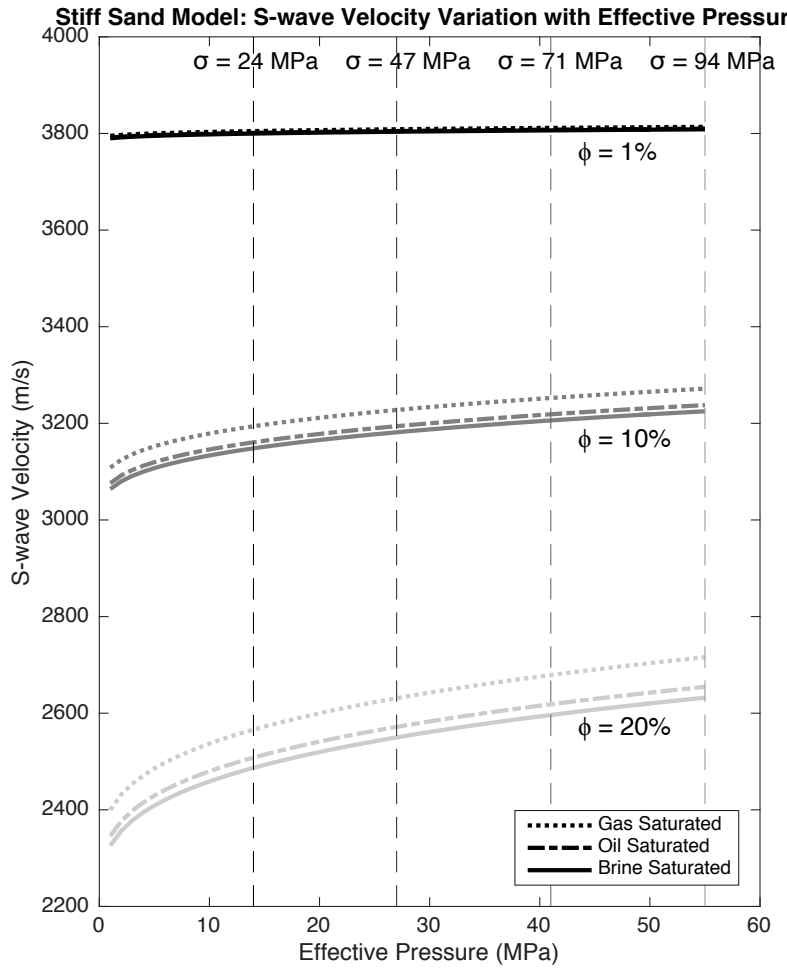

Figure 3.20: S-wave velocity versus effective stress for gas, oil and brine saturated rock shown for 1% (black), 10% (dark grey) and 20% (light grey) porosity values using the stiff-sand model at $2\,km$ depth. Variation in effective stress is due to lithostatic-stress variation and all other parameters are set to the default conditions stated in Figure 3.4.

varying less than a compressible rock in response to effective stress variation.

3.4.3 Pore-Pressure Variation

To investigate velocity sensitivity to pore pressure the confining stress is assumed constant, therefore any change in effective stress must be due to pore-pressure change. A plot of P- or S-wave velocity response to variable effective

stress for gas, oil and brine saturated rock at three porosity values (ϕ = 1%, 10%, 20%) using the soft-sand model at four depths (depth = $1\,km$, $2\,km$, $3\,km$, $4\,km$) is nearly identical to Figure 3.16. That is, an effective stress variation of a given magnitude from a given initial effective stress will result in the same change in velocity whether the pressure change is due to pore-pressure variation or lithostatic-stress variation. As a result, Figures 3.16 to 3.20 are nearly identical for effective stress due to pore-pressure variation. This is primarily a result of assuming the effective-pressure coefficient, α, in equation 3.1 is approximately equal to one. However, if we were to assume an effective stress coefficient of $\alpha < 1$, the seismic velocities would be less sensitive to pore-pressure variation than to lithostatic-stress variation.

Finally, it is instructive to compare the relative magnitude of isotropic velocity change due to fluid substitution versus effective stress variation for realistic reservoir conditions. We compare an effective stress change with no fluid substitution to a 100% brine substitution in an initially gas-saturated rock with no effective stress change. Modelling performed by Warpinski et al. (2004) gives a maximum effective stress variation in the vicinity of a hydraulic fracture of $-14\,MPa$. Using the stiff-sand model for a $2\,km$ depth reservoir with 10% porosity for a $14\,MPa$ effective stress decrease in a brine saturated rock, P-wave velocity changes by $\approx -40\,m/s$ and S-wave velocity by $\approx -30\,m/s$. Compare these values to the P- and S-wave velocity change when a 100% brine saturation replaces a 100% gas saturation in a reservoir at the same depth and porosity with no effective stress change: $\approx 60\,m/s$ and $\approx -30\,m/s$ respectively. Hence, under the stated reservoir conditions, the effect of fluid substitution and effective stress variation on isotropic P-wave and S-wave velocities are on the same order of magnitude and represent an approximately 1% overall change. In most unconventional reservoirs the porosity is actually significantly smaller than 10% which would result in even smaller isotropic velocity variations.

3.5 Conclusions

The volume of rock surrounding a hydraulic fracture experiences fluid invasion, lithostatic-stress increase, and pore-pressure increase. These three processes change the in-situ isotropic P- and S-wave velocities of the rock.

When a brine saturation replaces a 100% hydrocarbon gas saturation, P-wave velocity is most sensitive to variation in gas gravity and pore pressure at high porosity, and S-wave velocity is most sensitive to variation in gas gravity at high porosity. The porosity and the completeness of fluid replacement are the primary controls on P-wave velocity behaviour. If fluid replacement is inefficient and greater than 20% gas saturation remains in a moderate-to-high porosity reservoir, P-wave velocity remains constant or shows a slight decrease. However, if the reservoir is low porosity or if less than 20% gas saturation remains in a moderate-to-high porosity reservoir, P-wave velocity will show an increase. When brine replaces a hydrocarbon oil, P-wave velocity is moderately sensitive to variation in API, gas-oil ratio, pore pressure and temperature with higher sensitivities at high porosity. In contrast, S-wave velocity only shows minor sensitivity to API and only at high porosity.

Isotropic seismic velocites, both P- and S-wave velocity, also respond to change in effective stress with a higher velocity sensitivity at low initial effective stress and high porosity. The magnitude of change in P- and S-wave velocities are largely insensitive to the pore-saturating fluid type. Given a set magnitude of effective stress deviation from an initial effective stress with all other input parameters constant, the magnitude of P- and S-wave velocity responses are larger for an effective stress decrease than for an increase. Additionally, the stiff-sand model shows P- and S-wave velocity are less sensitive to effective stress than the soft-sand model shows.

These observations imply that in a low porosity, gas-saturated reservoir in the region adjacent to a shallow hydraulic fracture where pore-pressure increase

is greater than lithostatic-stress increase and incomplete displacement of the pore-saturating hydrocarbons takes place, P-wave velocity will increase slightly due to fluid replacement. However, this increase will be counteracted by the slight decrease in P-wave velocity due to effective stress decrease. The magnitude of P-wave velocity change under these conditions is sensitive to gas gravity, pore pressure and rock stiffness. In contrast, S-wave velocity will decrease due to both fluid replacement and effective stress decrease while the magnitude of S-wave velocity change is sensitive only to rock stiffness.

Given the above observations, the volume of rock in the vicinity of a hydraulic fracture can now be described in terms of effective-stress changes and the expected isotropic seismic velocity changes. Recall, the compressive, shear and tensile zones will not experience significant fluid replacement or pore-pressure changes. The compressive zone will experience effective-pressure increase and we expect to see a P- and S-wave isotropic velocity increase. The shear zone will experience low-magnitude effective-pressure changes and we expect to see little P- and S-wave velocity change. The tensile zone will experience effective-pressure decrease and we expect to see a P- and S-wave isotropic velocity decrease. Furthermore, given an equal-magnitude effective-pressure perturbation in the compressive and tensile zones, the velocity perturbation will be tend to be larger in the tensile zone. The determining the expected velocity perturbations in the proximal zone is more complicated, where fluid replacement, pore-pressure increase and confining-stress changes are happening simultaneously. For simplicity, let us assume the proximal zone is dominated by pore-pressure increase, therefore experiencing an effective-pressure decrease. Let us assume the reservoir is low-porosity, is initially hydrocarbon saturated and following the hydraulic fracture treatment a brine replaces the pore fluid within the proximal zone. In this case, we expect a P-wave isotropic velocity increase due to fluid replacement and a P-wave isotropic velocity decrease due to the effective-stress decrease. We expect the competing effects of fluid

replacement and effective-stress decrease will tend to result in low-magnitude P-wave isotropic velocity changes. In contrast, we expect an S-wave isotropic velocity decrease due to both fluid replacement and effective-stress decrease, resulting in a relatively large S-wave isotropic velocity decrease. Figure 3.21 shows the four spatiotemporal zones introduced in Chapter 2, along with the expected isotropic velocity changes in each zone.

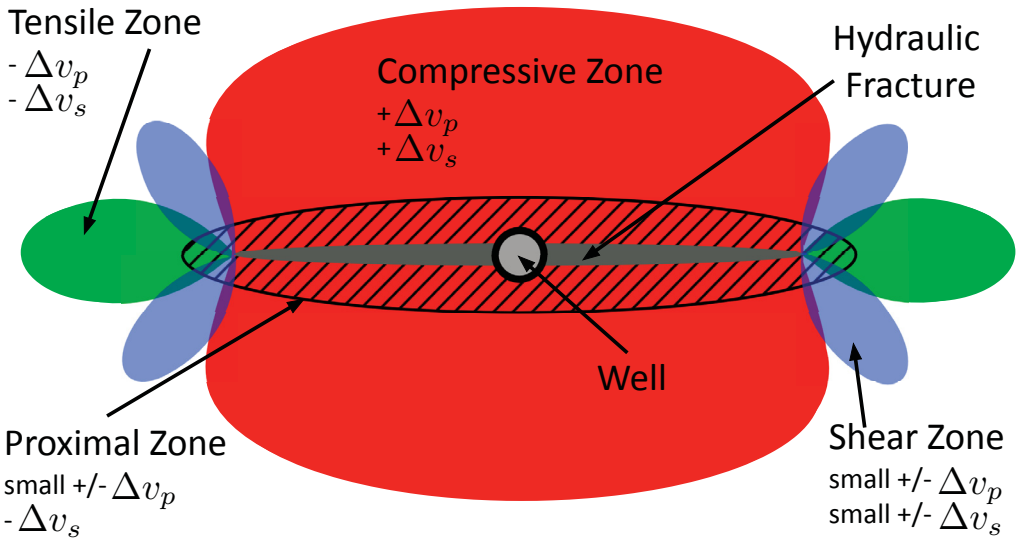

Figure 3.21: A horizontal cross-section through a vertical hydraulic fracture extending from a vertical well illustrating the four spatiotemporal zones in the surrounding region, modified from Cipolla et al. (2011). The area with black diagonal lines indicates the proximal zone, the solid red area indicates the compressive zone, the solid blue area indicates the shear zone and the solid green area indicates the tensile zone. For simplicity, we assume that the extent of fluid invasion corresponds to the extent of pore-pressure increase; however, this is not always true. Expected isotropic P-wave and S-wave velocity perturbations are indicated in each of the four zones, denoted by Δv_p and Δv_s respectively. A negative sign, '$-$', indicates a decrease, a positive sign, '$+$', indicates an increase and '$+/-$' indicates a possible increase or decrease.

Chapter 4

Pore-Pressure Diffusion and Confining-Stress Modelling in the Vicinity of a Hydraulic Fracture

4.1 Introduction

The material presented in this chapter is based on work that was presented orally at the 2017 Society of Exploration Geophysicists Annual International Meeting in Houston, Texas (Brisco and Van der Baan, 2017). Keeping in mind the ultimate goal of this thesis is to create a realistic model of the anisotropic velocity field around a hydraulic fracture, in Chapter 2 we discussed the three main processes acting around a hydraulic fracture affecting seismic velocites: pore-pressure diffusion, pore-fluid replacement and confining-stress change due to rock matrix deformation. In Chapter 3, we showed in low-porosity reservoirs, typical targets for hydraulic fracturing, variation in the properties of the pore-saturating fluid have little-to-no effect on seismic velocities. Also, in Chapter 3 we demonstrated that seismic velocities respond to the combined effects of

pore-pressure diffusion and confining-stress change, i.e. effective-stress change. That is, for common hydraulic fracturing environments, predictions of pore-pressure diffusion and confining-stress change are essential input parameters required to model the resulting anisotropic velocity field, but we can ignore the effects of pore-fluid replacement.

In this chapter, we consider the case of a hydraulic fracture growing in a low-porosity, isotropic, homogeneous reservoir. First, we use a classic analytical solution to model the triaxial confining-stress change that results from the pressurized fracture displacing a volume of rock in a direction normal to the fracture face. Then, we use a second-order partial differential diffusion equation in a three dimensional finite-difference scheme to model pore-pressure diffusion through the surfaces of the hydraulic fracture. We treat pore pressure as a hydrostatic stress. Next, we combine the confining-stress change and pore-pressure perturbation to obtain the triaxial effective-stress change in the vicinity of the hydraulic fracture. Confining and effective-stress changes are displayed in terms of mean stress values, in addition to, breaking the stress changes down into the three principle components. Finally, we discuss aspects of the modelled effective-stress changes in the context of eventually modelling the seismic velocity field around the hydraulic fracture.

4.2 Theory

4.2.1 Confining Stress

Eshelby (1957, 1959) derived a three dimensional solution for the stress field in and around an ellipsoidal inclusion and demonstrated that elastic stress within an ellipsoidal inclusion embedded in a matrix is homogeneous when the system is subjected to an external far-field stress. This holds true if the far-field stress is either lithostatic or triaxial in nature. In our case, the surrounding matrix is a fluid-saturated poroelastic medium. An inclusion, as described by Eshelby

(1957, 1959), can be used to approximate a hydraulic fracture held open by elevated fluid pressure. Following Eshelby (1957, 1959)'s work, the stress at any point inside an inclusion, $\boldsymbol{\sigma}$, is given by Ju and Sun (1999) as

$$\boldsymbol{\sigma} = \boldsymbol{\sigma}_\circ + \boldsymbol{C}_\circ \cdot [\boldsymbol{S} - \boldsymbol{I}] : \boldsymbol{\epsilon}_{**} \,, \tag{4.1}$$

where the symbol "$\cdot$" denotes tensor multiplication, the symbol ":" denotes tensorial contraction, $\boldsymbol{\sigma}_\circ$ is the far-field stress, $\boldsymbol{C}_\circ$ is the isotropic 4th-order stiffness tensor of the fluid-saturated poroelastic medium, $\boldsymbol{S}$ is the 4th-order Eshelby $\boldsymbol{S}$ tensor, $\boldsymbol{I}$ is the 4th-order identity tensor and $\boldsymbol{\epsilon}_{**}$ is the eigenstrain. The term eigenstrain was introduced by Mura (1987) in reference to Eshelby's 'strain-free stress' and in our case represents the strain that would result from the pore pressure in the inclusion if the inclusion was not confined by the fluid-saturated poroelastic medium. The Eshelby $\boldsymbol{S}$ tensor is invariant with respect to position within the inclusion (Eshelby, 1957, 1959). Ju and Sun (1999) express the eigenstrain as

$$\boldsymbol{\epsilon}_{**} = (\boldsymbol{S} + \boldsymbol{A})^{-1} : [\boldsymbol{B} : (\boldsymbol{\epsilon}_{\boldsymbol{t}} - \boldsymbol{\epsilon}_\circ)] \,, \tag{4.2}$$

where a tensorial variable raised to the power of -1 (eg. $(\boldsymbol{S} + \boldsymbol{A})^{-1}$) indicates the inverse of the tensor, $\boldsymbol{\epsilon}_{\boldsymbol{t}}$ is the prescribed eigenstrain and $\boldsymbol{\epsilon}_\circ$ is the far-field strain that can be calculated using Hooke's Law as follows:

$$\boldsymbol{\epsilon}_\circ = (\boldsymbol{C}_\circ)^{-1} : \boldsymbol{\sigma}_\circ \,. \tag{4.3}$$

The prescribed eigenstrain, $\boldsymbol{\epsilon}_{\boldsymbol{t}}$, is found in a similar manner to the far-field strain in equation 4.3 by instead using the inclusion material stiffness, $\boldsymbol{C_1}$, and the prescribed eigenstress, $\boldsymbol{\sigma}_{\boldsymbol{t}}$, which in our case is given by the injection pressure within the hydraulic fracture. In equation 4.2, the 4th-order elastic-phase "mismatch tensors" $\boldsymbol{A}$ and $\boldsymbol{B}$ are given by

$$\boldsymbol{A} = (\boldsymbol{C_1} - \boldsymbol{C_\circ})^{-1} \cdot \boldsymbol{C_\circ} \tag{4.4}$$

and

$$\boldsymbol{B} = (\boldsymbol{C_1} - \boldsymbol{C_\circ})^{-1} \cdot \boldsymbol{C_1}\,, \tag{4.5}$$

where $\boldsymbol{C_1}$ is the isotropic 4th-order stiffness tensor of the inclusion material. Using Voigt notation to express the stiffness tensor of an isotropic medium as a 6×6 matrix, $\boldsymbol{C_{ISO}}$, that is a function of bulk, K, and shear, μ modulus results in

$$\boldsymbol{C_{ISO}} = \begin{bmatrix} C_{11} & C_{12} & C_{12} & 0 & 0 & 0 \\ C_{12} & C_{11} & C_{12} & 0 & 0 & 0 \\ C_{12} & C_{12} & C_{11} & 0 & 0 & 0 \\ 0 & 0 & 0 & C_{44} & 0 & 0 \\ 0 & 0 & 0 & 0 & C_{44} & 0 \\ 0 & 0 & 0 & 0 & 0 & C_{44} \end{bmatrix}, \tag{4.6}$$

where $C_{11} = K + 4/3\mu$, $C_{12} = K - 2/3\mu$ and $C_{44} = \mu$. Poisson's ratio, ν can likewise be expressed as a function of bulk and shear modulus as follows:

$$\nu = \frac{3K + 2\mu}{2(3K + \mu)}\,. \tag{4.7}$$

The external stress field, $\boldsymbol{\sigma(x)}$, surrounding an ellipsoidal inclusion is position dependent and is given by

$$\boldsymbol{\sigma(x)} = \boldsymbol{\sigma_\circ} + \boldsymbol{C_\circ} \cdot \boldsymbol{G(x)} : \boldsymbol{\epsilon_{**}} \tag{4.8}$$

where $\boldsymbol{x}$ is the position vector of the point of interest and $\boldsymbol{G(x)}$ is a 4th-order tensor that is a function of ellipsoid geometry, the fluid-saturated poroelastic medium Poisson's ratio and the position vector (Ju and Sun, 1999).

If we assume a vertical hydraulic fracture is a specific case of ellipsoid, an

oblate spheroid with semi-axis dimensions of ($a_1 << a_2 = a_3$), explicit solutions for the Eshelby $\boldsymbol{S}$ and $\boldsymbol{G(x)}$ tensors can be used to calculate the internal and external stress fields within and around the inclusion. The remainder of this subsection is dedicated to describing the explicit expression of $\boldsymbol{S}$ and $\boldsymbol{G(x)}$.

Eshelby $\boldsymbol{G(x)}$ Tensor (Exterior Point)

The external stress field surrounding an oblate spheroid can be found using the explicit expression for the Eshelby $\boldsymbol{G(x)}$ tensor given by Ju and Sun (2001). In the remainder of this chapter, we assume that the centre of the ellipsoidal inclusion coincides with the origin of the coordinate system. The same tensorial indicial notation as decribed by Mura (1987) is used, where repeated lower-case indices are summed and upper-case indices take on the same values as the corresponding lower-case ones, but are not summed. All indices $i, j, k, l \in \{1, 2, 3\}$. Ju and Sun (1999) derive explicit expressions for all components of $\boldsymbol{G(x)}$ by introducing the outward facing unit normal vector, $\hat{\boldsymbol{n}}$, at any fluid-saturated poroelastic medium point $\boldsymbol{x}$ on an imaginary ellipsoid. This imaginary ellipsoid has the same centre point and the same geometry as the inclusion but is expanded in size. The components of $\boldsymbol{G(x)}$ are given by Ju and Sun (1999) as

$$\begin{aligned} G_{ijkl}(\boldsymbol{x}) = \frac{1}{4(1-\nu_\circ)} \Big[& S^{(1)}_{IK}(\omega)\delta_{ij}\delta_{kl} + S^{(2)}_{IJ}(\omega)(\delta_{ik}\delta_{jl} + \delta_{il}\delta_{jk}) \\ & + S^{(3)}_{I}(\omega)\delta_{ij}\hat{n}_k\hat{n}_l + S^{(4)}_{K}(\omega)\delta_{kl}\hat{n}_i\hat{n}_j + S^{(5)}_{I}(\omega)(\delta_{ik}\hat{n}_j\hat{n}_l + \delta_{il}\hat{n}_j\hat{n}_k) \\ & + S^{(6)}_{J}(\omega)(\delta_{jk}\hat{n}_i\hat{n}_l + \delta_{jl}\hat{n}_i\hat{n}_k) + S^{(7)}_{IJKL}(\omega)\hat{n}_i\hat{n}_j\hat{n}_k\hat{n}_l \Big] \end{aligned} \tag{4.9}$$

where $\nu_\circ$ is the fluid-saturated poroelastic medium Poisson's ratio, δ_{ij} is the Kroenecker delta tensor, $\hat{n}_i$ are the components of the outward facing unit normal vector and are given by

$$\hat{n}_i = \frac{x_i}{(a_I^2 + \omega)\sqrt{\Theta(\omega)}}\,, \tag{4.10}$$

where

$$\Theta(\omega) = \Theta_i(\omega)\Theta_i(\omega) \tag{4.11}$$

and

$$\Theta_i(\omega) = \frac{x_i}{(a_I^2 + \omega)}\,. \tag{4.12}$$

Recall, the repeated indices in equation 4.11 imply summation. All $S^{(m)}$ terms are described below and are functions of the fluid-saturated poroelastic medium Poisson's ratio, ellipsoidal geometry and observation position, where superscript numbers in brackets, (m), simply indicate the term number. Expressed as a matrix, the terms $S_{IK}^{(1)}(\omega)$ and $S_{IJ}^{(2)}(\omega)$ respectively take the forms of

$$\boldsymbol{S^{(1)}} = \begin{bmatrix} S_{11}^{(1)} & S_{12}^{(1)} & S_{12}^{(1)} \\ S_{21}^{(1)} & S_{22}^{(1)} & S_{22}^{(1)} \\ S_{21}^{(1)} & S_{22}^{(1)} & S_{22}^{(1)} \end{bmatrix} \tag{4.13}$$

and

$$\boldsymbol{S^{(2)}} = \begin{bmatrix} S_{11}^{(1)} & S_{12}^{(1)} & S_{12}^{(1)} \\ S_{12}^{(1)} & S_{22}^{(1)} & S_{22}^{(1)} \\ S_{12}^{(1)} & S_{22}^{(1)} & S_{22}^{(1)} \end{bmatrix}\,. \tag{4.14}$$

Explicit expression for all $S_{IK}^{(1)}(\omega)$ and $S_{IJ}^{(2)}(\omega)$ components are given by Ju and Sun (1999, 2001). However, Healy (2009) notes the first two terms of components $S_{11}^{(1)}(\omega)$, $S_{12}^{(1)}(\omega)$, $S_{11}^{(2)}(\omega)$ and $S_{12}^{(2)}(\omega)$ are reported with the incorrect sign in Ju and Sun (2001). The correct $S_{IK}^{(1)}(\omega)$ and $S_{IJ}^{(2)}(\omega)$ components are as follows:

$$S_{11}^{(1)}(\omega) = \left[4\nu_\circ + \frac{2}{\alpha_\circ^2 - 1}\right] g(\omega) - \frac{2}{3(\alpha_\circ^2 - 1)}\rho_1^3(\omega) + \left[4\nu_\circ + \frac{2}{\alpha_\circ^2 - 1}\right]\rho_1(\omega)\rho_2^2(\omega)\,, \tag{4.15}$$

$$S_{12}^{(1)}(\omega) = \left[4\nu_\circ - \frac{2\alpha_\circ^2 + 1}{\alpha_\circ^2 - 1}\right] g(\omega) + \left[4\nu_\circ + \frac{2\alpha_\circ^2}{\alpha_\circ^2 - 1}\right]\rho_1(\omega)\rho_2^2(\omega)\,, \tag{4.16}$$

$$S_{21}^{(1)}(\omega) = \left[- 2\nu_\circ - \frac{2\alpha_\circ^2 + 1}{\alpha_\circ^2 - 1}\right] g(\omega) - \frac{2\alpha_\circ^2}{\alpha_\circ^2 - 1}\rho_1(\omega)\rho_2^2(\omega)\,, \tag{4.17}$$

$$S_{22}^{(1)}(\omega) = \left[- 2\nu_\circ + \frac{4\alpha_\circ^2 - 1}{4(\alpha_\circ^2 - 1)}\right] g(\omega) + \frac{\alpha_\circ^2}{2(\alpha_\circ^2 - 1)}\frac{\rho_2^4(\omega)}{\rho_1(\omega)}\,, \tag{4.18}$$

$$S_{11}^{(2)}(\omega) = \left[4\nu_\circ - \frac{4\alpha_\circ^2 - 2}{\alpha_\circ^2 - 1}\right] g(\omega) - \frac{2}{3(\alpha_\circ^2 - 1)}\rho_1^3(\omega) - \left[4\nu_\circ - \frac{4\alpha_\circ^2 - 2}{\alpha_\circ^2 - 1}\right]\rho_1(\omega)\rho_2^2(\omega)\,, \tag{4.19}$$

$$S_{12}^{(2)}(\omega) = \left[\nu_\circ + \frac{\alpha_\circ^2 + 2}{\alpha_\circ^2 - 1}\right] g(\omega) - \left[2\nu_\circ + \frac{2}{\alpha_\circ^2 - 1}\right]\rho_1(\omega)\rho_2^2(\omega)\,, \tag{4.20}$$

$$S_{22}^{(2)}(\omega) = \left[2\nu_\circ - \frac{4\alpha_\circ^2 - 7}{4(\alpha_\circ^2 - 1)}\right] g(\omega) + \frac{\alpha_\circ^2}{2(\alpha_\circ^2 - 1)}\frac{\rho_2^4(\omega)}{\rho_1(\omega)}\,, \tag{4.21}$$

where

$$\alpha_\circ = \frac{a_1}{a_2}\,, \tag{4.22}$$

$$g(\omega) = -\frac{\alpha_\circ^2}{\alpha_\circ^2 - 1}\frac{\rho_2^2(\omega)}{\rho_1(\omega)} + \frac{\alpha_\circ}{(1 - \alpha_\circ^2)^{1.5}}\tan^{-1}\frac{\alpha_\circ}{\sqrt{1 - \alpha_\circ^2}\rho_1(\omega)}\,, \tag{4.23}$$

$$\rho_I(\omega) = -\frac{a_I}{\sqrt{a_I^2 + \omega}} \tag{4.24}$$

and

$$\omega = \frac{x_i x_i - a_1^2 - a_2^2 + \sqrt{(x_i x_i + a_1^2 - a_2^2)^2 - 4x_1^2(a_1^2 - a_2^2)}}{2}\,. \tag{4.25}$$

The remainder of the components of Eshelby's $G_{ijkl}(\boldsymbol{x})$ tensor in equation 4.9 are given as follows:

$$S_I^{(3)}(\omega) = 2\rho^3(\omega)[1 - \rho_I^2(\omega)]\,, \tag{4.26}$$

$$S_K^{(4)}(\omega) = 2\rho^3(\omega)[1 - 2\nu_\circ - \rho_K^2(\omega)]\,, \tag{4.27}$$

$$S_I^{(5)}(\omega) = 2\rho^3(\omega)[\nu_\circ - \rho_I^2(\omega)]\,, \tag{4.28}$$

$$S_J^{(6)}(\omega) = 2\rho^3(\omega)[\nu_\circ - \rho_J^2(\omega)] \tag{4.29}$$

and

$$\begin{aligned} S_{IJKL}^{(7)}(\omega) = 2\rho^3(\omega)\Bigg[&2[\rho_I^2(\omega) + \rho_J^2(\omega) + \rho_K^2(\omega) + \rho_L^2(\omega)] \\ &+ \rho_m(\omega)\rho_m(\omega) - \frac{4\rho_M^2(\omega)\Theta_m(\omega)\Theta_m(\omega)}{\Theta(\omega)} - 5\Bigg]\,, \end{aligned} \tag{4.30}$$

where

$$\rho(\omega) = [\rho_1(\omega)\rho_1(\omega)\rho_1(\omega)]^{1/3}\,. \tag{4.31}$$

Eshelby *S* Tensor (Interior Point)

Ju and Sun (1999) give the explicit expression of Eshelby's $\boldsymbol{S}$ tensor. For a spheroidal inclusion it takes the form:

$$S_{ijkl} = \frac{1}{4(1-\nu_\circ)}\left[S^{(1)}_{IK}(0)\delta_{ij}\delta_{kl} + S^{(2)}_{IJ}(0)(\delta_{ik}\delta_{jl} + \delta_{il}\delta_{jk})\right], \tag{4.32}$$

where S_{ijkl} is a function of only the ellipsoid dimensions and the Poisson's ratio of the fluid-saturated poroelastic medium. $S^{(1)}_{IK}(0)$ and $S^{(2)}_{IJ}(0)$ are special cases of $S^{(1)}_{IK}(\omega)$ and $S^{(2)}_{IJ}(\omega)$ where ω is set to zero. When expressed as a matrix, the components of $S^{(1)}_{IK}(0)$ and $S^{(2)}_{IJ}(0)$ take the same form as shown respectively in equations 4.13 and 4.14 and for the special case of an oblate spheroid are given by:

$$S^{(1)}_{11}(0) = \left[4\nu_\circ + \frac{2}{\alpha_\circ^2 - 1}\right]g(0) + 4\nu_\circ + \frac{4}{3(\alpha_\circ^2 - 1)}, \tag{4.33}$$

$$S^{(1)}_{12}(0) = \left[4\nu_\circ - \frac{2\alpha_\circ^2 + 1}{\alpha_\circ^2 - 1}\right]g(0) + 4\nu_\circ - \frac{2\alpha_\circ^2}{\alpha_\circ^2 - 1}, \tag{4.34}$$

$$S^{(1)}_{21}(0) = \left[-2\nu_\circ - \frac{2\alpha_\circ^2 + 1}{\alpha_\circ^2 - 1}\right]g(0) - \frac{2\alpha_\circ^2}{\alpha_\circ^2 - 1}, \tag{4.35}$$

$$S^{(1)}_{22}(0) = \left[-2\nu_\circ + \frac{4\alpha_\circ^2 - 1}{4(\alpha_\circ^2 - 1)}\right]g(0) + \frac{\alpha_\circ^2}{2(\alpha_\circ^2 - 1)}, \tag{4.36}$$

$$S^{(2)}_{11}(0) = \left[-4\nu_\circ + \frac{4\alpha_\circ^2 - 2}{\alpha_\circ^2 - 1}\right]g(0) - 4\nu_\circ + \frac{12\alpha_\circ^2 - 8}{3(\alpha_\circ^2 - 1)}, \tag{4.37}$$

$$S^{(2)}_{12}(0) = \left[-\nu_\circ - \frac{\alpha_\circ^2 + 2}{\alpha_\circ^2 - 1}\right]g(0) - 2\nu_\circ - \frac{2}{\alpha_\circ^2 - 1}, \tag{4.38}$$

$$S^{(2)}_{22}(0) = \left[2\nu_\circ - \frac{4\alpha_\circ^2 - 7}{4(\alpha_\circ^2 - 1)}\right]g(0) + \frac{\alpha_\circ^2}{2(\alpha_\circ^2 - 1)}, \tag{4.39}$$

where

$$g(0) = -\frac{\alpha_\circ^2}{(\alpha_\circ^2 - 1)^{1.5}} \left[\alpha_\circ \sqrt{1 - \alpha_\circ^2} - \cos^{-1} \alpha_\circ \right] . \tag{4.40}$$

As seen in equations 4.32 to 4.40, the Eshelby $\boldsymbol{S}$ tensor is a function of only the ellipsoidal inclusion aspect ratio, $\alpha_\circ$, and the Poisson's ratio of the fluid-saturated poroelastic medium surrounding the inclusion, $\nu_\circ$ (Eshelby, 1957, 1959). Voigt notation can be used to express the interior Eshelby $\boldsymbol{S}$ tensor as a 6×6 matrix gives the following form:

$$\boldsymbol{S} = \begin{bmatrix} S_{1111} & S_{1122} & S_{1133} & 0 & 0 & 0 \\ S_{1122} & S_{2222} & S_{2233} & 0 & 0 & 0 \\ S_{1133} & S_{2233} & S_{3333} & 0 & 0 & 0 \\ 0 & 0 & 0 & S_{2323} & 0 & 0 \\ 0 & 0 & 0 & 0 & S_{1313} & 0 \\ 0 & 0 & 0 & 0 & 0 & S_{1212} \end{bmatrix} . \tag{4.41}$$

4.2.2 Pore-Pressure Diffusion

For the case of a diffusively anisotropic homogeneous medium, Biot (1956, 1962)'s low-frequency limit equation for slow P-waves can be used to express pore-pressure perturbation in terms of hydraulic diffusivity as follows:

$$\frac{\partial P_{pore}}{\partial t} = D_{ij} \frac{\partial}{\partial x_i} \frac{\partial}{\partial x_j} P_{pore} , \tag{4.42}$$

where P_{pore} is pore pressure, t is time, D_{ij} are the components of the diffusivity tensor and x_i $(i = 1, 2, 3)$ are the components of the radial vector from the injection point to an observation point (Shapiro et al., 2002). If the poroelastic medium through which diffusion is taking place is elastically isotropic and homogeneous, Darcy's Law can be combined with the conservation of mass to relate hydraulic diffusivity to permeability as follows:

$$D_{ij} = \frac{N_m \kappa_{ij}}{\eta}\,, \tag{4.43}$$

where κ_{ij} are the components of the permeability tensor, η is the dynamic viscosity of the pore-saturating fluid and N_m is a poroelastic modulus (Mavko et al., 2009). The poroelastic modulus N_m is given by:

$$N_m = \frac{M P_d}{H}\,, \tag{4.44}$$

$$M = \left[\frac{\phi}{K_{fluid}} + \frac{(\iota - \phi)}{K_{matrix}}\right]^{-1}\,, \tag{4.45}$$

$$\iota = 1 - \frac{K_{dry}}{K_{matrix}}\,, \tag{4.46}$$

$$H = P_d + \iota^2 M \quad \text{and} \tag{4.47}$$

$$P_d = K_{dry} + \frac{4}{3\mu_{dry}}\,, \tag{4.48}$$

where ϕ is the rock porosity, K_{fluid} is the pore-fluid bulk modulus, K_{matrix} is the matrix material bulk modulus, K_{dry} is the dry rock bulk modulus and μ_{dry} is the dry rock shear modulus (Shapiro et al., 2002). If the poroelastic medium through which diffusion is taking place is diffusively isotropic and homogeneous, the diffusion tensor D_{ij} becomes a constant scalar value, D.

4.2.3 Central Scheme Finite Difference Method

We use a central differentiation scheme of order 2 to approximate the partial derivatives of pore pressure with respect to space. Time is treated as order 1. If we assume isotropic diffusivity, we can take advantage of the resultant radial symmetry of the spheroid about the x_1-axis and we are able to reduce

numerical calculation time by only calculating pore-pressure diffusion in a grid of the x_1x_2-plane for $x_3 = 0$ and only for positive x_2 values. In other words, a horizontal cross-section of one half of a vertical fracture through the centre of the fracture is used. The cross-section through the other half of the fracture is simply a mirror image. For the rest of this subsection, to avoid confusing notation we refer to (x_1, x_2, x_3) as (x, y, z). Subscripts on position variables refer to the grid node position and subscripts on t refer to time steps. For example, $x_i = (i-1)\Delta x$, where i is the grid index in the x-direction and Δx is the spatial sampling rate in the x-direction. For each time step ($t_{k=1}$ to $t_{k=k_{max}}$), we calculate the pore pressure as

$$P(x, y, t_{k+1}) = P(x, y, t_k) + \frac{\partial P(x, y, t_k)}{\partial t}\Delta t\,, \tag{4.49}$$

where Δt is the temporal sampling rate, k is the time index, k_{max} is the last time step and we shorten P_{pore} to P for ease of reading. If we assume the medium through which diffusion is taking place is isotropic and homogeneous with respect to diffusion, $\frac{\partial P}{\partial t}$ in equation 4.49 is given by

$$\frac{\partial P(x_i, y_j, t_k)}{\partial t} = D\Big(\frac{\partial^2 P(x_i, y_j, t_k)}{\partial x^2} + \frac{\partial^2 P(x_i, y_j, t_k)}{\partial y^2} + \frac{\partial^2 P(x_i, y_j, t_k)}{\partial z^2(y_j)}\Big)\,, \tag{4.50}$$

where D is the scalar diffusivity and j is the grid index in the y-direction. If i_{max} is the last grid node in the x-direction and j_{max} is the last grid node in the y-direction then for $i \in \{2, i_{max} - 1\}$ and $j \in \{2, j_{max} - 1\}$

$$\frac{\partial^2 P(x_i, y_j, t_k)}{\partial x^2} \approx \frac{P(x_{i+1}, y_j, t_k) - 2P(x_i, y_j, t_k) + P(x_{i-1}, y_j, t_k)}{\Delta x^2}\,, \tag{4.51}$$

$$\frac{\partial^2 P(x_i, y_j, t_k)}{\partial y^2} \approx \frac{P(x_i, y_{j+1}, t_k) - 2P(x_i, y_j, t_k) + P(x_i, y_{j-1}, t_k)}{\Delta y^2} \tag{4.52}$$

and, in order to enforce the condition of radial symmetry about the x-axis,

$$\frac{\partial^2 P(x_i, y_j, t_k)}{\partial z^2(y_j)} \approx \frac{2[P(x_i, y_{j+1}, t_k) - P(x_i, y_j, t_k)]}{\Delta z^2(y_{j+1})}\,, \tag{4.53}$$

where $\Delta z^2(y_{j+1})$ is a function of the distance from y_{j+1} to the x-axis such that

$$\Delta z^2(y_j) = y_{j+1} \sin\theta \tag{4.54}$$

and

$$\theta = \cos^{-1} \frac{y_j}{y_{j+1}}\,. \tag{4.55}$$

In the case that $j = 1$, that is any point perpendicular to the centre of the spheroid in the xy-plane, the condition of radial symmetry about the x-axis requires that

$$\frac{\partial^2 P(x_i, y_1, t_k)}{\partial y^2} = \frac{\partial^2 P(x_i, y_1, t_k)}{\partial z^2} \approx \frac{2[P(x_i, y_2, t_k) - P(x_i, y_1, t_k)]}{\Delta y^2}\,. \tag{4.56}$$

4.3 Method

In order to model confining stress and pore pressure at any point around a hydraulic fracture, we use code written in Matlab to implement Eshelby's solution and Shapiro's pore-pressure diffusion model. The Matlab code we have written for the confining-stress analytical model is primarily based on the Matlab code written by Healy (2009), and our Matlab code for the pore-pressure finite difference model is based on Matlab code provided by Professor David Eaton at

the University of Calgary. We use Voigt notation to express all 4th-order tensors as 6×6 matrices. Stress and strain tensors are expressed as 6-component column vectors.

We assume a hydraulic fracture grows at a defined constant velocity as an oblate spheroid with semi-axes dimensions such that ($a_1 << a_2 = a_3$). Hence, the oblate spheroid as defined represents a low aspect-ratio vertical hydraulic fracture with the fracture plane in the x_2x_3-plane. The spheroid is oriented such that the three semi-axes are aligned with the three principle stress directions which are in turn aligned with the Cartesian coordinate axes (i.e. $a_i \parallel \sigma_i \parallel x_i$). We also assume the fracture initiates as a small-radius spheroid and grows to reach a defined maximum radius.

To start, we first set a number of model input variables that are required for both the confining-stress and pore-pressure models. These variables fall under five categories: stress properties, inclusion or fracturing fluid properties, matrix frame or dry rock properties, matrix constituent material properties and matrix effective media properties. For inclusion properties, we assume the fracturing fluid has the same physical properties as the in-situ pore saturating fluid. This assumption allows us to ignore complications arising from two phase fluid flow. Recall, in Chapter 3 it is shown for a low-porosity stiff rock, seismic velocity change due to effective-stress change is relatively insensitive to pore fluid type, as long as the fluid is brine, oil or high pressured hydrocarbon gas. It is important to note, in order to allow us to find the fluid compliance, $\boldsymbol{C_1}^{-1}$ in equation 4.3, the fluid shear modulus can not equal zero. We set the following variables: injection pressure, in-situ far-field stress conditions, fluid bulk and shear moduli, fluid viscosity, dry rock bulk and shear moduli, matrix material bulk modulus, bulk and shear moduli of the isotropic effective medium representing the fluid-saturated poroelastic rock, fracture width, fracture propagation velocity and maximum fracture diameter. Table 4.1 gives the parameter values that we use for all simulations.

As the spheroid radius increases at the defined velocity, we calculate 'snapshots' of the external-stress field and the pore-pressure perturbation surrounding the spheroid at set times. For each time step, and the corresponding spheroid geometry, we implement the following workflows.

4.3.1 Confining-Stress Analytical Model

First, we set the far-field stress such that $\boldsymbol{\sigma_\circ} = [\sigma_h, \sigma_H, \sigma_v, 0, 0, 0]^T$ and the prescribed eigenstress such that $\boldsymbol{\sigma_t} = [-P_{inject}, -P_{inject}, -P_{inject}, 0, 0, 0]^T$, where the superscript T indicates the transpose.

Next, we perform the following steps:

1. Calculate the elasticity coefficients, $\boldsymbol{C_1}$, of the inclusion material using the defined bulk and shear moduli in equation 4.6.

2. Calculate the elasticity coefficients, $\boldsymbol{C_\circ}$, and Poisson's ratio, $\nu_\circ$ of the poroelastic matrix using the defined bulk and shear moduli in equations 4.6 and 4.7 respectively.

3. Calculate the Eshelby $\boldsymbol{S}$ tensor using equation 4.32 and equations 4.33 to 4.41.

4. Calculate the prescribed eigenstrain, $\boldsymbol{\epsilon_t}$, and the matrix strain due to the far-field stress, $\boldsymbol{\epsilon_\circ}$, using equation 4.3.

5. Calculate the total eigenstrain, $\boldsymbol{\epsilon_{**}}$ using equation 4.2 and equations 4.4 and 4.5

6. Calculate the Eshelby $\boldsymbol{G(x)}$ tensor using equation 4.9 and equations 4.10 to 4.31.

7. Calculate the external stress field, $\boldsymbol{\sigma(x)}$, using equation 4.8.

4.3.2 Pore-Pressure Diffusion Finite-Difference Model

First, we set a number of parameters for the central scheme finite-difference model, including the number of nodes in the grid, the distance between nodes, the temporal sampling rate, the total time for the model to run and the reservoir permeability, as seen in Table 4.2. These values are fixed for all simulations. We specify a uniform spatial sampling in the x- and y-directions. The grid boundaries are fixed at a constant pore pressure of zero MPa. Then we run the finite-difference code as outlined in equations 4.42 to 4.56 for all time steps. We specify that the fracture must grow in the yz-plane. To simulate fracture growth, at each time step we define all grid nodes in the yz-plane that fall within the radius of the spheroid as a point source injector. The magnitude of the spheroidal radius at each time step is obtained by multiplying the defined velocity of fracture propagation by the total propagation time.

4.3.3 Effective Stress

The effective stress is calculated using the modelled confining stress and pore-pressure diffusion results from the previous subsections. At all grid nodes, confining stress and pore pressure are fed into equation 2.9 to obtain effective stress. The effective-stress coefficient, α, is assumed to be equal to one.

4.4 Results

We outline the general behaviour of pore-pressure diffusion and confining-stress perturbation in the vicinity of a growing vertical hydraulic fracture by displaying and qualitatively discussing the model outputs for a single set of input parameters. Both models are computed with the input parameters contained in Table 4.1 with the pore-pressure diffusion finite-difference model requiring the additional inputs contained in Table 4.2. We allow the models to run for

$20\,hrs$ with the hydraulic fracture growing until it reaches a maximum diameter of $200\,m$ at $t = 9.3\,hrs$, at which point we force the fracture to stop growing. This allows us to observe both the evolving confining-stress and pore-pressure perturbations as the fracture is growing ($t = 0 - 9.3\,hrs$) and the evolving pore-pressure perturbation when the confining-stress field is constant after the fracture has stopped growing ($t = 9.3 - 20\,hrs$). Figures 4.1 to 4.4 display the modelled confining stress results, Figure 4.5 shows pore pressure results and figures 4.6 to 4.9 show effective stress from equation 3.1, assuming an effective-stress coefficient of one. The results in figures 4.1 to 4.9 are displayed as six horizontal cross-sections, panels (A) to (F), through the centre of the vertical hydraulic fracture at time steps of $4\,hrs$ or $240\,min$. Hence, for the first three time steps the fracture is growing and for the last three the fracture is static in size. All colourbars are formatted such that white is the in-situ stress/pressure while reds indicate an increase and blues indicate a decrease. In each cross-section, the hydraulic fracture is indicated by the horizontal black line in the centre of the plot. The x_1-direction is horizontal on the page, the x_2-direction is vertical on the page and the x_3-direction is into/out of the page. Additionally, in each cross-section, there are two points indicated by black dots, the compressive zone point and the tensile zone point, herein respectively referred to as the CZP and TZP. Each point is always located at the same spatial position. The CZP is located $40\,m$ perpendicular to the centre of the hydraulic fracture, and the TZP is located in the plane of the hydraulic fracture and $120\,m$ from the centre of the fracture.

4.4.1 Confining Stress

Figures 4.1 to 4.4 display the modelled confining-stress perturbation respectively for mean stress, stress measured in the x_1-direction (σ_{11}), stress measured in the x_2-direction (σ_{22}) and stress measured in the x_3-direction (σ_{33}). Mean stress is the average of ($\sigma_{11} + \sigma_{22} + \sigma_{33}$). In respect to all measured

Table 4.1: Stress model and pressure model input parameters.

Stress Properties	
Injection Pressure, P_{inject}	$28\,MPa$
Far-field Stress, $(\sigma_h, \sigma_H, \sigma_v)$	$(47, 47, 25)\,MPa$
Matrix Constituent Material Properties	
Bulk Modulus, K_{matrix}	$45.82\,GPa$
Matrix Frame Properties	
Bulk Modulus, K_{dry}	$45.71\,GPa$
Shear Modulus, μ_{dry}	$40.04\,GPa$
Matrix Effective Medium Properties	
Bulk Modulus, $K_\circ$	$45.73\,GPa$
Shear Modulus, $\mu_\circ$	$40.04\,GPa$
Fluid Properties	
Bulk Modulus, K_{fluid}	$2.72\,GPa$
Shear Modulus, μ_{fluid}	$1 \times 10^{-20}\,GPa$
Viscosity, η	$0.00019\,Pa \cdot s$
Fracture Properties	
Width, a_1	$1 \times 10^{-3}\,m$
Propagation Velocity	$0.003\,m/s$
Maximum Diameter, $a_2 = a_3(Max)$	$200\,m$

Table 4.2: Finite-difference model input parameters.

Grid Properties	
Grid Nodes (x-direction)	199
Grid Nodes (y-direction)	100
Initial Injection Point	(x_{100}, y_1)
Sampling Properties	
Temporal Sampling Rate	$0.04\,s$
Spatial Sampling Rate (x- and y-directions)	$2\,m$
Reservoir Properties	
Permeability	$0.1\,mD$

stresses, the perturbation pattern is proportional to the fracture radius. Also, the stress always decreases at the TZP and increases at the CZP. If we examine the perturbations of the four stress measurements in more detail, we note several important differences between the evolving stress patterns.

Figure 4.1 shows mean stress in the region perpendicular to the fracture face increases moderately near the fracture and gradually decreases as distance from the fracture increases. Mean stress decreases significantly in the region directly adjacent to the fracture tips with the magnitude of decrease becoming less pronounced with increasing distance from the fracture. The stress gradient moving away from the fracture, in the plane of the fracture, is steeper than the gradient moving perpendicular to the fracture face. This results from localized, large-magnitude, tensile stress concentrations at the fracture tips. Finally, the region experiencing a stress increase is significantly larger than the region experiencing a stress decrease.

Figure 4.2 shows confining stress in the x_1-direction, σ_{11}, exhibits roughly the same pattern as seen for mean confining stress with stress in the region perpendicular to the fracture face increasing significantly near the fracture and gradually decreasing as distance from the fracture increases. Observing the region perpendicular to the centre of the fracture face, there is a significant increase in confining stress in the x_1-direction up to a distance approximately equal to the fracture radius. Stress in the x_1-direction decreases significantly in a dual-lobed the region directly adjacent to the fracture tips with the lobes extending approximately 45° relative to the plane of the fracture. Similar to the pattern for mean stress, the magnitude of stress decrease becomes less pronounced with increasing distance from the fracture. However, the overall region experiencing a stress decrease in the x_1-direction is noticeably larger than seen for mean stress. Also similar to mean stress, the stress gradient moving away from the fracture, in the plane of the fracture, is steeper than the gradient moving perpendicular to the fracture face. This results from localized, large-

magnitude, tensile stress concentrations at the fracture tips. Finally, the region experiencing a stress increase is significantly larger than the region experiencing a stress decrease.

Figure 4.3 shows confining stress in the x_2-direction, σ_{22}, has a more complex pattern than seen for the x_1-direction, σ_{11}. Observing the region perpendicular to the centre of the fracture face, there is a moderate increase in stress near the fracture that gradually decreases to zero stress change as distance from the fracture approaches a distance approximately equal to the fracture radius. If we move farther from the fracture face, near the centre of the fracture, there is a lobe of low-magnitude stress decrease. Similar to mean stress, stress in the x_2-direction decreases significantly in the region directly adjacent to the fracture tips with the magnitude of decrease becoming less pronounced with increasing distance from the fracture. Between these two tensile regions are four regions of low-magnitude stress increase which have local maximum values located perpendicular to the outer parts of the fracture face. These stress increases dominate the shear stress zones seen in Figure 2.9. Hence, moving clockwise around the fracture, at a distance greater than the fracture radius, there are alternating regions of stress increase and stress decrease.

Figure 4.4 shows confining stress in the x_3-direction, σ_{33}, has the simplest stress pattern. Observing the region perpendicular to the fracture face, there is a moderate increase in stress near the fracture that gradually decreases to zero stress-change as distance from the fracture approaches a distance approximately equal to the fracture radius. If we move farther from the fracture, there is a lobe of low-magnitude stress decrease.

4.4.2 Pore Pressure

Figure 4.5 shows the pore-pressure perturbations are simpler than any of the previously mentioned elastic stress perturbation patterns. It is important to note, the pore pressure colourbar has double the range of the confining-stress

colourbars. There is a large pressure increase in the region directly adjacent to the fracture and the pressure decreases relatively quickly moving in any direction away from the fracture. The perturbation pattern is proportional to the time from initiation, as opposed to the proportionality to fracture radius seen for confining stress.

4.4.3 Effective Stress

Figures 4.6 to 4.9 show the combined effects of confining stress and pore pressure respectively as mean effective stress, effective stress measured in the x_1-direction (σ'_{11}), effective stress measured in the x_2-direction (σ'_{22}) and effective stress measured in the x_3-direction (σ'_{33}). Mean effective stress is the average of $(\sigma'_{11} + \sigma'_{22} + \sigma'_{33})$. Recall, an increase in pore pressure results in a decrease in effective stress. Based on our previous observations of a pore-pressure increase that is larger than the confining-stress increase near the fracture, we expect the region near the fracture to experience a decrease in effective stress which we see in all four effective stresses. For all cases, this region of effective-stress decrease grows in size for the entire time the model is run. In contrast, regions further away from the fracture tend to have pore-pressure and confining-stress perturbations of similar magnitude which results in the variable effective-stress patterns discussed below.

Figure 4.6 shows mean effective-stress decreases in the region close to the fracture. This region of effective-stress decrease is characterized by significant decrease in a small zone near the fracture tips and moderate decrease perpendicular to the fracture face. The magnitude of decrease diminishes with distance from the fracture. In the distal region perpendicular to the fracture faces, there is a moderately sized zone of low-magnitude effective-stress increase. As the fracture is growing ($t = 0 - 480\,min$) the largest effective-stress increase occurs perpendicular to the centre of the fracture face at a distance approximately equal to the fracture radius. When the fracture stops growing ($t \geq 720\,min$)

the two points of maximum effective-stress decrease in magnitude and migrate further away from the fracture faces.

As seen in Figure 4.7, effective stress in the x_1-direction, σ'_{11}, exhibits a similar pattern to mean effective stress but with larger magnitude effective-stress increases in the distal zones perpendicular to the fracture faces. In this case, the region experiencing effective-stress increase is approximately the same size as the region experiencing effective-stress decrease.

Figure 4.8 shows the effective-stress perturbation pattern in the x_2-direction, σ'_{22}, is similar to that seen for confining stress in the same direction with one important difference. The fracture-proximal region perpendicular the fracture faces experiences an effective-stress decrease, as opposed to the confining-stress increase seen in Figure 4.3.

Figure 4.9 shows effective stress in the x_3-direction, σ'_{33}, has a simple pattern with a moderate effective-stress decrease occurring adjacent to the fracture. The magnitude of this effective-stress decrease gradually decreases with increasing distance from the fracture. The effective-stress gradient is steepest moving away from the fracture tips in the plane of the fracture.

Finally, Table 4.3 qualitatively summarizes the confining-stress, pore-pressure and effective-stress perturbations observed at the TZP and CZP for all time steps. Positive symbols denote an increase and negative symbols denote a decrease in the measured value. Relatively small perturbations are denoted by a single symbol, relatively moderate perturbations are denoted by two symbols and relatively large perturbations are denoted by three symbols. For example, "$+++$" is a relatively large increase and "$-$" is a relatively small decrease. A very small perturbation is denoted by "≈ 0", meaning approximately no change.

Table 4.3: Summary of confining-stress, pore-pressure and effective-stress perturbations observed at the TZP and CZP.

		Time (min)					
Point	**Measurement**	**0**	**240**	**480**	**720**	**960**	**1200**
TZP	Confining Stress (x_1-dir.)	≈ 0	≈ 0	$-$	$--$	$--$	$--$
	Confining Stress (x_2-dir.)	≈ 0	$-$	$--$	$--$	$--$	$--$
	Confining Stress (x_3-dir.)	≈ 0	≈ 0	≈ 0	≈ 0	≈ 0	≈ 0
	Pore Pressue	≈ 0	≈ 0	≈ 0	≈ 0	$+++$	$+++$
	Effective Stress (x_1-dir.)	≈ 0	≈ 0	$-$	$--$	$--$	$--$
	Effective Stress (x_2-dir.)	≈ 0	≈ 0	$-$	$--$	$--$	$--$
	Effective Stress (x_3-dir.)	≈ 0	≈ 0	≈ 0	$-$	$-$	$--$
CZP	Confining Stress (x_1-dir.)	≈ 0	$++$	$+++$	$+++$	$+++$	$+++$
	Confining Stress (x_2-dir.)	≈ 0	$-$	$+$	$+$	$+$	$+$
	Confining Stress (x_3-dir.)	≈ 0	$-$	$+$	$+$	$+$	$+$
	Pore Pressue	≈ 0	$+$	$++$	$++$	$+++$	$+++$
	Effective Stress (x_1-dir.)	≈ 0	$+$	$+$	≈ 0	$-$	$-$
	Effective Stress (x_2-dir.)	≈ 0	≈ 0	$-$	$-$	$--$	$--$
	Effective Stress (x_3-dir.)	≈ 0	≈ 0	$-$	$-$	$--$	$--$

4.5 Discussion

It is academically interesting to discuss the fine variations seen in our models of pore-pressure diffusion, confining-stress change and effective-stress change. However, in the context of modelling seismic velocities in the vicinity of a hydraulic fracture, we are primarily interested in low-frequency effective-stress change patterns. The reason for this is threefold. First, in Chapter 3 we demonstrated that seismic velocities respond to effective stress: the combined effects of pore pressure and confining stress. Second, typical observable seismic wavelengths are on the order of tens to hundreds of meters, so high-frequency variations in effective stress will tend to be undetectable or averaged out by seismic signals. Third, in order for changes in seismic velocity to be detectable, the propagation path of two observed seismic waves must travel through a significant distance of rock exhibiting a perturbed velocity. For example, consider a case in which the initial seismic P-wave velocity of a reservoir is $4000\,m/s$ and the distance from source to receiver is $500\,m$ resulting in a travel-time of

$0.125\,s$. An effective-stress change then causes the seismic velocity in part of the reservoir to decrease by 5% or $200\,m/s$. If the path of seismic propagation travels through $200\,m$ of reduced velocity reservoir, the travel-time will increase by $0.003\,s$ which may be possible to detect. However, if the path of seismic propagation travels through only $100\,m$ of reduced velocity reservoir, the travel-time will increase by only $0.001\,s$ which is likely below detectability.

We now describe the low-frequency patterns of effective-stress perturbation in the vicinity of a growing vertical hydraulic fracture with a fracture normal in the x_1-direction, as seen in panels (A)-(C) of figures 4.6 to 4.9. Figure 4.10 shows four low-frequency zones of effective stress around a growing hydraulic fracture: the proximal zone, the compressive zone, the shear zone and the tensile zone. The proximal zone is defined as the region immediately adjacent to the fracture in which the mean effective-stress decreases significantly. In general, the effective stresses measured in all three principle directions decrease to some degree in the proximal zone. These decreases in effective stress are due to an increase in pore pressure greater than the increase in confining stress that has occurred in any given direction. It is important to note, the region experiencing pore-pressure increase extends beyond the proximal zone. However, beyond the proximal zone the magnitude of pore-pressure perturbation is smaller than or equal to the corresponding magnitude of confining-stress change. The compressive zone extends beyond the proximal zone in the region perpendicular to the fracture faces. The compressive zone is characterized by a small increase in mean effective stress, a moderate increase in effective stress in the x_1-direction and a very small decrease in effective stress in the x_2- and x_3-directions. It is interesting to note that the increase in mean effective stress is entirely due to effective-stress increase in the x_1-direction. As noted in Chapter 2, this uniaxial stress will tend to preferentially align crack sets in the reservoir which will lead to anisotropic velocities. The tensile zone extends beyond the proximal zone in the region sub-parallel to the fracture

plane and is characterized by no change in effective stress in the x_3-direction and a moderate to small decrease in mean effective stress and effective stress in the x_1- and x_2-directions. Finally, the shear zone exists beyond the proximal zone in the regions between the compressive and shear zones. The shear zone exhibits roughly no change in mean effective stress and effective stress in the x_3-direction, a small decrease in effective stress in the x_1-direction and a small increase in effective stress in the x_2-direction.

Now consider the case in panels (D)-(F) of figures 4.6 to 4.9, where the pressurized vertical hydraulic fracture is static in size. In each successive time step the size of the proximal zone increases but the magnitudes of effective-stress decrease do not significantly change. In contrast, the sizes of the compressive, shear and tensile zones decrease with each successive time step. Additionally, with increasing time, the magnitudes of effective-stress perturbation are increased in the tensile zone and decreased in the compressive and shear zones.

Although not shown here, it is worth commenting on the effect of variation in the confining-stress and pore-pressure model input parameters. If input parameter variation is realistic for a hydraulic fracture in a low-porosity reservoir, the majority of the input parameters do not have a significant effect on the overall pattern or magnitude of effective-stress change. As such, we will only discuss those parameters that do have a significant effect, including the hydraulic fracturing injection pressure, fluid viscosity, matrix permeability and fracture propagation velocity. A change in injection pressure tends to cause a proportional change in the magnitude of the effective-stress perturbations, whereas the general patterns of effective-stress change tend to remain more-or-less unchanged. Additionally, the relative size of the proximal zone versus the compressive zone will change slightly, but not in a significant way. An increase in fluid viscosity or a decrease in matrix permeability tends to decrease the extent of pore-pressure diffusion while having no effect on confining-stress change. This causes a steeper gradient of the magnitude of pore-pressure increase, and

this tends to reduce the distance the proximal zone extends away from the fracture. Finally, an increase in fracture propagation velocity means that for a given fracture size, the extent of pore-pressure diffusion will be smaller. This also reduces the distance the proximal zone extends away from the fracture.

4.6 Conclusions

Using Eshelby's solution for modelling confining stress and Shapiro's method for modelling pore-pressure diffusion in the vicinity of a hydraulic fracture in a low-porosity, isotropic, homogeneous medium, we find the resulting low-frequency effective-stress perturbation field can be categorized into four zones of influence: the proximal zone, compressive zone, shear zone and tensile zone. The proximal zone is located immediately adjacent to the fracture walls and tips. The proximal zone experiences the largest pore-pressure increase that results in a significant decrease in effective stress. It is important to note that the proximal zone is not defined by the extent of pore-pressure increase. Instead, the proximal zone is defined by a decrease in effective stress resulting from an increase in pore pressure greater than the increase in confining stress occurring in any of the three principle directions. While the fracture is growing the proximal zone tends to be confined to a relatively small region immediate adjacent to the fracture. After the fracture stops growing and elevated pore pressure continues to diffuse, the proximal zone expands away from the fracture with each time step. The compressive zone is relatively large and is found perpendicular to the fracture faces extending from the outer edge of the proximal zone. The compressive zone experiences an approximately uniaxial effective-stress increase in the direction perpendicular to the fracture faces. The tensile zone is the smallest zone and extends beyond the proximal zone in the region sub-parallel to the fracture plane. The tensile zone experiences moderate-magnitude to zero effective-stress decrease. The shear zone experiences low-magnitude or zero

effective-stress change and extends beyond the proximal zone in the regions between the compressive and tensile zones. We find fluid viscosity, reservoir permeability and fracture propagation velocity are important parameters controlling the relative sizes of the zones. Injection pressure can have a relatively small effect on the relative zone sizes but is an important parameter controlling the overall magnitude of effective-stress changes.

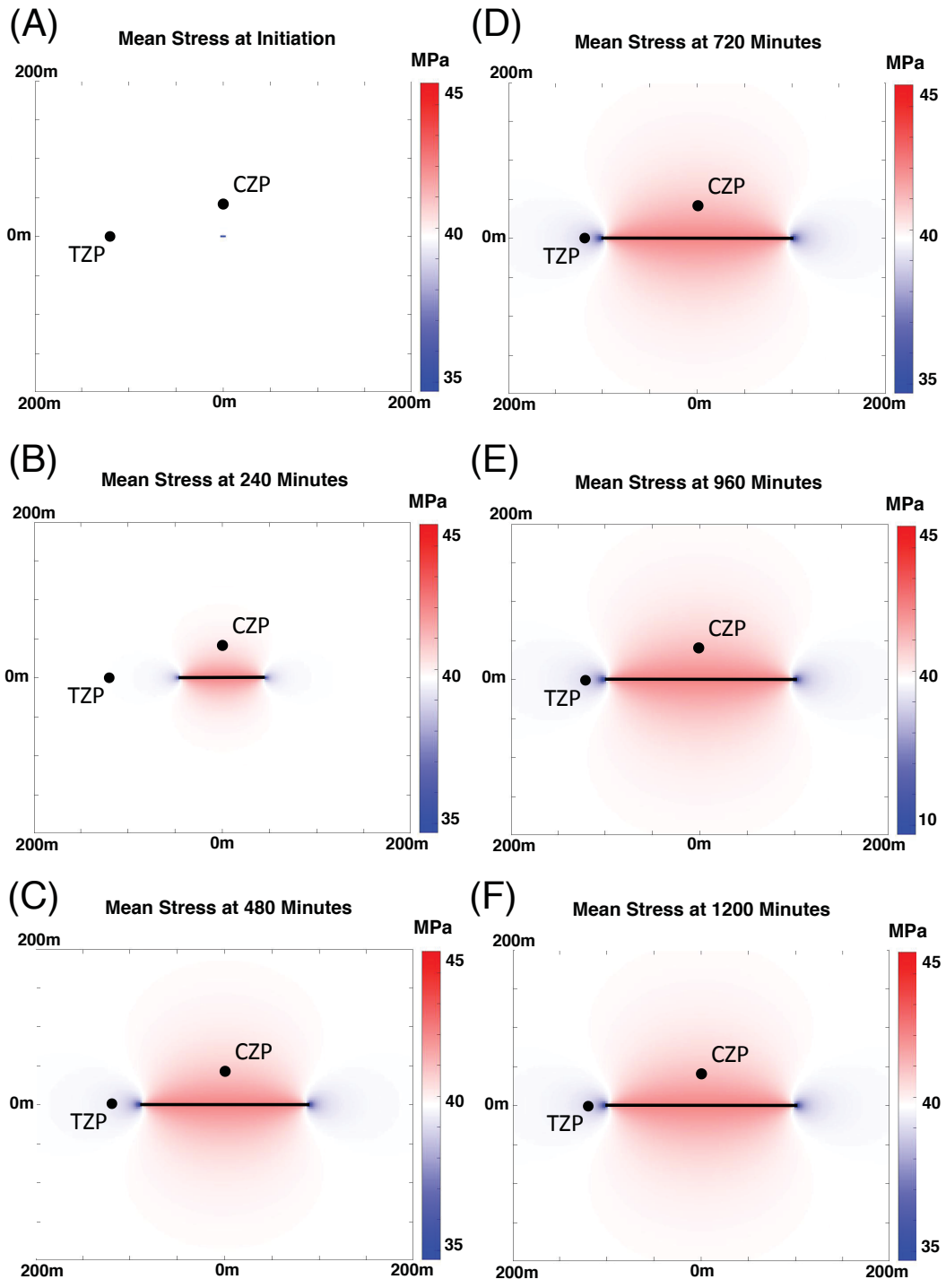

Figure 4.1: A series of horizontal cross-sections illustrating the evolution of mean confining stress in the vicinity of a spheroidal vertical hydraulic fracture at 240 minute time steps. The black line in the centre of each plot represents the fracture. The vertical axis corresponds to the x_1-direction, the horizontal axis corresponds to the x_2-direction and the x_3-direction is perpendicular to the page. As seen in Figures 4.2 to 4.4, stress perturbations in the x_1-direction dominate the mean stress perturbations.

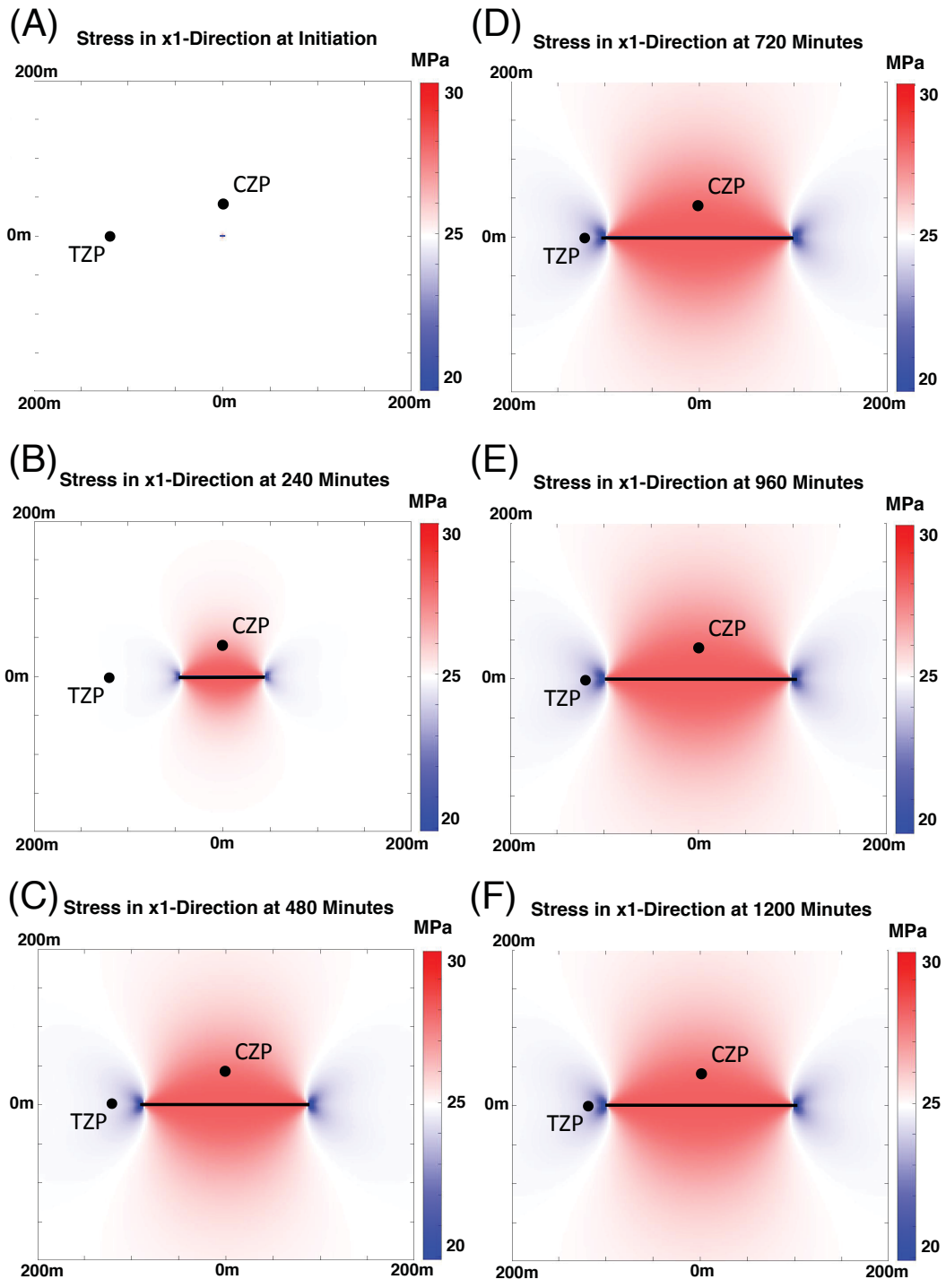

Figure 4.2: A series of horizontal cross-sections illustrating the evolution of confining stress in the x_1-direction in the vicinity of a spheroidal vertical hydraulic fracture at 240 minute time steps. The black line in the centre of each plot represents the fracture. The vertical axis corresponds to the x_1-direction, the horizontal axis corresponds to the x_2-direction and the x_3-direction is perpendicular to the page.

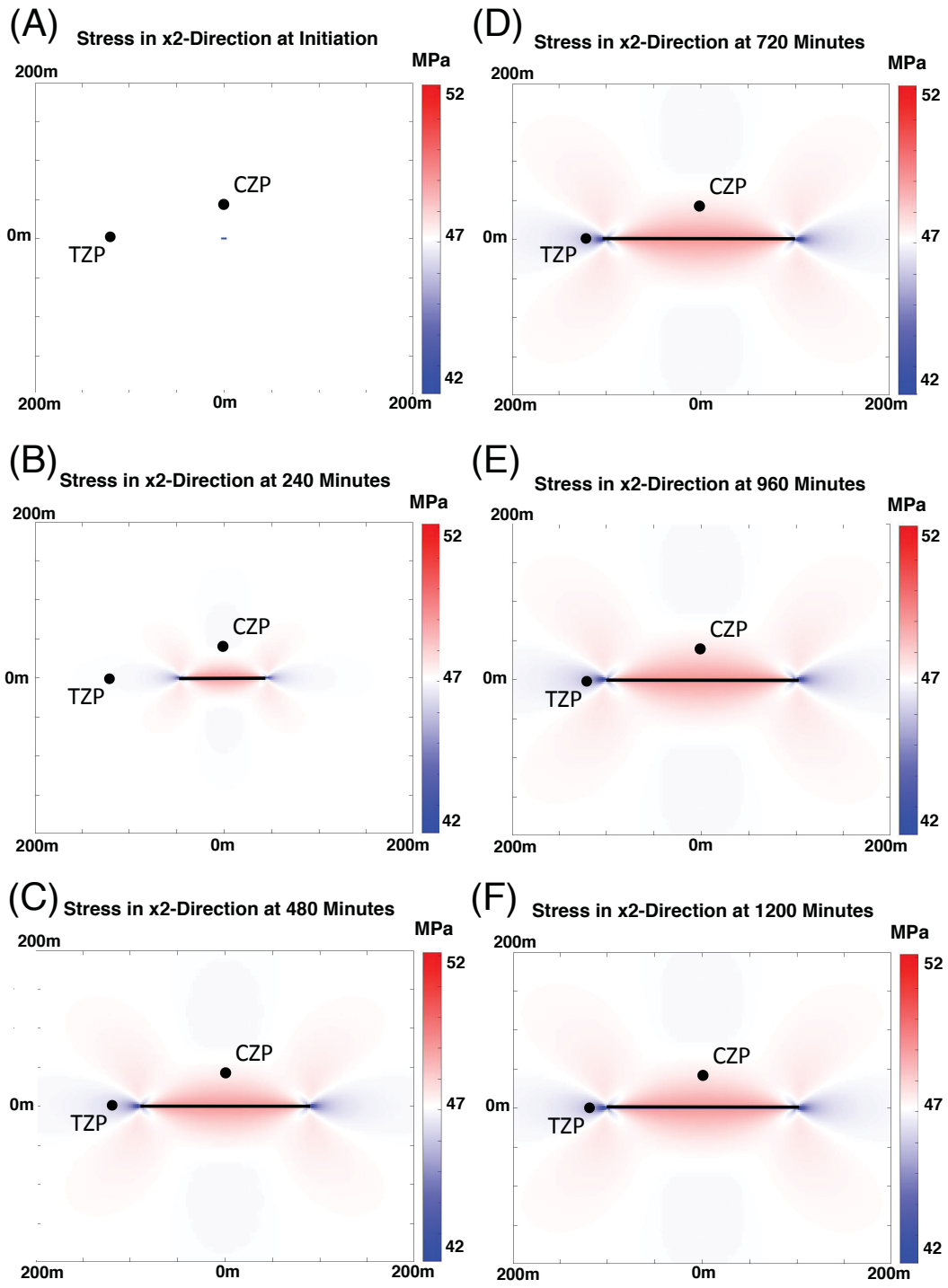

Figure 4.3: A series of horizontal cross-sections illustrating the evolution of confining stress in the x_2-direction in the vicinity of a spheroidal vertical hydraulic fracture at 240 minute time steps. The black line in the centre of each plot represents the fracture. The vertical axis corresponds to the x_1-direction, the horizontal axis corresponds to the x_2-direction and the x_3-direction is perpendicular to the page.

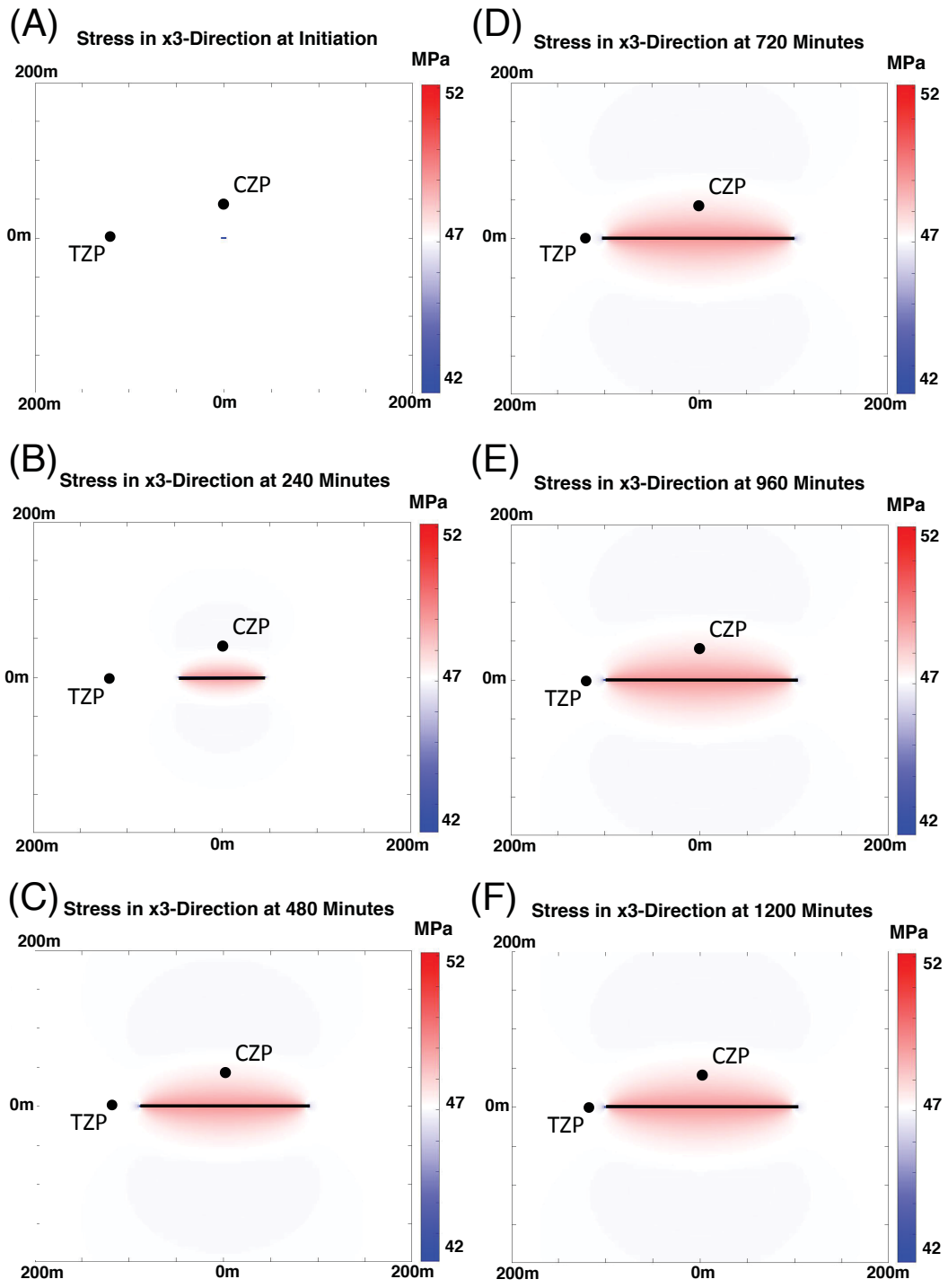

Figure 4.4: A series of horizontal cross-sections illustrating the evolution of confining stress in the x_3-direction in the vicinity of a spheroidal vertical hydraulic fracture at 240 minute time steps. The black line in the centre of each plot represents the fracture. The vertical axis corresponds to the x_1-direction, the horizontal axis corresponds to the x_2-direction and the x_3-direction is perpendicular to the page.

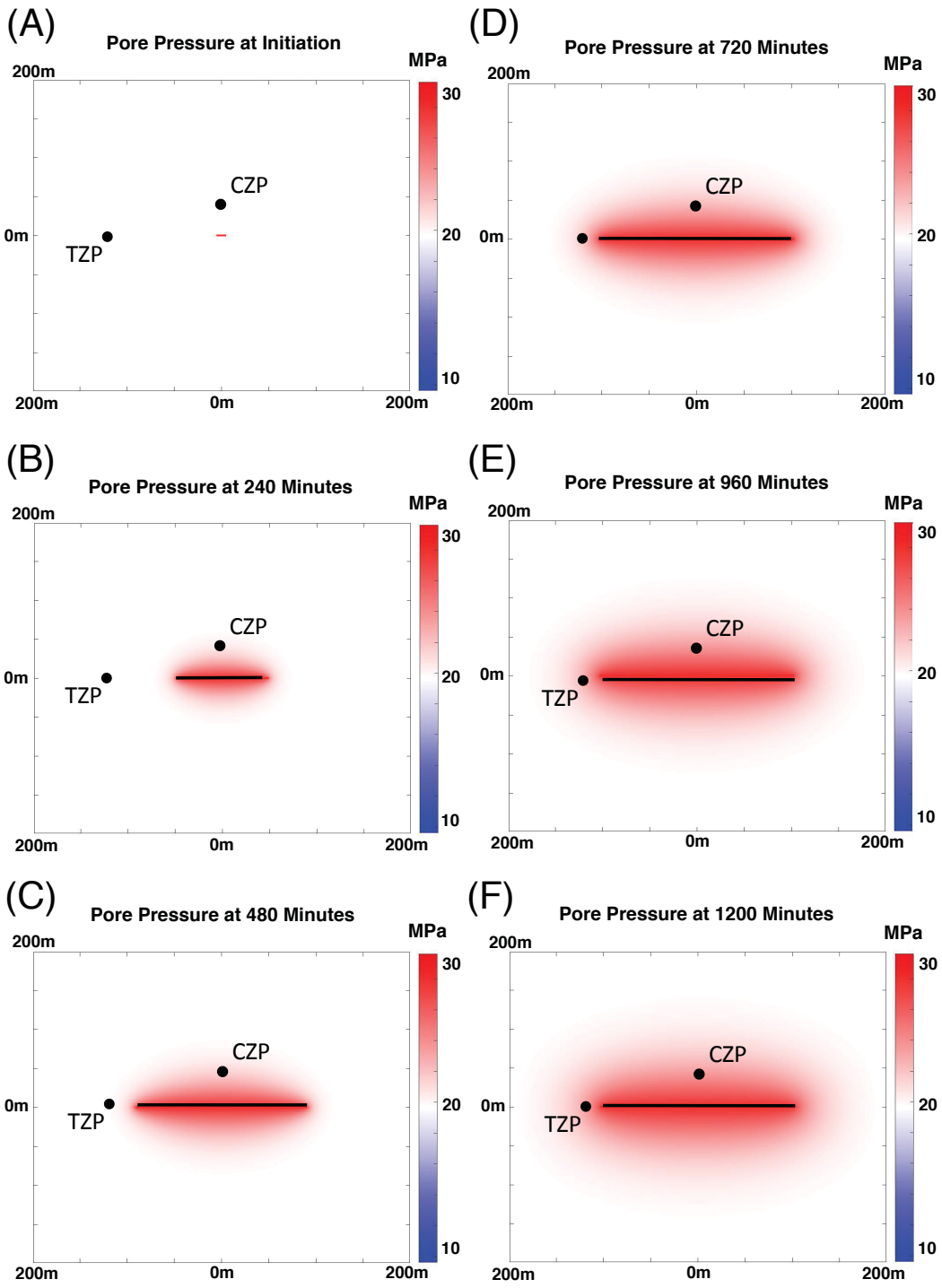

Figure 4.5: A series of horizontal cross-sections illustrating the evolution of pore-pressure diffusion in the vicinity of a spheroidal vertical hydraulic fracture at 240 minute time steps. The black line in the centre of each plot represents the fracture. The vertical axis corresponds to the x_1-direction, the horizontal axis corresponds to the x_2-direction and the x_3-direction is perpendicular to the page.

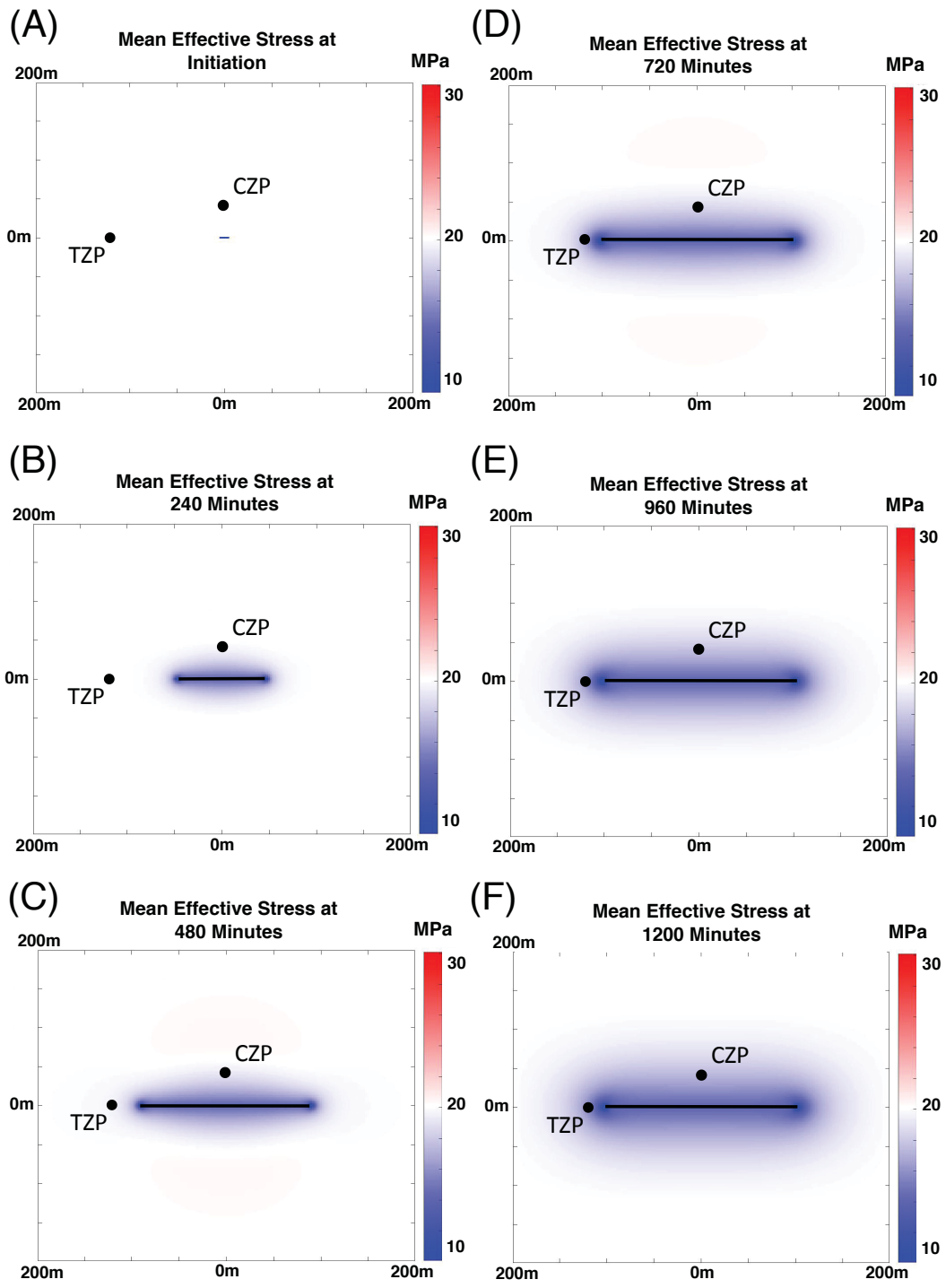

Figure 4.6: A series of horizontal cross-sections illustrating the evolution of mean effective stress in the vicinity of a spheroidal vertical hydraulic fracture at 240 minute time steps. The black line in the centre of each plot represents the fracture. The vertical axis corresponds to the x_1-direction, the horizontal axis corresponds to the x_2-direction and the x_3-direction is perpendicular to the page.

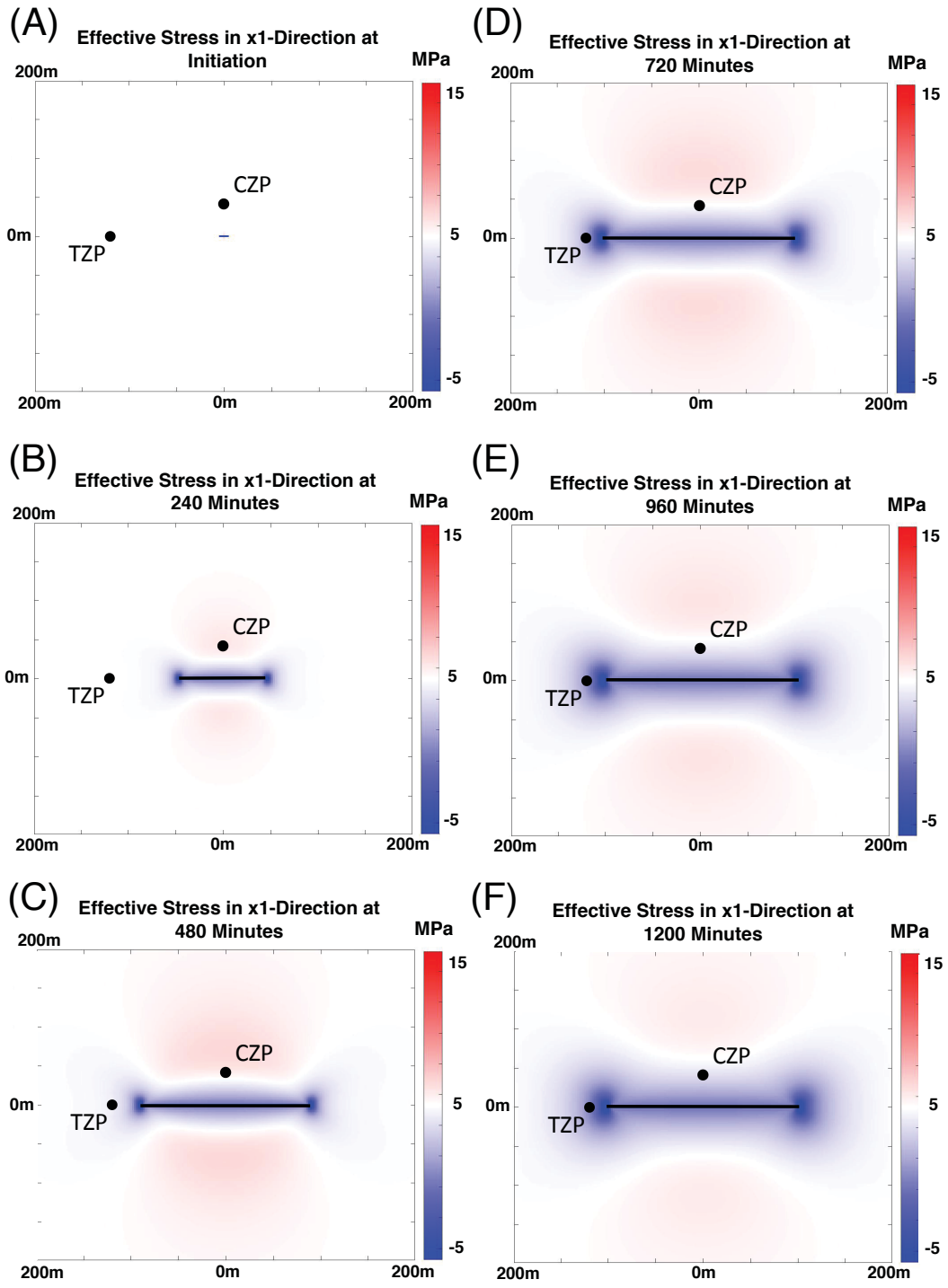

Figure 4.7: A series of horizontal cross-sections illustrating the evolution of effective stress in the x_1-direction in the vicinity of a spheroidal vertical hydraulic fracture at 240 minute time steps. The black line in the centre of each plot represents the fracture. The vertical axis corresponds to the x_1-direction, the horizontal axis corresponds to the x_2-direction and the x_3-direction is perpendicular to the page.

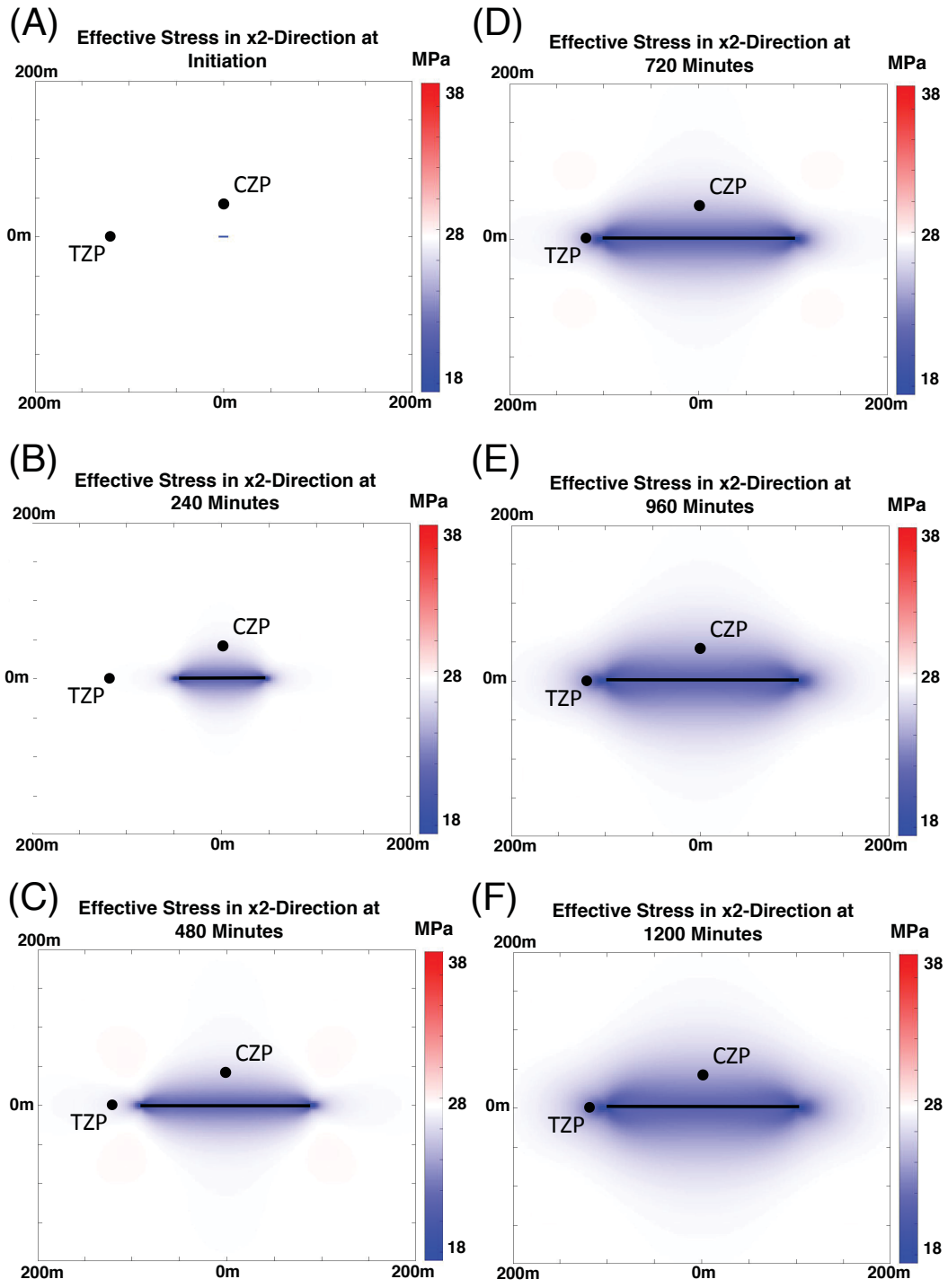

Figure 4.8: A series of horizontal cross-sections illustrating the evolution of effective stress in the x_2-direction in the vicinity of a spheroidal vertical hydraulic fracture at 240 minute time steps. The black line in the centre of each plot represents the fracture. The vertical axis corresponds to the x_1-direction, the horizontal axis corresponds to the x_2-direction and the x_3-direction is perpendicular to the page.

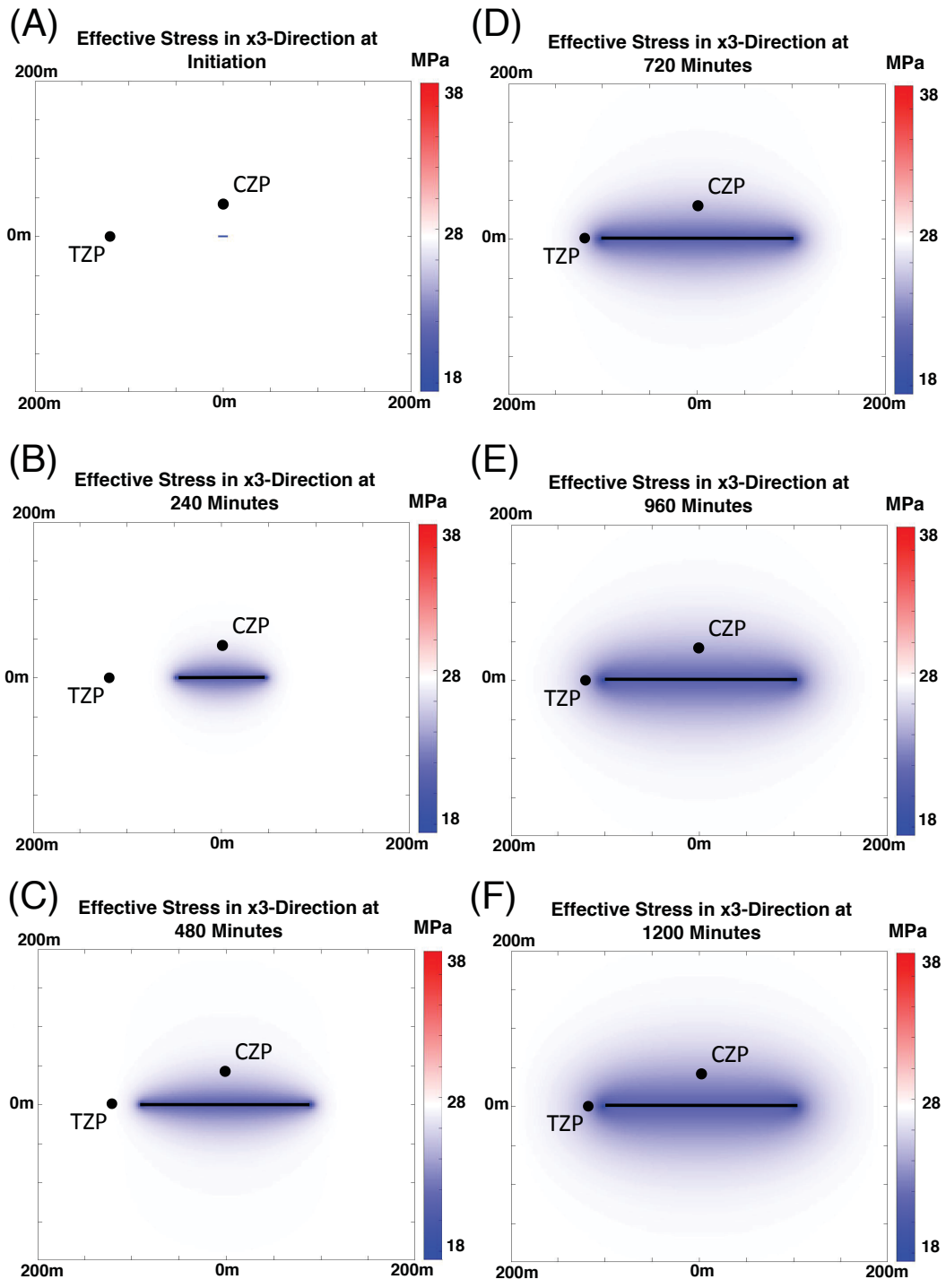

Figure 4.9: A series of horizontal cross-sections illustrating the evolution of effective stress in the x_3-direction in the vicinity of a spheroidal vertical hydraulic fracture at 240 minute time steps. The black line in the centre of each plot represents the fracture. The vertical axis corresponds to the x_1-direction, the horizontal axis corresponds to the x_2-direction and the x_3-direction is perpendicular to the page.

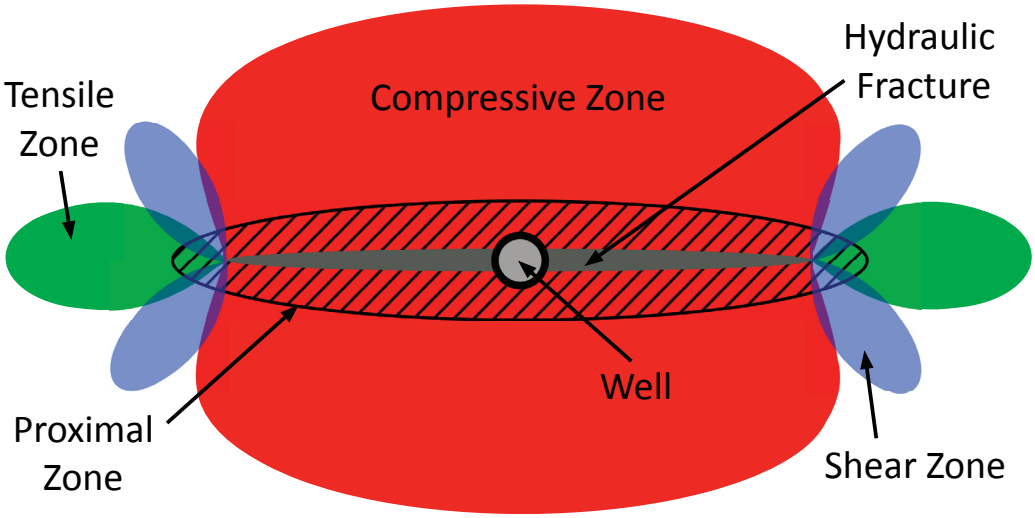

Figure 4.10: A horizontal cross-section through a growing vertical hydraulic fracture extending from a vertical well illustrating the relative size of the four low-frequency zones of effective-stress perturbation in the surrounding region, modified from Cipolla et al. (2011). The area with black diagonal lines indicates the proximal zone, the solid red area indicates the compressive zone, the solid blue area indicates the shear zone and the solid green area indicates the tensile zone.

Chapter 5

Uniaxial Stress: Anisotropic Velocity Sensitivity

5.1 Introduction

The material presented in this chapter is based on work that was presented orally at the 2017 Society of Exploration Geophysicists Annual International Meeting in Houston, Texas (Brisco and Van der Baan, 2017). We consider the case where a hydraulic fracture treatment is performed in an isotropic rock matrix with a pervasive and initially isotropic distribution of microcracks. As seen in Figure 4.10, the opened fracture creates a large region extending perpendicular to the fracture face that experiences a confining-stress increase and relatively small regions near the fracture tips that experience an increase in shear stress and tensile stress. As discussed in Chapter 4, the region of increased confining stress is characterized by a stress increase that is significantly larger in the direction normal to the fracture face than directions parallel to the fracture face. This stress perturbation can be approximated as a uniaxial compressive stress acting perpendicular to the fracture face. Uniaxial compression will tend to close those microcracks with face-normals that are parallel or nearly parallel to the direction of compression, see Figure 2.6. In contrast, those microcracks

with face-normals perpendicular or nearly perpendicular to the direction of compression will tend to remain open. This results in the development of an anisotropic microcrack distribution, and consequently an elastically anisotropic matrix (Nur, 1971). Several methods have been developed to model the effects of stress perturbations on the elastic properties of an effective medium. Sayers and Kachanov (1995) and Schoenberg and Sayers (1995) describe the fourth order compliance tensor of a fractured medium as the sum of the compliance tensor of the uncracked medium and an additional compliance tensor representing the contribution of aligned cracks or fracture system. Alternatively, stress induced anisotropy can be modelled with the theory of nonlinear elasticity, as developed by Prioul et al. (2004) and discussed by Fuck et al. (2009), where the second-order elasticity tensor of a stressed medium is described as a function of the second-order elasticity tensor of the unstressed medium, the strain tensor and the third-order elasticity tensor. Finally, Zatsepin and Crampin (1997) and Crampin and Zatsepin (1997) develop the anisotropic poroelasticity (APE) model to describe the elastic anisotropy behaviour of a pervasively microcracked medium as the sum of the variations in the elastic moduli due to changes in microcrack orientations due to the preferential opening and closing of microcracks and the variations in the elastic moduli due to changes in the geometry of individual microcracks. In this chapter, we conduct a sensitivity analysis for anisotropic changes in P-wave and S-wave velocities in response to variations in uniaxial confining stress using the APE model.

5.2 Theory

5.2.1 APE Model

The APE model assumes that all rock contains an isotropic distribution of uniform fluid-isolated microcracks, herein referred to simply as cracks (Zatsepin and Crampin, 1997; Crampin and Zatsepin, 1997). Fluids can flow from one

crack into some of the closest neighbouring cracks almost immediately in response to changes in the stress field. However, the permeability of the crack network is very low and no macroscopic fluid flow is possible. We describe a crack as an ellipsoidal body with semi-axes ($a_1 \geq a_2 \geq a_3$). A penny-shaped crack is the special case of an ellipsoidal body where ($a_1 \ll a_2 = a_3$) and the aspect ratio is given by ($\frac{a_1}{a_2} \ll 1$).The effective elasticity coefficients, $\boldsymbol{C^E}$, of a stressed rock matrix containing a particular crack distribution can be expressed as

$$\begin{aligned} \boldsymbol{C^E} = \boldsymbol{C^M} &+ \epsilon \iint_{\gamma \geq 0} \boldsymbol{R}(\Omega) \boldsymbol{C^D} \, d\Omega \\ &+ \epsilon \iint_{\gamma \geq 0} \boldsymbol{R}(\Omega) \boldsymbol{C^G} \, d\Omega \,, \end{aligned} \tag{5.1}$$

where $\boldsymbol{C^D}$ and $\boldsymbol{C^G}$ are fourth order tensors representing the perturbations to the elasticity coefficients due respectively to a distribution of cracks of a single orientation and the geometry of these cracks, $\boldsymbol{C^M}$ is a fourth order tensor containing the elasticity coefficients of the solid matrix, $\boldsymbol{R}(\Omega)$ is the fourth order rotation tensor, Ω is an orientation in spherical coordinates (ψ, θ)=$(inclination, azimuth)$ and $d\Omega$=$(4\pi)^{-1} \sin\psi \, d\psi \, d\theta$ is a normalized differential element of solid angle. Normalized crack density, ϵ, is a nondimensional parameter given by

$$\epsilon = \frac{N_{cr}}{V} a_2^3 \,, \tag{5.2}$$

where N_{cr} is the number of cracks in volume V with a radius of a_2. The limits of integration in equation 5.1 are defined by γ, a term describing crack geometry where $\gamma > 0$ for open cracks. Crack geometry is a function of stress acting normal to the crack face, σ_n, pore-fluid pressure within the crack, p_f, and the critical closing stress of the crack, σ_c, as follows:

$$\gamma = 1 - \frac{(\sigma_n - p_f)}{\sigma_c}. \tag{5.3}$$

The term in the numerator of equation 5.3 represents the effective pressure acting normal to the crack face. By convention we assign compressive stress and pore pressure as positive. For penny-shaped cracks, the critical closing stress can be expressed as

$$\sigma_c = \frac{1}{c_{cr}} = (\frac{\pi}{2})\frac{g_\circ \mu}{(1-\nu)}\,, \tag{5.4}$$

where c_{cr} is crack compressibility, $g_\circ$ is the initial aspect ratio, μ is the rock matrix shear modulus and ν is the rock matrix Poisson's ratio. The pore-fluid pressure in equation 5.3 is a function of crack face normal stress, σ_n, critical closing stress, σ_c, and fluid compressibility, c_f, and can be expressed as

$$p_f = \frac{\sigma_n}{1+r}\,, \tag{5.5}$$

where r is the normalized pore-fluid compressibility given by

$$r = \sigma_c c_f = \frac{c_f}{c_{cr}}\,. \tag{5.6}$$

For the case of penny-shaped cracks, γ approximately represents the normalized crack aspect ratio,

$$\gamma = \frac{g}{g_\circ}\,, \tag{5.7}$$

where g is the aspect ratio after the confining-stress perturbation is applied. By examining equations 5.3 and 5.7 we see that crack aspect ratio does not change when $\sigma_c \gg |\sigma_n - p_f|$ and cracks will close when $\sigma_c \leq (\sigma_n - p_f)$. For penny-shaped cracks, the normalized pore-fluid compressibility in equation 5.6 can be expressed as

$$r = (\frac{1}{2})\frac{\pi\mu c_f g_\circ}{(1-\nu)}\,. \tag{5.8}$$

The terms in equation 5.1 representing perturbation due to crack distribution, $\boldsymbol{C^D}$, and crack geometry, $\boldsymbol{C^G}$, can respectively be expressed as

$$C^D_{ijkl} = \mu\Lambda_{ijkl} \tag{5.9}$$

and

$$C^G_{ijkl} = \mu\Lambda_{ijkl}\left[\frac{\gamma r}{(1+\gamma r)}\right], \tag{5.10}$$

where Λ_{ijkl} is a dimensionless combination of Lamé parameters obtained from an appropriate crack model (see section 5.2.2). The fraction in square brackets in equation 5.10 acts as a scaling term and can have values between zero and one. This scaling term will decrease the influence of cracks that have squeezed partially shut (i.e. $0 < \gamma < 1$) and will increase the influence of cracks that have been forced open such that the aspect ratio is larger than the initial aspect ratio (i.e. $\gamma > 1$). Also, by examining equations 5.6 and 5.10 we can see that the perturbation due to pore geometry will be small if fluid compressibility, c_f, is much less than crack compressibility, c_{cr}.

The APE model can account for more than one isotropic distribution of cracks with different initial aspect ratios, as would be expected in the real world. To do this, simply include addition sets of $\boldsymbol{C^D}$ and $\boldsymbol{C^G}$ representing the crack distributions of each individual aspect ratio present. However, the selection of a single aspect ratio representing the average of all aspect ratios present should give a reasonable first order approximation of the overall response to variable confining stress.

Consider an isotropic rock matrix containing an initially isotropic distribution of uniform, low aspect ratio, spheroidal, fluid-isolated cracks that is subjected to a compressive uniaxial stress in the vertical (x_3) direction. In this

case, the APE model has a relatively simple expression in terms of dimensionless excess pore-fluid pressure, p, and dimensionless differential stress, s_{ij} as follows:

$$p = \frac{(p_f - p_{fo})}{\sigma_c} \tag{5.11}$$

and

$$s_{ij} = \frac{(\sigma_{ij} - \sigma_\circ \, \delta_{ij})}{\sigma_c} \,, \tag{5.12}$$

where δ_{ij} is the Kroenecker delta, p_f is the excess pore-fluid pressure induced by the applied stress, σ_{ij}. The initial pore-fluid pressure, p_{fo}, of an isotropic crack distribution is in equilibrium with the initial lithostatic stress, $\sigma_\circ$, such that

$$p_{fo} = \sigma_\circ \,. \tag{5.13}$$

At depth in the Earth, this would imply highly over-pressured cracks because generally pore pressure is determined by a surface connected water column and vertical stress determined by the rock overburden. Water is commonly half the density of rock. Hence, pore pressure should be less than vertical stress, $p_{fo} < \sigma_\circ$.

The boundary between open and closed cracks is independent of azimuth, θ, and is defined by the function $\psi_\circ$ where $\psi_\circ$ is the angle measured from the x_3 axis at which cracks begin to close. That is, all cracks with normals oriented at $\psi \leq \psi_\circ$ are closed by the applied differential stress, s_{ij}, and all cracks with normals oriented at $\psi > \psi_\circ$ remain open. We define the vertical differential stress, s_v, from equation 5.12 as $s_v = s_{33} - s_{11}$ and for the case of uniaxial vertical stress, ($s_{33} > s_{11} = s_{22} = 0$), we get $s_v = s_{33}$. When $s_v \leq \frac{3}{2}$ all cracks remain open giving

$$\psi_\circ = 0\,, \tag{5.14}$$

and the excess pore-fluid pressure is given by

$$p = \frac{s_v}{3}. \tag{5.15}$$

When all cracks are open the crack density remains constant and can be expressed as

$$\epsilon = \epsilon_\circ\,, \tag{5.16}$$

where ϵ is the current crack density and $\epsilon_\circ$ is the initial crack density. When $s_v > \frac{3}{2}$, some cracks are closed,

$$\cos\psi_\circ = (\frac{2}{3}s_v)^{-\frac{1}{3}}\,, \tag{5.17}$$

and the excess pore-fluid pressure is given by

$$p = s_v\cos^2\psi_\circ - 1\,. \tag{5.18}$$

As cracks begin to close the crack density will decrease as follows:

$$\epsilon = \epsilon_\circ\cos\psi_\circ\,. \tag{5.19}$$

For open cracks, the normalized crack aspect ratio can be expressed as

$$\gamma = s_v(\cos^2\psi_\circ - \cos^2\psi)\,, \tag{5.20}$$

which gives a maximum dilation of pore space occurring for vertical cracks of all azimuthal orientations ($\psi = \frac{\pi}{2}$) as follows:

$$\gamma_{max} = s_v\cos^2\psi_\circ\,. \tag{5.21}$$

5.2.2 Hudson's Model for Cracked Media

The Hudson Model, developed by Hudson (1980), allows us to express the effective elastic coefficients for cracked media, $\boldsymbol{C^E}$, as the sum of the elastic coefficients of the solid matrix, $\boldsymbol{C^M}$, and the perturbations due to a single crack set of a specified crack density, $\boldsymbol{C^D}$, as follows:

$$\boldsymbol{C^E} = \boldsymbol{C^M} + \boldsymbol{C^D}\,. \tag{5.22}$$

The first order corrections to the elasticity coefficients due to a single crack set of penny-shaped cracks with crack normals aligned with the x_3 axis are given by:

$$C^D_{1111} = -\frac{\lambda^2}{\mu}\epsilon U_3\,, \tag{5.23}$$

$$C^D_{1133} = -\frac{\lambda(\lambda+2\mu)}{\mu}\epsilon U_3\,, \tag{5.24}$$

$$C^D_{3333} = -\frac{(\lambda+2\mu)^2}{\mu}\epsilon U_3\,, \tag{5.25}$$

$$C^D_{2323} = -\mu\epsilon U_1 \tag{5.26}$$

and

$$C^D_{1212} = 0\,, \tag{5.27}$$

where λ and μ are the matrix Lamé parameters and the terms U_1 and U_3 depend on the conditions within the crack (Mavko et al., 2009). For the general case,

$$U_1 = \frac{16(\lambda+2\mu)}{3(3\lambda+4\mu)} \times \frac{1}{(1+\beta_H)} \tag{5.28}$$

and

$$U_3 = \frac{4(\lambda + 2\mu)}{3(\lambda + \mu)} \times \frac{1}{(1 + \kappa_H)}\,, \tag{5.29}$$

where

$$\beta_H = \frac{4\mu_I}{\pi g_\circ \mu} \times \frac{(\lambda + 2\mu)}{(3\lambda + 4\mu)}\,, \tag{5.30}$$

$$\kappa_H = \frac{(K_I + \frac{4}{3}\mu_I)(\lambda + 2\mu)}{\pi g_\circ \mu(\lambda + \mu)}\,, \tag{5.31}$$

$g_\circ$ is the crack aspect ratio and K_I and μ_I are the bulk and shear moduli of the crack-filling material. For infinitely thin, fluid-filled cracks we assume an incompressible fluid with a bulk modulus that is large enough and a crack aspect ratio that is small enough that the normal component of crack displacements is vanishingly small. Hence, the effective bulk modulus of the matrix remains unchanged with the introduction of the saturated crack distribution and $U_3 = 0$. By setting the crack-filling material shear modulus to zero in equation 5.30 we see that β_H reduces to zero and equation 5.28 simplifies to

$$U_1 = \frac{16(\lambda + 2\mu)}{3(3\lambda + 4\mu)}\,. \tag{5.32}$$

For dry cracks we set the bulk and shear moduli of the inclusion material to zero, causing equation 5.29 to simplify to

$$U_3 = \frac{4(\lambda + 2\mu)}{3(\lambda + \mu)}\,. \tag{5.33}$$

It should be noted that the bulk modulus of a hydrocarbon gas at high pressures approaches that of an incompressible fluid but can be significantly smaller (Mavko et al., 2009). For example, the bulk modulus of methane gas at $20\,MPa$ and $50\,^\circ C$ is two orders of magnitude smaller than a typical oil or brine at the same temperature and pressure. Thus, from equations 5.29 and 5.31, this methane gas could result in a non-vanishing U_3 value, depending on

the crack aspect ratio.

The perturbations due to more than one crack set are calculated separately, rotated to a consistent coordinate system and added together (Hudson, 1980). Certain special cases of crack distributions can be expressed with simple analytical equations. For example, the first order perturbations to the elasticity coefficients due to an isotropic distribution of infinitely thin, fluid-filled cracks are

$$C^D_{1111} = C^D_{2222} = C^D_{3333} = -\frac{8}{15}\mu\epsilon U_1, \tag{5.34}$$

$$C^D_{1122} = C^D_{2211} = C^D_{1133} = C^D_{3311} = C^D_{2233} = C^D_{3322} = \frac{4}{15}\mu\epsilon U_1 \tag{5.35}$$

and

$$C^D_{2323} = C^D_{1313} = C^D_{1212} = -\frac{2}{5}\mu\epsilon U_1. \tag{5.36}$$

The resulting effective medium satisfies the conditions for isotropy. Additionally, Mavko et al. (2009) gives the first order perturbations to the elasticity coefficients due to an azimuthally-random distribution of infinitely thin, fluid-filled cracks with crack normals at a fixed angle, ψ_i, from the x_3 axis as

$$C^D_{1111} = C^D_{2222} = -\frac{1}{2}\mu\epsilon_i U_1 \sin^2\psi_i(4 - 3\sin^2\psi_i), \tag{5.37}$$

$$C^D_{3333} = -4\mu\epsilon_i U_1 \cos^2\psi_i \sin^2\psi_i, \tag{5.38}$$

$$C^D_{1122} = C^D_{2211} = \frac{1}{2}\mu\epsilon_i U_1 \sin^4\psi_i, \tag{5.39}$$

$$C^D_{1133} = C^D_{3311} = C^D_{2233} = C^D_{3322} = 2\mu\epsilon_i U_1 \cos^2\psi_i \sin^2\psi_i, \tag{5.40}$$

$$\begin{aligned} C^D_{2323} = C^D_{1313} = &-\frac{1}{2}\mu\epsilon_i U_1 \sin^2\psi_i \\ &(\sin^2\psi_i + 2\cos^2\psi_i - 4\cos^2\psi_i \sin^2\psi_i) \end{aligned} \tag{5.41}$$

and

$$C^D_{1212} = -\frac{1}{2}\mu\epsilon_i U_1 \sin^2\psi_i(2 - \sin^2\psi_i). \tag{5.42}$$

In this case, the resulting effective medium satisfies the conditions for transverse isotropy. Also, crack density, ϵ_i, is independent of crack normal azimuth, θ, and is zero for all crack normal inclinations except for $\psi = \psi_i$.

5.2.3 Velocity

The P-wave and S-wave phase velocities for an isotropic medium are respectively given by

$$v_p = \sqrt{\frac{C_{1111}}{\rho}} \tag{5.43}$$

and

$$v_s = \sqrt{\frac{C_{2323}}{\rho}}\,, \tag{5.44}$$

where ρ is the density of the medium. In a transversely isotropic medium the quasi P-wave, v_{qp}, quasi S-wave, v_{qsv} and pure S-wave, v_{sh} phase velocities can be expressed as

$$v_{qp} = (C_{1111}\sin^2\psi + C_{3333}\cos^2\psi + C_{2323} + \sqrt{M_v})^{\frac{1}{2}}(2\rho)^{-\frac{1}{2}}, \tag{5.45}$$

$$v_{qsv} = (C_{1111}\sin^2\psi + C_{3333}\cos^2\psi + C_{2323} - \sqrt{M_v})^{\frac{1}{2}}(2\rho)^{-\frac{1}{2}} \tag{5.46}$$

and

$$v_{sh} = (\frac{C_{1212}\sin^2\psi + C_{2323}\cos^2\psi}{\rho})^{\frac{1}{2}}, \tag{5.47}$$

where ψ is the angle of propagation from the symmetry axis and

$$\begin{aligned} M_v = &[\,(C_{1111} - C_{2323})\sin^2\psi - (C_{3333} - C_{2323})\cos^2\psi\,]^2 \\ &+ (C_{1133} + C_{2323})^2 - \sin^2 2\psi\,, \end{aligned} \tag{5.48}$$

for example (Slawinski, 2015). A convenient measure of the degree of P-wave velocity anisotropy, PWA_T, of a transversely isotropic medium is given by

$$PWA_T = \frac{v_{qp}(\psi)_{max} - v_{qp}(\psi)_{min}}{v_{qp}(\psi)_{max}} \times 100\%\,, \tag{5.49}$$

where $\psi \in [\,0, \frac{\pi}{2}\,]$, $v_{qp}(\psi)_{max}$ is the maximum qP-wave velocity and $v_{qp}(\psi)_{min}$ is the minimum qP-wave velocity. The analogous measure of S-wave velocity anisotropy, SWA_T, of a transversely isotropic medium is given by

$$SWA_T = \frac{v_{s1}(\psi)_{max} - v_{s2}(\psi)_{min}}{v_{s1}(\psi)_{max}} \times 100\%\,, \tag{5.50}$$

where $\psi \in [\,0, \frac{\pi}{2}\,]$, $v_{s1}(\psi)_{max}$ is the maximum fast S-wave velocity and $v_{s2}(\psi)_{min}$ is the minimum slow S-wave velocity.

5.3 Method

To test the anisotropic velocity sensitivity of a medium containing an initially isotropic, fluid-isolated, crack distribution under a range of uniaxial compressive stresses we use the APE model along with the Hudson model to calculate the effective elasticity coefficients of the stressed medium. We first set the default parameter values for isotropic matrix P-wave velocity ($v_{p,matrix}$), isotropic matrix S-wave velocity ($v_{s,matrix}$), matrix density (ρ), initial crack aspect ratio ($g_\circ$), initial crack density ($\epsilon_\circ$), and pore-fluid compressibility (c_f), as seen Table 5.1. In order to test the anisotropic velocity sensitivity for a single input parameter, a series of values for the parameter of interest are used while holding all other input parameters at the default values.

Table 5.1: Uniaxial APE model default parameters.

Matrix $v_{p,matrix}$	$4700\,m/s$
Matrix $v_{s,matrix}$	$3000\,m/s$
v_p/v_s Ratio	1.567
Matrix Density, ρ	$2500\,kg/m^3$
Initial Crack Aspect Ratio, $g_\circ$	1×10^{-5}
Initial Crack Density, $\epsilon_\circ$	0.14
Pore-fluid Compressibility, c_f	$3 \times 10^{-10}\,Pa^{-1}$

The next step is to use the matrix property inputs ($v_{p,matrix}$, $v_{s,matrix}$ and ρ) in equations 5.43 and 5.44 to obtain the elasticity coefficients for the isotropic matrix. These elasticity coefficients along with the initial crack aspect ratio are used to calculate the crack critical closure stress with equation 5.4. The normalized pore-fluid compressibility is then obtained using the crack critical closure stress and the pore-fluid compressibility in equation 5.8.

The remaining steps are repeated for each value of uniaxial compressive stress in the desired range of stress. Equation 5.12 is used to obtain the normalized differential stress corresponding to an input stress. Then it is determined if all cracks will remain open, i.e. $s_v \leq \frac{3}{2}$, under this differential stress or if some cracks will be closed, i.e. $s_v > \frac{3}{2}$. If all cracks remain open, equations

5.14, 5.15 and 5.16 are used respectively to find the angle of crack closure, dimensionless excess pore-fluid pressure and crack density. If some cracks are closed, equations 5.17, 5.18 and 5.19 are used respectively to find the angle of crack closure, dimensionless excess pore-fluid pressure and crack density of the remaining open cracks. The differential stress and crack closure angle are then used in equation 5.7 to calculated normalized crack aspect ratio as a function of ψ for values of ψ between 0^o and 90^o. Next, equations 5.23 to 5.27, excluding the ϵ and μ terms, are used to obtain the perturbation to the elasticity coefficients for a random crack distribution with normals at a fixed angle from the x_3-axis for each value of ψ between $\psi_\circ$ and 90^o. In other words, elasticity perturbations are calculated for cracks that remain open. These values then feed into equations 5.9 and 5.10 to obtain the elasticity perturbations due to the remaining crack distribution and the elasticity perturbations due to the remaining crack geometries.

Now consider equation 5.1 for an evolving isotropic crack distribution uniaxial stress. In this case, the integration limits and the integrand are independent of azimuth. Furthermore, we have calculated all terms in the integrand in a common coordinate system, so equation 5.1 simplifies to

$$\begin{aligned} \boldsymbol{C^E} = \boldsymbol{C^M} &+ \epsilon \int_{\psi_\circ}^{\frac{\pi}{2}} \boldsymbol{C^D}(\psi) \sin\psi \, d\psi \\ &+ \epsilon \int_{\psi_\circ}^{\frac{\pi}{2}} \boldsymbol{C^G}(\psi) \sin\psi \, d\psi \,, \end{aligned} \tag{5.51}$$

for which there are no unknowns. We implement numerical integration of equation 5.51 to obtain the effective elasticity coefficients of the cracked medium for a specific value of applied stress. Then we use these effective elasticity coefficients in equations 5.45 to 5.48 to calculate v_p, v_{s1} and v_{s2} as a function of angle of propagation measured from vertical. Finally, we feed these velocities into equations 5.49 and 5.50 to calculate the degree of P-wave and S-wave

anisotropy respectively.

5.4 Results & Discussion

Using our default parameter values for an evolving isotropic crack distribution due to a uniaxial compressive stress, the APE model as outlined in equations 5.11 to 5.21 predicts an evolving crack distribution as a function of normalized differential stress alone: s_v. Figure 5.1 displays the behaviour of crack closure angle, normalized aspect ratio, normalized crack density and normalized excess pore-fluid pressure with increasing differential stress. Panel (A) shows that for $s_v \leq \frac{3}{2}$, the average normalized aspect ratio is constant at one: all cracks remain open. However, the maximum normalized aspect ratio begins to increase with the first increase in differential stress, i.e. $s_v > 0$, as cracks with normals parallel to the applied stress are squeezed. Panel (B) shows when $s_v > \frac{3}{2}$, the normalized crack density initially decreases rapidly but asymptotically approaches a value of approximately 40% of the initial crack density. Panel (C) shows that the normalized excess pore-fluid pressure matches the thermodynamic equilibrium until cracks begin to close. The crack closure angle, seen in Panel (D), shows an initially rapidly increasing value asymptotically approaching a value approximately equal to 65°.

We can use the observations made in Figure 5.1 to set a realistic upper bound to the expected PWA_T and SWA_T. The maximum degree of anisotropy possible due to a uniaxial compressive stress would be obtained if the crack density remained constant and only vertical cracks, normals of $\psi_\circ = \frac{\pi}{2}$, remained open. However, this situation is not feasible based on our observations because as applied stress increases crack density decreases to a minimum of 40% of the initial crack density and crack closure angle increases to a maximum of 65°. Additionally, Zatsepin and Crampin (1997) note that evolving crack distributions with crack closure angles greater than 45° behave similar

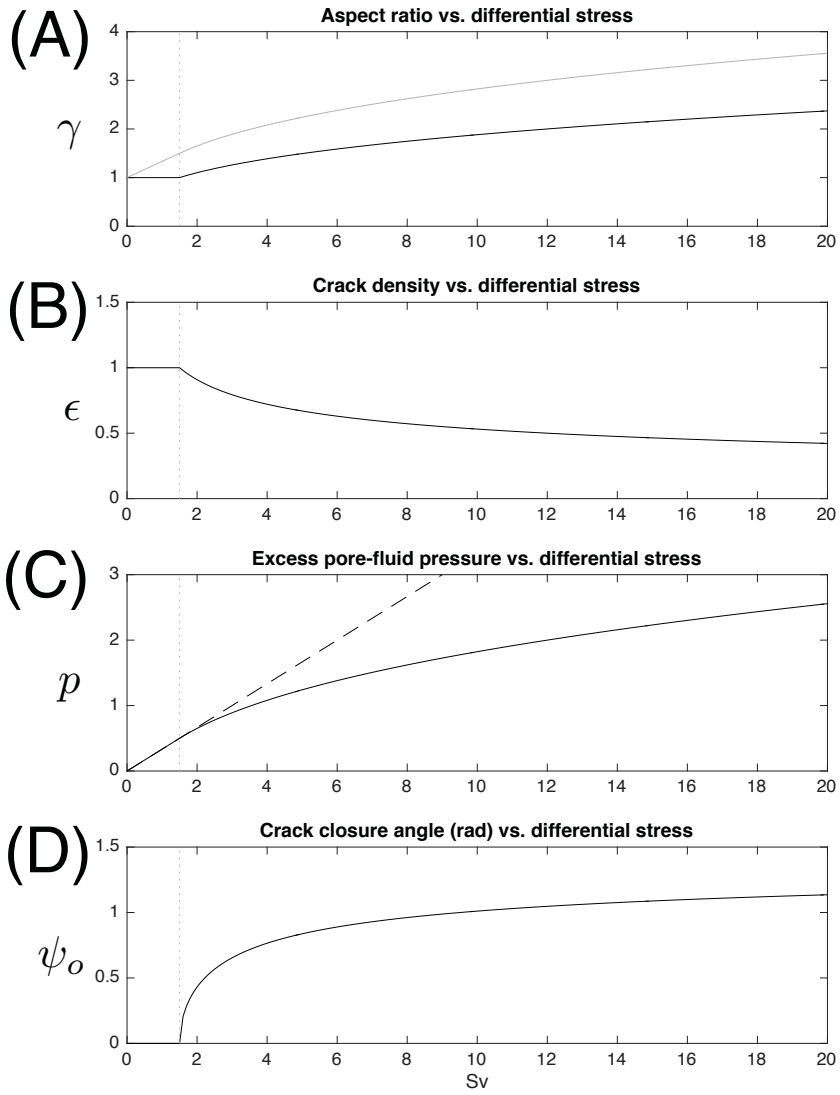

Figure 5.1: The behaviour of several APE model parameters as a function of applied differential stress, s_v. Note that the y-axis of Panel (D) is in radians and the y-axes of Panels (A) - (C) are dimensionless. (A) The black line is the average of the normalized aspect ratio, γ, for all open cracks and the grey line is the maximum normalized aspect ratio, γ_{max}, which is found for vertically oriented cracks. (B) Shows the normalized crack density, ϵ. (C) The black line is the normalized excess pore-fluid pressure, p, and the dashed line is the normalized thermodynamic equilibrium pressure, $p = s_v/3$. (D) Shows the crack closure angle, $\psi_\circ$.

to a vertical crack distribution with normals randomly distributed through azimuths of $0 \leq \theta \leq 2\pi$. Crampin (1994) gives a maximum initial crack density in

natural rock approximately equal to the percolation threshold of $\epsilon_\circ = 0.14$. Using this along with crack closure angles $\psi_\circ = 45°$ and $\psi_\circ = 60°$ in equation 5.19 we obtain corresponding values for normalized crack density of 0.10 and 0.07. Now, we obtain a range for the maximum expected anisotropy by approximating these two crack distributions scenarios respectively as vertical crack distributions with crack densities of 0.10 and 0.07. As we will demonstrate later, maximum PWA_T and SWA_T due to a increasing uniaxial applied stress tends to increase with smaller values of matrix v_p/v_s ratios and is unaffected by the initial crack aspect ratio, matrix P-wave velocity, matrix density and pore-fluid compressibility, as long as the pore-fluid is incompressible. Using a reasonable minimum v_p/v_s ratio for a low-porosity sandstone of 1.4 in the 0.10 and 0.07 vertical crack density scenarios, we obtain a range for the maximum expect anisotropy, as seen in Figure 5.3. Panel (A) shows $PWA_T = 3.3\%$ for the 65° crack closure angle scenario and $PWA_T = 4.7\%$ for the 45° crack closure angle scenario. Panel (B) shows $SWA_T = 3.7\%$ for the 65° crack closure angle scenario and $SWA_T = 5.3\%$ for the 45° crack closure angle scenario. However, the actual degree of anisotropy due to uniaxial stress will be less than these maximums because the crack distributions will not be uniformly aligned. Instead, the crack distributions will be sub-vertical sets with normals evenly oriented over inclinations of $\psi_\circ \leq \psi \leq 90°$, resulting in interference effects. Throughout the remainder of this thesis, we use upper hemisphere projections of crack normal orientation, as outlined in Figure 5.2, to visualize crack distributions.

The crack distribution and velocity behaviours of the APE model in response to increasing uniaxial stress for our default parameters are illustrated in Figures 5.4 to 5.7. When s_v is at the point just before crack closure commences, less than 0.001% velocity anisotropy has developed due entirely to changing pore geometries, as seen in Figure 5.4. When s_v is doubled to 3, Figure 5.5 shows an increase in PWA_T to 0.5% and SWA_T to 1.4%. Figures 5.6 and 5.7 show that PWA_T stays constant at 0.5% as s_v is increased to 10 and 20

while SWA_T decreases slightly to 1.0% and 0.8% respectively. It is interesting to note that PWA_T is less than half the SWA_T for all scenarios.

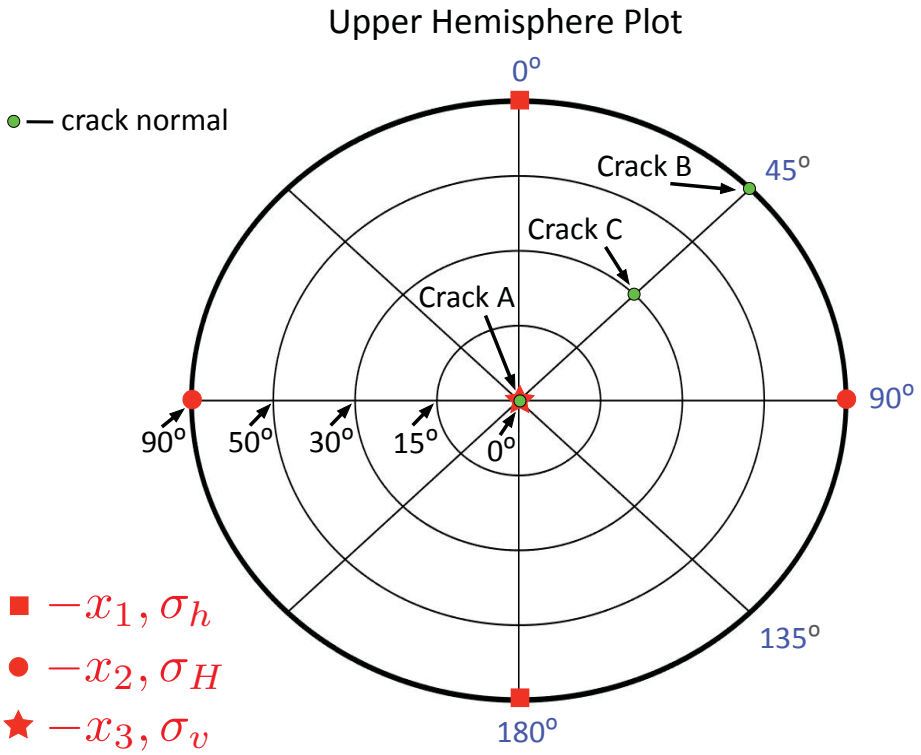

Figure 5.2: An example upper hemisphere projection showing the orientation of the three coordinate axes (x_1, x_2, x_3), the three principle stress directions $(\sigma_h, \sigma_H, \sigma_v)$ and three example crack normal orientations. Azimuthal value is indicated by red numbers and is measure clockwise from the x_1-axis around the circle. The straight lines on the projection are isoclines of azimuth. Inclination is indicated by black numbers and is measured from the x_3-axis. The circles on the projection are isoclines of inclination. Crack A is a horizontal crack with vertical crack normal. Crack B is a vertical crack with a crack normal azimuthally oriented 45 degrees from the x_1-direction and crack C has a crack normal inclined 30 degrees from the x_3-axis and having the same azimuth as crack B. The fracture normal for a vertical hydraulic fracture with a fracture plane perpendicular to the minimum horizontal stress (σ_h) plots at the same point as the x_1-axis and σ_h.

Observing the behaviour of PWA_T and SWA_T as a function of applied stress, σ_v, is convenient way to analyze the velocity anisotropy sensitivity to various input parameter perturbations. Figure 5.8 shows PWA_T and SWA_T as a function

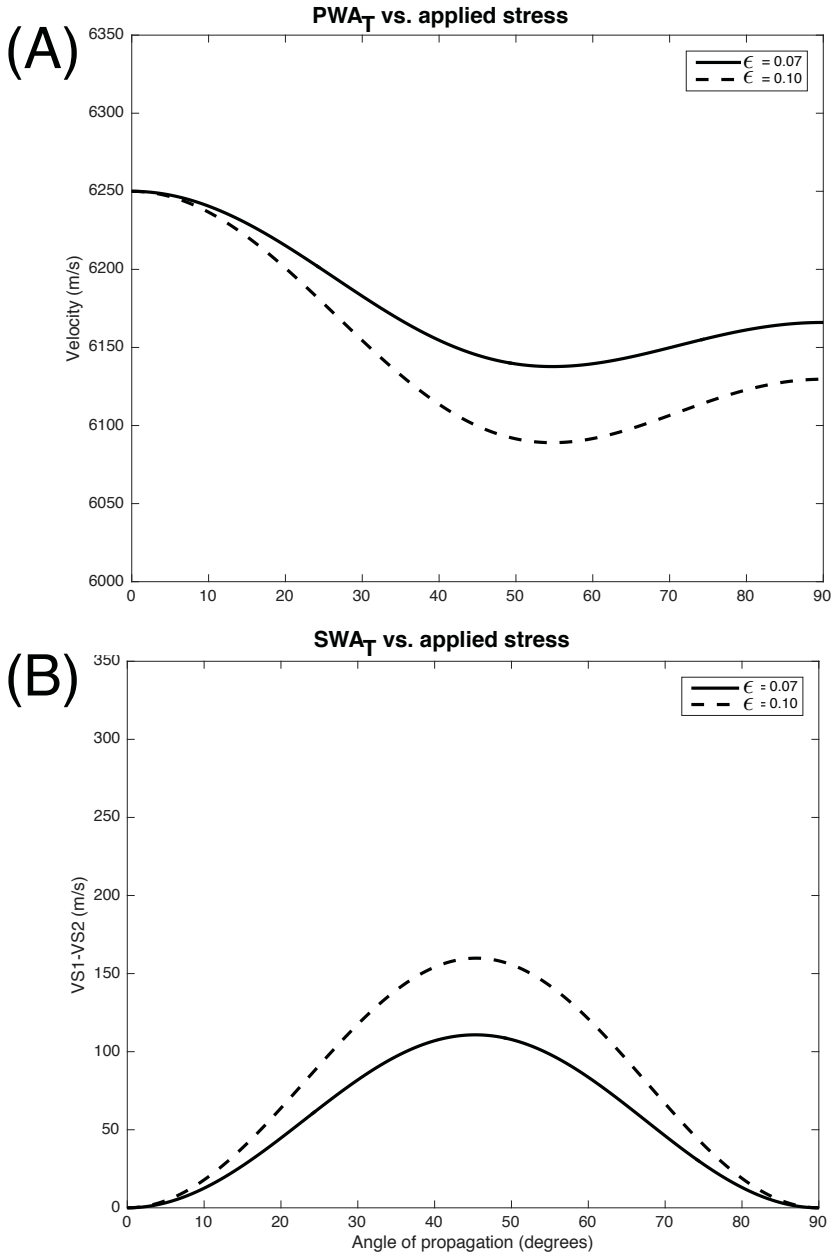

Figure 5.3: Velocity behaviour as a function of the angle of propagation for two separate azimuthally isotropic distributions of vertical cracks. The first distribution has a normalized crack density of $\epsilon = 0.07$ and the second distribution has a normalized crack density of $\epsilon = 0.10$. (A) P-wave phase velocity. (B) S-wave phase velocity splitting.

of applied stress for our parameter default settings. The SWA_T curve shows five segments that are characterized by distinct S-wave splitting behaviour as a

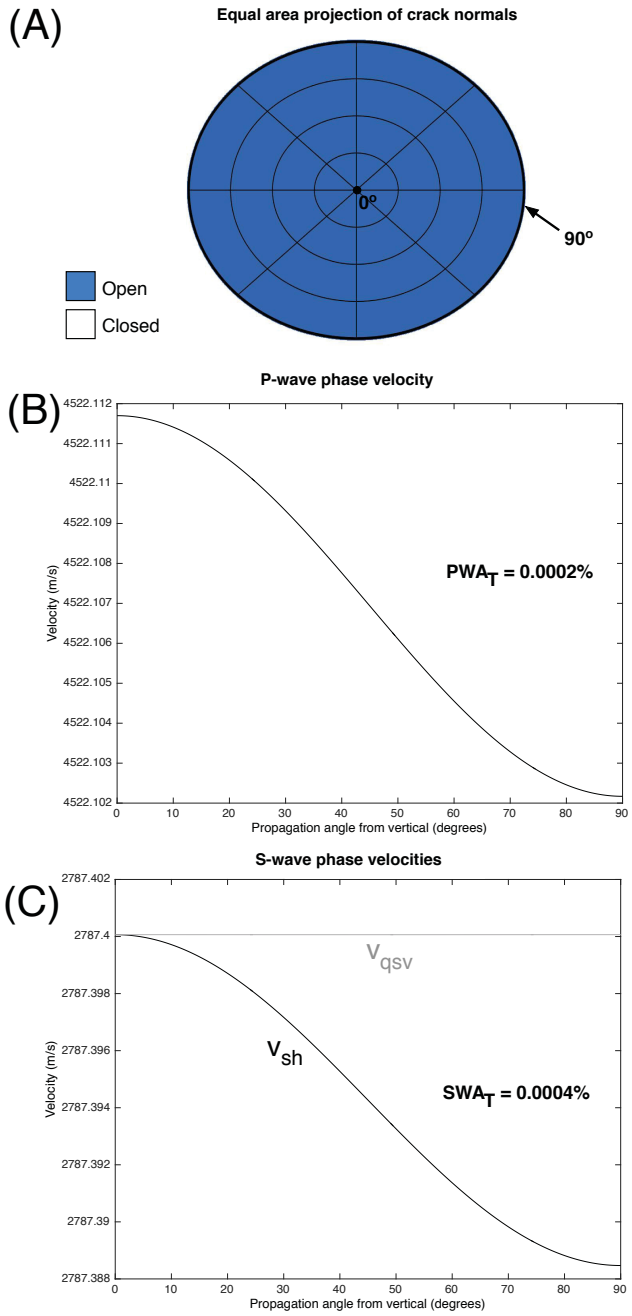

Figure 5.4: APE model crack distribution and velocity behaviour in response to a uniaxial vertical different stress of $s_v = 1.49$ with all of the model parameters set to the default values, see Table 5.1. (A) An equal area projection of crack normal orientation. The black numbers indicate degrees inclination from vertical. (B) P-wave velocity as a function of propagation angle. (C) S-wave velocities as a function of propagation angle.

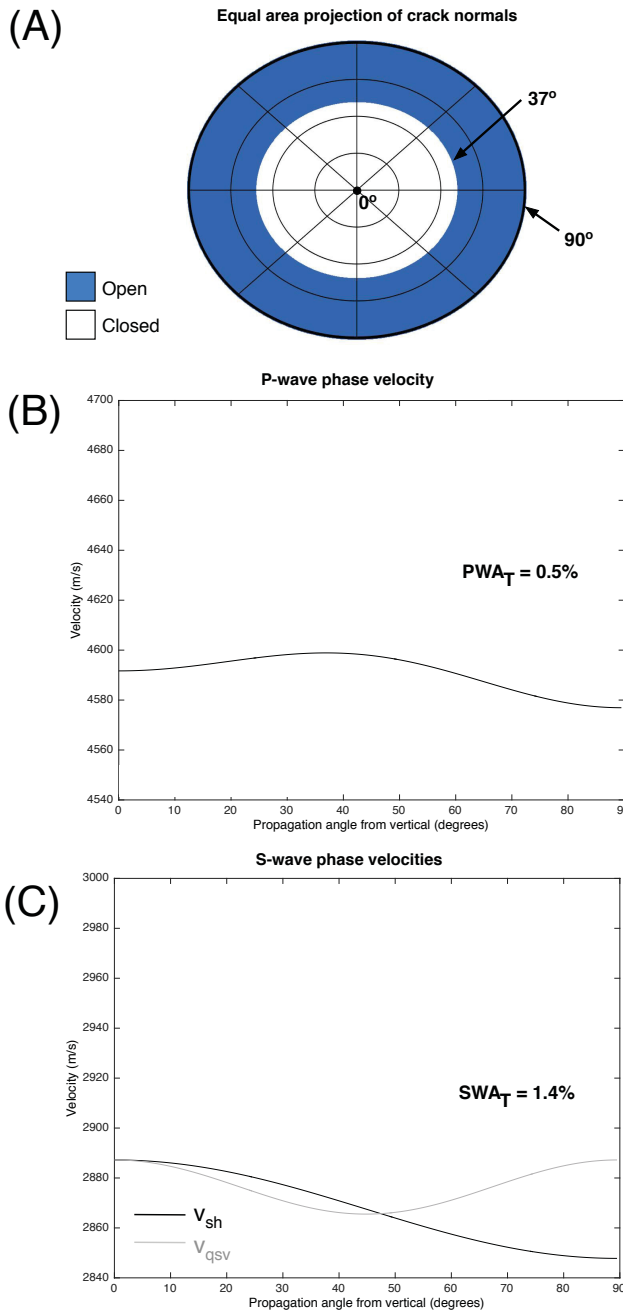

Figure 5.5: APE model crack distribution and velocity behaviour in response to a uniaxial vertical different stress of $s_v = 3$ with all of the model parameters set to the default values, see Table 5.1. (A) An equal area projection of crack normal orientation. The black numbers indicate degrees inclination from vertical with the critical angle of crack closure being $\psi_\circ = 37°$ (B) P-wave velocity as a function of propagation angle. (C) S-wave velocities as a function of propagation angle.

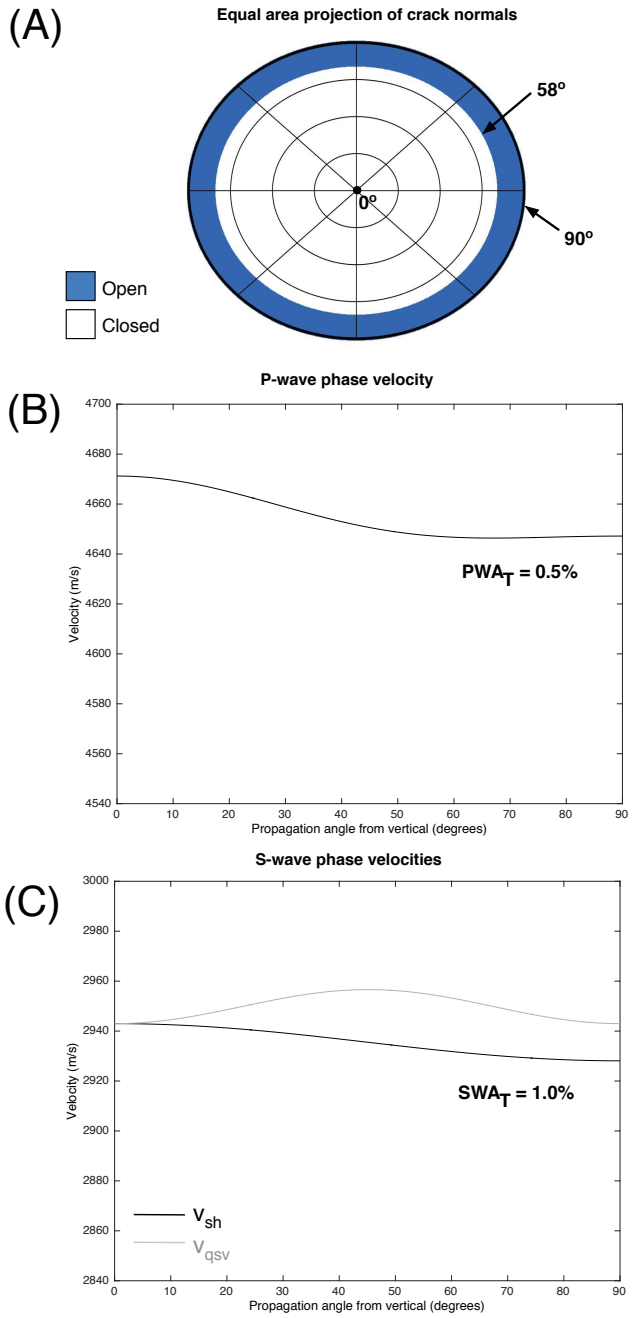

Figure 5.6: APE model crack distribution and velocity behaviour in response to a uniaxial vertical different stress of $s_v = 10$ with all of the model parameters set to the default values, see Table 5.1. (A) An equal area projection of crack normal orientation. The black numbers indicate degrees inclination from vertical with the critical angle of crack closure being $\psi_\circ = 58°$ (B) P-wave velocity as a function of propagation angle. (C) S-wave velocities as a function of propagation angle.

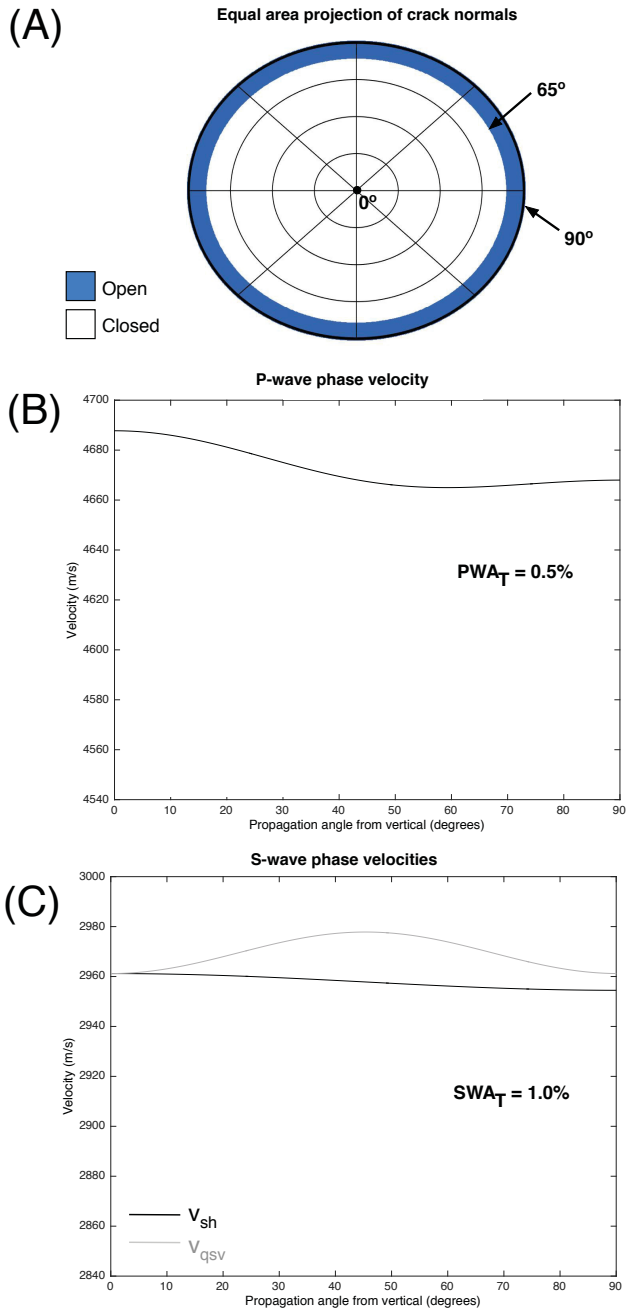

Figure 5.7: APE model crack distribution and velocity behaviour in response to a uniaxial vertical different stress of $s_v = 20$ with all of the model parameters set to the default values, see Table 5.1. (A) An equal area projection of crack normal orientation. The black numbers indicate degrees inclination from vertical with the critical angle of crack closure being $\psi_\circ = 65°$ (B) P-wave velocity as a function of propagation angle. (C) S-wave velocities as a function of propagation angle.

function of angle of propagation, as shown in Figures 5.9 and 5.10 where each panel (A) - (D) corresponds to the labelled segments (a) - (d) in Figure 5.8. In segment (o), all cracks remain open and all anisotropy is due to crack geometry alteration and is characterized by very little to no SWA_T. In segment (b), cracks begin to close and SWA_T increases rapidly to a global maximum value that corresponds to $s_v = 2.7$. As seen in Figure 5.9, the S-wave splitting shows a low-angle local maximum, a zero-angle and a mid-angle zero-splitting point and a global maximum at 90°. Both the low-angle local maximum and the mid-angle zero-splitting point shift to smaller angles as applied stress increases. The S-wave splitting value at the global maximum rapidly increases with applied stress. Segment (c) is characterized by moderately decreasing SWA_T to a local minimum that corresponds to $s_v = 5.4$, see Figure 5.8. As seen in Figure 5.9, the S-wave splitting low-angle local maximum rapidly decreases and eventually disappears as it, and the mid-angle zero-splitting point, migrate towards and eventually merge with the zero-angle zero-splitting point as applied stress increases. The global maximum moderately decreases but remains at 90°. Segment (d) is characterized by a gradually increasing SWA_T to a local maximum that corresponds to $s_v = 7.4$, see Figure 5.8. Figure 5.10 shows that as applied stress increases the S-wave splitting global maximum migrates away from 90° to a smaller angle and the S-wave splitting curve between approximately 55° and 90° flattens out. Figure 5.8 shows that in segment (e), SWA_T gradually decreases when $s_v > 7.4$. As applied stress increases, the S-wave splitting global maximum slowly becomes more pronounced and migrates towards 45°, while a local non-zero minimum occurs at 90°, see Figure 5.10. The S-wave splitting behaviour as a function of propagation angle now resembles that expressed by wholly vertical cracks as seen in Figure 5.3.

The SWA_T segments in Figure 5.8 are defined in terms of s_v values. However, the amount of applied stress, σ_v, required to reach a particular value of s_v and the absolute value of SWA_T reached in each segment will vary depending

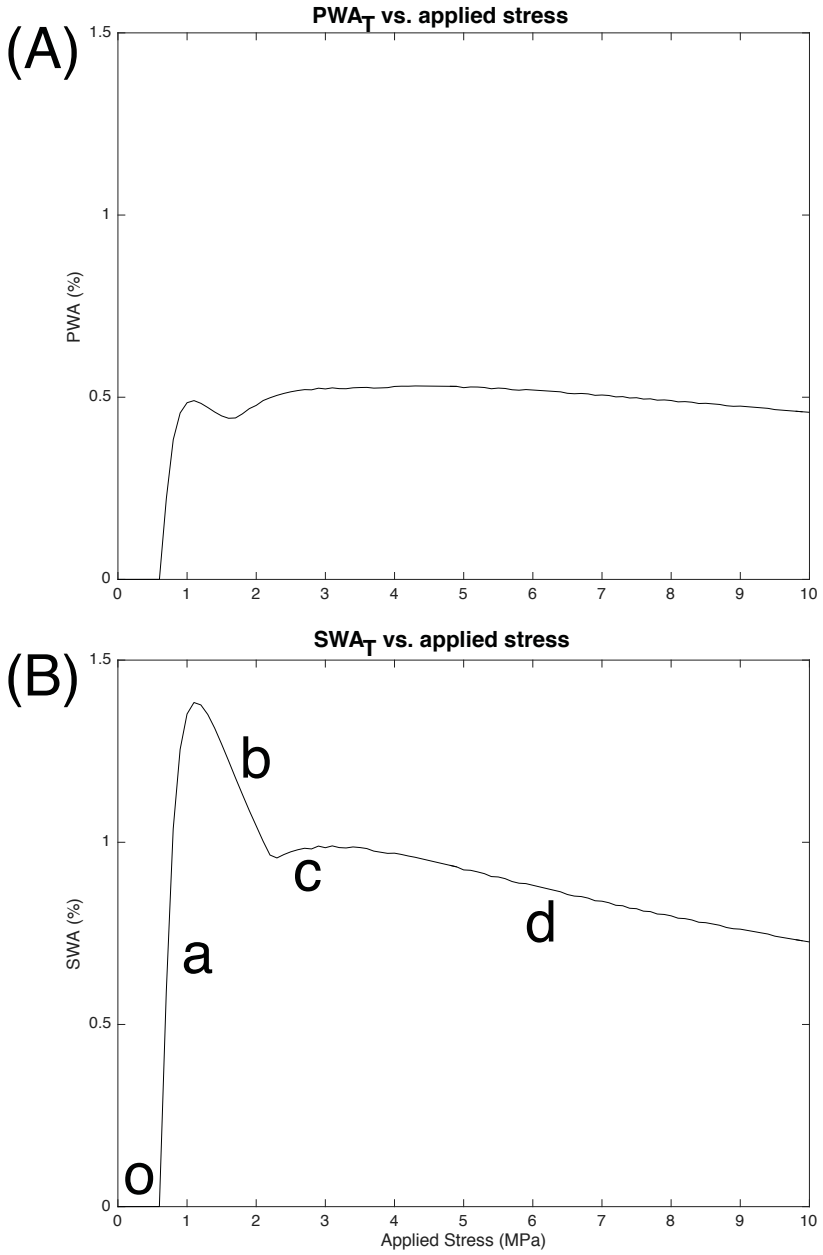

Figure 5.8: Phase velocity anisotropy as a function of applied uniaxial stress, σ_v, when all parameters are set to the default values. (A) PWA_T and (B) SWA_T where the segments (o) and (a) - (d) represent regions of the SWA_T curve with common S-wave splitting character. The characteristics of each segment are shown in Figures 5.9 and 5.10.

on the input parameter values. That is, as input parameters are varied, the SWA_T curves may be stretched or squeezed in the $x-$ and/or $y-$direction but

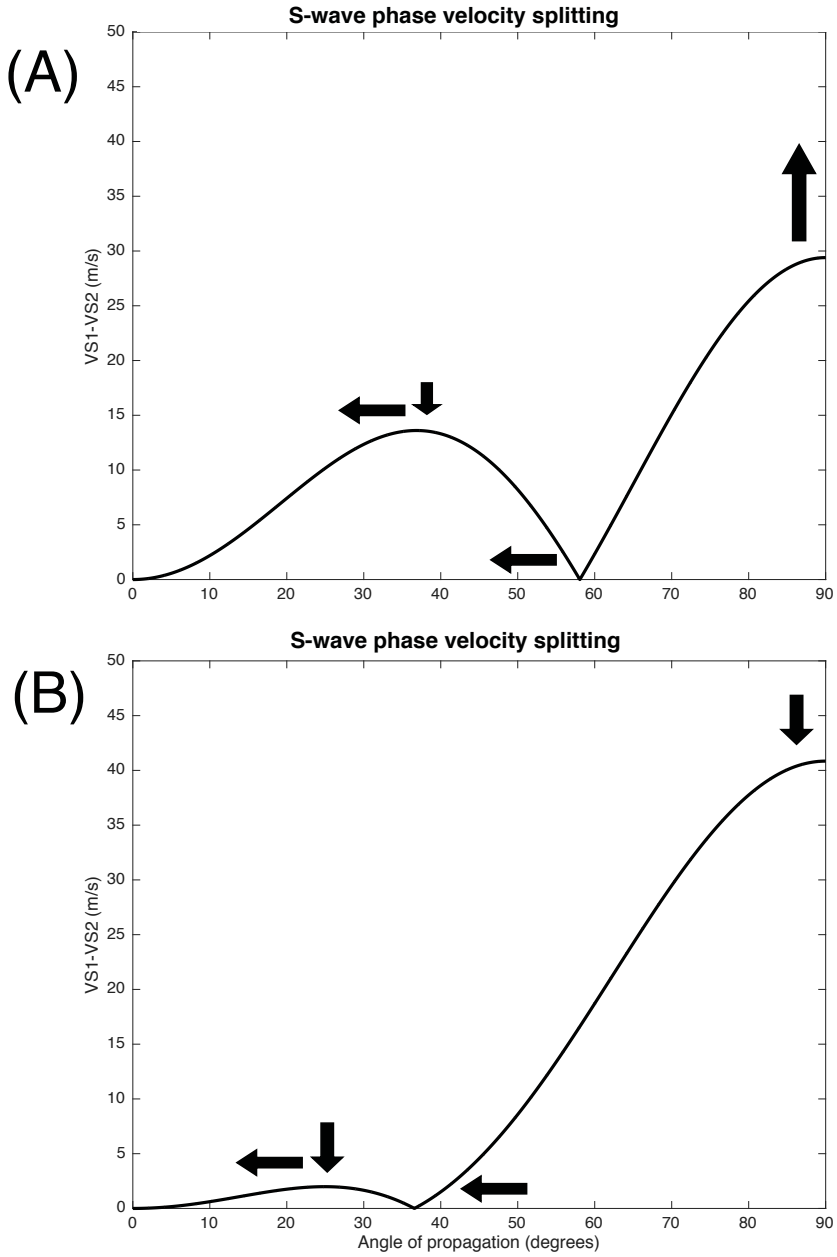

Figure 5.9: S-wave phase velocity splitting as a function of propagation angle. The black arrows show the migration direction of the associated maxima and minima as applied stress is increased. Panels (A) and (B) correspond to the segments of the SWA_T curve that are labelled in Figure 5.8.

they will always exhibit the five segments (o) and (a) to (d). Figures 5.11 to 5.16 show the SWA_T sensitivity to various input parameters. As seen in Figure 5.11, the SWA_T curve is stretched only in the vertical direction as initial

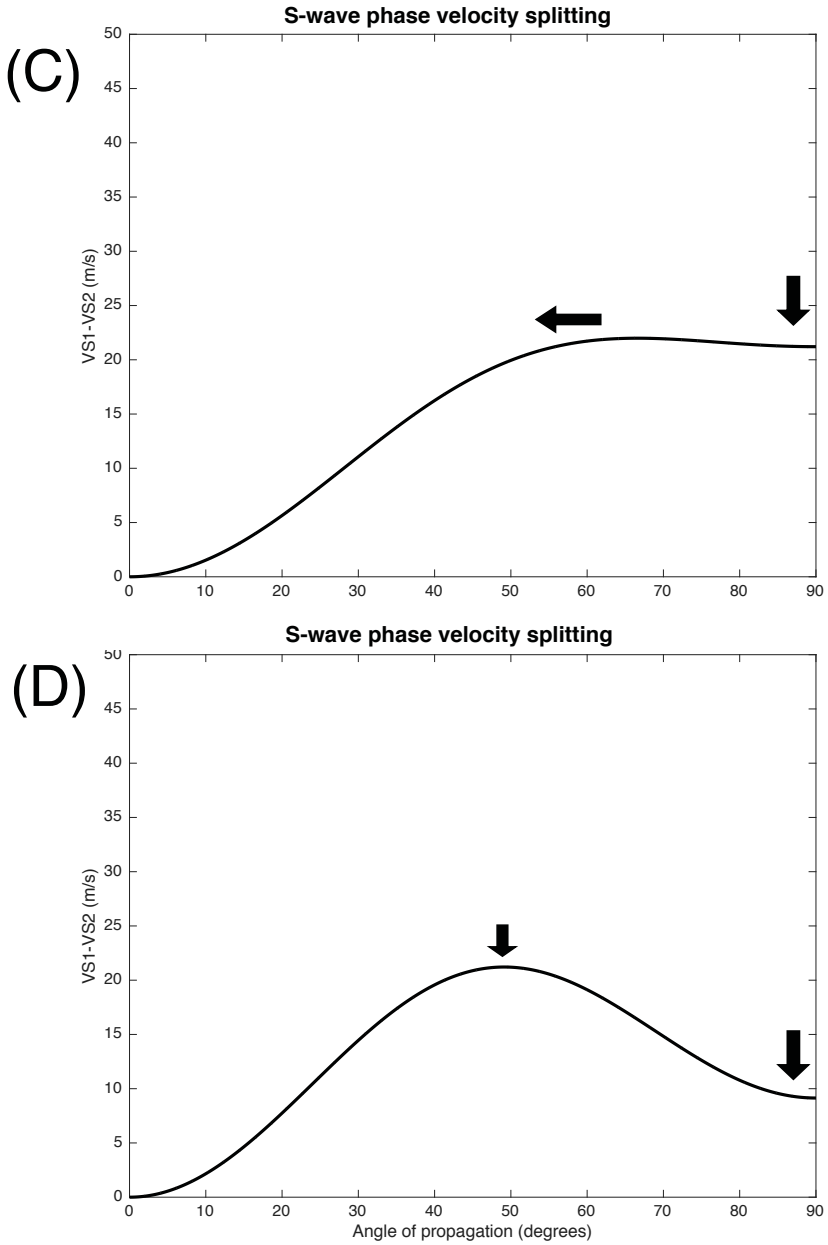

Figure 5.10: S-wave phase velocity splitting as a function of propagation angle. The black arrows show the migration direction of the associated maxima and minima as applied stress is increased. Panels (C) and (D) correspond to the segments of the SWA_T curve that are labelled in Figure 5.8.

normalized crack density is increased. The magnitude of SWA_T as a function of applied differential stress, s_v, shows a significant sensitivity to initial normalized crack density, and the amount of applied stress, σ_v, required to reach

a segment on the SWA_T curve is insensitive to initial normalized crack density. In contrast, Figures 5.12 to 5.14 show the SWA_T curve is stretched only in the horizontal direction as matrix density, matrix P-wave velocity, and initial crack aspect ratio are respectively increased. The magnitude of SWA_T as a function of applied differential stress, s_v, is insensitive to these three input parameters. However, the amount of applied stress, σ_v, required to reach a segment on the SWA_T curve is slightly sensitive to matrix density and is significantly sensitive to matrix P-wave velocity and initial crack aspect ratio. This makes sense as crack aspect ratio is important in determining the critical stress of crack closure, see equation 5.4. Figure 5.15 shows that both SWA_T magnitude as a function of applied differential stress, s_v, and the amount of applied stress, σ_v, required to reach a segment are moderately sensitive to v_p/v_s ratio. Larger SWA_T magnitudes are achieved and more applied stress is required as v_p/v_s ratio is decreased. Finally, although not shown here, when the pore-saturating fluid is incompressible the SWA_T curve is insensitive to fluid compressibility. As an addition, while not strictly valid for the APE model, it is instructive to look at SWA_T behaviour when the compressibility of the pore-saturating fluid is slightly larger than a truly incompressible fluid. Figure 5.16 illustrates that SWA_T magnitude as a function of applied differential stress, s_v, is slightly larger for increasing fluid compressibility. Also, we see that segment (o) now shows non-zero SWA_T. This results from the elasticity coefficient perturbations due to crack geometry having a larger contribution to the overall elasticity coefficient perturbations when fluid compressibility is large.

As illustrated in Figure 5.17, the volume of rock surrounding an open hydraulic fracture can now be described in terms of S-wave splitting behaviour. Recall, the large region normal to the fracture face is characterized by compressive stress increase. The magnitude of increased stress is significantly larger in the direction normal to the fracture face than in the other two principle directions. This fracture-normal component of stress is largest adjacent to the

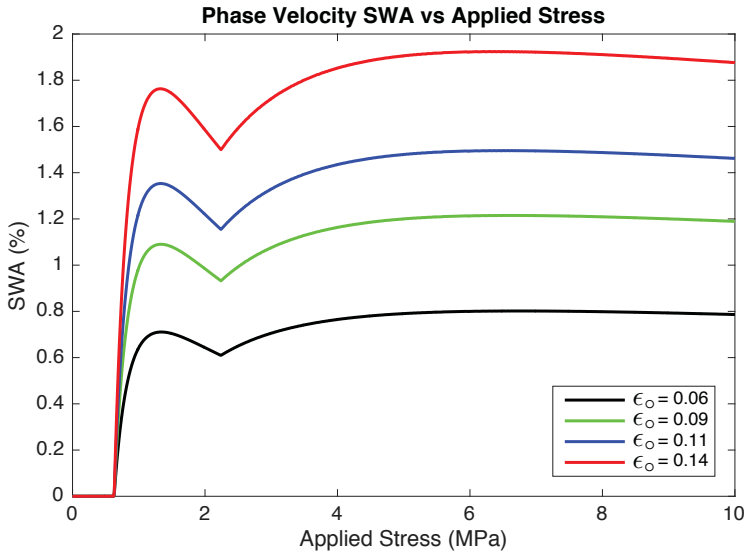

Figure 5.11: Phase velocity SWA_T versus uniaxial applied stress for various values of initial normalized crack density, $\epsilon_\circ$.

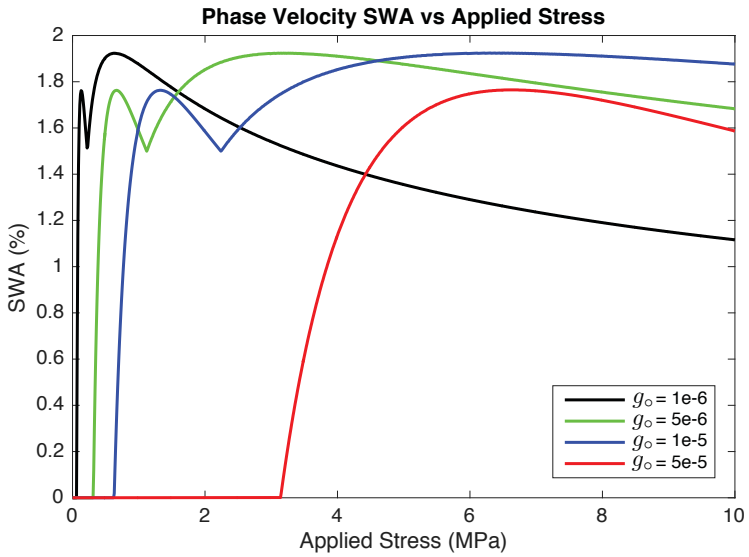

Figure 5.12: Phase velocity SWA_T versus uniaxial applied stress for various values of initial crack aspect ratio, $g_\circ$. The range of initial crack aspect ratios is representative of common real-world microcrack aspect ratios (Kranz, 1983).

fracture and gradationally decreases as distance from the fracture increases. Assuming the reservoir permeability is small enough to restrict pore-pressure diffusion to a negligible distance from the fracture and the stress field in this region can be approximated as a uniaxial compressive stress, we can use our

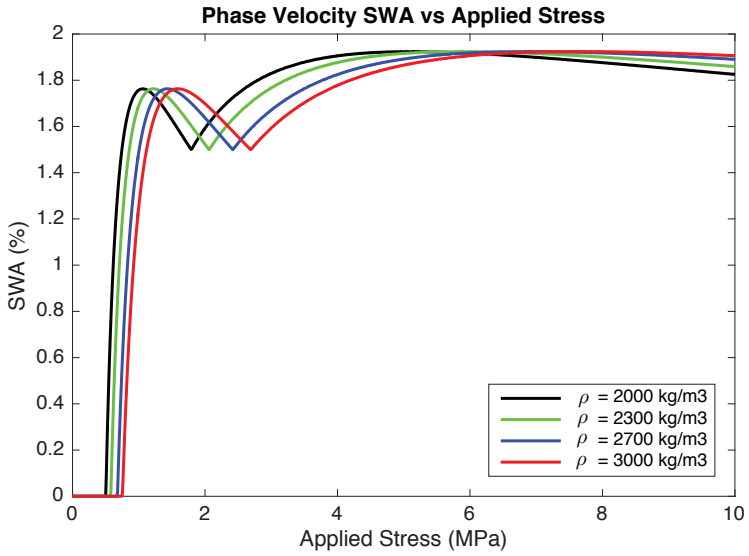

Figure 5.13: Phase velocity SWA_TA versus uniaxial applied stress for various values of matrix density, ρ. The range of matrix density is representative of hydrocarbon-reservoir rock types that are commonly targeted for hydraulic fracturing, including dolostone, limestone and low-porosity sandstone (Mavko et al., 2009).

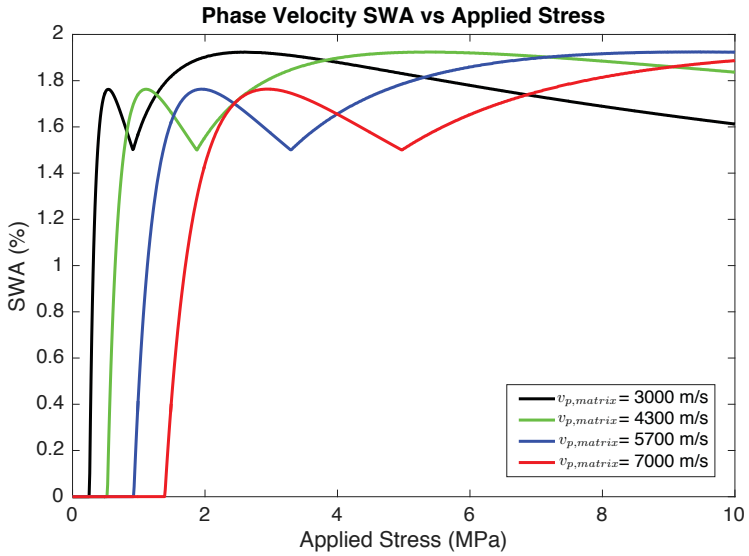

Figure 5.14: Phase velocity SWA_TA versus uniaxial applied stress for various values of matrix P-wave velocity, $v_{p\circ}$. The range of matrix P-wave velocity is representative of hydrocarbon-reservoir rock types that are commonly targeted for hydraulic fracturing, including dolostone, limestone and low-porosity sandstone (Mavko et al., 2009).

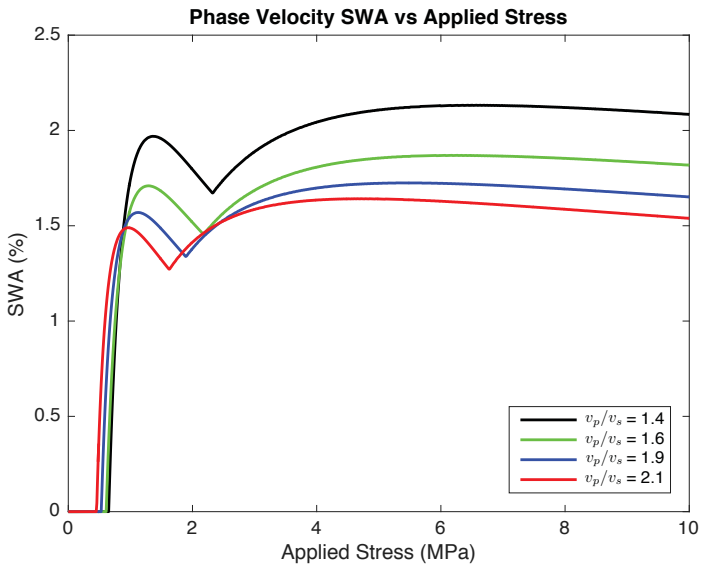

Figure 5.15: Phase velocity SWA_T versus uniaxial applied stress for various values of matrix v_p/v_s ratio, keeping v_p and density constant. The range of matrix v_p/v_s ratio is representative of hydrocarbon-reservoir rock types that are commonly targeted for hydraulic fracturing, including dolostone, limestone and low-porosity sandstone (Mavko et al., 2009).

observations in Figures 5.8 to 5.10 to predict the expected S-wave splitting. To properly apply our observations we must keep in mind that the uniaxial stress normal to the fracture face corresponds to the s_v direction discussed throughout this chapter. The APE model predicts that S-wave splitting will manifest when $s_v > 1.5$, and for our default parameters this occurs at $\sigma_v = 0.6\,MPa$, a relatively small stress perturbation. The maximum SWA_T occurs at $s_v = 2.7$ or $\sigma_v = 1\,MPa$. The local SWA_T minimum between segments (b) and (c) occurs at $s_v = 5.4$ or $\sigma_v = 2.3\,MPa$ and the local maximum between segments (c) and (d) occurs at $s_v = 7.4$ or $\sigma_v = 3.1\,MPa$. Let us assume the uniaxial fracture-normal stress has a maximum value of $\sigma_v = 3.5\,MPa$ immediately adjacent to the fracture faces. In this case, Figure 5.17 shows the volume of rock around the fracture experiencing increased compressive stress will exhibit the full range of SWA_T seen in Figure 5.8 and S-wave splitting character seen in Figures 5.9 and 5.10. Moving from fracture-distal to fracture-proximal, we expect to see

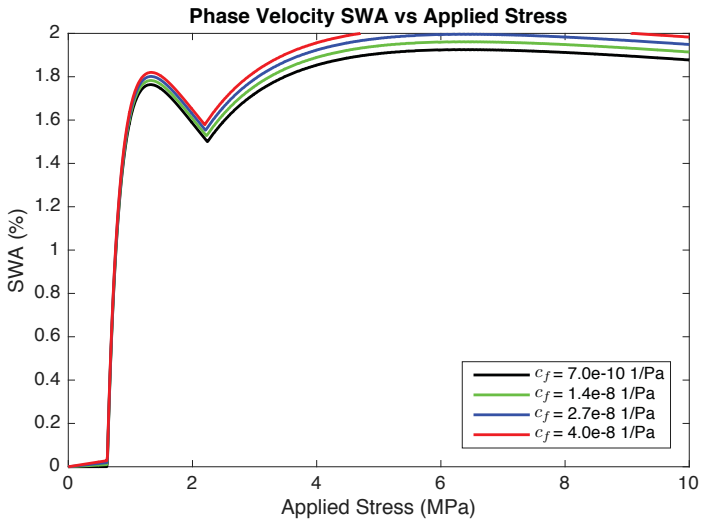

Figure 5.16: Phase velocity SWA_T versus uniaxial applied stress for various values of quasi-incompressible pore-fluid compressibility. In other words, for pore-fluids with relatively large compressibility. The range of pore-fluid compressibility is representative of hydrocarbon gases at high pressures (Mavko et al., 2009). The largest compressibility corresponds to pure methane at 20 MPa and 50°C. The smallest compressibility corresponds to a heavy gas at 50 MPa and 50°C.

SWA_T as described for segment (o) at the outer edge of the compressive region and then segments (a) through to (d) as we move closer to the fracture. Hence, starting directly adjacent to the fracture face and moving away from it, initially we would expect to see moderate and approximately constant SWA_T with the maximum S-wave splitting occurring for propagation sub-parallel to the fracture plane. There will be a small increase followed by a small decrease but the magnitude of these changes will be relatively small. With continued separation from the fracture, the SWA_T will increase to a maximum value occurring at a distance where $s_v = 2.7$ and then rapidly decrease to zero SWA_T beyond that point. This somewhat counterintuitive behaviour is the result of two opposing processes. As compressive stress increases cracks begin to close, increasing the degree of preferential crack alignment and this tends to increase SWA_T. However, as a result of cracks closing the crack density decreases and this tends to decrease SWA_T. Also, as seen in Figure 5.1 Panel (D), the APE

model predicts the crack distribution near the fracture face will consist of cracks with normals oriented sub-parallel to the fracture face. As distance from the fracture face increases the crack distribution will move toward and eventually achieve an isotropic configuration. Alternatively, we can describe the region normal to the fracture face in terms of S-wave splitting as a function of propagation direction. Moving from fracture-distal to fracture-proximal, we expect to see S-wave splitting as a function of propagation direction as described for segment (o) at the outer edge of the compressive region and then segments (a) through to (d) as we move closer to the fracture. Hence, starting directly adjacent to the fracture face and moving away from it, initially we would expect to see maximum S-wave splitting occurring for propagation directions sub-parallel to the fracture plane. There is a lower magnitude local maximum occurring close to 50 degrees from the fracture plane. Moving further from the fracture, this local minimum S-wave splitting value reduces in magnitude to approximately zero and all propagation directions sub-perpendicular to the fracture face will experience approximately zero S-wave splitting. With increased distance from the fracture, the magnitude of maximum S-wave splitting decreases and is spread out over a range of propagation directions less than 40 degrees from the fracture plane. Moving further from the fracture, maximum S-wave splitting migrates to propagation directions approximately 45 degrees from the fracture plane and gradually decreases to zero magnitude.

5.5 Conclusions

The volume of rock normal to an open hydraulic fracture face experiences increased compressive stress. This change in stress will tend to change the microcrack distribution in the rock. The APE model can be used to predict the changes in crack distribution and the resulting S-wave and P-wave velocity anisotropy. Assuming an initially isotropic crack distribution experiencing a

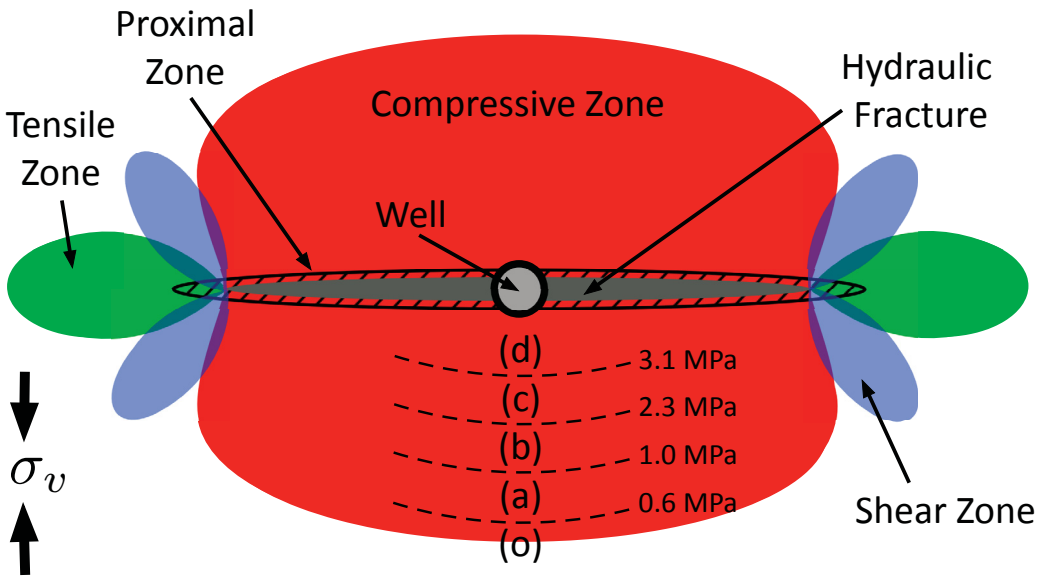

Figure 5.17: A horizontal cross-section through a growing vertical hydraulic fracture extending from a vertical well illustrating the relative size of the four low-frequency zones of confining-stress perturbation in the surrounding region, modified from Cipolla et al. (2011). We assume a very low permeability hence, the proximal zone (the area with black diagonal lines) is restricted to the region immediately adjacent to the facture. The solid blue area indicates the shear zone and the solid green area indicates the tensile zone. We assume the compressive zone (the solid red area) can be approximated as experiencing a uniaxial stress perpendicular to the fracture plane, σ_v. A case example is shown where we assume a maximum confining stress of $3.5 MPa$ adjacent to the fracture face. In the lower compressive zone, the letters in brackets indicate the segment of the SWA_T curve expressed at that point given our default input parameters and the dashed lines are hypothetical isobars of compressive stress. The same pattern is mirrored in the upper compressive zone.

uniaxial compressive stress, we expect S-wave anisotropy to be approximately double the P-wave anisotropy. We find the SWA_T curve as a function of applied stress displays five distinct segments that are characterized by unique S-wave splitting behaviour. Furthermore, the maximum SWA_T occurs at relatively small applied stresses. The sensitivity of SWA_T to various input parameters can be described in two ways; either the amount of applied stress required to reach a particular segment of the SWA_T curve or the absolute value of SWA_T achieved within a particular segment. In regards to the former description,

SWA_T is most sensitive to initial crack aspect ratio and matrix P-wave velocity with slight sensitivity to matrix density and matrix v_p/v_s ratio. As for the latter description, SWA_T is most sensitive to initial crack density with moderate sensitivity to matrix v_p/v_s ratio. Also, SWA_T is not sensitive to the type of saturating pore-fluid, as long as the fluid is an incompressible liquid hydrocarbon or brine. However, if the saturating fluid is a high pressure hydrocarbon gas, the magnitude of SWA_T is only slightly sensitive to the saturating pore-fluid.

Chapter 6

Triaxial Stress: Shear Wave Anisotropy in the Vicinity of a Hydraulic Fracture

6.1 Introduction

In this chapter, we consider the case where a hydraulic fracture treatment is performed in a isotropic rock matrix containing a certain microcrack distribution and experiencing an initially triaxial in-situ stress field. The microcrack distribution is assumed to be isotropic under zero effective-stress conditions resulting in elastic isotropy. However, as discussed in Chapter 5, a triaxial confining-stress field will tend to close some of the microcracks and produce a particular expression of elastic anisotropy in the surrounding rock. As discussed in Chapter 4, the opened fracture creates a large region normal to the fracture face that experiences a compressive confining stress and several smaller regions near the crack tips that experience shearing confining stress and tensile confining stress. Additionally, the region adjacent to the fracture will experience a gradient of pore-pressure increase with the largest increase immediately adjacent to the fracture. In Chapter 3 we showed the effective stress, a combination

of confining stress and pore pressure, controls the behaviour of seismic velocities and Figure 4.10 illustrates the four zones of effective-stress character in the vicinity of a hydraulic fracture as defined in Chapter 4: the proximal zone, compressive zone, shear zone and tensile zone. The effective-stress perturbations caused by the hydraulic fracture treatment superimpose on the in-situ triaxial far-field stress and will alter the particular initial expression of elastic anisotropy in the surrounding rock. In this chapter, we model the heterogeneous elastic anisotropy resulting from triaxial effective-stress perturbations in the vicinity of a hydraulic fracture in a normal faulting regime.

6.2 Theory

The uniaxial stress model, as described by Roche and Van der Baan (2017), can be used to determine a reasonable value for the minimum horizontal in-situ stress in a normal faulting regime. Using this model, the minimum horizontal stress is given by

$$\sigma_h = \frac{\nu_\circ(\sigma_v - \alpha P_{pore})}{(1-\nu_\circ)} + \alpha P_{pore}, \tag{6.1}$$

where σ_h is the minimum horizontal stress, σ_v is the vertical stress, $\nu_\circ$ is Poisson's ratio of the fluid-saturated porous rock, α is Biot's effective-stress coefficient and P_{pore} is the hydrostatic pore pressure. By convention, we assign a compressive stress and pore pressure as positive values.

The condition for hydraulic fracture propagation is given by the following:

$$\sigma_h - \alpha P_{inject} \geq \frac{K_f\sqrt{\pi}}{2\sqrt{f_\circ}} \tag{6.2}$$

where P_{inject} is injection pressure in the fracture, K_f is the fracture toughness, $f_\circ$ is the initial radius of the fracture (Fischer-Cripps, 2007). The fracture is a low aspect ratio spheroid such that the dimensions are given by $f_\circ \gg f_w$, where f_w is the fracture half-width. Taking a closer look at equation 6.2, the

left hand side of the equation represents the effective pressure acting in the direction normal to the fracture plane and the right hand side of the equation is the geometry-scaled fracture toughness.

As discussed in Chapter 5 the Anisotropic Poroelasticity (APE) model developed by Crampin and Zatsepin (1997) and Zatsepin and Crampin (1997) provides a link between confining stress, pore pressure and elastic anisotropy. The general concept of this model can be expressed as follows:

$$\boldsymbol{C^E} = \boldsymbol{C^R} + \boldsymbol{C^D} + \boldsymbol{C^G}, \tag{6.3}$$

where $\boldsymbol{C^E}$ are the elasticity coefficients of a stressed rock containing a particular microcrack distribution, $\boldsymbol{C^R}$ are the effective elastic coefficients of the fluid-saturated porous rock matrix and $\boldsymbol{C^D}$ and $\boldsymbol{C^G}$ are respectively the perturbations to the elasticity coefficients due to a distribution of microcracks and the geometries of these microcracks. A triaxial confining stress can result in an anisotropic crack distribution which will produce an anisotropic medium, $\boldsymbol{C^E}$. The size of these microcracks are on the order of the width of a human hair and will herein be referred to simply as cracks. In Chapter 5 we applied the APE model in only the compressive zone for the approximated case of uniaxial stress in an effectively zero-permeability reservoir, allowing us to ignore pore-pressure diffusion, and this enabled a relatively simple implementation of the APE model. However, the implementation of the APE model for the triaxial stress case is more complicated requiring the use of numerical methods of non-linear optimization to solve a system of equations. A full description of this system of equations is beyond the scope of this thesis but can be found in Section 5 of Zatsepin and Crampin (1997), specifically equations 5.19 and 5.20.

We wish to model realistic properties commonly observed in tight gas reservoirs targeted for hydraulic fracturing, meaning reservoir permeabilities in the range of $0.001\,mD$ to $1\,mD$ and porosities in the range of 5% to 10%. Zatsepin and Crampin (1997) note under these conditions individual cracks are able to

communicate fluid via the macropore system and, therefore, are no longer fluid isolated. A fluid isolated crack system is a core condition for the validity of the APE model. However, Zatsepin and Crampin (1997) postulate that the APE model can be used a first order approximation of the stress dependent elastic reservoir properties by assuming the crack pore-fluid pressure, p_f, is known and equal to the macropore fluid pressure. The limits of integration for the fluid-filled crack distribution in equation 5.1 are then given by

$$\gamma = 1 + p - s_h - s_H \sin\psi^2 \sin\theta^2 - s_v \cos\psi^2 \,, \tag{6.4}$$

where γ is crack aspect ratio, p is dimensionless excess pore-fluid pressure given by equation 5.11, (s_h, s_H, s_v) are components of dimensionless differential stress given by equation 5.12, (ψ, θ) are angles of inclination and azimuth in spherical coordinates and open crack-normal orientations are given by $\gamma > 0$.

Pore-pressure diffusion around the hydraulic fracture can be modelled using the method of Shapiro et al. (2002) and the confining-stress perturbation due to the opening of a hydraulic fracture can be calculated analytically using Eshelby (1957)'s equivalent inclusion method as outlined in Chapter 4.

6.3 Method

The general workflow for modelling the evolution of S-wave velocity anisotropy (*SWA*) in the volume of rock around a hydraulic fracture is outlined in Figure 6.1. Each step in this workflow will be described in detail in each of the following subsections. The *SWA* is calculated as the difference between the fast and the slow S-wave velocity scaled by the fast S-wave velocity, expressed as a percentage. It is important to note, in the previous chapter SWA_T refers to the scaled percent difference between the maximum fast S-wave and the minimum slow S-wave velocities over all propagation directions in a transversely isotropic medium; whereas, in this chapter *SWA* is the scaled percent difference between

the fast and slow S-wave velocities for a single propagation direction in any non-isotropic media.

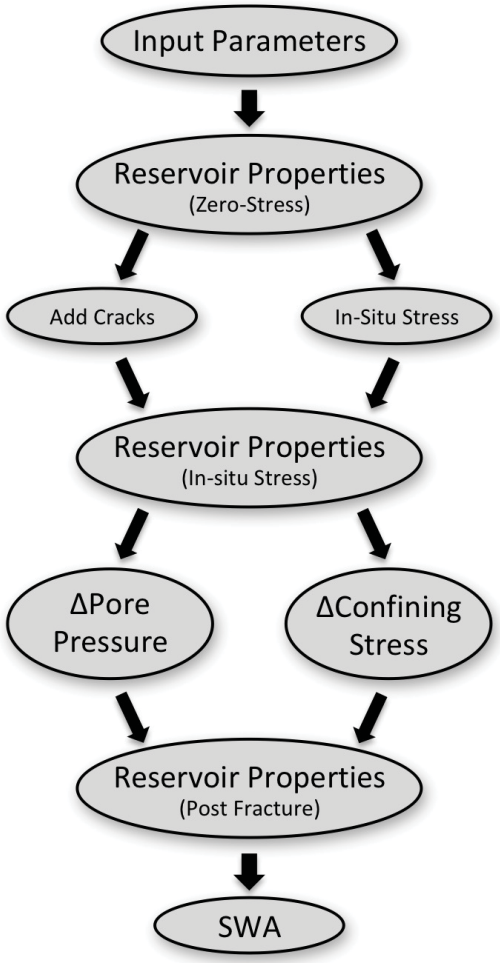

Figure 6.1: The main steps involved in modelling S-wave velocity anisotropy in the vicinity of a hydraulic fracture.

6.3.1 Input Parameters

In order to model the seismic velocity field in the vicinity of a hydraulic fracture we require several input parameters. The required input parameters fall into several categories as follows:

1. Reservoir properties

2. In-situ confining-stress field

3. Initial crack properties

4. Injection pressure and duration

5. Modelling accuracy and duration

6. Hydraulic fracture properties

Several reservoir input properties are required including depth, porosity, permeability, initial pore pressure, pore-saturating fluid and rock matrix mineral composition. We assume a normal pore-pressure gradient and obtain the initial pore pressure using an average water column density of $1000\,kg/m^3$ and an acceleration due to gravity of $9.81\,m/s^2$. The pore-saturating fluid can be a brine, a hydrocarbon oil, a hydrocarbon gas or a mixture of the three where the properties for each type of fluid are defined separately. Brines are defined by salinity, gases are defined by gas gravity and oils are defined by API, GOR and gas gravity. We assume a temperature gradient of $25^oC/km$. In addition, pore-fluid viscosity, η, is defined independently of the preceding fluid properties.

For the in-situ confining-stress field, we assume a normal faulting regime and define a triaxial confining stress at the target reservoir depth. The maximum principle stress, σ_v, is in the vertical direction and is obtained using an average overburden density of $2400\,kg/m^3$ and an acceleration due to gravity of $9.81\,m/s^2$. The minimum horizontal stress, σ_h, is calculated later using the uniaxial stress model. The maximum horizontal stress, σ_H, is arbitrarily defined within the range of $\sigma_v \geq \sigma_H \geq \sigma_h$.

For the initial crack properties, we assume an initially isotropic distribution of cracks with a defined aspect ratio and normalized distribution density. The crack distribution is assumed to be filled with the same fluid as the macropore system. Additionally, the individual cracks are assumed to be low aspect ratio spheroidal cracks, such that the crack dimensions are $(a = b \gg c)$.

The injection pressure, P_{inject}, is the pressure maintained in the hydraulic fracture and is arbitrarily defined. The injection duration, t_{inject}, is the length of time the hydraulic fracture treatment and is arbitrarily defined such that $t_{inject} > 0\,min$.

The modelling duration, t_{model}, is the length of time that we calculate pore-pressure diffusion, confining-stress change and the resulting velocity field. The duration can be set to continue model calculations beyond the hydraulic fracture treatment. The modelling accuracy is determined to a large extent by three interval parameters set to obtain a reasonable compromise between sampling density and computation times. The first and second parameters are used to determine the coarseness of a grid search over all orientation directions to find the crack distribution after a triaxial confining stress is applied. The first parameter, int_1, defines the search interval for inclination of orientation and the second parameter, int_2, defines the interval for azimuth of orientation. The third parameter, int_3, gives the interval of inclination and azimuth used to calculate S-wave velocities in a particular propagation direction when creating upper hemisphere plots of *SWA*, as seen in Figure 6.4.

In order to understand the evolution of *SWA* around a hydraulic fracture we perform the workflow described below for four different initial in-situ stress scenarios at two different reservoir depths. The first depth is $2\,km$ and the second depth is $1\,km$ below surface level. The four initial in-situ stress scenarios are chosen such that the ratio of maximum horizontal stress to minimum horizontal stress, σ_H/σ_h, is equal to 1, 1.3, 1.6 and 1.9 respectively. The injection pressure is set to be $3\,MPa$ larger than the minimum horizontal stress. Both the total injection time and the model calculation time are run for 20 hours. The model accuracy parameters are set to the following in radians: $int1 = \pi/700$, $int2 = \pi/500$ and $int3 = \pi/90$. All other input parameters are held constant and can be seen in Table 6.1. The mineral composition of the sandstone matrix is 70 % quartz and 30 % calcite. The hydraulic fracture in-

Table 6.1: Triaxial APE model input parameters.

Porosity, ϕ	$5\,\%$
Permeability, κ	$0.1\,mD$
Pore Fluid	$5\,\%$ salinity brine
Fluid Viscosity, η	$0.00019\,Pa{\cdot}s$
Matrix Composition	Sandstone
Initial Crack Aspect Ratio, $g_\circ$	0.0001
Initial Normalized Crack Density, $\epsilon_\circ$	0.14
Initial Fracture Radius, $f_\circ$	$2\,m$
Maximum Fracture Radius	$100\,m$
Fracture Width, f_w	$0.01\,m$
Fracture Toughness, K_f	$2\,MPa{\cdot}\sqrt{m}$
Fracture Propagation Velocity, v_{frac}	$0.003\,m/s$

puts are set to reasonable values for a hydraulic fracture in a sandstone and include fracture propagation velocity, v_{frac}, initial fracture size, $f_\circ$, maximum fracture size, fracture width, f_w, and fracture toughness, K_f. If condition 6.2 is satisfied, the fracture initiates growth from the defined initial fracture size at $t{=}0min$ and continues to grow at a constant propagation velocity until the maximum defined fracture radius is reached. At this point, fracture growth stops irrespective of condition 6.2. We assume the hydraulic fracture grows as a spheroidal fracture in the vertical plane perpendicular to the direction of minimum horizontal stress with the defined propagation velocity and maintains a constant fracture width. The assumption of a constant fracture width, although not realistic, simplifies the confining-stress perturbation calculations. In reality, we would expect the fracture aspect ratio to remain more-or-less constant. We justify using the constant fracture width assumption by recalling the observation made in Chapter 4 that the magnitude of stress perturbations in the vicinity of the fracture are not affected significantly by realistic variations

of hydraulic fracture width, i.e. on the order of $10\,cm$.

6.3.2 Elastic Properties for Zero Effective Stress

We first obtain approximate rock properties for the reservoir by assuming an isotropic rock experiencing a lithostatic stress at the reservoir depth. The reservoir rock has all of the previously defined properties with the lithostatic stress equal to the vertical confining stress. However, at this point we have not included the crack distribution. We then obtain the isotropic, stress-sensitive, effective elastic properties, $\boldsymbol{C^r}$, for the fluid-saturated porous reservoir rock using the process outlined in Figure 6.2. The full details of this process are described in Chapter 3. Next, we simulate moving the reservoir rock to a shallow depth. In our case we choose $200\,m$, but this is an arbitrary choice. At this shallow depth we assume a zero effective-stress state with pore pressure equal to the calculated lithostatic stress at $200\,m$ depth. The APE model requires the crack distribution to initially exist in a state of zero effective stress. The isotropic, stress-sensitive, effective elastic properties, $\boldsymbol{C^s}$, of the shallow reservoir rock are now obtained using the same process as before but with the new lithostatic stress and pore pressure at $200\,m$ depth, see Figure 6.2. We lower the gas-oil ratio to account for degassing at lower pore pressure.

6.3.3 Elastic Properties at Hydraulic Fracture Depth

The next step is to simulate moving the shallow reservoir back to the actual reservoir depth. First, the uniaxial stress model is used to determine the minimum horizontal stress, σ_h. We use the elastic moduli of the reservoir under lithostatic conditions at the target depth, $\boldsymbol{C^r}$, and assume a Biot's effective-stress coefficient of one in equation 6.1. Now we have the triaxial in-situ confining-stress state at the reservoir level before the hydraulic fracture treatment is initiated, $(\sigma_v, \sigma_H, \sigma_h)$, and the initial hydrostatic pore pressure due

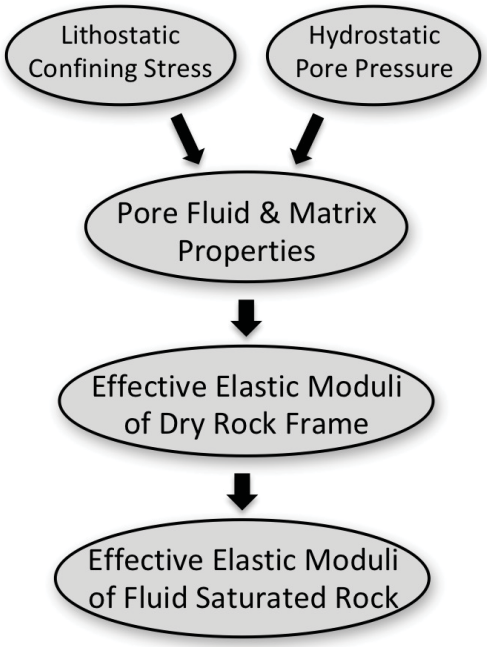

Figure 6.2: The main steps involved in modelling stress-sensitive elastic moduli of an isotropic porous medium. Chapter 3 provides a comprehensive description of each step. In brief, the fluid properties are calculated using the Batzle-Wang equations and Reuss averaging and the matrix properties are calculated using Hashin-Strikman-Walpole averaging. The dry rock frame effective elastic moduli are obtained using the Hertz-Mindlin model and the Stiff-Sand model. The effective elastic moduli and the density of the fluid saturated rock are calculated with the Gassmann equations.

to the water column, P_{pore}. The APE model, equations 5.1 , 5.2 , 5.4 and 5.7 to 5.10, is then used to determine the initial state of elastic anisotropy present, $\boldsymbol{C^E}$, after the in-situ triaxial confining stress is applied at the actual reservoir depth. The limits of intergration in equation 5.1 are given by equation 6.4 and the value of Λ_{ijkl} in equations 5.9 and 5.10 is obtained using the Hudson Model as outlined in Chapter 5 with equations 5.23 to 5.31. Finally, the elasticity perturbations due to the open crack distribution are added to the elasticity coefficients of the uncracked, zero-stress state reservoir, that is $\boldsymbol{C^R} = \boldsymbol{C^s}$ in equation 5.1.

It is necessary to comment on our use of $\boldsymbol{C^s}$. To be more realistic we should have instead used the initial uncracked reservoir rock under lithostatic

conditions, $\boldsymbol{C^r}$. The problem with using $\boldsymbol{C^s}$ is the perturbations due to a crack distribution, $\boldsymbol{C^D} + \boldsymbol{C^G}$ in equation 6.3, are only strictly compatible with $\boldsymbol{C^r}$ because $\boldsymbol{C^D} + \boldsymbol{C^G}$ depends on the reservoir elasticity coefficients. In general, the elasticity coefficients are larger at greater depth, so the coefficients due to a crack distribution would be slightly different using $\boldsymbol{C^r}$. However, the APE model requires a zero-stress state as a starting point, and this is unrealistic at the reservoir depth. Hence, we should not determine $\boldsymbol{C^D} + \boldsymbol{C^G}$ from the elasticity coefficients of the uncracked reservoir at depth, $\boldsymbol{C^r}$. In practice, for low porosities the difference between $\boldsymbol{C^r}$ and $\boldsymbol{C^s}$ is small, so we can justify using $\boldsymbol{C^s}$ as a reasonably good approximation.

6.3.4 Elastic Properties after Pore-Pressure Diffusion and Confining-Stress Change

Pore-pressure diffusion and confining-stress change are calculated at a uniform grid of nodal points as outlined in Chapter 4, specifically see section 4.3 for the method of implementation. We use the input values for fluid shear modulus, fluid velocity and the fracture properties seen in Table 4.1 and the grid, sampling and reservoir properties seen in Table 4.2. To find the stress field in the vicinity of the hydraulic fracture, we add the sum of the pore-pressure perturbations and the confining-stress perturbations to the initial in-situ triaxial stress field. We have now evolved from a homogeneous anisotropic stress field into an heterogeneous, anisotropic stress field. The APE model is then used as outlined in the previous subsection to calculate the resulting elasticity coefficients at all grid nodes in the vicinity of the hydraulic fracture.

6.3.5 S-Wave Velocity Anisotropy

The SWA_{vert} is SWA for propagation in the vertical direction and is calculated at all grid nodes. Additionally, to gain a deeper understanding of the anisotropy

behaviour, we observe the *SWA* for all possible propagation directions at two spatially fixed points: the compressive zone point (CZP) and the tensile zone point (TZP). These are the same two spatial points discussed in Chapter 4. Recall, the first point is located $40\,m$ perpendicular to the centre of the hydraulic fracture and the second point is located in the plane of the hydraulic fracture and $120\,m$ from the centre of the fracture. In general, as the hydraulic fracture grows, the CZP experiences increased confining stress and pore pressure and the TZP experiences confining-stress decrease with pore-pressure increase. The reader is directed to Chapter 4 for a more detailed discussion regarding the evolution of pore pressure, confining stress and effective stress at the CZP and TZP with Table 4.3 providing a useful summary. The fast and slow S-wave velocities and their polarization directions are calculated using the classic Christoffel equations (Slawinski, 2015).

6.4 Results

For each case, we present the modelling results for times $t=0\,min$ to $1200\,min$ at time steps of $240\,min$. The modelling results include the initial crack distribution, the initial *SWA*, the evolution of SWA_{vert} at all points around the hydraulic fracture and the evolution of *SWA* for all propagation directions at the CZP and TZP. Propagation directions are described in terms of degrees inclination measured from vertical and degrees azimuth measured clockwise from the direction of σ_h (i.e. perpendicular to the fracture face).

6.4.1 $2\,km$ Depth Reservoir

In each of the following sub-subsections, we present the modelling results for the four in-situ confining-stress cases (σ_H/σ_h of 1, 1.3, 1.6 and 1.9 respectively for Cases 1 to 4) at $2\,km$ depth.

2 km **Depth - Case 1:** σ_H/σ_h=1

The in-situ confining-stress field is given by σ_V=47 MPa, σ_H=25 MPa and σ_h= 25 MPa. It is important to note that in this case where σ_H=σ_h there would be no preferential orientation for the hydraulic fracture to open. We modelled this situation for comparison even though the formation of simple planar hydraulic fracture is not realistic to expect. As seen in panel (A) of Figure 6.3, the resulting initial crack distribution consists of azimuthally isotropic, sub-vertical crack sets. Figure 6.4 shows that this crack distribution produces a transversely isotropic medium with a vertical axis of symmetry. There is 0 % *SWA* in the vertical direction and a maximum $SWA_{max} \approx 1.7$ % at inclination $\approx 50°$ and all azimuths.

The evolution of *SWA* at the CZP and TZP are not shown because the changes are very subtle. At the CZP, a slight deviation from TI symmetry gives an orthotropic *SWA* symmetry immediately. However, the change in *SWA* pattern is very small with the inclination and magnitude of the SWA_{max} being relatively unchanged. At the TZP, the same trend is seen but the changes are almost imperceptible.

The SWA_{vert} is not shown because there are only very low magnitude increases, less than $\pm$0.5%, seen for all time steps. The compressive zone and shear zone experience a very small SWA_{vert} increase. There is no SWA_{vert} change observed in the part of the compressive zone directly adjacent to the fracture, the tensile zone, and the zone of transition between the compressive zone and shear zone.

2 km **Depth - Case 2:** σ_H/σ_h=1.3

The in-situ confining-stress field is given by σ_V=47 MPa, σ_H=32 MPa and σ_h= 25 MPa. Panel (B) of Figure 6.3 shows the resulting initial crack distribution consists of sub-vertical crack sets that are sub-parallel to the hydraulic fracture face and panel (A) of Figure 6.5 shows this distribution produces an orthotropic

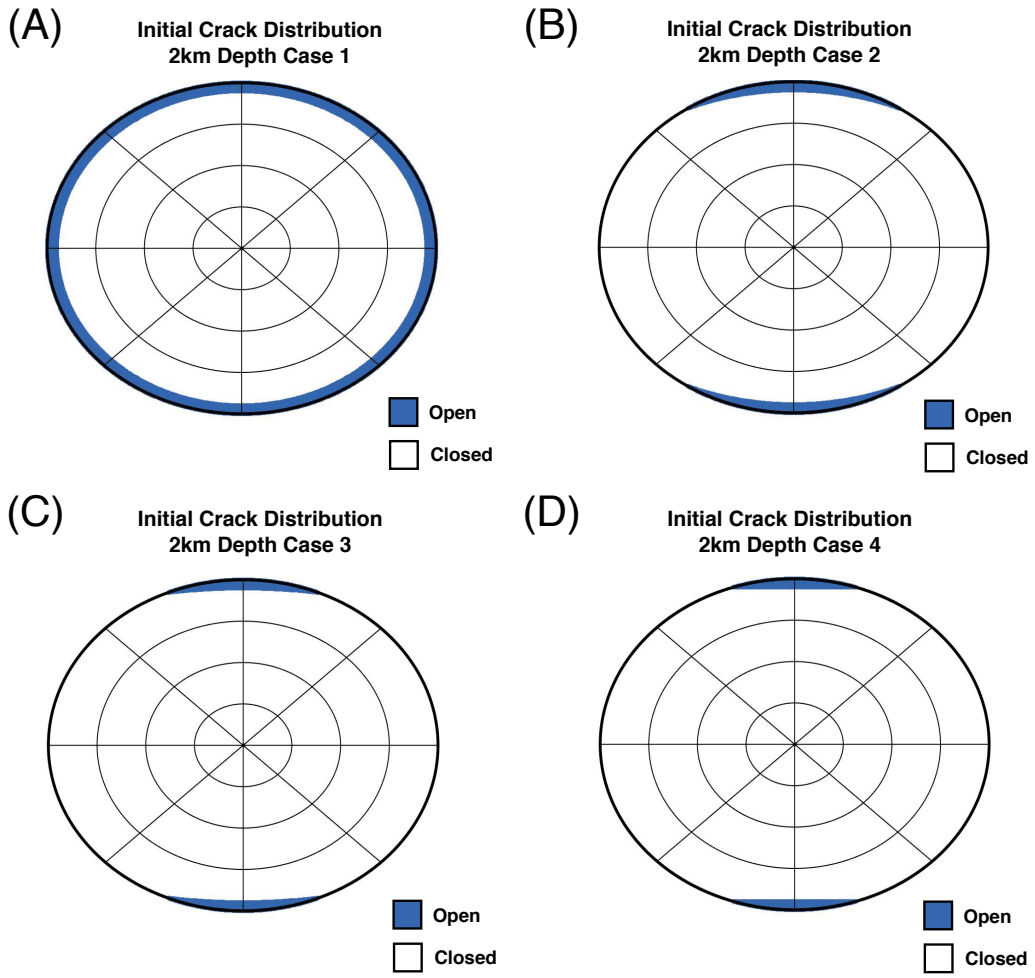

Figure 6.3: This figure shows four upper hemisphere projections illustrating the initial crack distribution of the four in-situ stress conditions at $2\,km$ depth where panels (A) through (D) respectively show Cases 1 through 4. See Figure 5.2 for a description of upper hemisphere projection. The projections show open crack normal orientations with blue and closed crack normal orientations with white. The centre of the plot indicates a vertical crack normal orientation and the concentric circles indicate degrees inclination measured from vertical. Horizontal crack normal orientation occurs at inclinations of 90° and plots on the outer most circle. The azimuth of crack normal orientation is given by the position on a circle measured clockwise from 12 o'clock which corresponds to 0°. For reference, σ_V plots in the centre of the projection, σ_H plots on the outer circle at 12 and 6 o'clock and σ_h plots on the outer circle at 3 and 9 o'clock.

medium with $SWA_{max} = 3.2\%$ in the vertical direction. There is a band of high SWA at all inclinations with azimuths approximately parallel to the fracture face and SWA is small or zero for propagation directions within 65° of σ_h.

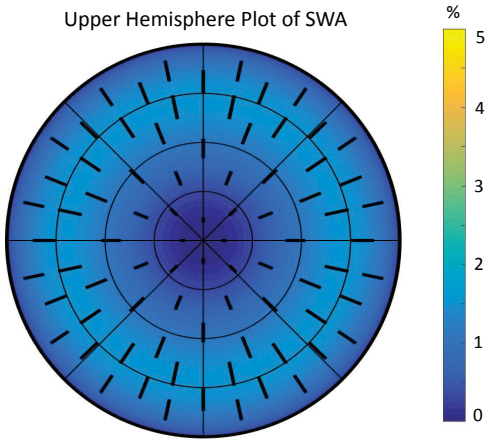

Figure 6.4: $2\,km$ Depth - Case 1: The initial *SWA* pattern displayed as an upper hemisphere projection. See Figure 5.2 for a description of upper hemisphere projection. The centre of the plot indicates a vertical propagation direction and the concentric circles indicate degrees inclination measured from vertical. Horizontal propagation occurs at inclinations of 90° and plots on the outer most circle. The azimuth of propagation is given by the position on a circle measured clockwise from 12 o'clock which corresponds to 0°. The colour indicates the magnitude of *SWA* and the short bold lines indicate the polarization orientation of the fast S-wave. For reference, σ_V plots in the centre of the projection, σ_H plots on the outer circle at 12 and 6 o'clock and σ_h plots on the outer circle at 3 and 9 o'clock.

Figure 6.5 and 6.6 show the evolution of *SWA* at the CZP and TZP respectively. At the CZP, the pattern of *SWA* remains relatively unchanged. However, the band of high *SWA* initially decreases by approximately 0.5% followed by a return to the initial values and then decreases again by less than 0.5%. At the TZP, the pattern of *SWA* initially remains relatively unchanged. When the fracture tip and the proximal zone approach, the band of high *SWA* is successively reduced until all propagation directions have less than 1.6% *SWA*.

As seen in Figure 6.7, SWA_{vert} shows distinct character in the compressive zone, shear zone, tensile zone and a fourth zone adjacent to the fracture. Herein referred to as the proximal zone, this fourth zone corresponds to the effective-stress proximal zone discussed in Chapter 4. The proximal zone extends a variable distance away from the fracture and is defined as the region where the

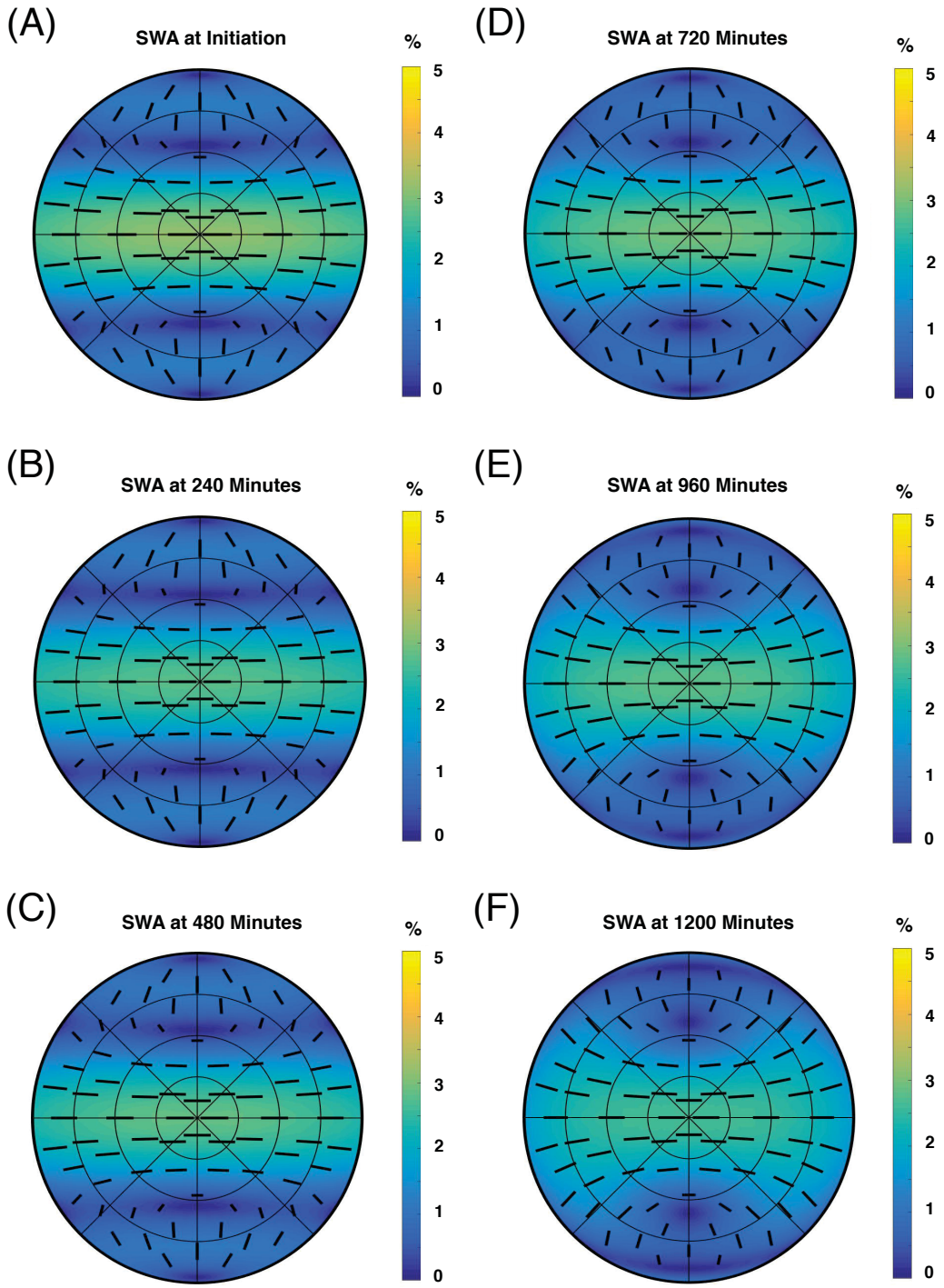

Figure 6.5: $2\,km$ Depth - Case 2: Upper hemisphere projections of the *SWA* at $t=0$ to $1200\,min$ at time steps of $240\,min$ modelled at the CZP. See Figure 5.2 for a description of upper hemisphere projection.

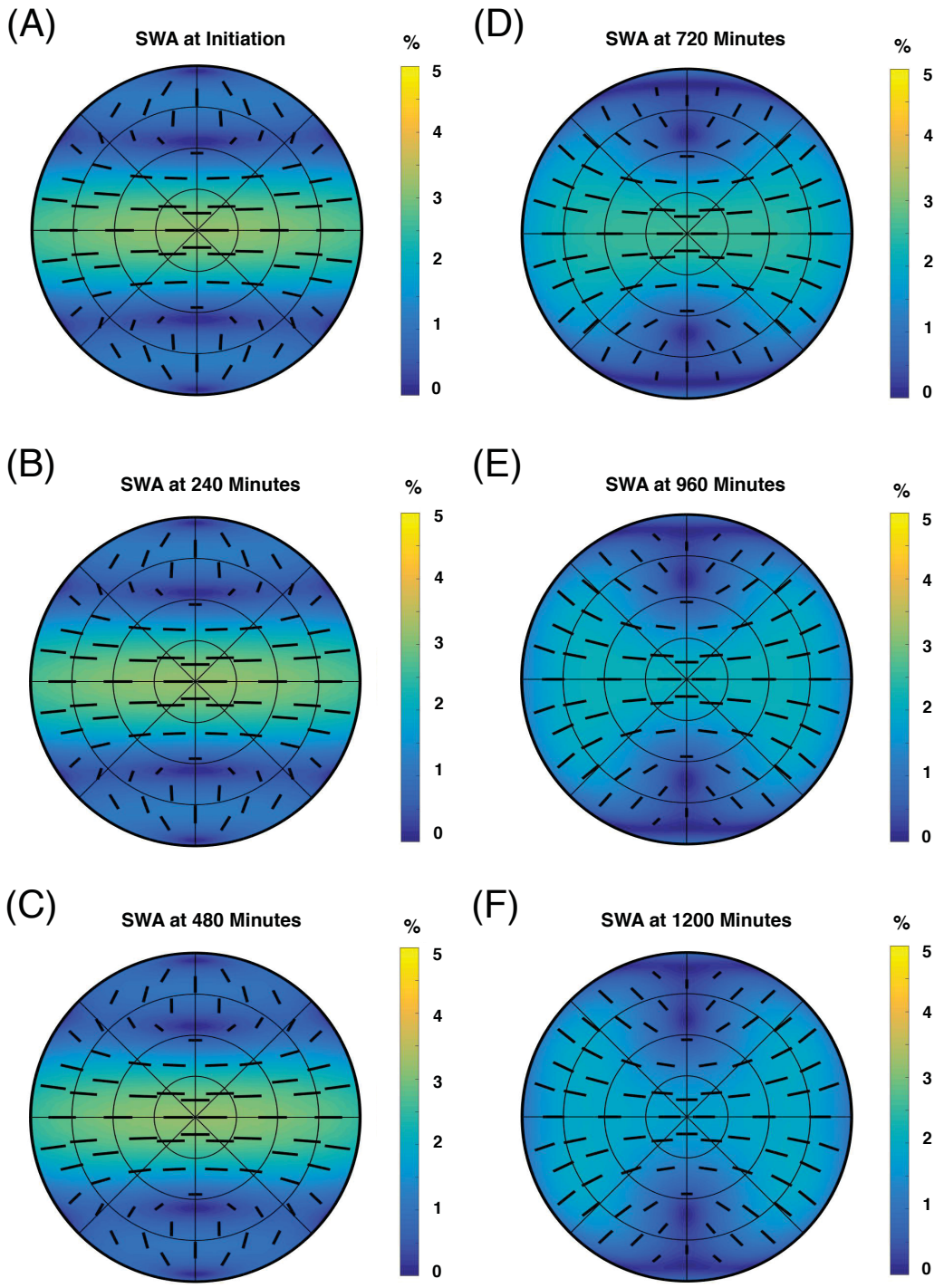

Figure 6.6: $2\,km$ Depth - Case 2: Upper hemisphere projections of the *SWA* at $t=0$ to $1200\,min$ at time steps of $240\,min$ modelled at the TZP. See Figure 5.2 for a description of upper hemisphere projection.

mean effective stress decreases significantly. The transition from the proximal zone to any of the other three zones is characterized by a pore-pressure gradient that is significantly steeper than the confining-stress gradient. Figure 6.7 shows in Case 2 at 2 km depth, the proximal zone experiences a large decrease in SWA_{vert} of up to 3.2%. The proximal zone expands in size with each time step reaching a maximum distance of 25 m from the fracture tips. The transition between the proximal zone and the other three zones experiences very little to zero change in SWA_{vert}. The compressive zone experiences a small decrease in SWA_{vert} of less than 0.5% with a local minimum value occurring perpendicular to the centre of the fracture and close to the proximal-compressive zone transition. The compressive zone expands in size as long as the fracture is growing. When the fracture reaches the maximum radius, the compressive zone starts to shrink in size as the continually expanding proximal zone encroaches on it. Also, the local minimum value becomes more pronounced with each time step as the fracture grows, but becomes less pronounced with each time step at which the fracture size is constant. The shear zone and tensile zone beyond the proximal zone experience a small increase in SWA_{vert} of less than 0.5%.

2 km Depth - Case 3: σ_H/σ_h=1.6

The in-situ confining-stress field is given by σ_V=47 MPa, σ_H=40 MPa and σ_h= 25 MPa. Panel (C) of Figure 6.3 shows the resulting initial crack distribution is very similar to that seen in Case 2 at 2 km depth, and consists of sub-vertical crack sets that are sub-parallel to the hydraulic fracture face. As seen in panel (A) of Figure 6.8, this distribution produces an orthotropic medium with SWA_{max} = 3.5% in the vertical direction. There is a band of high SWA at all inclinations with azimuths approximately parallel to the fracture face. SWA is small or zero for propagation directions within 65° of σ_h.

Figures 6.8 and 6.9 show the evolution of SWA at the CZP and TZP respectively. At the CZP and TZP, the patterns of SWA remain relatively unchanged.

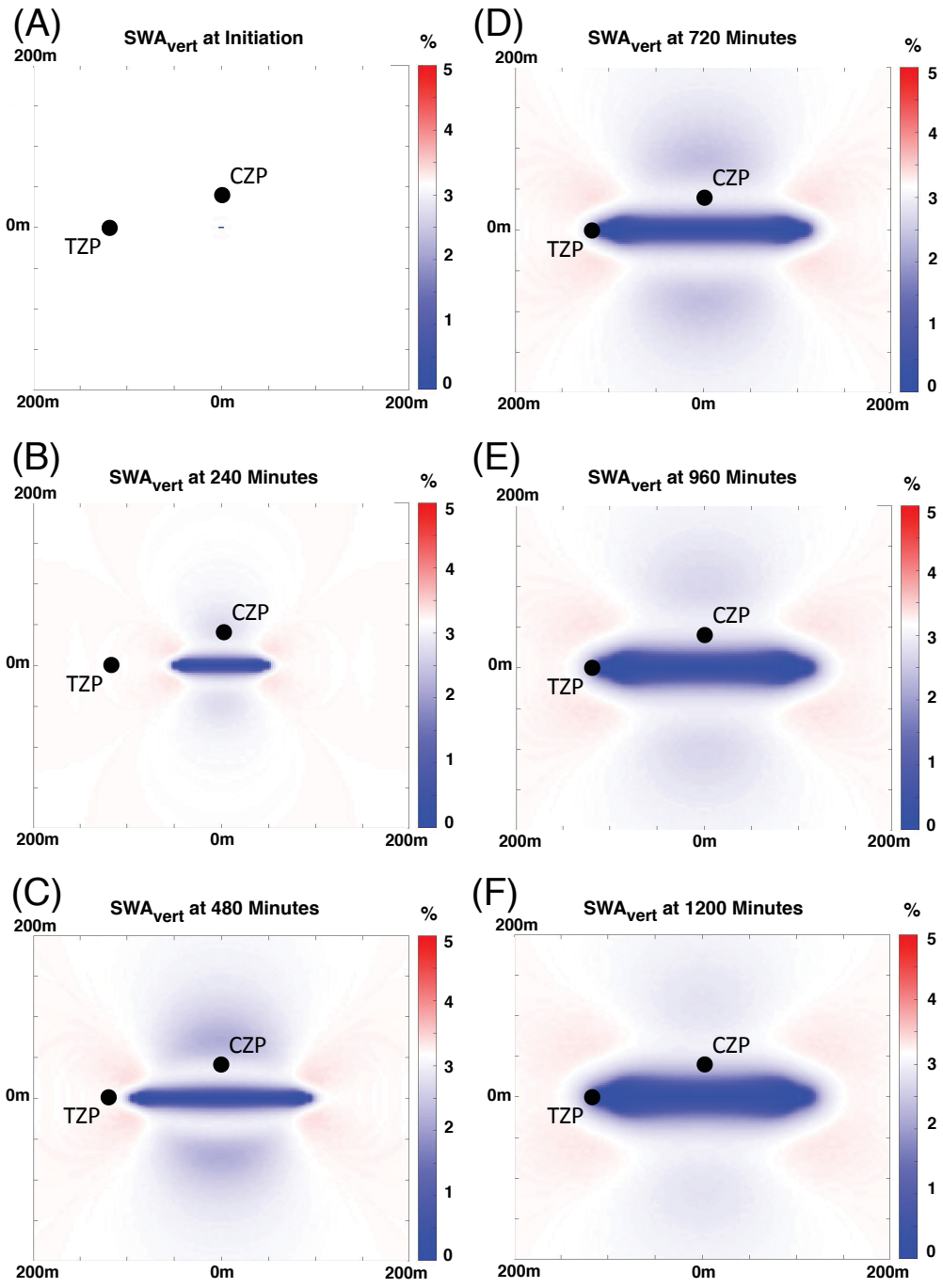

Figure 6.7: $2\,km$ Depth - Case 2: The SWA_{vert} at $t = 0$ to $1200\,min$ at time steps of $240\,min$. In this figure and all similar figures to follow, the colour scale is set such that the initial SWA_{vert} is white. Increases in SWA_{vert} are indicated by shades of red and decreases in SWA_{vert} are indicated by shades of blue.

At the CZP, the band of high *SWA* initially decreases by approximately 0.5% and then gradually increases to reach a final value of 4%. At the TZP, the band of high *SWA* initially remains relatively unchanged. When the fracture tip and the outer proximal zone approach, the band of high *SWA* is increased to 4% and then as the transition to the inner proximal zone approaches the *SWA* magnitudes return to the initial values.

As seen in Figure 6.10, the SWA_{vert} shows distinct character in the compressive zone, shear zone, tensile zone and proximal zone. In this case, the proximal zone displays a dual character with inner and outer regions. The inner proximal zone experiences no change in SWA_{vert} adjacent to the fracture face and experiences a decrease of up to 3.5% adjacent to the fracture tips. The outer proximal zone experiences an increase in SWA_{vert} of up to 1%. The proximal zone expands in size with each time step reaching a maximum distance of $75\,m$ from the fracture tips. The transition from the inner and outer proximal zone experiences very little to zero change in SWA_{vert}. Beyond the proximal zone, the compressive zone experiences a small decrease in SWA_{vert} of less than 0.5% with a local minimum value occurring perpendicular to the centre of the fracture and close to the proximal-compressive zone transition. The compressive zone expands in size as long as the fracture is growing. When the fracture reaches the maximum radius, the compressive zone shrinks in size as the continually expanding proximal zone encroaches on it. Also, the local minimum value in the compressive zone becomes more pronounced with each time step as the fracture grows, but this local minimum becomes less pronounced with each time step after the fracture has reached its maximum size. The shear zone and tensile zone beyond the proximal zone experience a small increase in SWA_{vert} of less than 0.5%.

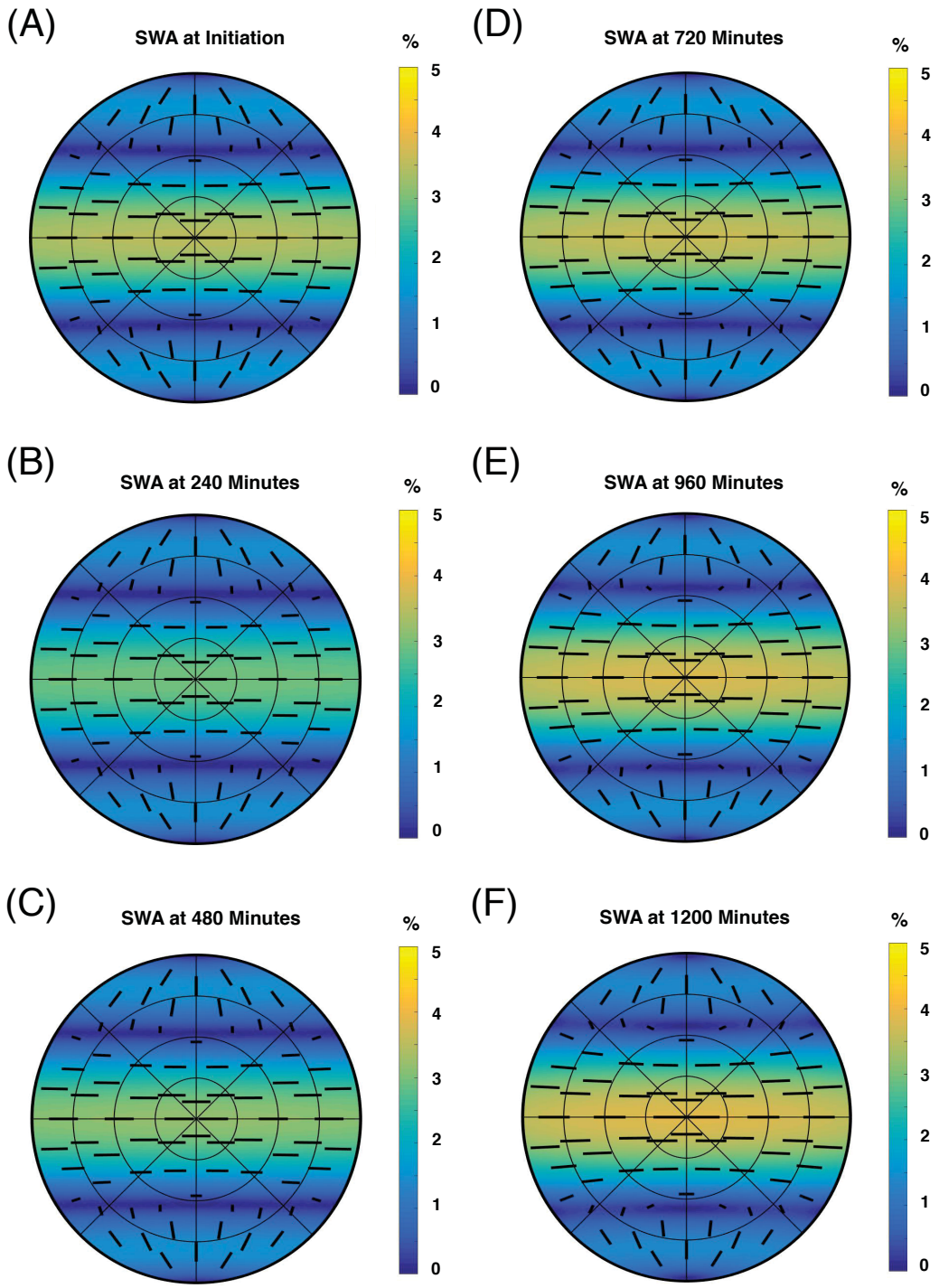

Figure 6.8: $2\,km$ Depth - Case 3: A upper hemisphere projection of the *SWA* at $t=0$ to $1200\,min$ at time steps of $240\,min$ modelled at the CZP. See Figure 5.2 for a description of upper hemisphere projection.

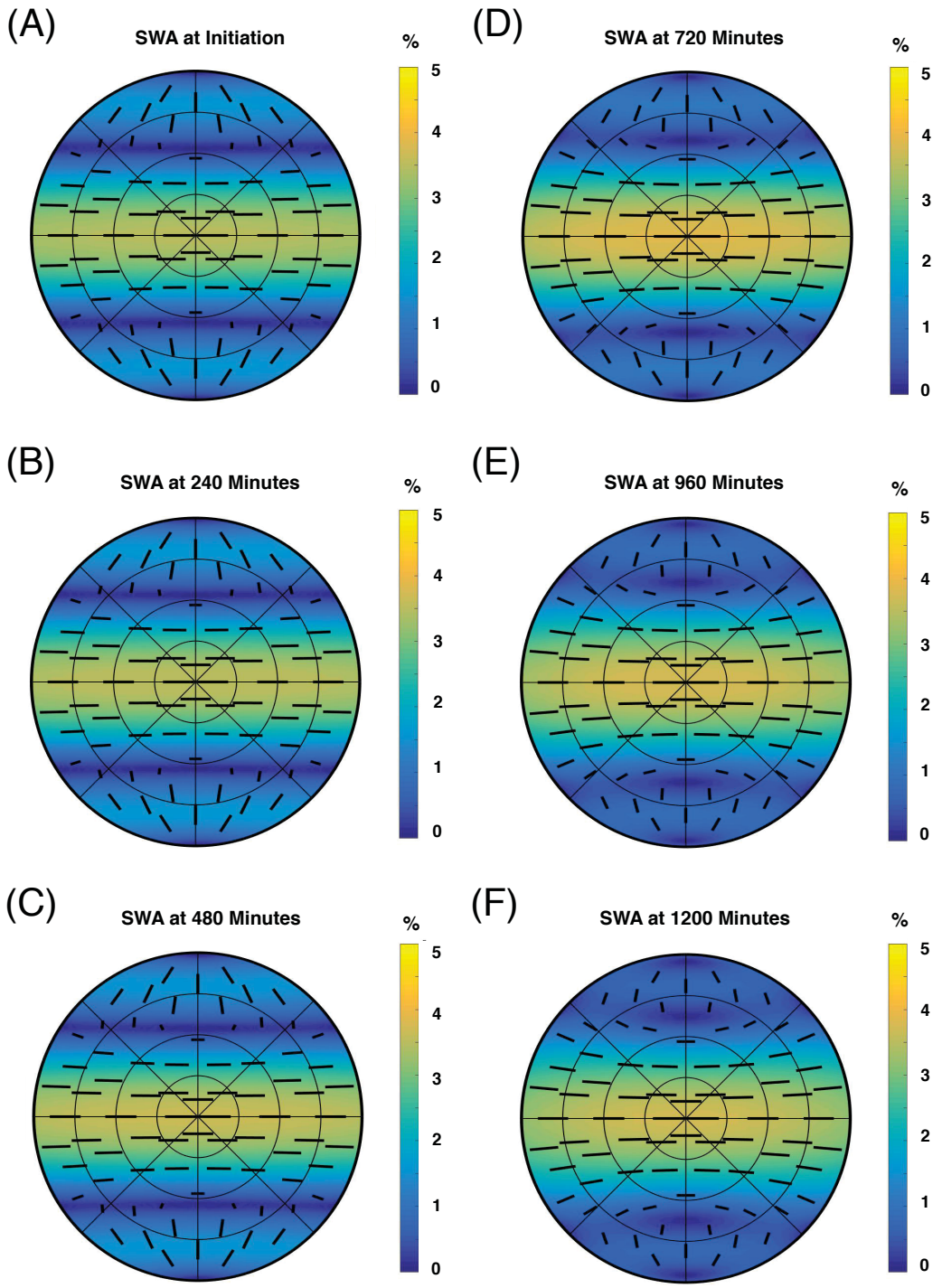

Figure 6.9: $2\,km$ Depth - Case 3: A upper hemisphere projection of the *SWA* at $t=0$ to $1200\,min$ at time steps of $240\,min$ modelled at the TZP. See Figure 5.2 for a description of upper hemisphere projection.

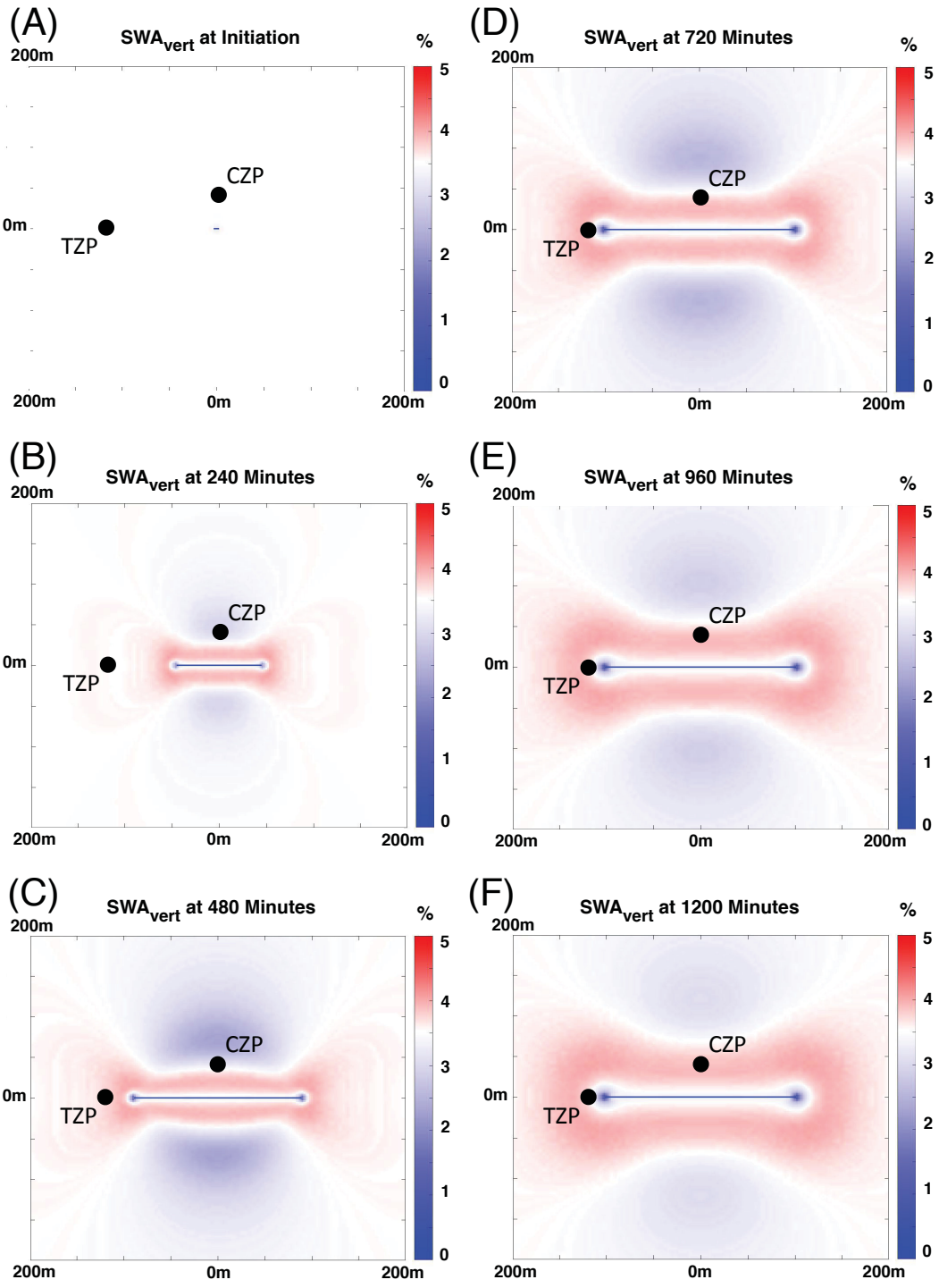

Figure 6.10: 2 km Depth - Case 3: The SWA_{vert} at $t = 0$ to 1200 min at time steps of 240 min.

2 km Depth - Case 4: σ_H/σ_h=1.9

The in-situ confining-stress field is given by σ_V=47 MPa, σ_H=47 MPa and σ_h= 25 MPa. Panel (D) of Figure 6.3 shows the resulting initial crack distribution is very similar to that seen in Case 3 at 2 km depth, and consists of sub-vertical crack sets that are sub-parallel to the hydraulic fracture face. However, this slightly different distribution now produces a transversely isotropic medium with an axis of symmetry parallel to σ_h, see Figure 6.11. There is a band of $SWA_{max} = 3.6\%$ at all inclinations with azimuth normal to the fracture face. SWA is small or zero for propagation directions within 65° of σ_h.

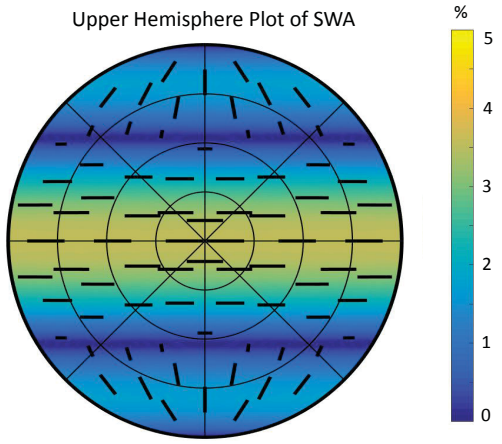

Figure 6.11: 2 km Depth - Case 4: The initial SWA pattern displayed as an upper hemisphere projection. See Figure 5.2 for a description of upper hemisphere projection.

In this case, the SWA_{vert} evolves almost identically to that seen in Figure 6.10 with two important differences. First, the inner proximal zone is not present adjacent to the fracture face and only manifests in a smaller region at the fracture tips. Second, the magnitude of SWA_{vert} expressed in the outer proximal zone is slightly larger at 4.3%. Additionally, the evolution of SWA at the CZP and TZP is very similar to that seen in Figures 6.8 and 6.9. The sole difference at the CZP is that the band of high SWA increases to a larger magnitude of 4.3%. The TZP differs in that the inner proximal zone does not

approach the point as close as seen in Case 3 at $2\,km$ depth, hence the *SWA* decreases by a smaller amount between $t = 720\,min$ and $1200\,min$.

6.4.2 $1\,km$ Depth - Reservoir

In each of the following sub-subsections, we present the modelling results for the four in-situ confining-stress cases at a depth of $1\,km$.

$1\,km$ Depth - Case 1: σ_H/σ_h=1

The in-situ confining-stress field is given by $\sigma_V = 24\,MPa$, $\sigma_H = 12\,MPa$ and $\sigma_h = 12\,MPa$. Again, it is important to note that in this case where $\sigma_H = \sigma_h$ there would be no preferential orientation for the hydraulic fracture to open. We modelled this situation for comparison even though the formation of simple planar hydraulic fracture is not realistic to expect. Panel (A) of Figure 6.12 shows the resulting initial crack distribution consists of azimuthally isotropic, sub-vertical crack sets that produce a transversely isotropic medium with a vertical axis of symmetry. All cracks with crack normal inclination of greater than 50° are open. There is 0 % *SWA* in the vertical direction and a $SWA_{max} \approx$ 1.6 % at all azimuths in the horizontal plane. The initial *SWA* pattern can be seen in panel (A) of Figure 6.13.

The SWA_{vert} is nearly identical to that seen in Case 1 at $2\,km$ depth, except the magnitude of increase is smaller at all time steps. However, Figure 6.13 shows that the evolution of *SWA* at the CZP is significantly different from that seen in Case 1 at $2\,km$ depth. At the CZP, the *SWA* immediately decreases to approximately 0% for all azimuths and inclinations less than 50°. Additionally, in this range of propagation direction, the polarization direction of the fast S-wave rotates by 90°. With each successive time step the range of inclination experiencing this polarization rotation gradually increases reaching a maximum range of less than 60°. The same trend is seen at the TZP but at a slower rate and the maximum inclination range experiencing the polarization rotation is

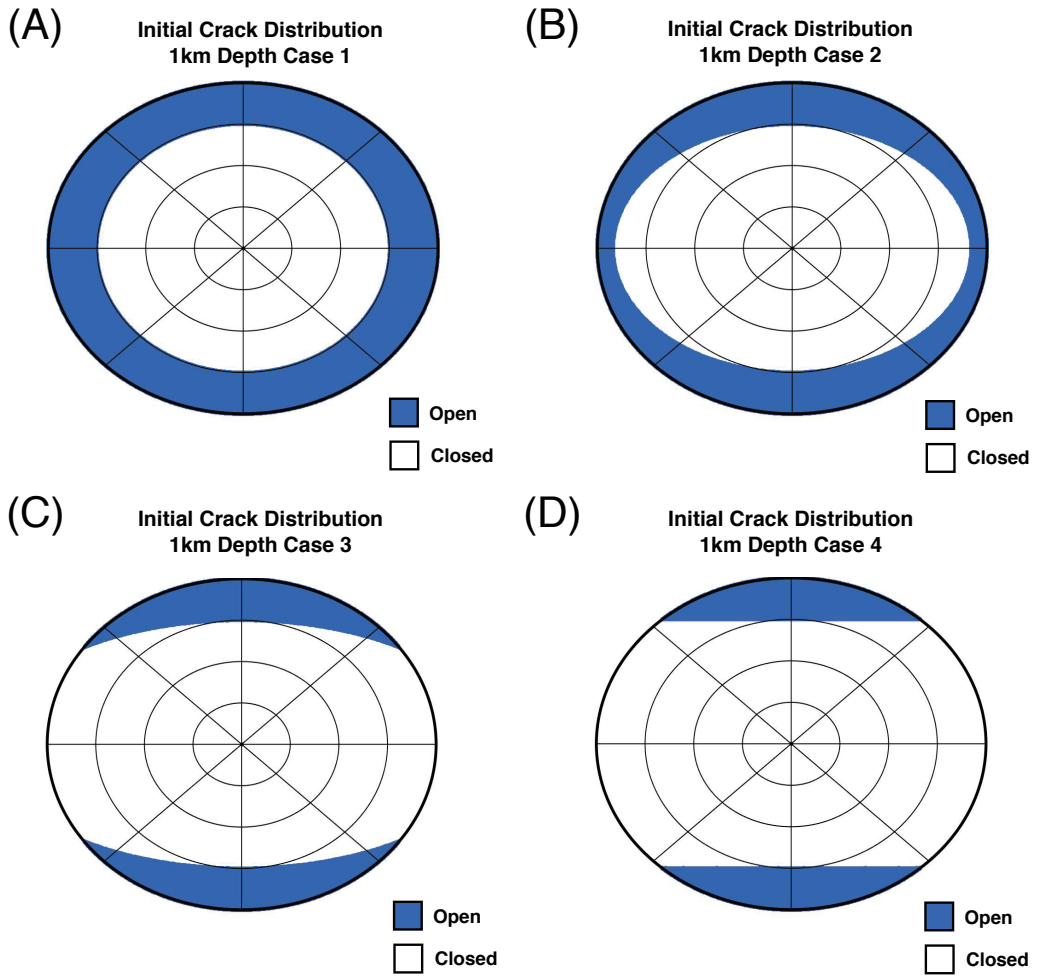

Figure 6.12: This figure shows four upper hemisphere projections illustrating the initial crack distribution of the four in-situ stress conditions at $1\,km$ depth where panels (A) through (D) respectively show Cases 1 through 4. The projections show open crack normal orientations with blue and closed crack normal orientations with white. See Figure 5.2 for a description of upper hemisphere projection.

slightly smaller at approximately 55°.

$1\,km$ Depth - Case 2: σ_H/σ_h=1.3

The in-situ confining-stress field is given by σ_V=24 MPa, σ_H=16 MPa and σ_h= 12 MPa. Panel (B) of Figure 6.12 shows the resulting initial crack distribution consists of azimuthally anisotropic sub-vertical crack sets. The maximum range

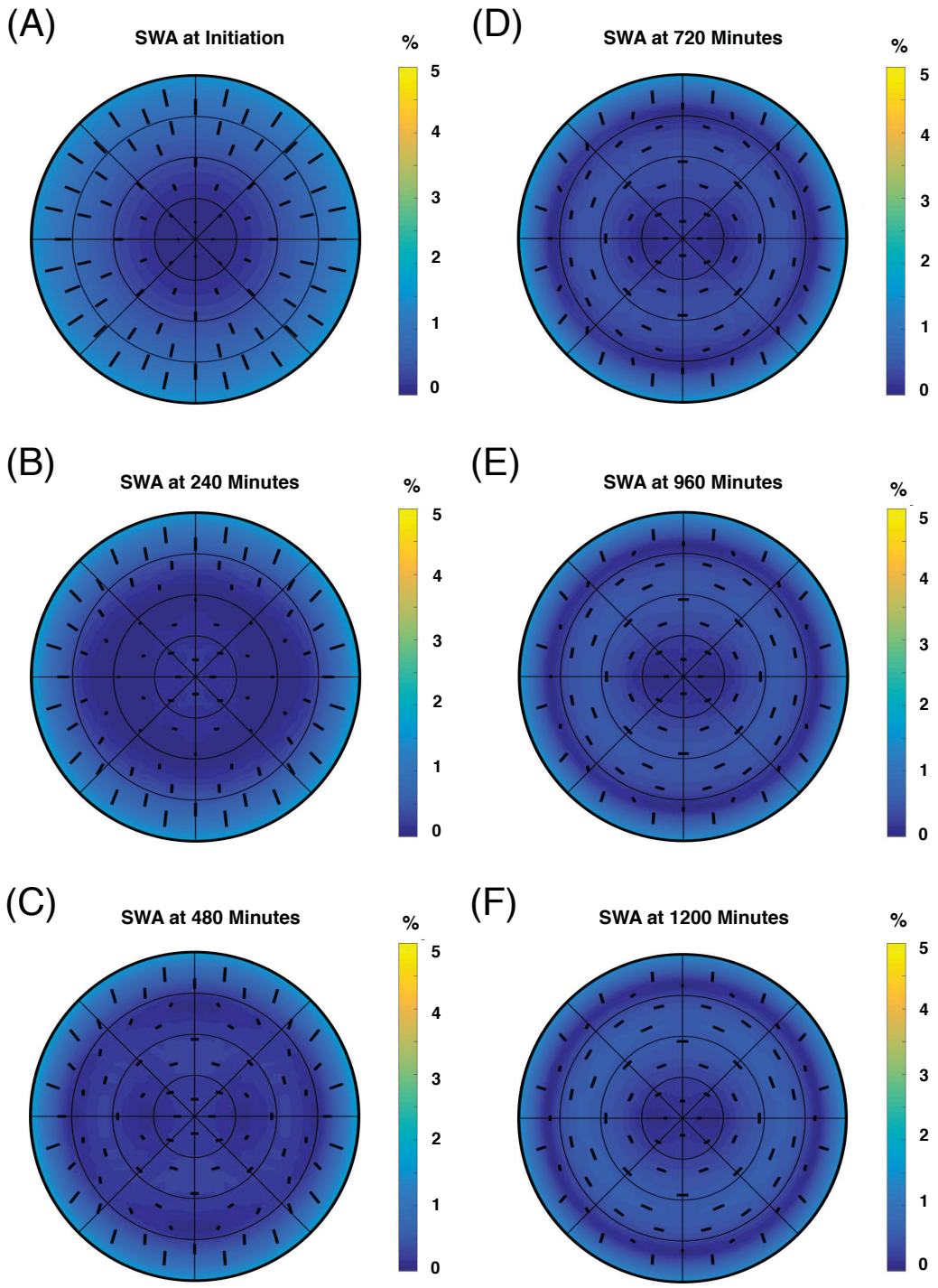

Figure 6.13: $1\,km$ Depth - Case 1: A upper hemisphere projection of the *SWA* at $t=0$ to $1200\,min$ at time steps of $240\,min$ modelled at the CZP. See Figure 5.2 for a description of upper hemisphere projection.

of crack normal inclination occurs in the azimuthal direction of σ_h and the minimum range occurs in the direction of σ_H. There is approximately 0 % *SWA* in sub-vertical propagation directions and the polarization direction of the fast S-wave is rotated 90° with respect to all other propagation directions. The initial orthotropic *SWA* pattern can be seen in Figure 6.14.

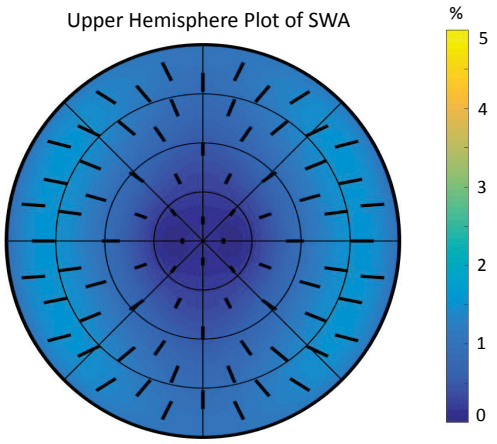

Figure 6.14: 1 km Depth - Case 2: The initial *SWA* pattern displayed as an upper hemisphere projection. See Figure 5.2 for a description of upper hemisphere projection.

The SWA_{vert} is very similar to that seen in Case 2 at 2 km depth, except the magnitudes of increase/decrease are much smaller at all time steps, i.e. less than 0.2%. The evolution of *SWA* at the CZP is very similar to that seen in at the TZP in Case 1 at 1 km depth but with the range of inclination experiencing the polarization rotation reaching a smaller maximum range of less than 30°. Also, the evolution of *SWA* at the TZP is very similar to that seen in Figure 6.13 at the CZP in Case 1 at 1 km depth but with the range of inclination experiencing the polarization rotation reaching a smaller maximum range of less than 50°.

1 km **Depth - Case 3:** σ_H/σ_h=1.6

The in-situ confining-stress field is given by σ_V=24 MPa, σ_H=20 MPa and σ_h= 12 MPa. Panel (C) of Figure 6.12 shows the resulting initial crack distribution is similar to that seen in Case 3 at 2 km depth, and consists sub-vertical crack sets that are sub-parallel to the hydraulic fracture face but with a larger range of crack normal inclination and azimuth. That is, the crack distribution is further from a purely vertical crack set parallel to the fracture face. As seen in panel (A) of Figure 6.15, this distribution produces an orthotropic medium with SWA_{max} = 2.7% in the vertical direction. There is a diffuse band of high *SWA* at all inclinations with azimuths sub-parallel to the fracture face. *SWA* is small or zero for propagation directions within approximately 40° of σ_h.

Figures 6.15 and 6.16 show the evolution of *SWA* at the CZP and TZP respectively. At the CZP, the pattern of *SWA* initially remains relatively unchanged. However, as the proximal zone approaches, the band of high *SWA* is successively reduced until all propagation directions have less than 2% *SWA*. At the TZP, the pattern of *SWA* initially remains relatively unchanged. However, as the fracture tip and the proximal zone approach, the band of high *SWA* is reduced so all propagation directions have less than 1.5% *SWA* with the largest reduction occurring for sub-vertical propagation directions. Then, as the proximal zone overtakes that TZP, the polarization direction of the fast S-wave rotates by 90° for sub-vertical propagation directions. The range of inclinations experiencing this polarization rotation is greater in the direction of σ_h than in the direction of σ_H: 0° − 50° versus 0° − 30° respectively.

As seen in Figure 6.17, the SWA_{vert} shows distinct character in the compressive zone, tensile zone and proximal zone. Also, the shear zone is not detectable in this case. The proximal zone experiences a large decrease in SWA_{vert} of up to 2.7% and expands in size with each time step reaching a maximum distance of 50 m from the fracture face. The transition between the proximal zone and tensile zone is gradational while the transition between the proximal zone and

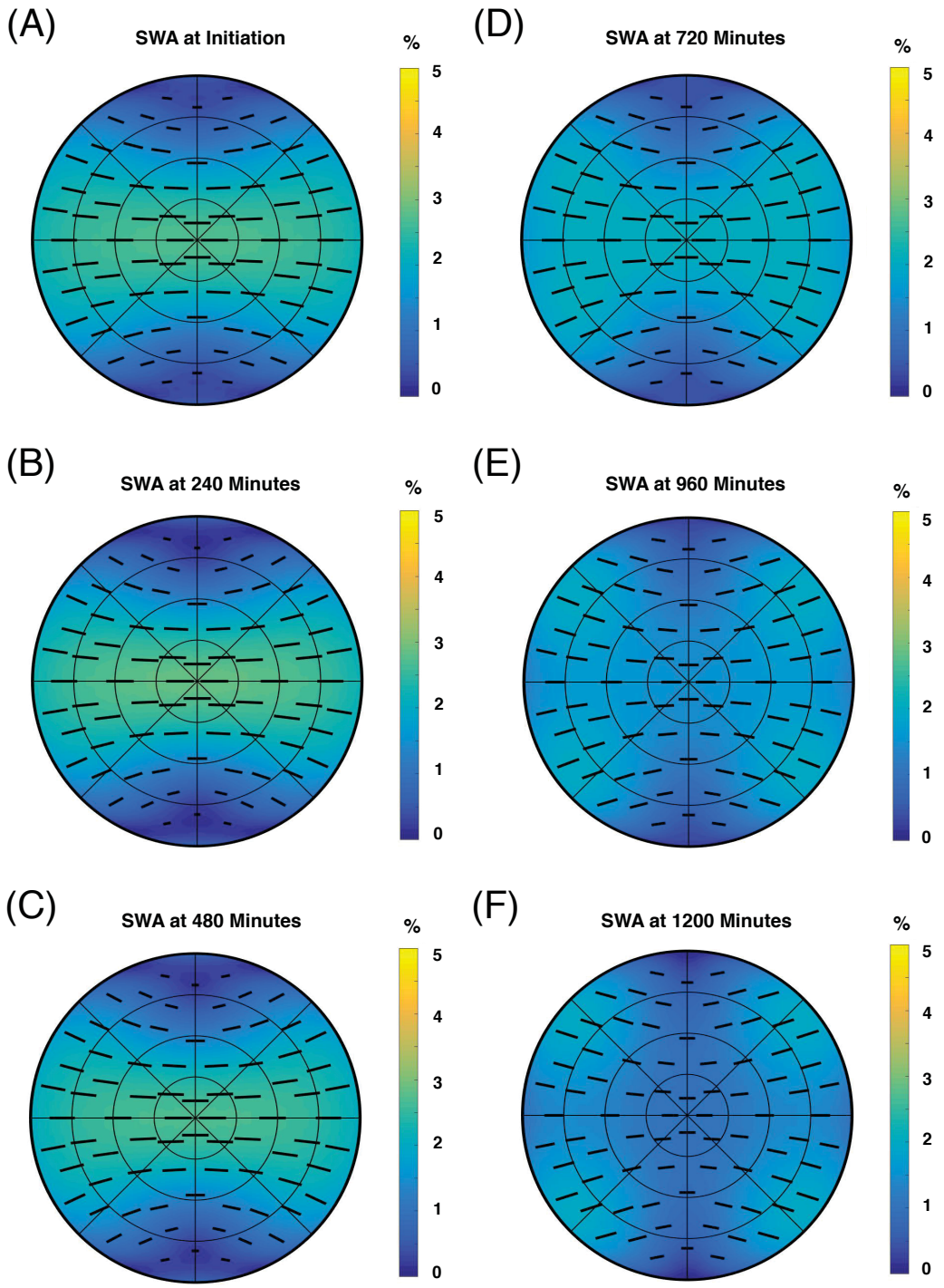

Figure 6.15: $1\,km$ Depth - Case 3: A upper hemisphere projection of the *SWA* at $t=0$ to $1200\,min$ at time steps of $240\,min$ modelled at the CZP. See Figure 5.2 for a description of upper hemisphere projection.

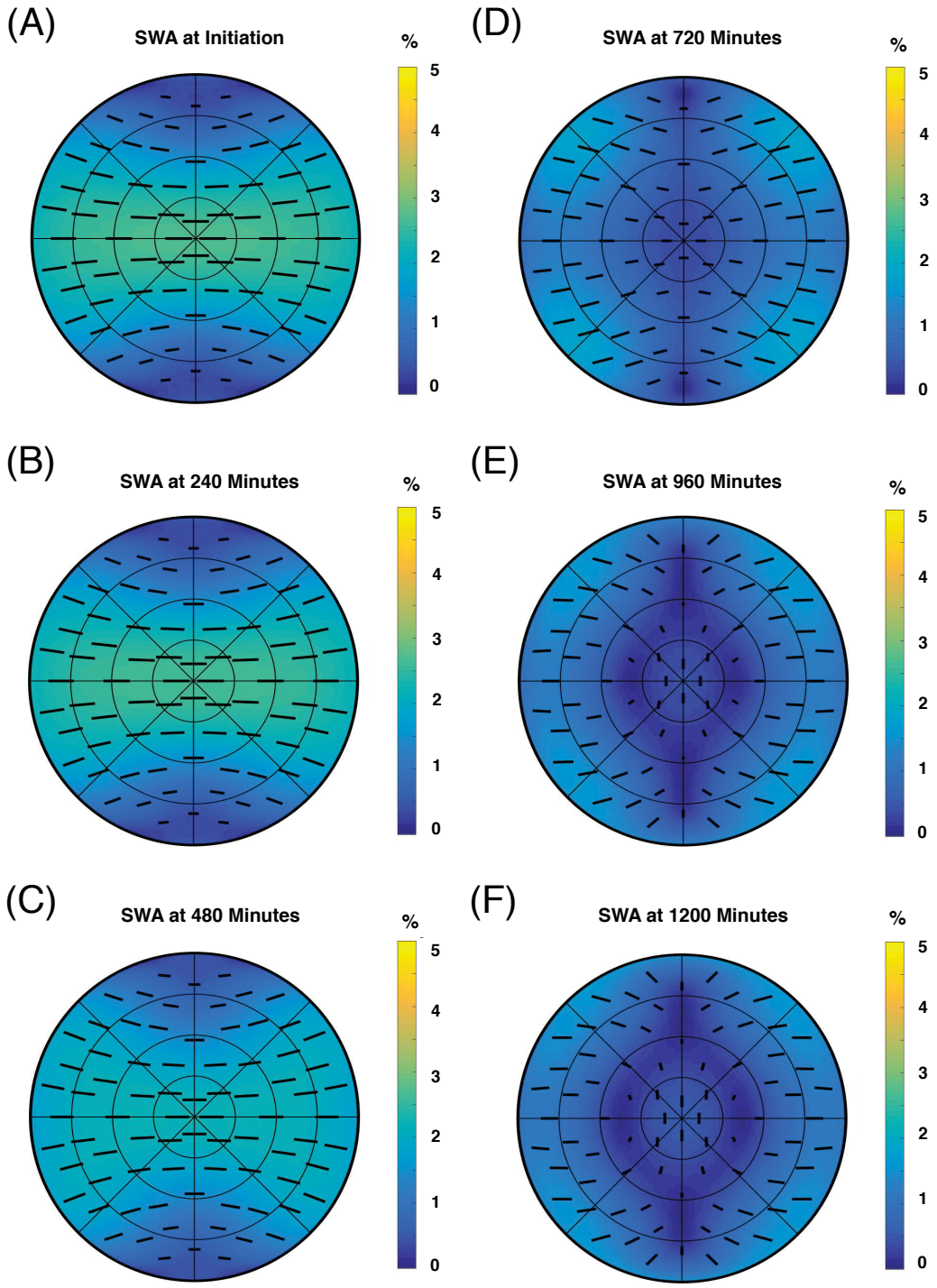

Figure 6.16: $1\,km$ Depth - Case 3: A upper hemisphere projection of the *SWA* at $t=0$ to $1200\,min$ at time steps of $240\,min$ modelled at the TZP. See Figure 5.2 for a description of upper hemisphere projection.

compressive zone experiences very little to zero change in SWA_{vert}. The compressive zone experiences an increase in SWA_{vert} of less than 0.5% with a local maximum value occurring perpendicular to the centre of the fracture and close to the proximal-compressive zone transition. The compressive zone expands in size as long as the fracture is growing. When the fracture reaches the maximum radius, the compressive zone starts to shrink in size as the continually expanding proximal zone encroaches on it. Also, the local maximum value becomes more pronounced with each time step as the fracture grows, but become less pronounced with each time step that the fracture size is constant. The beyond the proximal zone, the tensile zone experiences a small decrease in SWA_{vert} of less than 1%.

1 km Depth - Case 4: σ_H/σ_h=1.9

The in-situ confining-stress field is given by σ_V=24 MPa, σ_H=24 MPa and σ_h= 12 MPa. Panel (D) of Figure 6.12 shows the resulting initial crack distribution is very similar to that seen in Case 3 at 1 km depth, and consists of sub-vertical crack sets that are sub-parallel to the hydraulic fracture face. However, this slightly different distribution now produces a transversely isotropic medium with an axis of symmetry parallel to σ_h, see panel (A) of Figure 6.18. There is a band of high *SWA* at all inclinations with azimuths sub-parallel to the fracture face. There is a SWA_{max} = 3.6% at all inclinations with azimuth parallel to the fracture face. *SWA* is small or zero for propagation directions within 45° of σ_h. The initial *SWA* pattern is very similar as to that observed for Case 4 at 2 km depth.

Figures 6.18 and 6.19 show the evolution of *SWA* at the CZP and TZP respectively. At the CZP, the pattern of *SWA* remains relatively unchanged. Initially, the band of high *SWA* increases by 0.2% and then as the proximal zone approaches and eventually overtakes the CZP the band of high *SWA* is successively reduced to 2.8% *SWA*. At the TZP, the pattern of *SWA* initially

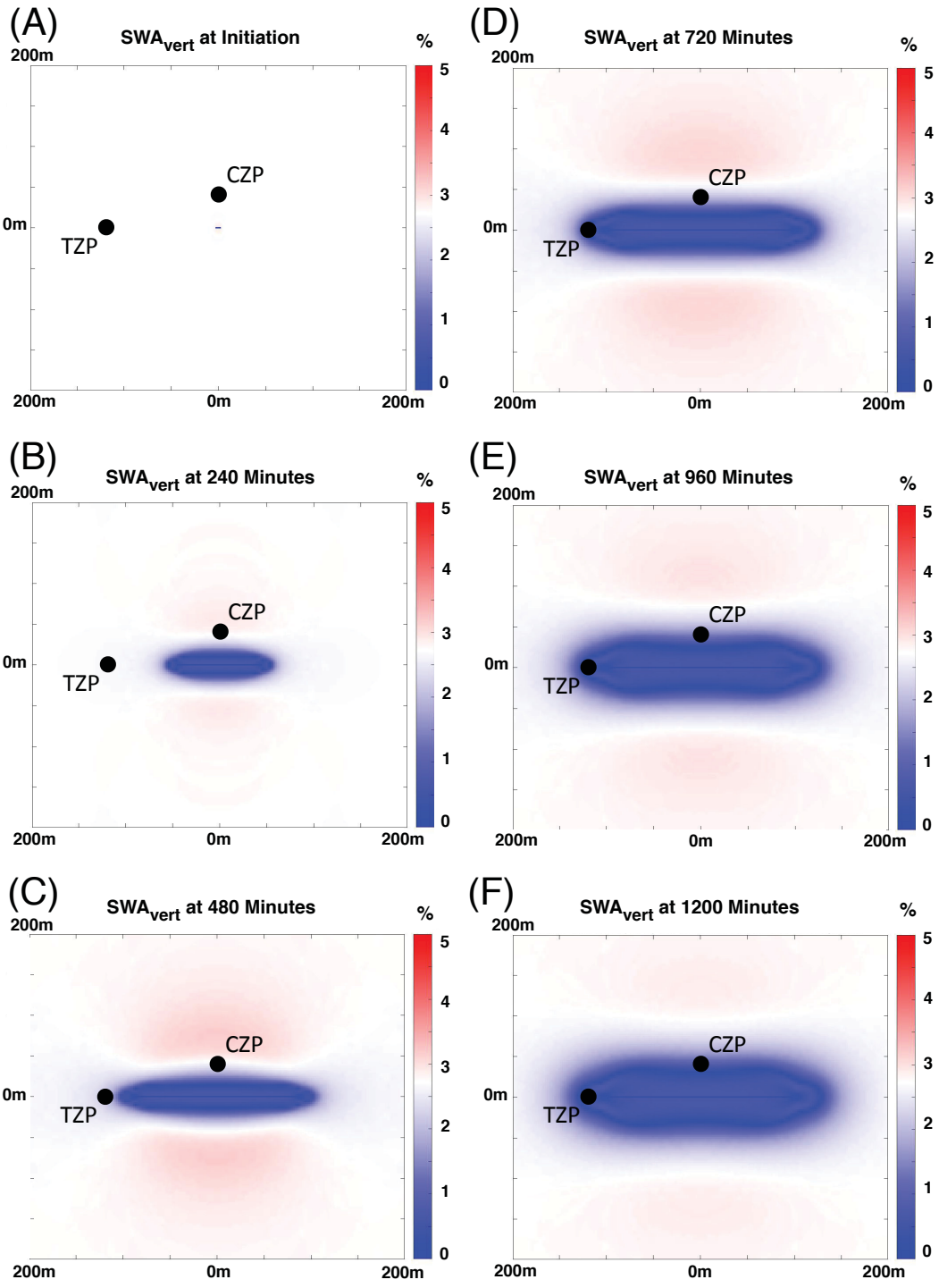

Figure 6.17: 1 km Depth - Case 3: The SWA_{vert} at $t = 0$ to 1200 min at time steps of 240 min.

remains relatively unchanged. However, as the proximal zone approaches and overtakes the TZP, the band of high *SWA* is rapidly reduced and diffused so all propagation directions have less than 2% *SWA* and only propagation directions within 20° of σ_h having less than 0.5% *SWA*.

In this case, the SWA_{vert} evolves similarly to that seen in Figure 6.17 with two important differences. First, the proximal zone displays a dual character with a fracture tip region and a fracture face region. The tip-proximal zone region experiences a large decrease in SWA_{vert} of up to 3.6% and the face-proximal zone region experience a moderate SWA_{vert} decrease of up to 1.6%. Second, the proximal-compressive zone transition occurs slightly closer to the fracture face. For example, at $t = 1200\,min$ the proximal-compressive zone transition occurs at $100\,m$ perpendicular to the fracture centre for Case 3 at $1\,km$ depth and $75\,m$ for Case 4 at $1\,km$ depth.

6.5 Discussion

Our results indicate that in a normal faulting regime where σ_h is determined by the uniaxial stress model the behaviour of *SWA* in the vicinity of a hydraulic fracture is highly variable. The type of behaviour depends on the initial in-situ effective-stress field, including both the confining-stress field and the initial pore-pressure components with reservoir depth determining the initial pore pressure. The in-situ effective-stress field determines the initial crack distribution and the resulting initial *SWA*.

Although the specific *SWA* behaviour depends on the reservoir depth and in-situ confining stress, there are a number of characteristics that are observed for all cases tested. In general, the magnitude of *SWA* decreases in any given scenario are always larger than the *SWA* increases for the same scenario. Also, there are four distinct zones of behaviour in the vicinity of the fracture for each case, the compressive zone, shear zone, tensile zone and proximal zone.

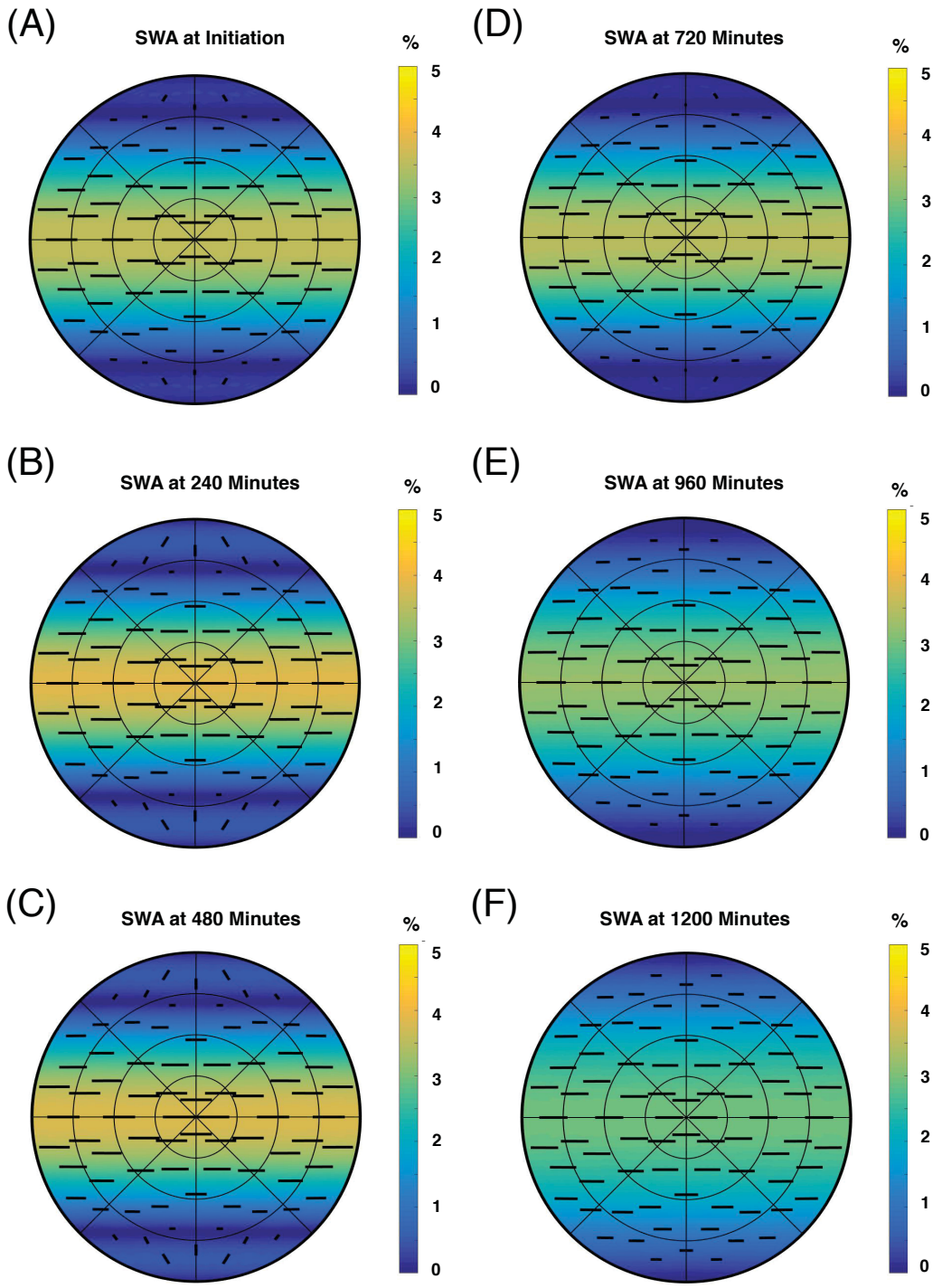

Figure 6.18: $1\,km$ Depth - Case 4: A upper hemisphere projection of the *SWA* at $t=0$ to $1200\,min$ at time steps of $240\,min$ modelled at the CZP. See Figure 5.2 for a description of upper hemisphere projection.

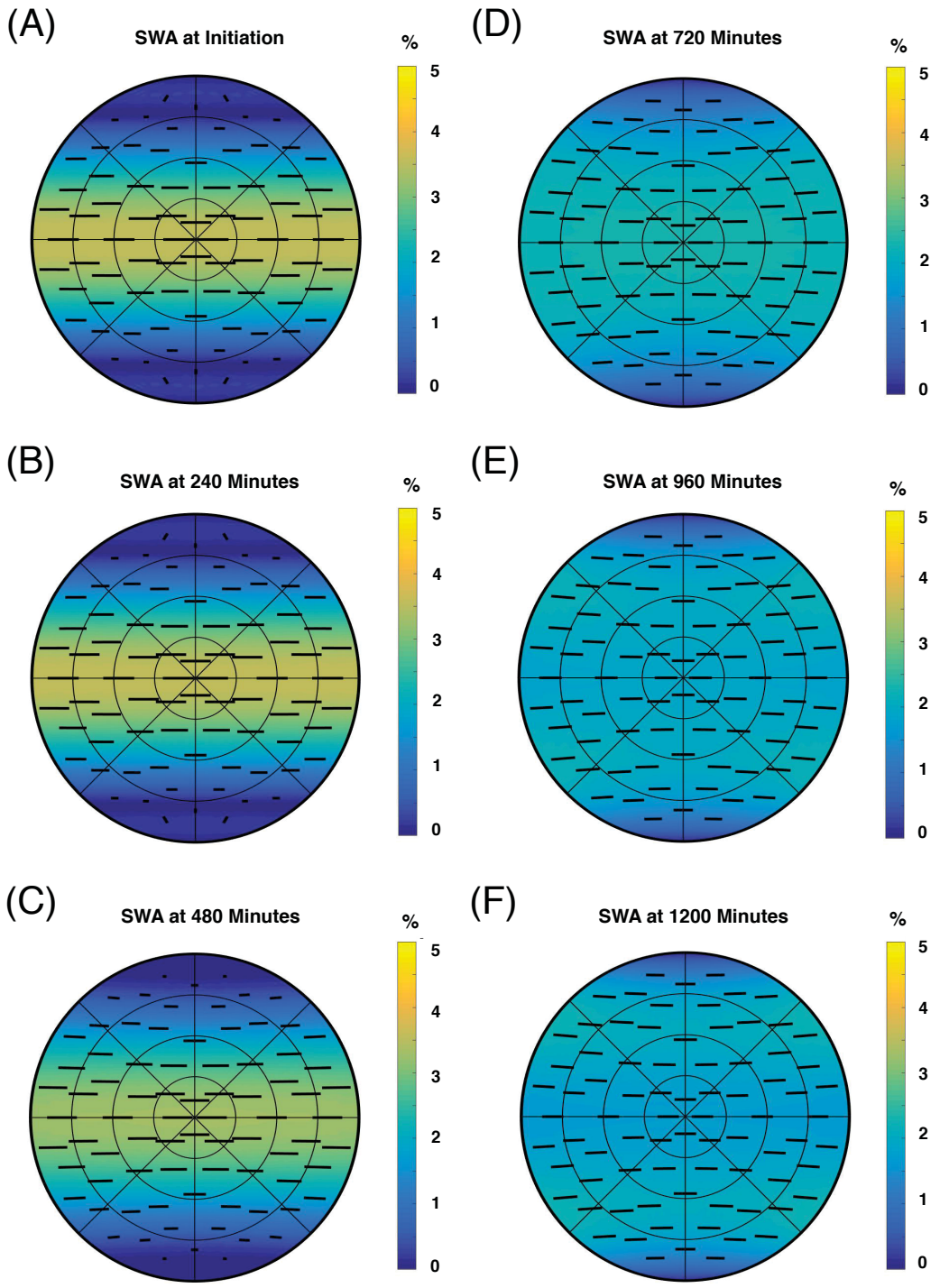

Figure 6.19: $1\,km$ Depth - Case 4: A upper hemisphere projection of the *SWA* at $t=0$ to $1200\,min$ at time steps of $240\,min$ modelled at the TZP. See Figure 5.2 for a description of upper hemisphere projection.

The relative sizes of these zones are variable but the proximal zone always experiences the largest degree of *SWA* pattern change and continues to grow as long as the injection pressure is maintained in the fracture. Finally, the shear zone typically experiences very little to zero change in SWA_{vert} and the compressive zone and tensile zone alway exhibit opposite SWA_{vert} changes. That is, if the magnitude of SWA_{vert} increases in the compressive zone then SWA_{vert} will decrease in the tensile zone and vice versa. This suggests that the contrast in *SWA* between ray paths through the two zones at a single time may be more detectable than observing the temporal change in *SWA* along a ray path through a single zone or along a ray path through both zones.

In the following two subsections we compare and contrast the *SWA* behaviour observed for the reservoirs at $1\,km$ and $2\,km$ depths.

6.5.1 $2\,km$ Depth - Reservoir

Of the four $2\,km$ depth reservoir cases, we observe the largest change in SWA_{vert} when $\sigma_H/\sigma_h = 1.3$. In this case, SWA_{vert} decreases by up to $3.2\,\%$ in the proximal zone and up to $0.9\,\%$ in the compressive zone. The spatial extent of the proximal zone is relatively small, being restricted to a maximum of $40\,m$ from the fracture. For the cases where $\sigma_H/\sigma_h > 1.3$ we observe moderate to small changes in SWA_{vert} with the proximal zone now experiencing increases up to $0.7\,\%$ and the compressive zone experiencing decreases up to $1\,\%$. However, the size of the proximal zone is larger for cases where $\sigma_H/\sigma_h > 1.3$.

Considering the pattern of *SWA* for the four $2\,km$ depth reservoir cases, we only observe a significant pattern change in the proximal zone when $\sigma_H/\sigma_h = 1.3$. In this case, the band of high magnitude *SWA* is diffused and reduced by $\approx 1.6\,\%$. For all other cases, the pattern of *SWA* is relatively unchanged. Furthermore, the magnitude of *SWA* change for all propagation directions does not exceed $\pm 1\,\%$.

Considering the above observations, our modelling suggests that it will be

difficult to detect the changes in SWA_{vert} and SWA in general for a reservoir at $2\,km$ depth. The conditions giving the best chance for detection are for vertical or sub-vertical propagation through the proximal zone when $\sigma_H/\sigma_h = 1.3$.

6.5.2 $1\,km$ Depth - Reservoir

Of the four reservoir cases at $1\,km$ depth, we observe the largest change in SWA_{vert} of up to a 3.6 % decrease when $\sigma_H/\sigma_h = 1.9$ and this decrease occurs in the relatively small tip-proximal zone. When $\sigma_H/\sigma_h = 1.6$, we observe a smaller decrease of up to 2.7 % in the entire proximal zone which is significantly larger in extent. In contrast to the reservoir cases $2\,km$ depth, when $\sigma_H/\sigma_h < 1.6$ we observed very little to zero change in SWA_{vert}.

Considering the pattern of SWA for the four $1\,km$ depth reservoir cases, we observe two distinct types of pattern change. First, when $\sigma_H/\sigma_h \leq 1.6$ we observe a 90° rotation of the polarization direction of the fast S-wave for vertical and sub-vertical propagation directions. When $\sigma_H/\sigma_h = 1.6$ this rotation is observed only in the proximal zone and when $\sigma_H/\sigma_h \leq 1.3$ this rotation is observed in the compressive zone, tensile zone and proximal zone. Furthermore, this rotation should be detectable with 3-component geophones. The second type of change involves the diffusion of the band of high SWA over a larger range of inclination and azimuth. Concurrent with this diffusion, the magnitudes of SWA in the band are reduced. This behaviour is observed in the proximal-tensile zone and proximal-compressive zone transition zones when $\sigma_H/\sigma_h \geq 1.6$ and SWA reaches a maximum reduction of 1.2 %. Additionally, this behaviour is observed in the face-proximal zone when $\sigma_H/\sigma_h = 1.9$ and SWA reaches a maximum reduction of 2 %.

6.5.3 General Implications

Considering the above observations, the region around a pressurized hydraulic fracture can be classified into four spatio-temporal zones of S-wave anisotropy behaviour: the compressive zone, the shear zone, the tensile zone and the proximal zone. These zones are closely aligned with the four spatio-temporal zones of effective-stress perturbation observed in Chapter 4. Figure 6.20 shows the relative spatial location of the four zones and their temporal development. Panel (A) illustrates as long as the fracture is growing in radius, the proximal zone remains relatively small compared to the compressive zone. However, panel (B) illustrates if the fracture remains pressurized and static in size, the proximal zone continues to grow into the other three zone while the maximum extent of the other three zones remains constant. It is possible for the proximal zone to completely override one or more of the other zones.

Additionally, our modelling suggests that in general it will be easier to detect the changes in SWA_{vert} and SWA for a reservoir at $1\,km$ depth. The conditions giving the best chance for the detection of a fast S-wave polarization rotation are for vertical or sub-vertical propagation through the compressive zone, tensile zone or proximal zone when σ_H/σ_h is close to one. The conditions giving the best chance for the detection of a reduction and diffusion of the high SWA band are for propagation directions that are greater than 45° from σ_h and travel through the face-proximal zone or the proximal-tensile zone and proximal-compressive zone transition zones when $\sigma_H/\sigma_h = 1.9$.

Finally, although we have not shown results for a relatively stiff versus a relatively compliant reservoir, it is worth commenting on. If we were to model the above cases with a more compliant reservoir and all other input parameters held constant, including the in-situ confining stress (i.e. the in-situ minimum confining stress is no longer determined by the uniaxial stress model), we are unable to make general predictions regarding the SWA response. We would expect different changes in the SWA evolution for each case due to the

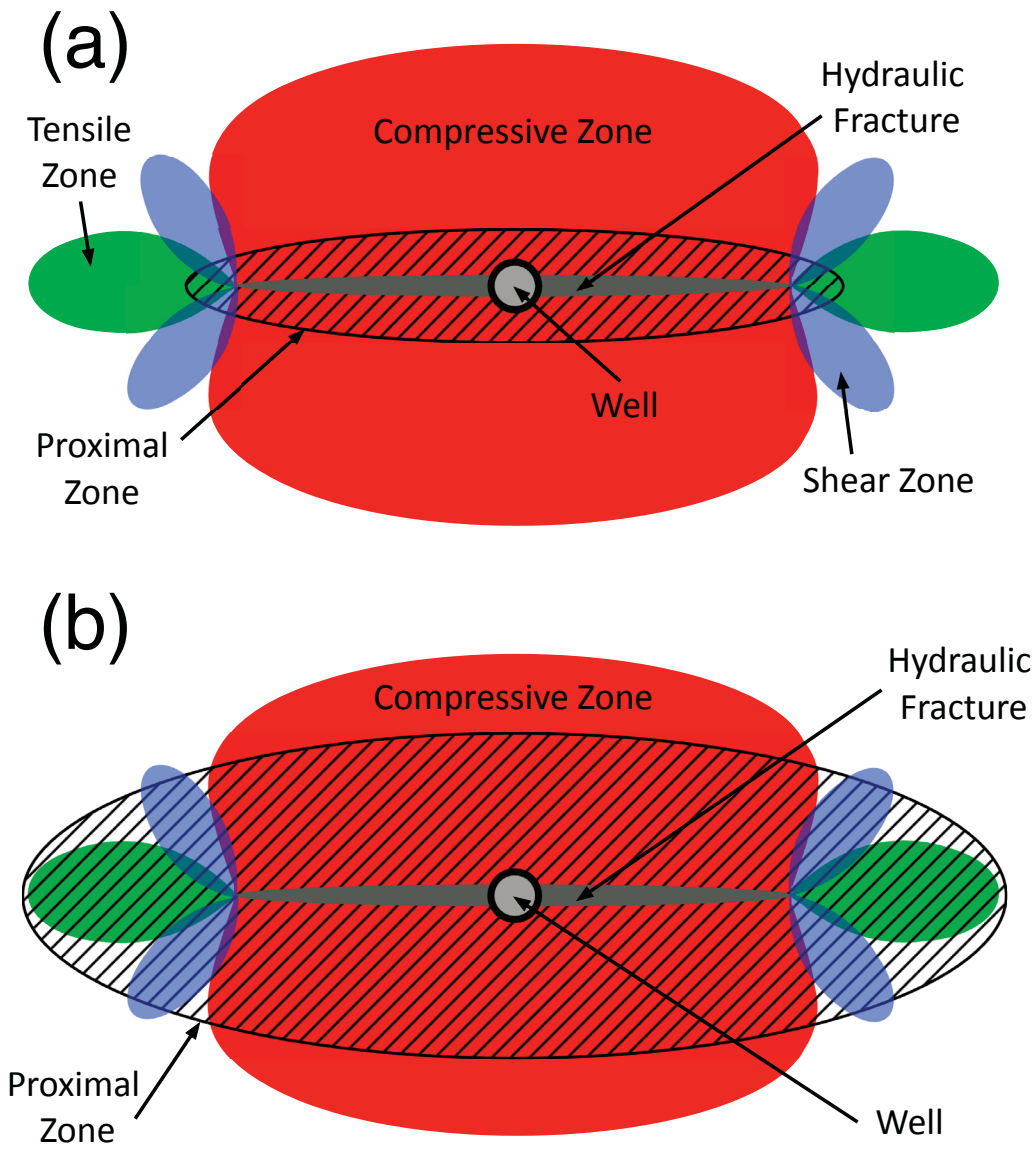

Figure 6.20: Panel (A) A horizontal cross-section through a growing vertical hydraulic fracture extending from a vertical well illustrating the relative size of the four zones of S-wave anisotropy in the surrounding region, modified from Cipolla et al. (2011). The area with black diagonal lines indicates the proximal zone, the solid red area indicates the compressive zone, the solid blue area indicates the shear zone and the solid green area indicates the tensile zone. Panel (B) A horizontal cross-section through the same fracture at a later time where the fracture has remained pressurized for a length of time after it has stopped growing. Note the relative size of the proximal zone has increased at the expense of the spatial extent of the other three zones, modified from Cipolla et al. (2011).

complexity of the interaction between the in-situ confining stress, the initial pore pressure and the initial crack distribution and the resulting *SWA*. For example, consider a case where $\sigma_H/\sigma_h = 1$. In this case, there is an initial crack distribution of sub-vertical crack sets that are sub-parallel to the hydraulic fracture face and this distribution produces a transversely isotropic medium with an axis of symmetry parallel to σ_h. The sub-vertical crack sets have normals that are oriented with inclinations within a certain number degrees from σ_h. If the reservoir compliance is increased, the cracks are easier to close and the range of inclinations for open crack normals is reduced. There are two possible responses for this single case. First, it is possible that all of the cracks will close, resulting in an initially isotropic medium. Hence, there would be no change in *SWA* due to increased confining stress and the only possible change in *SWA* would be an increase due to increased pore pressure in the proximal zone and decreased confining stress in the tensile zone. In the second possible response, assume the increase in compliance is smaller; this results in only a portion of the initial sub-vertical crack sets closing. The sub-vertical crack sets now have a higher degree of preferential alignment which tends to result in a higher degree of *SWA*. However, the open crack distribution also has a smaller normalized crack density which tends to decrease *SWA*. These two counteracting effects occur at different rates from each other and the magnitude of difference depends on the initial crack distribution.

6.6 Conclusions

In modelling the four in-situ stress scenarios where σ_H/σ_h is equal to 1, 1.3, 1.6 and 1.9 at $1\,km$ and $2\,km$ depth, we find that there is no simple connection between *SWA* and the pore-pressure increases and confining-stress changes in the vicinity of a hydraulic fracture. The complex interplay between in-situ stress-induced background *SWA* and that from the growing hydraulic fracture

and pore-pressure diffusion into the rock matrix gives rise to significantly different *SWA* evolution for the majority of the modelled scenarios. However, we are able to identify some general characteristics that may be used to identify the position of a hydraulic fracture. As discussed in Chapter 4, the proximal zone experiences an effective-stress decrease caused by the relatively large pore-pressure increase present in this zone. In this chapter, we find that the effective-stress decrease in the proximal zone tends to produce the largest variations in SWA_{vert}, either increases or decreases, while the compressive zone tends produce a smaller and opposite SWA_{vert} variation. The only exception is for Case 2 at $2\,km$ depth where both the proximal and compressive zones produce a decrease in SWA_{vert}. Additionally, the cases at $1\,km$ depth all show a 90° rotation of the polarization direction of the fast S-wave for vertical and sub-vertical propagation directions in the proximal zone.

Chapter 7

Summary and Future Work

In this thesis, we develop a comprehensive workflow for forward modelling the anisotropic velocity field around a hydraulic fracture. This integrated model involves three main components. First, we analytically model triaxial confining-stress change due to the opening of a hydraulic fracture. Next, we numerically model pore-pressure diffusion through the walls of a spheroidal fracture. Then, we give the resulting anisotropic velocity by modelling the preferential opening and closing of an initially isotropic distribution of microcracks. Using this workflow, we investigate two broad categories of subsurface scenario. In Chapter 5, we assume an initially isotropic reservoir with low permeability. Hence, pore-pressure diffusion does not significantly penetrate into the reservoir rock and the proximal zone is virtually non-existent. We, also, assume the confining-stress perturbation in the compressive zone can be approximated as uniaxial. In Chapter 6, we assume an initially anisotropic reservoir, and we include pore-pressure diffusion and triaxial confining-stress perturbation. We find that the resulting anisotropic velocity fields for each scenario are significantly different from each other. Hence, the simplified uniaxial implementation of the unmodified Anisotropic Poroelasticity model with no pore-pressure diffusion does not provide an adequate approximation of the modified Anisotropic Poroelasticity model taking pore-pressure diffusion into account. This demonstrates the

somewhat intuitive fact that the in-situ reservoir stress state and pore-pressure diffusion must not be ignored.

In Chapter 3, we find that given an equal magnitude effective-stress change from a common initial effective stress, isotropic P- and S-wave velocities are more sensitive to an effective-stress decrease. In Chapter 4, we find that a relatively large region around a hydraulic fracture is predicted to experience effective-stress perturbation leading to expected velocity changes. In Chapter 5, we find that S-wave velocities are more sensitive to effective-stress changes than P-wave velocities. This coupled with the added advantage that anisotropy along a single ray path can be determined using the time delay between the two orthogonally polarized S-waves means that S-wave observations in addition to P-wave observations are far more useful than P-wave observations alone.

The region around a hydraulic fracture can be divided into four spatiotemporal zones: the proximal zone, the compressive zone, the shear zone and the tensile zone. These four zones can be characterized in terms of size, effective-stress perturbation, isotropic velocity change and anisotropic velocity changes. As shown in Chapter 5 and 6 the anisotropic velocity changes depend strongly on the initial reservoir stress state, so a simple description is not possible. However, the four zones can be generally characterized as seen in Table 7.1.

7.1 Future Work

There are several interesting directions that we could take from this point forward including investigating a more complex fracture network using the current integrated forward model, applying the current model to the inverse problem or current model refinement. We touch on aspects of each of these investigation directions below.

We have shown the forward modelled anisotropic velocity predictions for a simple scenario: a single vertical hydraulic fracture. What would the predicted

Table 7.1: The general characteristics of the four zones of influence in the vicinity of a hydraulic fracture.

Zone	**General Characteristics**
Proximal	- size and relative size increases with time. - permeability has a large effect on the size of this zone. - effective stress decreases - isotropic P-wave velocity remains relatively unchanged. - isotropic S-wave velocity decreases.
Compressive	- size increases with fracture radius. - larger in relative size than shear and tensile zones. - effective stress increases. - isotropic P- and S-wave velocities increase.
Shear	- size increases with fracture radius. - effective stress remains relatively unchanged. - isotropic P- and S-wave velocities remain relatively unchanged.
Tensile	- size increases with fracture radius. - effective stress increases. - isotropic P- and S-wave velocities increase.

velocity field look like for multiple parallel fractures or a more complicated fracture network? What would the predicted velocity field look like if the reservoir permeability is anisotropic?

If we accept the current integrated model as a reasonable approximation of the resulting velocity field in the vicinity of a single planar fracture, we can apply the model to an appropriate field dataset and predict the hydraulic fracture position and geometry from S-wave splitting observations. Ideally, we would want a time-lapse three-component microseismic dataset with a low signal to noise ratio in which the event locations show a single defined planar feature. We would need to perform S-wave picking and polarization direction determination. An important factor in the uncertainty of the fracture position and geometry is the coverage of ray propagation directions. A larger range of coverage will give a lower uncertainty. Therefore, it would be beneficial to have more than one monitoring well and a surface array, as this will increase the possible propagation directions that can be measured.

In our current integrated model we make a number of simplifying assumptions to reduce model complexity and computation time. What if our model could be significantly more accurate by increasing the model complexity? We assume an average initial crack aspect ratio. However, there could be a wide array of micropore aspect ratios present in real rock. Low aspect ratio cracks will be more sensitive to triaxial stress changes than high aspect ratio crack. Hence, possibly more realistic modelling could be completed by assuming a certain distribution of aspect ratios. Additionally, we assume a hydraulic fracture can be modelled as a low-aspect ratio spheroid. Hydraulic fractures may be more accurately modelled as low-aspect ratio ellipsoids. We could develop a new method of modelling confining-stress change and pore-pressure diffusion that is valid for an ellipsoidal fracture geometry. Finally, we assume that poroelastic feedback effects are small enough that we can ignore them. That is, confining stress and pore pressure are uncoupled in our model. We could refine our model by including a one-way or two-way coupling of stress and pore pressure such that changes in confining stress induce pore-pressure changes and/or changes in pore pressure induce confining-stress changes. There are many assumptions that we could discard. However, in our opinion, removing model assumptions should not take priority over modelling multiple fracture scenarios or obtaining field data and inverting for fracture properties using the current model.

Bibliography

Barkved, O., 2012, Seismic surveillance for reservoir delivery from a practitioner's point of view: European Association of Geoscientists and Engineers Publications.

Bass, J., 1995, Elasticity of minerals, glasses, and melts, *in* Mineral Physics and Crystallography: A Handbook of Physical Constants: American Geophysical Union, 45–63.

Batzle, M., and Z. Wang, 1992, Seismic properties of pore fluids: Geophysics, **57**, 1396–1408.

Berryman, J., 1992, Mixture theories for rock properties: Journal of Geophysical Research, **97**, 17409–17424.

———, 1995, Mixture theories for rock properties, *in* Mineral Physics and Crystallography: A Handbook of Physical Constants: American Geophysical Union, 205–228.

Biot, M., 1956, Mechanics of deformation and acoustic propagation in porous media: Journal of Applied Physics, **33**, 1482–1498.

———, 1962, Theory of propagation of elastic waves in a fluid saturated porous solid. i. low frequency range and ii. higher-frequency range: Journal of the Acoustical Society of America, **28**, 168–191.

Boroumand, N., and D. Eaton, 2012, Comparing Energy Calculations - Hydraulic Fracturing and Microseismic Monitoring, C042: Presented at the 74th EAGE/SPE Europec Conference, Copenhagen.

Brandt, H., 1955, A study of the speed of sound in porous granular media:

Journal of Applied Mechanics, **22**, 479–486.

Brisco, C., and M. Van der Baan, 2016, A review of seismic velocity response to variations in pore pressure, pore-saturating fluid and confining stress: Presented at the GeoConvention, Calgary.

———, 2017, Velocity anisotropy in the region near a hydraulic fracture: A sensitivity analysis: Presented at the SEG Annual International Meeting, Houston.

Cipolla, C., S. Maxwell, M. Mack, and R. Downie, 2011, A practical guide to interpreting microseismic measurements: SPE Americas Unconventional Gas Conference, 363–390.

Crampin, S., 1994, The fracture criticality of crustal rocks: Geophysical Journal International, **118**, 428–438.

———, 2003, The new geophysics: shear-wave splitting provides a window into the crack-critical rocks mass: The Leading Edge, **22**, 536–549.

Crampin, S., and S. Zatsepin, 1997, Modelling the compliance of crustal rock - II. response to temporal changes before earthquakes: Geophysical Journal International, **129**, 495–506.

Dvorkin, J., and A. Nur, 1996, Elasticity of high-porosity sandstones: Theory for two north sea datasets: Geophysics, **61**, 1363–1370.

Eshelby, J., 1957, The determination of the elastic field of an elliptical inclusion, and related problems: Royal Society of London, Series A, Mathematical and Physical Sciences, 376–396.

———, 1959, The elastic field outside an ellipsoidal inclusion, and related problems: Royal Society of London, Series A, Mathematical and Physical Sciences, 561–569.

Fischer-Cripps, A., 2007, Introduction to contact mechanics, 2nd ed.: Springer.

Fuck, R., A. Bakulin, and I. Tsvankin, 2009, Theory of traveltime shifts around compacting reservoirs: 3d solutions for heterogeneous anisotropic media: Geophysics, **74**, D25–D36.

Gassmann, F., 1951, Elastic waves through a packing of spheres: Geophysics, **16**, 673–685.

Green, A., and I. Sneddon, 1950, The distribution of stress in the neighbourhood of a flat elliptical crack in an elastic solid: Mathematical Proceedings of the Cambridge Philosophical Society, **46**, 159–163.

Hashin, Z., and S. Shtrikman, 1963, A variational approach to the elastic behavior of multiphase materials: Journal of Mechanic and Physics of Solids, **11**, 127–140.

Healy, D., 2009, Elastic field in 3d due to a spherodial inclusion matlab code for eshelby's solution: Computers & Geosciences, **35**, 2170–2173.

Hill, R., 1963, Elastic properties of reinforced solids: Some theoretical principles: Journal of Mechanic and Physics of Solids, **13**, 213–222.

Howard, G., 1970, Hydraulic fracturing: Society of Petroleum Engineers of AIME.

Hudson, J., 1980, Overall properties of a cracked solid: Mathematical Proceedings of Cambridge Philosophical Society, **88**, 317–384.

Jaeger, R., N. Cook, and N. Zimmerman, 2007, Fundamentals of rock mechanics, 4th ed.: Blackwell Publishing Ltd.

Ju, J., and L. Sun, 1999, A novel formulation for the exterior-point eshelby's tensor of an ellipsoidal inclusion: Journal of Applied Mechanics, **66**, 570–574.

———, 2001, Effective elastoplastic behaviour of metal matrix composites containing randomly located aligned spheroidal inhomogeneities, part i: micromechanics-based formulation: International Journal of Solids and Structures, **38**, 183–201.

King, G., 2012, Hydrualic fracturing 101: What every representative, environmentalist, regulator, reporter, investor, university researcher, neighbor and engineer should know about estimating frac risk and improving frac performance in unconventional gas and oil wells: SPE Internation Hydraulic Fracturing Technology Conference, 1–80.

Kranz, R., 1983, Microcracks in rocks: A review: Tectonophysics, **100**, 449–480.

Landro, M., 2001, Discrimination between pressure and fluid saturation changes from time lapse seismic data: Geophysics, **66**, 836–844.

Mavko, G., T. Mukerji, and J. Dvorkin, 2009, The rock physics handbook: Tools for seismic analysis of porous media, 2nd ed.: Cambridge University Press.

Maxwell, S., J. Shemata, E. Campbell, and D. Quirk, 2008, Microseismic deformation rate monitoring, SPE 116596: Presented at the Annual SPE Technical Conference, Denver.

———, 2009, Microseismic deformation rate monitoring, A18: Presented at the EAGE Passive Seismic Workshop: Case Studies and Applications for Field Development and Exploration.

Mindlin, R., 1949, Compliance of elastic bodies in contact: Journal of Applied Mechanics, **16**, 259–268.

Mura, T., 1987, Micromechanics of defects in solids: Kluwer Academic.

Nolte, K., G. Tsoflias, T. Bidgoli, and W. Watney, 2017, Shear-wave anisotropy reveals pore fluid pressure-induced seismicity in the u.s. midcontinent: Science Advances, **3**, 1–6.

Nur, A., 1971, Effects of stress on velocity anisotropy in rocks with cracks: Journal of Geophysical Research, **76**, 2022–2034.

Nur, A., and G. Simmons, 1969, Stress-induced velocity anisotropy in rock: An experimental study: Journal of Geophysical Research, **74**, 6667–6674.

Ostrander, W., 1985, Plane-wave reflection coefficients for gas sands at non-normal angles of incidence: Geophysics, **49**, 1637–1648.

Prioul, R., A. Bakulin, and V. Bakulin, 2004, Nonlinear rock physics model for estimation of 3d subsurface stress in anisotropic formations: Theory and laboratory verification: Geophysics, **69**, 415–425.

Reuss, A., 1929, Berechnung der fleischereien von mischkristallen auf grund

der plastizitatsbedingung fur eiskristalle: Zeitschrift fur Angewandte Mathematik und Mechanik, **9**, 49–58.

Roche, V., and M. Van der Baan, 2017, Modeling of the in situ state of stress in elastic layered rock subject to stress and strain-driven tectonic forces: Solid Earth, **8**, 479–498.

Sayers, C., and M. Kachanov, 1995, Microcrack-induced elastic wave anisotropy of brittle rocks.: Journal of Geophysical Research: Solid Earth, **100**, 4149–4156.

Sayers, C., J. Van Munster, and M. King, 1990, Stress-induced ultrasonic anisotropy in berea sandstone: International Journal of Rock Mechanics and Mining Sciences and Geomechanics Abstracts, **27**, 429–436.

Schmitt, D., 2015, Geophysical properties of the near surface earth: Seismic properties, *in* Treatise on Geophysics, 2nd ed.: Oxford Elsevier.

Schoenberg, M., and C. Sayers, 1995, Seismic anisotropy of fractured rock: Geophysics, **60**, 204–211.

Scott, T. J., Q. Ma, and J. Roegiers, 1993, Acoustic velocity changes during shear enhanced compaction of sandstone: International Journal of Rock Mechanics and Mining Sciences and Geomechanics Abstracts, **30**, 763–769.

Shao, H., S. Kabilan, S. Stephens, N. Suresh, A. Beck, T. Varga, P. Martin, A. Kuprat, H. Jung, W. Um, A. Bonneville, D. Heldebrant, K. Carroll, J. Moore, and C. Fernandez, 2015, Environmentally friendly, rheoreversible, hydraulic-fracturing fluids for enhanced geothermal systems: Geothermics, **58**, 22–31.

Shapiro, S., E. Rothert, V. Rath, and J. Rindschwentner, 2002, Characterization of fluid transport properties of reservoirs using induced microseismicity: Geophysics, **67**, 212–220.

Slawinski, M., 2015, Waves and rays in elastic continua, 3rd ed.: World Scientific Publishing Co.

Smith, W., P. Foote, and P. Busand, 1929, Packing of homogeneous spheres:

Physical Review, **34**, 1271–1274.

Smyth, J., and T. Mccormick, 1995, Crystallographic data for minerals, *in* Mineral Physics and Crystallography: A Handbook of Physical Constants: American Geophysical Union, 1–17.

US EIA, 2016, United States Energy Information Administration Annual Energy Outlook: Accessed online at https://www.eia.gov/forecasts/aeo.

Van der Baan, M., D. Eaton, and M. Dusseault, 2013, Microseismic monitoring developments in hydraulic fracturing stimulation, *in* Effective and sustainable hydraulic fracturing: Intech, 439–466.

Walpole, L., 1966, On bounds for the overall elastic moduli of inhomogeneous systems - I: Journal of the Mechanics and Physics of Solids, **14**, 151–162.

Warpinski, N., 1994, Interpretation of hydraulic fracture mapping experiments: Presented at the University of Tulsa Centennial Petroleum Engineering Symposium, Society of Petroleum Engineers.

———, 2009, Microseismic monitoring: Inside and out: Journal of Petroleum Technology, **61**, 80–85.

Warpinski, N., M. Mayerhofer, K. Agarwal, and J. Du, 2013, Hydraulic-fracture geomechanics and microseismic-source mechanisms: SPE Journal, **18**, 766–780.

Warpinski, N., S. Wolhart, and C. Wright, 2004, Analysis and prediction of microseismicity induced by hydraulic fracturing: SPE Journal, **9**, 24–33.

Wyllie, M., A. Gregory, and G. Gardner, 1956, Elastic wave velocities in heterogeneous and porous media: Geophysics, **21**, 41–70.

Zatsepin, S., and S. Crampin, 1997, Modelling the compliance of crustal rock - I. response of shear-wave splitting to differential stress: Geophysical Journal International, **129**, 477 – 494.

Zimmerman, R., 1991, Compressibility of sandstones: Elsevier.